

Four Dimensional Trace Space Measurement*

Michael E. Hernandez

Stanford Linear Accelerator Center
Stanford University
Stanford, CA 94309

SLAC-Report-741

Prepared for the Department of Energy
under contract number DE-AC02-76SF00515

Printed in the United States of America. Available from the National Technical Information Service, U.S. Department of Commerce, 5285 Port Royal Road, Springfield, VA 22161.

* Ph.D. thesis, Stanford University, Stanford, CA 94309


FOUR DIMENSIONAL TRACE
SPACE MEASUREMENT

A DISSERTATION
SUBMITTED TO THE DEPARTMENT OF PHYSICS
AND THE COMMITTEE ON GRADUATE STUDIES
OF STANFORD UNIVERSITY
IN PARTIAL FULFILLMENT OF THE REQUIREMENTS
FOR THE DEGREE OF
DOCTOR OF PHILOSOPHY

Michael E. Hernandez
March 2003


© Copyright by Michael E. Hernandez 2003
All Rights Reserved

I certify that I have read this dissertation and that, in my opinion, it is fully adequate in scope and quality as a dissertation for the degree of Doctor of Philosophy.



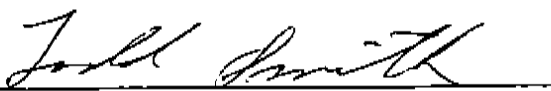
Helmut Wiedemann
(Principal Adviser)

I certify that I have read this dissertation and that, in my opinion, it is fully adequate in scope and quality as a dissertation for the degree of Doctor of Philosophy.



Herman Winick
(Applied Physics)

I certify that I have read this dissertation and that, in my opinion, it is fully adequate in scope and quality as a dissertation for the degree of Doctor of Philosophy.



Todd Smith
(Physics)

Approved for the University Committee on Graduate Studies:

Abstract

Future high energy colliders and FELs (Free Electron Lasers) such as the proposed LCLS (Linac Coherent Light Source) at SLAC require high brightness electron beams. In general a high brightness electron beam will contain a large number of electrons that occupy a short longitudinal duration, can be focused to a small transverse area while having small transverse divergences. Therefore the beam must have a high peak current and occupy small areas in transverse phase space and so have small transverse emittances. Additionally the beam should propagate at high energy and have a low energy spread to reduce chromatic effects.

The requirements of the LCLS for example are pulses which contain 10^{10} electrons in a temporal duration of 10 ps FWHM with projected normalized transverse emittances of 1π mm mrad[1]. Currently the most promising method of producing such a beam is the RF photoinjector. The GTF (Gun Test Facility) at SLAC was constructed to produce and characterize laser and electron beams which fulfill the LCLS requirements

Emittance measurements of the electron beam at the GTF contain evidence of strong coupling between the transverse dimensions of the beam. This thesis explores the effects of this coupling on the determination of the projected emittances of the electron beam. In the presence of such a coupling the projected normalized emittance is no longer a conserved quantity. The conserved quantity is the normalized full four dimensional phase space occupied by the beam. A method to determine the presence and evaluate the strength of the coupling in emittance measurements made in the laboratory is developed. A method to calculate the four dimensional volume the beam occupies in phase space using quantities available in the laboratory environment is

also developed. Results of measurements made of the electron beam at the GTF that demonstrate these concepts are presented and discussed.

Acknowledgements

I would like to thank my advisor Helmut Wiedemann for introducing me to and guiding me through the field of accelerator physics. I was able to perform experiments on the SPEAR storage ring, at the SUNSHINE facility on Stanford campus and at the GTF facility at SSRL due to Professor Wiedemann's desire to make my experience at Stanford as broad as possible. In particular, the SUNSHINE facility allowed students full control of a world class accelerator and the students were expected to work on all aspects of the accelerator. From this base I was able to participate in the construction of the GTF facility at SSRL. At SUNSHINE I worked with Dr.s HungChi Lihn, David Bocek, Pam Kung, Chitlada Settakorn and Professor Wiedemann's other students Kristina Woods and Jim Sebek. All of whom helped me in my journey to understand accelerator physics. I am grateful to all of them for discussions on physics and life and assistance with all of the struggles of graduate work.

I wish to thank Professor Herman Winick who was instrumental in the construction and commissioning of the GTF. Professor Winick is a master at getting people and resources together to accomplish challenging tasks such as the construction of the GTF accelerator and laser systems. Professor Winick always had a valuable opinion about all aspects of the GTF. He also understood the difficulties involved with construction and operation of the GTF especially the toll that long hours takes on ones spirit. During the construction of the GTF I was fortunate to work with the late Jim Weaver who was a one of kind RF engineer who taught me much about RF design and engineering. He showed me how to make RF measurements by constructing individual circuits as they did before the days of network analyzers. Jim taught me about thermionic RF guns, Photocathode RF guns and the associated RF systems to

drive them. I also thank Drs Jym Clendenin and John Schmerge for their technical assistance in the operation of the GTF. I would also like to express appreciation to Professor Todd Smith for participating in my oral exam and in the reading of this thesis

I wish to thank the SSRL technical staff especially Gary Woodcock and Mike Nalls for their hard work and for "keeping me out of trouble" when constructing the mechanical and vacuum systems of the GTF respectively. I am also grateful to have worked with two fabulous machinists Mike Swanson and Jim Hammer who manufactured most of the GTF components, dealt with my non-ANSI drawings and always had suggestions to improve everything I designed. I also am indebted to ALL of the SSRL operators who gave me technical assistance and seemingly endless accesses to the Linac vault. Especially P.J. Boussina who was instrumental in the creation of the control system of the GTF.

The drive laser system at the GTF was a wonderful and painful learning experience and I am grateful to have worked with Dr. David Reis from the University of Rochester while he was working on his thesis. David taught me much about high power CPA Nd:Glass laser systems. I also wish to thank Bob Eittlebrick from Positive Light Laser Company who was instrumental in the debugging of the new regen system.

I wish to thank my family for all of their support and encouragement. I am especially grateful to my mother for providing all manner of encouragement and support through my entire educational experience. I wish that my father could have lived to see me complete the process. Finally I wish to thank my wife Stephanie who always supported me in the journey through graduate school. I could not have completed this journey without her.

Contents

Abstract	iv
Acknowledgements	vi
1 Introduction	1
1.1 GTF	1
1.2 Brightness	3
1.3 Emittance	3
1.4 Collider Luminosity	6
1.5 Free Electron Laser Performance	7
1.6 Accelerator System	8
1.7 Drive Laser System	11
2 Emittance Measurement	16
2.1 Phase Space	16
2.2 Trace Space	21
2.3 Linear Beam Dynamics	24
2.4 Moments Of The Distribution	31
2.5 Transformation Of The Moments Of The Distribution	35
2.6 Determination Of The Distribution Moments	37
2.7 Experimental System	41
2.8 Numerical Analysis Considerations	43

3	Simulations	45
3.1	Generation Of The Distributions	45
3.2	Simulation With A Symmetric Beam	48
3.2.1	Simulation With An Asymmetric Beam	52
3.3	Solenoidal Magnets And Coupling	57
3.3.1	Simulations With Coupling	59
3.3.2	Astigmatic Beam	59
3.3.3	Simulations With Symmetric Beams	67
3.3.4	Simulations With Bi-Symmetric Beams	70
4	Four Dimensional Trace Space Analysis	74
4.1	Two Dimensional Coupling	74
4.2	Four Dimensional Beam Matrix With Partial Coupling	76
4.3	Four Dimensional Beam Matrix With Full Coupling	79
4.4	Measuring The Four Dimensional Trace Space Volume	82
4.4.1	Horizontal Information	83
4.4.2	Vertical Information	86
4.4.3	Correlation Information	87
4.5	Normalization	92
5	Simulations With Coupling	94
5.1	Simulation Method	94
5.2	Astigmatic Beams	97
5.3	Variation Of Doublet Parameters	108
5.4	Determination Of The Initial Rotation Of The Beam	113
5.5	Symmetric Distribution	118
5.6	Simulations With Bi-Symmetric Beams	127
5.7	Characterization Of σ_{13} And r_{13}	132
6	PARMELA Simulations	141
6.1	Simulation Parameters	142
6.2	Asymmetric Distribution on the Cathode	143

6.3	Quantities From The Distribution At The Doublet Entrance	144
6.4	Quantities From 4-D Quadrupole Scan	151
7	Measurements	157
7.1	System Parameters	158
7.2	Data Collection Method	161
7.3	Data Reduction Technique	165
7.4	Results	174
7.4.1	Raw Data	174
7.4.2	Data Reduction	188
7.4.3	qs1 Isol=140A	201
7.4.4	qs2 Isol=145A	203
7.4.5	qs3 Isol=150A	205
7.4.6	qs4 Isol=142A	207
7.4.7	qs5 Isol=147A	209
7.5	Discussion Of Results	211
7.6	Conclusions	216
7.7	Future	218
	Bibliography	220

List of Tables

3.1	Plot of x-y and x-x' distributions for three different q2 strengths . . .	51
3.2	Plots of x-y and x-x' distributions for asymmetric beam for three different q2 strengths	55
3.3	Plots of x-y and x-x' distributions for three different q2 strengths for rotated asymmetric beam	61
3.4	Plots of x-y and x-x' distributions for symmetric beam rotated for three different q2 strengths	68
3.5	Plot of x-y and x-x' distributions for bi-symmetric beam rotated for three different q2 strengths	71
5.1	Values for 4-DVol Initial, Calculated and relative error	99
5.2	Values for 4-DVol Initial, 1/2exey calculated and the relative error between them	100
5.3	Individual Sigma Vector elements for the initial distribution and for the calculated values at various rotation angles	103
5.4	Plots of sigma11 and sigma33 versus q2 strength for three different rotation angles	105
5.5	Plots of sigma13 and r13 versus q2 strength for three different rotation angles	106
5.6	Plots of sigma11 and sigma33 versus q2 strength for three different doublet parameters	110
5.7	Plots of sigma13 and r13 versus q2 strength for three different doublet parameters	111
5.8	Projected and 4-DVol quantities for three different doublet parameters	112

5.9	Table of values for projected and 4-DVol	116
5.10	Values for 4-DVol initial, calculated and their relative error for different rotation angles for symmetric distribution	121
5.11	Values for 4-DVol initial and $1/2ex_{ey}$ calculated and their relative error for different rotation angles for symmetric distribution	122
5.12	Values for ex and ey for different rotation angles for symmetric distribution	123
5.13	Values for sigma vector for initial distribution and three different rotation angles for symmetric distribution	125
5.14	Elements of sigma vector for initial distribution and three different rotation angles for bi-symmetric distribution	130
6.1	Normalized 4-D Volume vs projected quantities at doublet entrance for asymmetric distributions on cathode	147
6.2	Transverse-Longitudinal Correlation coefficients for asymmetric distributions on the cathode	149
6.3	Normalized 4-DVol initial, calculated and projected quantities for asymmetric distributions on cathode	155
7.1	Constraints on the projected spaces	192
7.2	Results for all solenoid settings	199

List of Figures

1.1	Ellipse surrounding beam distribution in trace space	4
1.2	GTF Accelerator System	10
1.3	GTF Laser System	15
2.1	Ellipse surrounding beam distribution in trace space	32
3.1	Initial x-y distribution for symmetric distribution	49
3.2	Initial x-x' distribution for symmetric distribution	50
3.3	Square of beam half width vs q2 strength for symmetric distribution .	52
3.4	Initial x-y distribution for asymmetric distribution	53
3.5	Initial x-x' distribution for asymmetric distribution	54
3.6	Square of beam half width vs q2 strength for asymmetric distribution	56
3.7	Square of beam half width vs q2 strength for rotated asymmetric dis- tribution	62
3.8	Images of the beam from a quadrupole scan at the GTF the horizontal and vertical axes are x and y pixel number respectivley	63
3.9	Projected normalized emittance vs rotation angle for asymmetric beam	65
3.10	Projected normalized emittance vs rotation angle for symmetric beam	69
3.11	Projected normalized emittance vs rotation angle for bi-symmetric dis- tribution	72
4.1	Ellipse surrounding beam distribution in trace space	75
4.2	Ellipse surroundinig beam distribution in x-y space	88

5.1	Plot of projected normalized emittances versus rotation angle for astigmatic beam	98
5.2	Plot of projected normalized $1/2\epsilon_x\epsilon_y$ and V_{4-D} Calculated and V_{4-D} Initial versus rotation angle for astigmatic beam	98
5.3	$V_{4-D,RelativeError}$ for different number of particles	101
5.4	$\frac{1}{2}\epsilon_x\epsilon_y$ Relative Error for different number of particles	102
5.5	Values for the Calculated Sigma Vector for three rotation angles . . .	103
5.6	Plot of r13 versus q2 strength for no rotation of the beam	107
5.7	Plot of r13 versus q2 strength for different rotation angles	108
5.8	Calculated $1/2\epsilon_x\epsilon_y$ and V_{4-D} versus rotation angle α_1	114
5.9	Calculated $1/2\epsilon_x\epsilon_y$ and V_{4-D} versus rotation angle α_1 change of horizontal scale	115
5.10	Elements of the sigma vector	117
5.11	Plot $1/2\epsilon_x\epsilon_y$, V_{4-D} calc and initial versus rotation angle	120
5.12	Plot ϵ_x and ϵ_y versus rotation angle	120
5.13	Values for calculated sigma vector for three different rotation angles for symmetric distribution	124
5.14	Plot r13 versus q2 strength for different rotation angles for symmetric distribution	126
5.15	Plot $1/2\epsilon_x\epsilon_y$ and 4-DVol calculated and initial for different rotation angles for bi-symmetric distribution	128
5.16	Plot calculated sigma vector elements for three different rotation angles for bi-symmetric distribution	129
5.17	Plot r13 versus q2 strength for different rotation angles for bi-symmetric distributions	131
5.18	Plot of elements of the transfer matrix used in the simulations	133
5.19	Plot of r13 versus q2 strength for $\sigma_x = \sigma_y$ and vary σ_y	138
5.20	Plot of r13 versus q2 strength for $\sigma_x = \sigma_y$ and vary σ_y	139
5.21	Plot of r13 versus q2 strength vary σ_y and σ_y with ϵ_y constant	140

6.1	Initial sigma vector elements at the doublet entrance for asymmetric distributions on the cathode	145
6.2	Correlation coefficients at the doublet entrance as a function of asymmetry in the initial distributions on the cathode	146
6.3	Transverse-longitudinal correlation coefficients as a function of asymmetry in the initial distributions on the cathode	148
6.4	All correlation coefficients as a function of asymmetry in the initial distributions on the cathode	150
6.5	Sigma11 vs q2 strength for different asymmetry in the initial distribution on the cathode	151
6.6	Sigma33 vs q2 strength for different asymmetry in the initial distributions on the cathode	152
6.7	Sigma13 vs q2 strength for different asymmetry in the initial distributions on the cathode	153
6.8	r13 vs q2 strength for different asymmetry in the initial distributions on the cathode	154
7.1	Image of beam illustrating the cathode defect	161
7.2	Line out through the peak in a typical image of the beam (background not subtracted). Horizontal axis is pixel number and vertical axis is intensity.	164
7.3	Typical background subtracted image of the electron beam	169
7.4	Typical background subtracted image of the electron beam rotated view	170
7.5	qs1 Isol=140[A] Sigma33 vs q2 strength change of vertical scale . . .	185
7.6	qs2 Isol=145[A] Sigma33 vs q2 strength change of vertical scale . . .	186
7.7	qs3 Isol=150[A] Sigma33 vs q2 strength change of vertical scale . . .	186
7.8	qs4 Isol=142[A] Sigma33 vs q2 strength change of vertical scale . . .	187
7.9	qs5 Isol=147[A] Sigma33 vs q2 strength change of vertical scale . . .	187
7.10	Plot qs1 sigma11 versus q2 strength measured and fit values	201
7.11	Plot qs1 sigma33 versus q2 strength measured and fit values	202
7.12	Plot qs1 sigma13 versus q2 strength measured and fit values	202

7.13	Plot qs2 sigma11 versus q2 strength measured and fit values	203
7.14	Plot qs2 sigma33 versus q2 strength measured and fit values	204
7.15	Plot qs2 sigma13 versus q2 strength measured and fit values	204
7.16	Plot qs3 sigma11 versus q2 strength measured and fit values	205
7.17	Plot qs3 sigma33 versus q2 strength measured and fit values	206
7.18	Plot qs3 sigma13 versus q2 strength measured and fit values	206
7.19	Plot qs4 sigma11 versus q2 strength measured and fit values	207
7.20	Plot qs4 sigma33 versus q2 strength measured and fit values	208
7.21	Plot qs4 sigma13 versus q2 strength measured and fit values	208
7.22	Plot qs5 sigma11 versus q2 strength measured and fit values	209
7.23	Plot qs5 sigma33 versus q2 strength measured and fit values	210
7.24	Plot qs5 sigma13 versus q2 strength measured and fit values	210
7.25	Normalized V_{4-D} vs Solenoid Strength	213
7.26	Normalized V_{4-D} and projected quantities ϵ_x , ϵ_y and $\frac{1}{2}\epsilon_x\epsilon_y$ vs solenoid strength	213

Chapter 1

Introduction

1.1 GTF

The GTF (Gun Test Facility) at SLAC (Stanford Linear Accelerator Center) was constructed to create and characterize a high brightness electron beam. The system consists mainly of an Nd:Glass drive laser system, a 1.6 cell copper cathode RF gun, a single S-band SLAC linac section and diagnostics to measure the charge, energy and emittance of the electron beam. The goal of the GTF is to generate an electron beam that meets the LCLS (Linac Coherent Light Source) requirements of a 1 nC of charge with a normalized transverse emittance of 1 mm mrad[1]. While these goals were not met during my time at the GTF I learned a great deal about RF photoinjectors, Nd:Glass laser systems and especially the intricacies of measuring such small an electron beam emittance.

This thesis examines problems encountered in the emittance measurement process for the electron beam at the GTF. Specifically, measurements of the electron beam indicate a strong coupling between the transverse degrees of freedom of the beam. In the presence of such a coupling, the projected emittance is no longer a conserved quantity[2],[3]. The conserved quantity is the full four dimensional phase space occupied by the electron beam[2],[3]. In this thesis I first discuss the basic concepts of brightness, emittance and how they relate to collider and FEL (Free Electron Laser) performance. Then the details of the GTF accelerator system and laser systems are

presented. A more detailed examination of emittance and the fundamentals of linear beam dynamics which form the building blocks for how the emittance is measured in the laboratory using standard quadrupole scan technique are presented. Then using Monte Carlo methods to simulate Gaussian distributions that demonstrate the reliability of the quadrupole scan techniques are presented. With the inclusion of a rotation which couples the transverse coordinates, simulations using the quadrupole scan technique of the beam demonstrate the non-conservation of the projected emittance and the presence of coupling effects as seen in the experimental data. Such rotations are present in the solenoid that is used to focus the beam as it exits the gun in the RF photoinjector at the GTF. The simulations are then used to demonstrate the conservation of the four dimensional volume that is determined by calculation of all of the moments and couplings in the distribution. However, all of this information is not available in the laboratory environment. A method to determine the four dimensional trace space of the electron beam utilizing quantities available in the laboratory environment is developed and simulated. Since the coupling between the transverse degrees of freedom indicates a violation of the conservation of the projected quantities a method to detect the presence and determine the strength of the coupling is presented. And finally the algorithm for four dimensional trace space volume measurement is applied to data from measurements of the electron beam at the GTF. Problems traced to the effects of limited system resolution were encountered and solved. The resulting measurements serve to demonstrate the presence of transverse coupling effects in the data and illustrate the effects of the coupling on the relationship between the four dimensional trace space volume and the projected quantities.

My contributions to the GTF project were the construction of a large portion of the electron accelerator system and electron beam diagnostics for charge, energy and emittance measurement. I was very fortunate to work with the late Jim Weaver on portions of the RF system and especially the construction of the 1.6 cell RF gun. I rebuilt the laser system after the oscillator and regenerative amplifier were returned to the generous lenders, ANL and University of Rochester respectively. I spent much time trying to improve the system performance and learned a great deal about CPA

(Chirped Pulse Amplification) and the production of the UV pulses through harmonic generation. Finally I contribute the method of four dimensional trace space analysis which in the presence of coupling between the transverse dimensions of an electron beam allows the measurement of the conserved quantity, the four dimensional trace space volume occupied by the beam.

1.2 Brightness

High brightness electron beams are required for future high energy colliders and the proposed LCLS. In general a high brightness electron beam consists of a distribution which contains a large number of electrons with total charge q and within a short temporal duration, Δt , that can be focused to a small transverse area with low transverse divergence. The beam will then have a high peak current, charge divided by pulse duration. The beam will also occupy a small area in transverse phase space which is approximately given by the minimum spot size times the transverse divergence. This quantity is known as the emittance of the beam at the location of the minimum spot size. The brightness is then given by [4], [5]:

$$B = \frac{I_p}{\frac{\pi^2}{2} \epsilon_x \epsilon_y} \quad (1.1)$$

where $I_p = \frac{q}{\Delta t}$ is the peak current and ϵ_x and ϵ_y are the horizontal and vertical emittances of the beam which are discussed in the next section.

1.3 Emittance

Initially I will present a simplistic introduction to emittance in order to motivate its importance to the requirements of colliders and FELs. In the following chapters I will discuss the emittance in greater detail. The basic definition for the emittance of a particle beam is that it is the area the beam occupies in trace space. This simple definition belies the complexity of trying to associate information obtained in the

laboratory with the elegant theory of Hamiltonian mechanics. At any given time or position along the accelerator system each of the particles of the beam occupies a particular position in x, y and z space and has a particular value for each of the momenta p_x, p_y and p_z . In the Hamiltonian formalism these variables constitute canonical variables provided $\frac{\partial H}{\partial q_i} = -\frac{dp_i}{dt}$ and $\frac{\partial H}{\partial p_i} = \frac{dq_i}{dt}$ where $q_1 = x, p_1 = p_x, q_2 = y, p_2 = p_y$ and $q_3 = z, p_3 = p_z$ and H is the Hamiltonian of the system[6]. The six dimensional volume formed by the six coordinates of all of the particles in the beam is known as phase space and is a conserved quantity[7]. However, for the particles in the beam of an accelerator one cannot directly measure p_x and p_y . The quantities $x' = p_x/p_z$ and $y' = p_y/p_z$ where $p_z \gg p_x, p_y$ which are the direction tangents or angles the particles make with the longitudinal direction can be measured. Utilizing these new variables the beam then occupies a region of the six dimensional space formed by x, x', y, y', z and p_z . This space is known as trace space. Under appropriate conditions trace space is a conserved quantity[8], [9]. If the spatial coordinates of the beam are not coupled we can separately study the subspace $x - x', y - y'$ and $z - p_z$ which are formed by projecting them out from the full six dimensional distribution [3]. The distribution of the beam in $x - x'$ space can be represented by an ellipse which surrounds the distribution.

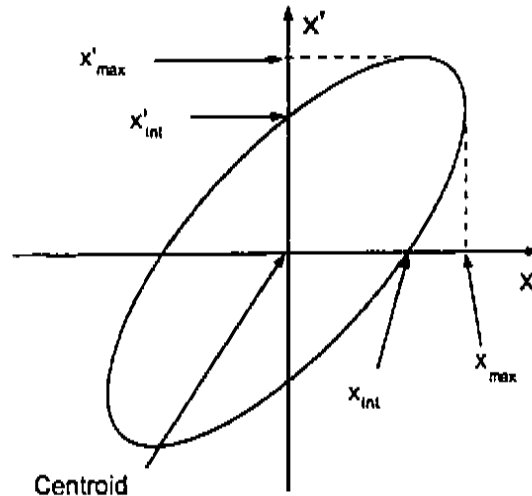


Figure 1.1: Ellipse surrounding beam distribution in trace space

The ellipse is centered about the centroid of the distribution. The ellipse is characterized by three quantities: the projected lengths of ellipse along the two axes, x_{\max} and x'_{\max} , and the orientation of the ellipse, xx' , in $x - x'$ space. There is a correlation between x and x' in the distribution that is shown as a tilt of the ellipse in the $x - x'$ diagram. The correlation indicates whether the beam is converging, diverging or transforming between converging to diverging. The area of the ellipse is given by[10]:

$$A = \pi \sqrt{(x_{\max})^2 (x'_{\max})^2 - (xx')^2} \quad (1.2)$$

and the geometric emittance of the beam is defined by:

$$\epsilon = \frac{A}{\pi} = \sqrt{(x_{\max})^2 (x'_{\max})^2 - (xx')^2}. \quad (1.3)$$

If the system is conservative and there is no acceleration the area of the ellipse will be constant as the beam propagates through the accelerator system by Liouville's theorem[7]. In order to compare beams of different energy one can use the so called normalized emittance which is found by multiplying the geometric emittance by the factor $\beta\gamma$ to transform the direction tangent terms into true canonical variables[11]:

$$\epsilon_n = \beta\gamma\epsilon = \beta\gamma \sqrt{(x_{\max})^2 (x'_{\max})^2 - (xx')^2} \quad (1.4)$$

where γ is given by the beam energy, $\gamma = \frac{E}{mc^2} + 1$, and $\beta = v/c$. The geometric emittance is the quantity measured in the laboratory. The specific details for methods to measure the emittance will be presented in detail in the following chapters.

As a simple example of the implications of emittance consider the situation where the ellipse is oriented upright so that $xx' = 0$ then $\epsilon = x_{\max}x'_{\max}$. Now suppose one wishes to minimize the width of the distribution in order to create a small spot with the beam. The quantity x_{\max} represents the horizontal half width of the beam. If x_{\max}

is decreased then the quantity x'_{\max} which represents the divergence of the beam must increase in order for the area of the ellipse $A = \pi\epsilon = x_{\max}x'_{\max}$ to remain constant. At some point the physical constraints of the system may be violated, and some particles may strike the vacuum chamber containing the beam due to the increased angle the beam makes with the longitudinal axis. So for an upright ellipse in order to have a small emittance one needs to have small values for BOTH x_{\max} and x'_{\max} since minimizing only one would be made at the expense of increasing the other. The point is that the conservation of area forms a constraint on the possible values for the beam size and divergence.

1.4 Collider Luminosity

The emittance of the beam affects the performance of high energy colliders. These machines contain interaction regions where particle beams are brought together to interact. The beams must be confined to a small volume formed by the transverse spatial area and the temporal duration of the beam such that the particle densities at the interaction region are as high as possible. These requirements are characteristic of a high brightness beam. The measure of the efficiency of the collision process is given by the Luminosity[12]:

$$L = \frac{N_1 N_2 \nu_{\text{rev}}}{4\pi\sigma_x\sigma_y B} \quad (1.5)$$

This is a general expression where it is assumed that both of the beams have the same cross section and where σ_x and σ_y are the transverse dimensions of the beams at the interaction point, N_1 and N_2 are the number of particles in each beam, B is the number of bunches in each of the beams and ν_{rev} is the revolution frequency of the bunches. In order to reach higher Luminosity one should increase any of the quantities: the number of particles or the revolution frequency; and the transverse dimensions of the beam must be reduced or the number of bunches reduced for the same number of particles per beam. The transverse dimensions of the distribution are

given by $\sigma_x = \sqrt{\beta_x \epsilon_x}$ where β_x is the horizontal betatron function at the interaction point and ϵ_x is the emittance of the particle beam distribution. The betatron function is determined by the accelerator components, and so the minimum achievable transverse dimensions of the beam are limited by the emittance, the area the beam occupies in phase space. Therefore a high brightness beam is important for colliders.

1.5 Free Electron Laser Performance

With regards to FEL (Free Electron Laser) performance, the emittance of the electron beam is one of the factors which limits the wavelengths of the radiation produced from the FEL. Electrons in the beam will emit synchrotron radiation if the beam is made to accelerate by bending the beam using magnetic fields. If a series of magnets is arranged to periodically deflect the beam the amount of radiation that is produced can be increased. This is a very simplistic description of the FEL but the concept is clear the free electrons in a beam will radiate energy in the presence of particular magnetic fields. Since the radiation is emitted from the electron distribution, the cross sectional area of the distribution forms the source area for the radiation. It is well known that for a distribution of electrons coherent radiation can be produced at wavelengths equal to and greater than the dimensions of the distribution[13]. If the electron beam dimensions can be reduced the shortest wavelength of the coherent radiation can be reduced. However, the source size alone does not determine the limits to the shortest coherent wavelengths that can be produced from the FEL. The coherent photon beam is subject to diffraction effects.

The image plane or observation plane will be far from the source so the diffraction pattern will be that of Fraunhofer diffraction. An examination of the Fraunhofer diffraction for a Gaussian source distribution shows that the emittance of the photon beam will determine the distribution of the radiation field $U(p)$ of the coherent radiation at the observation point p . If the electron beam source is considered to be a radially symmetric Gaussian, with standard width σ_r , then the radiation field pattern at the observation point P will be of the form[13]:

$$U(p) = Const * \exp \left[\frac{-(k\sigma_r\sigma_{r'})^2}{2} \right] \quad (1.6)$$

where $k = \frac{2\pi}{\lambda}$ is the wavenumber of the radiation and σ_r is the standard divergence of the radiation. The distribution for the radiation field is a Gaussian with a standard width of $(k\sigma_r\sigma_{r'})^2 = 1$ where the amplitude of $U(p)$ becomes a factor $\exp\{-\frac{1}{2}\}$ of the maximum value. Rewriting the standard width as $\sigma_r\sigma_{r'} = \frac{\lambda}{2\pi}$ and since $\sigma_{x,y} = \sqrt{2}\sigma_r$ and $\sigma_{x',y'} = \sqrt{2}\sigma_{r'}$ then in terms of the emittance of the photon beam:

$$\epsilon_{\text{photon}} = \sigma_{x,y}\sigma_{x',y'} = \frac{\lambda}{4\pi} \quad (1.7)$$

In order to produce spatially coherent radiation at the wavelength λ , the electron beam emittance must be less than or equal to the photon beam emittance:

$$\epsilon_{\text{electron}} \leq \frac{\lambda}{4\pi} \quad (1.8)$$

The emittance in the expression above is the geometric emittance. Using this criterion, in order to produce spatially coherent *5Angstrom* radiation from a 15GeV electron beam the required geometric emittance of the electron beam would be $4 * 10^{-11}$ mrad and the normalized emittance would be 1.2mm mrad. So the electron beam emittance dictates the performance of an FEL.

1.6 Accelerator System

In order to attempt to produce and study a low emittance, high brightness electron beam the GTF (Gun Test Facility) at SLAC (Stanford Linear Accelerator Center) was constructed. The GTF consists of a Nd:glass drive laser system, a 1.6 cell S-band copper cathode RF gun, an emittance compensation solenoid, a single s-band linac

section and diagnostics to measure the charge, energy and transverse emittance of the electron beam. The RF gun was produced through a collaboration between SLAC, BNL (Brookhaven National Laboratory) and UCLA. There are two XK-5 klystrons that produce the RF power used to accelerate the electron beam. One klystron powers the gun and other powers the linac. The laser system forms the master clock for the accelerator, and the klystrons amplify low power RF that is generated from the 24th harmonic of the 119MHz laser oscillator.

The accelerator beam line is shown in Fig. 1.2 on the next page. The accelerator is designated as Gun, Gun To Linac (GTL) the section after the gun and before the linac, Linac, and Linac To Dump (LTD) the section after the linac to the beam dump. The GTL contains a solenoid to focus the beam after it exits the gun. The solenoid is a linear focusing lens and is intended to compensate linear defocusing space charge effects that lead to an enlargement of the projected emittance. This theory of emittance compensation is well developed and the interested reader is referred to several papers on the subject[14],[15],[16]. After the solenoid there is an ICT, (Integrating Current Toroid) to nondestructively measure the beam charge from the gun. Other diagnostics in the GTL are two combination normal incidence SLAC chromate[17] screens and stainless steel Faraday Cups that can be inserted into the beam to view the electron beam and measure the charge after it exits the gun. The second screen/Faraday Cup station contains an in vacuum mirror which directs the UV pulses from the laser transport system onto the cathode at near normal incidence.

After the beam exits the GTL section it is injected into a single 3-meter SLAC type linac section that is capable of accelerating the electron beam up to 35MeV with the available RF from the single XK-5 klystron. After the beam exits the linac there is a quadrupole doublet that consists of a horizontally defocusing quadrupole, Q1, followed by a horizontally focusing quadrupole Q2. The Q2 quadrupole is used as the scanning quadrupole for emittance measurements discussed in detail in the next chapter. The LTD diagnostics include another ICT, a 45 degree incidence phosphor screen to view the beam, a normal incidence YAG screen to measure the beam size for quadrupole scan emittance measurements, a spectrometer magnet to determine the beam energy and energy spread and a final Faraday Cup to measure the charge.

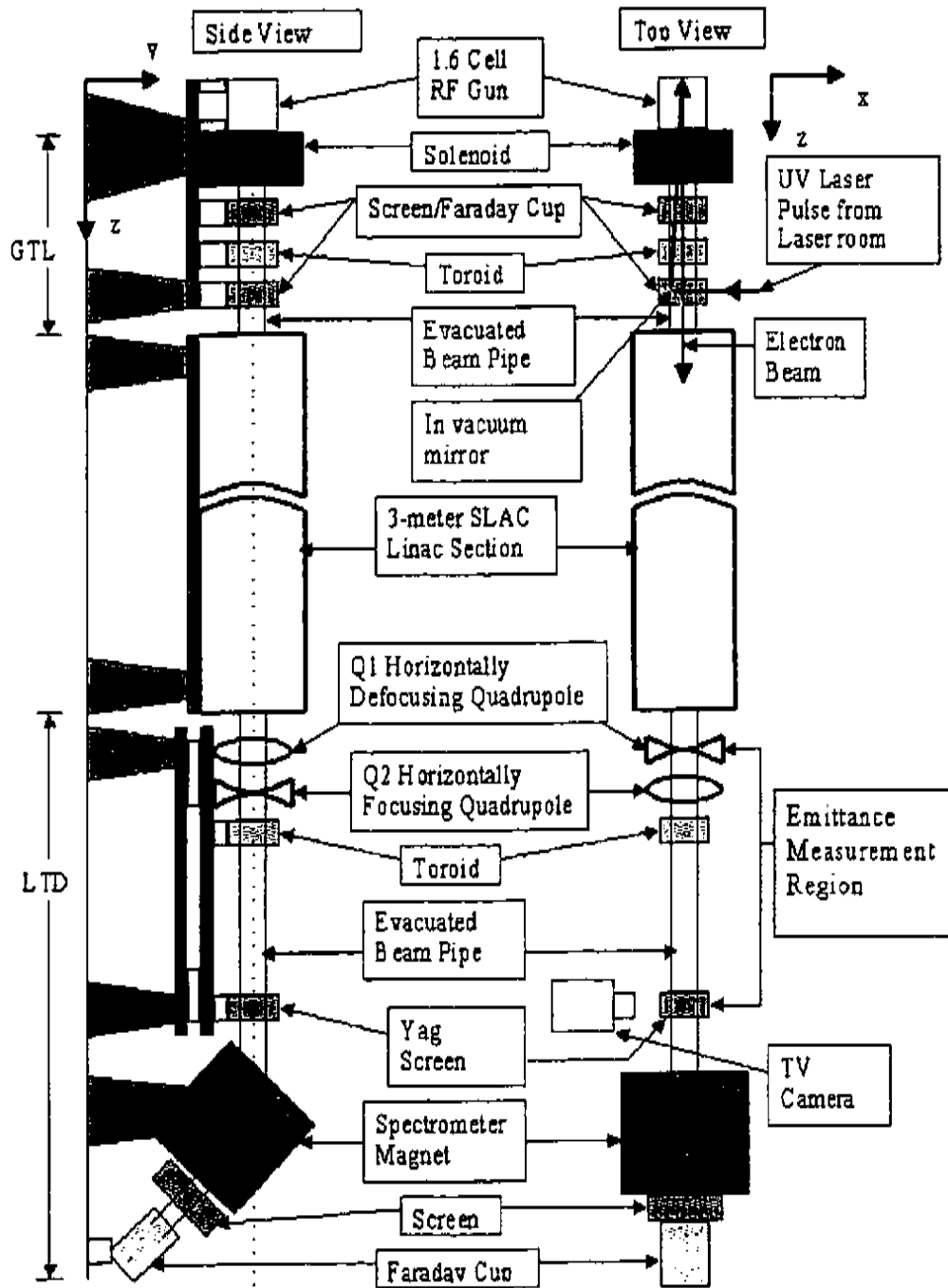


Figure 1.2: GTF Accelerator System

1.7 Drive Laser System

The GTF drive laser system utilizes CPA, chirped pulse amplification, with Nd:Glass as the gain medium to create the UV pulses used to produce the photoelectrons from the copper cathode of the RF electron gun. The laser system used in the measurements presented in this thesis consisted of a Nd:Glass Time Bandwidth oscillator, a stretcher, a Positive Light dual head Nd:Glass regenerative amplifier or "regen", a compressor and nonlinear harmonic generation crystals. The oscillator lases at $\lambda=1054$ nm $\Delta\lambda=6$ nm and produces a pulse train which contains individual pulses of about 1 nJ of energy in 150 fs at a repetition rate of 119 MHz. The oscillator serves as the master clock for the RF system. A small amount of energy that leaks from one of the cavity mirrors is fed to a photodiode that produces a signal which is multiplied up 24 times to produce a low level 2856 MHz signal. This signal is amplified by an RF driver amplifier that produces the RF which is fed to the klystron amplifiers.

The oscillator also provides a low energy seed pulse, about 1nJ in 150fs, that is amplified by the regen to typically 8 mJ, producing a gain of 1 million. A gain that large can be accomplished without damaging the glass gain medium of the regen only if the temporal duration of the seed pulse is increased from 150 fs to about 850 ps by the stretcher to lower the peak power inside the amplifier. The stretcher consists of two gratings which are arranged to produce a wavelength dependent optical path for the seed pulse which stretches the seed pulse by placing a wavelength dependent chirp on the pulse. This reduces the peak power, energy divided by temporal duration of the pulse, in the regen by a factor of about 1.4 million for the last pass through the regen. The regen consists of two "heads" each of which contain a single Nd:glass rod and two flashlamps oriented above and below the rod to pump the rod into an excited state. The vertical orientation of the flash lamps causes asymmetric pumping of the rods which leads to asymmetric gain in the rods. This produces a transversely asymmetric beam in each rod. In order to produce a beam which is transversely symmetric a birefringence compensator is placed between the two heads to rotate the beam about the longitudinal axis of the cavity by 90° so that the asymmetric pumping from one head is approximately canceled by the other head. There are also two Pockel's cells

in the regen cavity that are used in combination with a $\frac{1}{4}\lambda$ waveplate to control the polarization state of the cavity which determines quality factor or "q" of the cavity. The cavity is switched from low to high q for injection of the seed pulse and the q is switched from high to low to eject the amplified pulse. Thus the term q-switched cavity.

The cavity will lase due to spontaneous emission in the rods that is amplified by the excited rods. This situation is known as unseeded operation and produces pulses which are in the mJ range of energy but in the 10 ns range temporally which is much longer than the picosecond duration desired for photoelectron production. This is because the transverse modes in the cavity are limited to the TEM₀₀ mode by a pinhole in the cavity but there is no control of the longitudinal modes in the cavity and all possible longitudinal modes are present in the unseeded operation. The seed produced by the oscillator serves to lock the longitudinal mode of the regen amplifier. Once the seed is injected into the by switching the injection Pockel's cell it is trapped in the cavity for about 80 round trips in the cavity then the ejection Pockel's cell is switched to spoil the q of the cavity. The pulse which is now at about 8 mJ of energy in about 650 ps is ejected from the cavity. The pulse has become slightly shorter due to nonlinear processes in the regen cavity but it is much longer than the desired length of 10 ps. The chirp on the pulse from the stretcher is removed by utilizing another set of gratings identical to those of the stretcher arranged to undo the chirp from the stretcher. The gratings have a low damage threshold and before the high energy pulse from the regen is sent to the compressor, the pulse is spatially filtered. This is accomplished by focusing the beam to a small spot and passing it through a 100 μm diameter pinhole which serves to remove unwanted high frequency structure on the pulse, a second lens is used to re-collimate the beam after the pinhole. Due to the high energy, 8 mJ, and small beam size < 100 μm the beam is capable of breaking down air and causing arcing so the spatial filter is placed in vacuum. After the compressor the removal of the chirp from spatially filtered regen pulse is not complete due to higher order effects in the regen amplifier which modify the chirp. The shortest pulses from the regen from the system discussed here were 3 ps FWHM measured with a streak camera.

The pulse must now be converted from infrared, $\lambda=1054$ nm, to an ultraviolet wavelength $\lambda=263$ nm or photon energy of 4.7 eV to excite the copper cathode. This is accomplished by harmonic generation using nonlinear crystals. There are two BBO crystals in the system. The first crystal is the "doubler" that doubles the frequency of the infrared converting the infrared, $\lambda=1054$ nm, to green, $\lambda=1054/2=527$ nm. The second crystal converts this green light into Ultraviolet $\lambda=263$ nm. This crystal is the "quadrupler" since it quadruples the frequency of the original infrared. The conversion process is relatively low in efficiency. The largest conversion efficiencies obtained were about 20% and typical value were $<20\%$ for each crystal. The conversion efficiency of the crystals is dependent on the brightness input beam. The conversion is increased by using an input pulse which is short in temporal duration and has small transverse dimensions. Ideally the crystals are driven into saturation where the output of the crystals remains constant regardless of the input power to the crystal. This has the advantage of producing an output which is spatially uniform and has an energy that independent of any fluctuations in the input beam energy. However, the crystals have a low damage threshold energy so care must be used when trying to increase the conversion efficiency of the crystals. Since there were no BBO spares the crystals were not driven into saturation . In order to produce the most green and UV, the longitudinal duration of the input IR was made as short as possible by adjusting the compressor to produce the maximum compression. The transverse dimensions of the input were adjusted using a down collimation telescope to reduce the input beam size to $\lesssim 2$ mm diameter. The crystals were placed in tandem so that the output of the first crystal was the input of the second crystal. This allowed for easy tuning of the input beam and the crystals to produce maximum conversion in each crystal.

There was typically $<200 \mu\text{J}$ of ultraviolet available for transverse shaping from an input of ~ 8 mJ 3 ps FWHM infrared or about 15% conversion efficiency for each crystal. After the crystals there was another telescope and aperture combination to spatially filter and up collimate the transverse Gaussian pulse to a transverse sigma of 1 mm. A 2 mm diameter aperture is used to remove the tails of the distribution. This aperture is relay imaged to cathode by placing the aperture at the focus of the

first lens of another telescope with the cathode at the focus of the second lens of the telescope. Due to the tandem orientation of the crystals, the output beam from the crystals contains infrared, green and ultraviolet light. The remaining twelve mirrors in the system are all coated to reflect only ultraviolet wavelengths so after each mirror the amount of green and infrared is reduced to $<.1\%$ of the input value this led to non-measurable amounts of either at the cathode. Before each experimental run of the accelerator system the UV was sampled using a photodiode to ensure that there were no pre- or post-pulses due to improperly setting the timing of the ejection Pockel's cell. This is important since any UV separated in time from the intended pulse would serve to produce additional electrons from the cathode at unwanted phases. Once the beam is transported into the linac vault containing the accelerator system a quartz window with an ultraviolet antireflection coating is used to pass the ultraviolet pulse from air to the vacuum of the accelerator system. And an in-vacuum mirror reflects the laser pulse at near normal incidence onto the cathode.

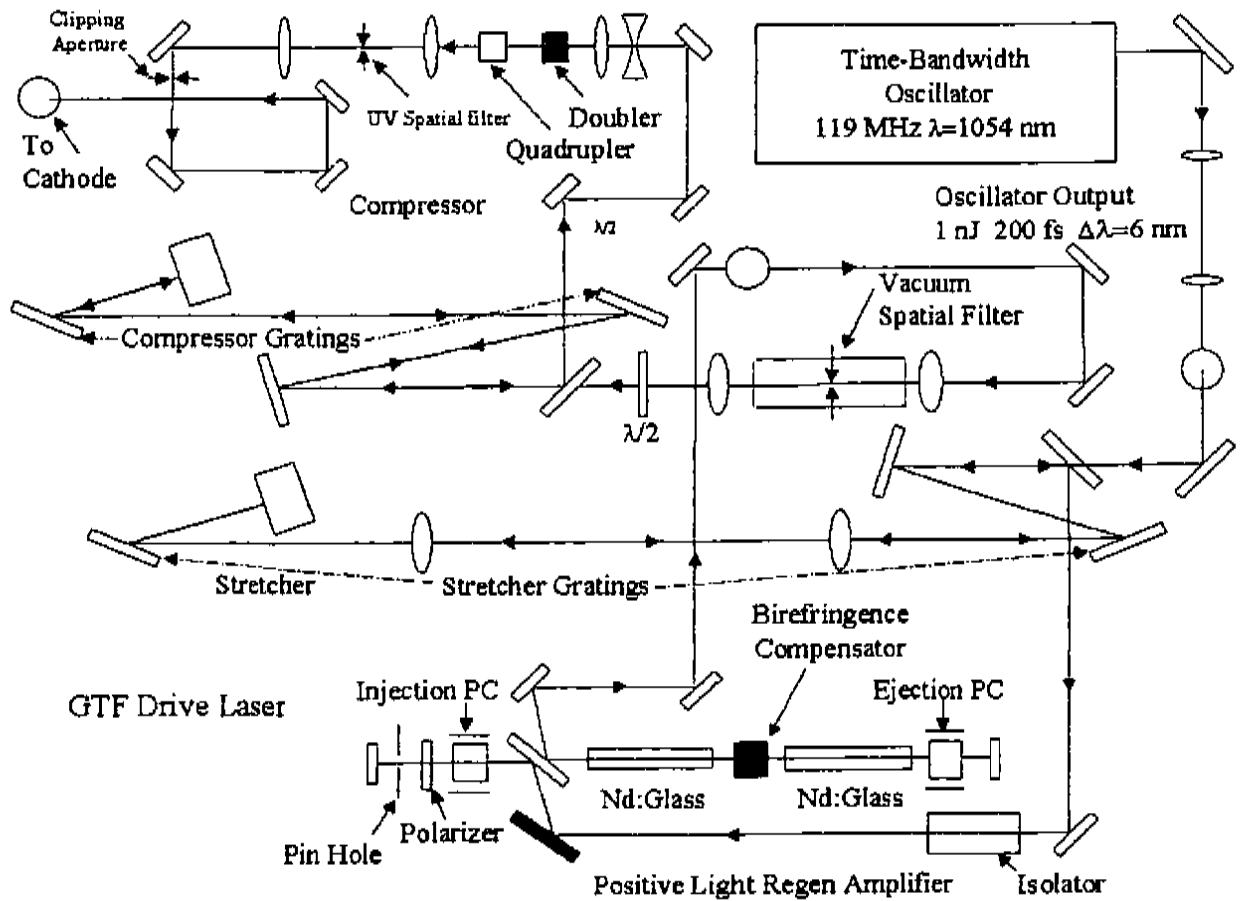


Figure 1.3: GTF Laser System

Chapter 2

Emittance Measurement

In this chapter I discuss the basic concepts which underlie the concept of emittance measurement. First the behavior of a simple harmonic oscillator model is used to introduce the concept of phase space in the Hamiltonian formalism. Issues which arise that must be addressed in applying the Hamiltonian formalism into the laboratory environment are discussed leading to the concept of trace space. The basics of linear beam dynamics are presented in order to understand how to propagate individual particles through a portion of an accelerator. The description of a beam distribution and emittance in terms of the moments of the distribution is discussed. Propagation of the moments of the distribution through a portion of an accelerator using first order beam dynamics is presented. With this background the quadrupole scan technique is described. This technique enables the determination of the moments of the distribution, and so the emittance, using information available in the laboratory environment.

2.1 Phase Space

A typical particle accelerator consists of a source to generate the particles, a transport system to contain the particles and possibly acceleration systems to increase the energy of the beam of particles. In order to understand the behavior of the particle beam it may be treated in the Hamiltonian formalism as a collection of particles

that are subject to forces derivable from potentials. In general the particle beam is treated in the simplest approximation as a collection of non-interacting particles. In the actual beam there are interactions between the particles primarily due to space charge effects. In a beam of identical particle such as electrons, the particles will tend to repel each other due to their charge. For this thesis I will ignore space charge effects. If the beam consists of a collection of n particles, there will be $3n$ degrees of freedom and $6n$ equations of motion. The phase space which the beam occupies will consist of the 6 dimensions $x, p_x, y, p_y, z,$ and p_z . Where $x, y,$ and z are the spatial dimensions of the distribution and $p_x, p_y,$ and p_z are the canonical momenta which are the conjugate variables to x, y and z respectively[6]. The coordinate system for the beam is chosen so that the direction of beam propagation is the z direction and the two transverse directions x and y form a plane which is perpendicular to z . Further if we assume no coupling between the various dimensions then we may consider each of the spatial dimensions and their associated momentum as independent from the other dimensions. Then each sub-space $x - p_x, y - p_y,$ and $z - p_z$ may be studied as an independent system[3].

In order to understand phase space first consider the simplest possible system in an $x - p_x$ sub-space, a single one dimensional harmonic oscillator system. The system consists of a mass, m , connected to a linear spring with spring constant k . The mass moves horizontally on a frictionless surface. The system then allows for exchange between kinetic and potential energy of the mass $\frac{1}{2}mv^2$ and $\frac{1}{2}kx^2$ respectively. The phase space for this simple one dimensional harmonic oscillator consists of the displacement of the mass, x , measured along the horizontal axis and linear momentum of the mass, $p_x = mv$, measured along the vertical axis. Since the system is conservative the equation relating the sum of the kinetic and potential energies to the total energy is given by[18]:

$$\frac{kx^2}{2} + \frac{p_x^2}{2m} = E. \quad (2.1)$$

This relation can be rewritten as:

$$\frac{kx^2}{2E} + \frac{p_x^2}{2mE} = 1 \quad (2.2)$$

This is the equation for an ellipse that describes the trajectory of the mass in $x - p_x$ space or phase space as time evolves. The major and minor axes are aligned with the horizontal and vertical axes. The area of the ellipse is given by[19]:

$$A = \pi(x_{\max})(p_{x\max}) \quad (2.3)$$

Where $x_{\max} = \sqrt{\frac{2E}{k}}$ and $p_{x\max} = \sqrt{2mE}$ are the maximum values of x and p_x respectively. The larger the values for the maxima the greater the area the trajectory of the one dimensional oscillator occupies in phase space. This would represent a system with either large kinetic or potential energy or both, and so a large total energy. Conversely if the area occupied by the trajectory in phase space is small then the maximum excursions of the beam are small which represents a system with small kinetic and potential energy and so small total energy. So if we can determine the quantities x_{\max} and $p_{x\max}$ we can calculate the area in phase space contained by the trajectory of the oscillator in phase space. The size of the area would indicate the total energy of the system. In terms of the quantities x_{\max} , $p_{x\max}$ and A , the equation for the elliptical trajectory in phase space is:

$$\frac{x^2}{x_{\max}^2} + \frac{p_x^2}{p_{x\max}^2} = 1. \quad (2.4)$$

or multiplying both sides by $(x_{\max}p_{x\max})^2 = \left(\frac{A}{\pi}\right)^2$

$$(p_{x\max}x)^2 + (x_{\max}p_x)^2 = \left(\frac{A}{\pi}\right)^2 \quad (2.5)$$

The two equations (2.3), (2.4) and (2.5) above are relatively simple. This is due

to the judicious choice of the coordinate system. If we were to rotate the coordinate system, the total energy of the system is unchanged but the equations above become more complicated. The equation for the ellipse which represents the trajectory in phase space as time evolves becomes in the new coordinate system $x_r - p_{x_r}$, where r denotes rotation:

$$(p_{x_{r\max}} x_r)^2 + 2(xp_x)_r x_r p_{x_r} + (x_{r\max} p_{x_r})^2 = \left(\frac{A}{\pi}\right)^2 \quad (2.6)$$

There is now a coupling between the x_r and p_{x_r} whose strength is given by $2(xp_x)_r$ as indicated by the second term on the left in the equation above. And the area of the ellipse is now given by:

$$A = \pi \sqrt{(x_{r\max})^2 (p_{x_{r\max}})^2 - (xp_x)_r^2} = \pi (x_{\max}) (p_{x_{\max}}). \quad (2.7)$$

where $(xp_x)_r$ is the correlation between x_r and p_{x_r} and x_{\max} and $p_{x_{\max}}$ are measured in the non-rotated coordinate system. Notice that

$$x_{r\max} p_{x_{r\max}} \geq x_{\max} p_{x_{\max}}$$

since

$$(xp_x)_r^2 > 0$$

if the ellipse is rotated since the area of the ellipse is the same regardless of the rotation. So by the inclusion of the correlation term the area of the ellipse is the same in both cases. This point seems somewhat academic but if it is not taken into account the whole foundation of conservation of energy will not be valid for this system since the area of the ellipse is related to the total energy of the system.

And the total energy of the system must be constant regardless of the choice of the coordinate system.

One can easily argue that the complications introduced such as the coupling term $(xp_x)_r$ and the additional term in the equations for the ellipse and the area of the ellipse are unnecessary. They can be removed by the proper rotation of the axis. Also since the energy of the system and area of the ellipse are unchanged, why bother with the unnecessary complications? While these points are true, what if the rotation angle is unspecified? This complication may seem artificial but such complications are encountered all the time. So in order to calculate the area of the ellipse in the new more complicated system we must determine the coupling term $(xp_x)_r$. The next sections of this thesis will show in detail how such coupling effects can be treated.

Now since we consider the beam as consisting of non-interacting particles, the whole distribution is then a collection of non-interacting particles. In the actual accelerator there is a reference trajectory which the particles are guided along by magnetic elements. All of the particles do not follow the reference trajectory exactly, they undergo small deviations about this trajectory[20]. If the particles in the beam are considered as a collection of particles which behave as harmonic oscillators performing oscillations about the reference trajectory, the trajectories of the individual particles in the $x - p_x$ and $y - p_y$ phase spaces are again ellipses. The sizes of the ellipses will vary if the particles have different total energies. The orientation of the individual trajectories may also vary depending on the particular coupling between x and p_x and y and p_y . Recall we consider the subspaces of the full six dimensional phase space as uncoupled. So for now I will restrict the discussion to the $x - p_x$ space. Now if a snapshot of the collection of particles is taken at a fixed point in time or position along the accelerator, the collection of particles will be represented by a distribution of points in phase space. If we utilize an ellipse to surround the distribution[21], the ellipse can be characterized by the quantities x_{dmax} , p_{xdmax} which represent the maxima of the two coordinates and the term $(xp_x)_d$ which characterizes the orientation of the ellipse surrounding the distribution. The subscript d designates the quantity applies to the distribution. The area of the ellipse is again given by[10]:

$$A = \pi \sqrt{(x_{d\max})^2 (p_{xd\max})^2 - ((xp_x)_d)^2} \quad (2.8)$$

In terms of the quantities $x_{d\max}$, $p_{xd\max}$, $(xp_x)_d$ and A the equation of the ellipse is then[22]:

$$(p_{xd\max})x_d^2 + 2((xp_x)_d)x_d p_{xd} + (x_{d\max})p_{xd}^2 = \left(\frac{A}{\pi}\right)^2 \quad (2.9)$$

Now according to Liouville's theorem the area enclosed by the ellipse in phase space remains constant as the beam is transported along the beam line if the system is conservative[23] and subject to symplectic transformations[24] which preserve phase space areas. So if the quantities $x_{d\max}$, $p_{xd\max}$, and $(xp_x)_d$ can be determined the equation of the ellipse which encloses the distribution in phase space and its area can be formed. The size of the area of the ellipse is a measure of the quality of the beam. A smaller area in general indicates a better quality of beam[25]. This is true for both the transverse phase spaces $x - p_x$ and $y - p_y$ as well as the longitudinal phase space $z - p_z$. In this thesis only the transverse phase space will be considered in detail.

2.2 Trace Space

There are several points that must be addressed when applying the concepts presented above to an actual particle beam. In the laboratory environment the particle beam is usually confined inside an evacuated beam pipe. To transport the particles from one point to another requires electric and/or magnetic elements to steer, focus and bend the beam. In the presence of external electric and magnetic fields the canonical momentum is not the same as the mechanical momentum

$$\vec{p}_{mech} = m \vec{v} \quad (2.10)$$

where m is the mass of the particle. In the presence of external electro-magnetic fields the canonical momentum becomes:

$$\vec{p} = m \vec{v} + \frac{q}{c} \vec{A} \quad (2.11)$$

where \vec{A} is the magnetic vector potential and q is the charge of the particle[26]. Normally measurements of the beam are performed in field free regions where $\vec{A} = 0$ so this is only an issue if $\vec{A} \neq 0$. Also we may measure the spatial dimensions of the beam, as discussed in the experimental results section of this thesis, but we cannot directly measure their conjugate momenta p . We can determine the direction tangents which are the slopes of the trajectories of the particles with respect to the reference trajectory. If $p_z \gg p_x$ and $p_z \gg p_y$ then the direction tangents are:

$$x' = \frac{p_x}{p_z} \quad (2.12)$$

$$y' = \frac{p_y}{p_z}. \quad (2.13)$$

Now if the beam is relativistic in the z direction only then

$$p_z = \beta \gamma m c \quad (2.14)$$

and the relations for the direction tangents become:

$$x' = \frac{p_x}{\beta \gamma m c} \quad (2.15)$$

$$y' = \frac{p_y}{\beta \gamma m c}. \quad (2.16)$$

Inverting these relations we obtain:

$$p_x = \beta\gamma mcx' \quad (2.17)$$

$$p_y = \beta\gamma mcy' \quad (2.18)$$

where $\beta = \frac{v_x}{c}$ and $\gamma = \frac{1}{\sqrt{1 - \beta^2}}$.

This is an important point since it allows us to relate canonical variables, p_x and p_y , whose use ensure phase space conservation with quantities accessible in the laboratory, x' and y' . The pairs of variables (x, x') and (y, y') form what is known as "trace space" [8],[9]. So we can perform measurements to determine the area the beam occupies in $x - x'$ trace space that is given by:

$$A_t = \pi \sqrt{(x_{\max})^2 (x'_{\max})^2 - (xx')^2} \quad (2.19)$$

This expression involves the quantity x' which is not a canonical variable and so strictly speaking the area in trace space is not conserved. However, since the quantity $p_x = \beta\gamma mcx'$ is a canonical variable, if we multiply the expression for the area A_t by the quantity $\beta\gamma$, we obtain a conserved quantity A_n :

$$\begin{aligned} A_n &= \beta\gamma A_t \quad (2.20) \\ &= \beta\gamma\pi \sqrt{(x_{\max})^2 (x'_{\max})^2 - (xx')^2} \\ &= \pi \sqrt{(x_{\max})^2 (\beta\gamma x'_{\max})^2 - (x\beta\gamma x')^2} \\ &= \left(\frac{\pi}{mC}\right) \sqrt{(x_{\max})^2 (p_{x\max})^2 - (xp_x)^2}. \end{aligned}$$

The quantity

$$\epsilon = \sqrt{(x_{\max})^2 (x'_{\max})^2 - (xx')^2} \quad (2.21)$$

is known as the "geometric emittance" of the beam for the x dimension. It is formed

from quantities which can be determined experimentally, it is strictly speaking not a conserved quantity. The associated conserved quantity is known as the "normalized emittance" which is formed by multiplying the geometric emittance by $\beta\gamma$ or:

$$\epsilon_n = \beta\gamma\epsilon \quad (2.22)$$

$$= \beta\gamma\sqrt{(x_{\max})^2(x'_{\max})^2 - (xx')^2} \quad (2.23)$$

In first order, areas in trace space are conserved[8] so the normalization above may seem unnecessary. However in order to compare the emittance of beams which differ in energy one would have to use the normalized emittance in order to account for the effects of the different longitudinal momentum, p_z , on the quantities $x' = \frac{p_x}{p_z}$ and $y' = \frac{p_y}{p_z}$.

2.3 Linear Beam Dynamics

In order to describe the propagation of the beam of particles through the accelerator an extensive transfer matrix theory has been developed[27], [28]. The theory describes elements of beam line in terms of transfer matrices which transform an initial vector containing all or part of the six coordinates $x_0, x'_0, y_0, y'_0, l_0, \delta_0$ of a particle into a final vector $(x_1, x'_1, y_1, y'_1, l_1, \delta_1)$ which have been altered by the action of the particular beam line element. In six dimensional coordinates listed above $l = z - z_r$ represents the longitudinal deviation between the position of a particle, z , and the position of a reference particle of the distribution, z_r , and $\delta = \frac{p_0 - p_r}{p_r}$ is the relative momentum deviation between a particle and the reference particle. And x, y and x', y' are the transverse spatial dimensions and the transverse direction tangents respectively. The transformation is performed as follows:

$$X(1) = RX(0) + (\text{higher order terms}) \quad (2.24)$$

where R is called the transformation matrix. In terms of the individual components of the vectors and matrices:

$$X_i(1) = \sum_j R_{ij} X_j(0) + \sum_{j>k} T_{ijk} X_j(0) X_k(0) + \sum_{j>k>l} U_{ijkl} X_j(0) X_k(0) X_l(0) + \quad (2.25)$$

Where

$$X = \begin{bmatrix} x \\ x' \\ y \\ y' \\ l \\ \delta \end{bmatrix} \quad (2.26)$$

Then if the discussion is restricted to first order the transformation is truncated to:

$$X(1) = RX(0) \quad (2.27)$$

or

$$X_i(1) = \sum_j R_{ij} X_j(0) \quad (2.28)$$

Transfer matrices have been developed for all of the basic beam line elements used to manipulate a particle beam. Two basic beam line elements the quadrupole and the drift section will be utilized in the theory of the quadrupole scan emittance measurement procedure that is presented in the next section.

The quadrupole magnet is used to focus the beam and the drift space describes the effects of a field free region of the beam line. The transfer matrix for a drift

section of length d is presented below:

$$R_d = \begin{bmatrix} 1 & d & 0 & 0 & 0 & 0 \\ 0 & 1 & 0 & 0 & 0 & 0 \\ 0 & 0 & 1 & d & 0 & 0 \\ 0 & 0 & 0 & 1 & 0 & 0 \\ 0 & 0 & 0 & 0 & 1 & 0 \\ 0 & 0 & 0 & 0 & 0 & 1 \end{bmatrix} \quad (2.29)$$

The effect of a drift section on a particle represented by the initial vector $X(0)$ is demonstrated by multiplying the initial vector $X(0)$ with the transfer matrix R_d which yields:

$$\begin{aligned} X(1) &= R_d X(0) & (2.30) \\ x(1) &= x(0) + dx'(0) \\ x'(1) &= x'(0) \\ y(1) &= y(0) + dy'(0) \\ y'(1) &= y'(0) \\ l(1) &= l(0) \\ \delta(1) &= \delta(0) \end{aligned}$$

From the relations above the transverse dimensions of the beam change if $x'(0) \neq 0$ and or $y'(0) \neq 0$. The other dimensions of the beam remain unchanged. This seems intuitively clear if $x'(0) \neq 0$ and or $y'(0) \neq 0$, the size of the beam will shrink or grow depending on if the beam is converging or diverging and the amount of convergence or divergence will remain unchanged. If the beam is converging and it comes to a focus it will diverge after the focus. Also evident is that there is no coupling between the different degrees of freedom. The new horizontal dimensions are a function of only the old horizontal dimensions, the same is true for the vertical and longitudinal dimensions. So the horizontal, vertical and longitudinal dimensions can be treated

separately by considering only the 2×2 submatrices of the full 6×6 transfer matrix as follows:

$$\begin{bmatrix} x(1) \\ x'(1) \end{bmatrix} = \begin{bmatrix} 1 & d \\ 0 & 1 \end{bmatrix} \begin{bmatrix} x(0) \\ x'(0) \end{bmatrix} \quad (2.31)$$

$$\begin{bmatrix} y(1) \\ y'(1) \end{bmatrix} = \begin{bmatrix} 1 & d \\ 0 & 1 \end{bmatrix} \begin{bmatrix} y(0) \\ y'(0) \end{bmatrix} \quad (2.32)$$

$$\begin{bmatrix} l(1) \\ \delta(1) \end{bmatrix} = \begin{bmatrix} 1 & 0 \\ 0 & 1 \end{bmatrix} \begin{bmatrix} l(0) \\ \delta(0) \end{bmatrix} \quad (2.33)$$

The three 2×2 matrix multiplications above convey the same information as the single 6×6 matrix multiplication above. This is true since there is no coupling between the three degrees of freedom. Also of importance is that the determinant of the 6×6 and each of the three 2×2 transfer matrices is unity. This is a consequence of Liouville's theorem[29].

Next I consider the magnetic quadrupole which is used to focus the beam. Unlike photon optics where a lens may be focusing in both the horizontal and vertical dimensions, due to Maxwell's equations the quadrupole is focusing in one plane only and defocusing in the other. Therefore a "focusing" quadrupole will focus the beam in the horizontal dimension and defocus the beam in the vertical dimension. Conversely a "defocusing" quadrupole will defocus the beam in the horizontal dimension and focus in the vertical dimension. Since the beam is contained within an evacuated beam pipe or chamber there is a physical boundary that limits the size of the beam. The defocusing effects of the quadrupole can cause the beam to strike the vacuum chamber. In order to contain the beam the quadrupole magnets must be arranged in pairs known as doublets where one quadrupole is focusing and the other is defocusing and even in triplets, three quadrupoles, so that the defocusing effects from one quadrupole are countered by focusing effects from another quadrupole. The specifics of quadrupole modeling and design can be found in many texts[30],[31]etc. As with any model one chooses what to include and what to ignore. In the simplest model

the quadrupole is treated as a thin lens with no physical extent. The focusing effect of the lens is characterized by the focal length, f , which is the longitudinal distance from the lens to the point where a beam which is initially parallel to the longitudinal axis comes to a focus. The transfer matrix for a focusing quadrupole of focal length f is presented below:

$$R_f = \begin{bmatrix} 1 & 0 & 0 & 0 & 0 & 0 \\ -f^{-1} & 1 & 0 & 0 & 0 & 0 \\ 0 & 0 & 1 & 0 & 0 & 0 \\ 0 & 0 & f^{-1} & 1 & 0 & 0 \\ 0 & 0 & 0 & 0 & 1 & 0 \\ 0 & 0 & 0 & 0 & 0 & 1 \end{bmatrix} \quad (2.34)$$

The difference in focusing between horizontal and vertical is evident by the different signs of the term $1/f$. The effect of the thin lens is demonstrated by multiplying the initial vector $X(0)$ by the transfer matrix R_f which yields:

$$\begin{aligned} X(1) &= R_f X(0) & (2.35) \\ x(1) &= x(0) \\ x'(1) &= -f^{-1}x(0) + x'(0) \\ y(1) &= y(0) \\ y'(1) &= f^{-1}y(0) + y'(0) \\ l(1) &= l(0) \\ \delta(1) &= \delta(0) \end{aligned}$$

From the relations above the transverse dimensions and longitudinal dimensions of the beam do not change. Only the transverse direction tangents change. The lens alters the transverse angles the beam makes with the reference beam axis. Now if the lens is followed by a drift the transverse dimensions of the beam will change depending

on the values of the x' and y' after the lens. It is evident that there is no coupling between the different degrees of freedom for a quadrupole thin lens in first order. The new horizontal dimensions are a function of only the old horizontal dimensions, the same is true for the vertical and longitudinal dimensions. So the horizontal, vertical and longitudinal dimensions can be treated separately by considering only the 2×2 sub-matrices of the full 6×6 transfer matrix as follows:

$$\begin{bmatrix} x(1) \\ x'(1) \end{bmatrix} = \begin{bmatrix} 1 & 0 \\ -f^{-1} & 1 \end{bmatrix} \begin{bmatrix} x(0) \\ x'(0) \end{bmatrix} \quad (2.36)$$

$$\begin{bmatrix} y(1) \\ y'(1) \end{bmatrix} = \begin{bmatrix} 1 & 0 \\ f^{-1} & 1 \end{bmatrix} \begin{bmatrix} y(0) \\ y'(0) \end{bmatrix} \quad (2.37)$$

$$\begin{bmatrix} l(1) \\ \delta(1) \end{bmatrix} = \begin{bmatrix} 1 & 0 \\ 0 & 1 \end{bmatrix} \begin{bmatrix} l(0) \\ \delta(0) \end{bmatrix} \quad (2.38)$$

The three 2×2 matrix multiplications above convey the same information as the single 6×6 matrix multiplication above. This is true since there is no coupling between the three degrees of freedom. Also of importance is that the determinant of the 6×6 and each of the three 2×2 transfer matrices is unity. Again this is a consequence of Liouville's theorem.

Just as the drift section has physical extent so does a real quadrupole magnet. In order to improve on the model of the quadrupole the so-called thick lens approximation may be utilized [28],[30]. In this model the quadrupole has a physical length l and the focal length is now given by:

$$f^{-1} = k^2 l \quad (2.39)$$

where k is the "focusing strength" given by:

$$k^2 = \frac{e}{cp}g = \frac{e}{\beta E}g \quad (2.40)$$

and e is the electrons charge, c is the speed of light, p is the momentum and g is the field gradient of the quadrupole $\frac{dB_x}{dx}$ for the horizontal dimension. The full six dimensional transfer matrix for a focusing quadrupole of finite length is given by:

$$R_f = \begin{bmatrix} \cos(kl) & (1/k)\sin(kl) & 0 & 0 & 0 & 0 \\ -k\sin(kl) & \cos(kl) & 0 & 0 & 0 & 0 \\ 0 & 0 & \cosh(kl) & (1/k)\sinh(kl) & 0 & 0 \\ 0 & 0 & k\sinh(kl) & \cosh(kl) & 0 & 0 \\ 0 & 0 & 0 & 0 & 1 & 0 \\ 0 & 0 & 0 & 0 & 0 & 1 \end{bmatrix} \quad (2.41)$$

The effect of the thick lens transformation is demonstrated by multiplying the initial vector $X(0)$ by the transfer matrix R_f which yields:

$$\begin{aligned} X(1) &= R_f X(0) & (2.42) \\ x(1) &= \cos(kl)x(0) + (1/k)\sin(kl)x'(0) \\ x'(1) &= -\sin(kl)x(0) + \cos(kl)x'(0) \\ y(1) &= \cosh(kl)y(0) + (1/k)\sinh(kl)y'(0) \\ y'(1) &= k\sinh(kl)y(0) + \cosh(kl)y'(0) \\ l(1) &= l(0) \\ \delta(1) &= \delta(0) \end{aligned}$$

The transformations for the horizontal dimensions contain terms that oscillate but remain finite so these dimensions can be made to converge. The vertical dimensions contain hyperbolic terms which diverge. Thus the horizontal focusing and vertical

defocusing behavior of the transform is evident. The longitudinal dimensions remain unchanged. Again there is no coupling between the horizontal, vertical and longitudinal dimensions of the beam. So these dimensions can be studied independently as in the drift and thin lens quadrupole. The determinant of the full 6×6 transform and each of the three 2×2 transforms is again equal to one which is due to Liouville's theorem.

Longitudinally the magnetic field extends beyond the physical iron poles of the quadrupole and the strength of the magnetic field does not rise from zero outside of the quadrupole to the maximum value at the center of the quadrupole, g_0 , in a step function manner. To account for these effects an effective magnetic length given by[30]:

$$l_{\text{eff}} = \frac{\int g dz}{g_0} \quad (2.43)$$

is used in place of the physical length l . In the relation above g is the field gradient of the quadrupole that is a function of longitudinal position in the quadrupole and g_0 is the maximum value of the gradient.

2.4 Moments Of The Distribution

The trajectories of the particles in phase space form a distribution $\rho(x, x')$. Following the notation of TRANSPORT[32] and Carey[33] the distribution can be characterized by its second moments:

$$\sigma_{11} = \frac{\iint x^2 \rho(x, x') dx dx'}{\iint \rho(x, x') dx dx'} \quad (2.44)$$

where $\sqrt{\sigma_{11}}$ is the half width of the beam envelope

$$\sigma_{22} = \frac{\iint x'^2 \rho(x, x') dx dx'}{\iint \rho(x, x') dx dx'} \quad (2.45)$$

where $\sqrt{\sigma_{22}}$ is the half angular divergence of the beam,

$$\sigma_{12} = \frac{\iint xx' \rho(x, x') dx dx'}{\iint \rho(x, x') dx dx'} \quad (2.46)$$

and σ_{12} is a measure of the correlation between x and x' . The moments are taken about the centroid of the distribution which are given by the first moments of the beam:

$$\tilde{x} = \frac{\iint x \rho(x, x') dx dx'}{\iint \rho(x, x') dx dx'} \quad (2.47)$$

and

$$\tilde{x}' = \frac{\iint x' \rho(x, x') dx dx'}{\iint \rho(x, x') dx dx'} \quad (2.48)$$

In order to characterize the distribution it is bounded as shown in the following diagram, Fig. 2.1, by an ellipse that is specified by the moments listed above .

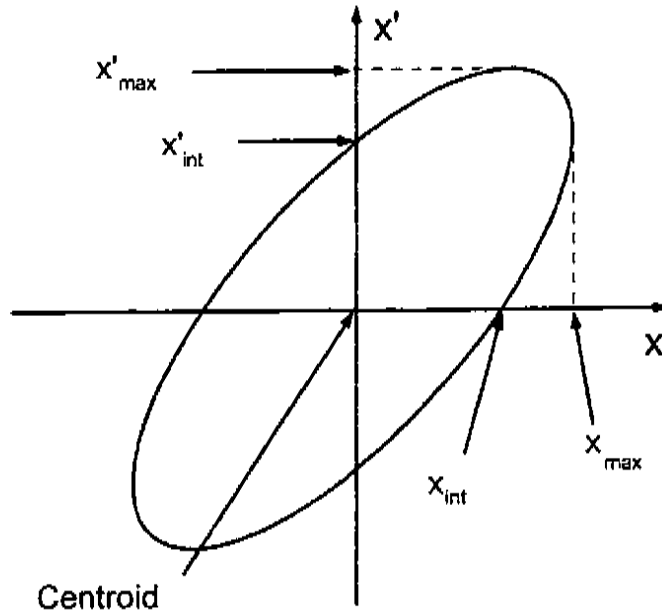


Figure 2.1: Ellipse surrounding beam distribution in trace space

In order to organize the information about the moments of the beam distribution we may define a symmetric matrix called the beam matrix and given by:

$$\sigma = \begin{bmatrix} \sigma_{11} & \sigma_{12} \\ \sigma_{12} & \sigma_{22} \end{bmatrix} \quad (2.49)$$

where the diagonal elements are the squares of the maximum extents of the beam in trace space:

$$\sigma_{11} = x_{\max}^2 \quad (2.50)$$

$$\sigma_{22} = x'_{\max}{}^2 \quad (2.51)$$

and the off diagonal element, σ_{12} , characterizes the correlation between x and x' or tilt of the ellipse in phase space. The area in trace space occupied by the beam is then given by:

$$Area = \pi \sqrt{\det(\sigma)} = \pi \sqrt{\sigma_{11}\sigma_{22} - \sigma_{12}^2} = \pi \epsilon_x \quad (2.52)$$

Where ϵ_x is known as the geometric emittance of the beam which is a measure of beam quality. A normalized quantity known as the correlation coefficient is defined by:

$$r_{12} = \frac{\sigma_{12}}{\sqrt{\sigma_{11}\sigma_{22}}} \quad (2.53)$$

such that

$$|r_{12}| \leq 1. \quad (2.54)$$

This is true since in order for the relation $Area = \pi \sqrt{\det(\sigma)} = \pi \sqrt{\sigma_{11}\sigma_{22} - \sigma_{12}^2} = \pi \epsilon_x$

to be a real quantity it follows that

$$(\sigma_{11}\sigma_{22} - \sigma_{12}^2) \geq 0$$

must be true, or

$$\sigma_{11}\sigma_{22} \geq \sigma_{12}^2$$

which implies

$$1 \geq \frac{\sigma_{12}^2}{\sigma_{11}\sigma_{22}}$$

$$1 \geq \sqrt{\frac{\sigma_{12}^2}{\sigma_{11}\sigma_{22}}} = \left| \frac{\sigma_{12}}{\sqrt{\sigma_{11}\sigma_{22}}} \right| = |r_{12}|$$

If $\sigma_{12} = 0$ then $r_{12} = 0$ and this indicates an upright ellipse, i.e. there is no $x - x'$ correlation in the beam distribution. In terms of the correlation coefficient the values where the ellipse intercepts the axes are given by:

$$x_{\text{int}} = \sqrt{\sigma_{11}(1 - r_{12}^2)} \quad (2.55)$$

$$x'_{\text{int}} = \sqrt{\sigma_{22}(1 - r_{12}^2)} \quad (2.56)$$

The area of the trace space ellipse can also be given in terms of the maxima and intercepts:

$$\text{Area} = \pi x_{\text{max}} x'_{\text{int}} = \pi x_{\text{int}} x'_{\text{max}} \quad (2.57)$$

The equation of the ellipse is given by[33]:

$$X^t \sigma^{-1} X = 1 \quad (2.58)$$

where X^t is the transpose of the vector:

$$X = \begin{bmatrix} x \\ x' \end{bmatrix} \quad (2.59)$$

2.5 Transformation Of The Moments Of The Distribution

The ellipse may be transformed from one point to another along the beam line by using the linear transforms as follows. Starting with the equation for the ellipse in $x - x'$ space that is given by:

$$X^t(0) \sigma^{-1}(0) X(0) = 1 \quad (2.60)$$

where the initial location is designated by the argument 0. Next we utilize the relation for transforming one vector of particle coordinates x and x' from the initial position designated by 0 to the final position designated by 1.

$$X(1) = R(1)X(0) \quad (2.61)$$

If we solve for $X(0)$ we obtain $X(0) = R^{-1}X(1)$ and also using the properties of the transpose $X^t(0) = (R^{-1}X(1))^t = X^t(1)(R^t)^{-1}$ [33]. Substituting these relations into the expression for the equation of the ellipse(2.60) gives:

$$X^t(1)(R^t)^{-1} \sigma(0)^{-1} R^{-1} X(1) = 1 \quad (2.62)$$

The equation for the ellipse at the final location is also given by

$$X^t(1)\sigma^{-1}(1)X(1) = 1. \quad (2.63)$$

Comparing these two relations we obtain:

$$\sigma(1)^{-1} = (R^{-1})^t \sigma(0)^{-1} R^{-1} \quad (2.64)$$

Now $(R^t)^{-1} \sigma(0)^{-1} R^{-1} = (R \sigma(0) R^t)^{-1}$ and so the sigma matrix transformed to the new position is given by:

$$\sigma(1) = R \sigma(0) R^t \quad (2.65)$$

This relation shows how to transform the sigma matrix from one point to another along the beam line. This result is quite useful since it provides a method to transform the moments of the distribution between two locations along the beam line if the transform between the two positions, R , is known. The moments give the maximum extents of the beam envelope and the correlation in trace space. This is far more information than that obtained using the transformation $X(1) = R(1)X(0)$ for an individual trajectory.

Now the determinant of the transfer matrix R and its transpose R^t are unity since the transforms are linear[29]. The determinant of a product of matrices is the product of the determinants of the individual matrices so we have taking the determinant of (2.65) :

$$\begin{aligned} \det(\sigma(1)) &= \det(R \sigma(0) R^t) & (2.66) \\ &= \det(R) \det(\sigma(0)) \det(R^t) \\ &= (1) \det(\sigma(0)) (1) \end{aligned}$$

$$\det \det(\sigma(1)) = \det(\sigma(0)) \quad (2.67)$$

But $\pi\sqrt{\det(\sigma)}$ is the area of the ellipse. So the above relation also shows that the area of the ellipse is preserved under linear transformations or those with determinants equal to unity, which is simply Liouville's theorem. We now have a way of transforming the moments of the beam ellipse from one position to another along the beam line and we are guaranteed that the area of the ellipse is preserved. If we are able to determine the moments of the beam ellipse at one point along the beam line we can calculate the emittance of the beam which is a conserved quantity and we can calculate the moments at any new position if the two are connected by a linear transformation.

2.6 Determination Of The Distribution Moments

If we wish to determine the moments of an actual electron beam distribution we are confronted with certain physical limitations. The electron beam is usually confined inside an evacuated beam chamber. So the square of the beam half-width or σ_{11} is the only second moment that can be directly determined experimentally. This can be done by inserting into the electron beam a screen material that produces visible radiation, light, when struck by the electrons in the beam. From the pattern of the emitted light which is usually captured by a television camera one can determine the half width of the electron beam $\sqrt{\sigma_{11}(1)}$ at the screen location. In order to determine $\sigma_{12}(1)$ and $\sigma_{22}(1)$ the other two elements of the sigma matrix at the screen location, we utilize the fact that $\sigma_{11}(1)$ at the screen position is determined by all three of terms $\sigma_{11}(0)$, $\sigma_{12}(0)$ and $\sigma_{22}(0)$ from an upstream position that is denoted by the argument 0. This is shown by expanding the expression for the $\sigma_{11}(1)$ term in the relation (2.65) which represents the transformation from location 0 to location 1, we obtain:

$$\sigma_{11}(1) = R_{11}^2\sigma_{11}(0) + 2R_{11}R_{12}\sigma_{12}(0) + R_{12}^2\sigma_{22}(0). \quad (2.68)$$

Rewriting the above relation in a matrix form yields:

$$\sigma_{11}(1) = \begin{bmatrix} R_{11}^2 & 2R_{11}R_{12} & R_{12}^2 \end{bmatrix} \begin{bmatrix} \sigma_{11}(0) \\ \sigma_{12}(0) \\ \sigma_{22}(0) \end{bmatrix}. \quad (2.69)$$

At this point we have one equation with three unknowns. If we can obtain at least two more relations with different values for $\sigma_{11}(1)$, R_{11} and R_{12} we can form a linear system of independent equations which can be inverted to yield the initial moments $\sigma_{11}(0)$, $\sigma_{12}(0)$ and $\sigma_{22}(0)$ of $\sigma(0)$ the sigma matrix at the initial location. From these moments the area of the ellipse can be determined and the emittance can be calculated.

One way to obtain the desired additional relations is to measure $\sqrt{\sigma_{11}}$ at two other locations along the beam line. Since this requires a total of three screens it is known as the “three screen” method. The method requires multiple screens and the equipment for viewing the screens. The additional equipment increases the expense of the measurement and increases the space along the beamline required for the measurement since the screens must be spatially separated. Also the separation of the screens is fixed so the behavior of the beam can only be sampled under a limited set of conditions determined by the drift distances which separate the screens.

Another method to determine the beam moments is to vary $\sqrt{\sigma_{11}}$ at a single screen location by changing the values of R_{11} and R_{12} of the transfer matrix R between the two positions. This can be accomplished by using a variable focusing element such as a quadrupole magnet and a drift section between the quadrupole and the screen. By varying the strength of the quadrupole the beam width at the screen can be changed. Typically the beam size is measured as the beam is brought through a waist or minimum during the “scanning” of the quadrupole magnet. One then forms the system of equations containing the squares of the beam half widths at the screen for each value of the elements of the transfer matrix $R = R_q R_d$ and the unknown elements of the $\sigma(0)$, sigma matrix at the entrance to the quadrupole magnet. The equations are then as follows:

$$\begin{bmatrix} \sigma_{11}(1)_1 \\ \sigma_{11}(1)_2 \\ \vdots \\ \sigma_{11}(1)_i \\ \vdots \\ \sigma_{11}(1)_n \end{bmatrix} = \begin{bmatrix} R_{11_1}^2 & 2(R_{11}R_{12})_1 & R_{12_1}^2 \\ R_{11_2}^2 & 2(R_{11}R_{12})_2 & R_{12_2}^2 \\ \vdots & \vdots & \vdots \\ R_{11_i}^2 & 2(R_{11}R_{12})_i & R_{12_i}^2 \\ \vdots & \vdots & \vdots \\ R_{11_n}^2 & 2(R_{11}R_{12})_n & R_{12_n}^2 \end{bmatrix} \begin{bmatrix} \sigma_{11}(0) \\ \sigma_{12}(0) \\ \sigma_{22}(0) \end{bmatrix} \quad (2.70)$$

Rewriting the equations in matrix notation one obtains a more compact form:

$$\vec{\sigma}_{11}(1) = \tilde{R} \vec{\sigma}(0). \quad (2.71)$$

Now $\vec{\sigma}(0)$ is found by inverting \tilde{R} and multiplying on the right on both sides of the equation above which yields:

$$\vec{\sigma}(0) = \tilde{R}^{-1} \vec{\sigma}_{11}(1) \quad (2.72)$$

where $\vec{\sigma}(0)$ contains the elements of the beam matrix at the entrance to the quadrupole. The area in phase space occupied by the beam is then given by:

$$A = \pi \sqrt{\det(\sigma(0))} = \pi \sqrt{\sigma_{11}(0)\sigma_{22}(0) - \sigma_{12}^2(0)} = \pi \epsilon_x \quad (2.73)$$

And the emittance is given by:

$$\epsilon_x = \sqrt{\sigma_{11}(0)\sigma_{22}(0) - \sigma_{12}^2(0)} \quad (2.74)$$

The normalized emittance is given by:

$$\epsilon_x = \beta\gamma\sqrt{\sigma_{11}(0)\sigma_{22}(0) - \sigma_{12}^2(0)} \quad (2.75)$$

The method described above is known as the "quadrupole scan" technique. It has the features that it requires only one screen and set of equipment to view the beam size on the screen. One can choose the number of relations in the set of equations (2.70) above by selecting the number of strengths of the quadrupole to be scanned. Also, the beam size can be made to significantly vary at the screen location by adjusting the range of the strengths of quadrupole that is scanned. This is important as discussed in the last section of this chapter. And in general the experimental setup for the quadrupole scan occupies less space along the beam line than the three screen method for the same significant variation of the beam size.

Another method commonly used to measure the emittance of an electron beam involves inserting a mask into the beam. The mask contains sets of holes or slits which allow beamlets, small portions of the beam, to pass while blocking the remaining beam. The beamlets drift to a screen where the widths of the resulting distributions are measured. If the mask contains holes the method is known as the "pepper pot" technique since the mask and resulting image resembles that of a pepper pot. From the size of the holes or width of the slits, the drift distance to the screen and the widths of the resulting distributions on the screen one can determine the emittance of the beamlets as discussed in detail in [7]. Typically this type of measurement is performed at low energy, a few MeV. In order to apply this method to beams at higher energy one must consider a few technical issues. As the beam energy is increased the transverse dimensions of the beam shrink and so size of the holes must be reduced to produce the same relative beamlet size. In order to completely stop the beam at higher energy the thickness of the mask must be increased. Therefore one needs to create long straight holes or slits in dense materials such as tungsten. These holes or slits must be precisely aligned to the beam and beamline so that the effective dimensions of the holes or slits are not reduced by missalignment. Also one can design a screen to view the beam that produces minimal radiation from the

electrons which are intercepted. However, completely stopping the beam produces additional radiation which creates additional shielding requirements. At the GTF the emittance of the beam was to be measured after the linac at an energy of 30 MeV within a limited amount of beamline space in a pre-existing radiation shielded vault. Therefore due to financial, beamline real estate and pre-existing radiation constraints the quadrupole scan technique was employed to measure the emittance of the electron beam.

2.7 Experimental System

In order to complete the model of a quadrupole scan the matrix R for the elements of the lattice between the screen and the entrance to the focusing quadrupole must be formed. The matrix R is created from the transfer matrix for the quadrupole in the thick lens model and drift which are given by:

$$R = R_d R_{qf} \quad (2.76)$$

where,

$$R_d = \begin{bmatrix} 1 & d \\ 0 & 1 \end{bmatrix} \quad (2.77)$$

and,

$$R_{qf} = \begin{bmatrix} \cos(kl) & (\frac{1}{k})\sin(kl) \\ -k\sin(kl) & \cos(kl) \end{bmatrix} \quad (2.78)$$

with d the drift distance, k and l are the strength and the effective length of the quadrupole in the thick lens model. After performing the matrix multiplication we obtain:

$$R_{11} = \cos(kl) - kd\sin(kl) \quad (2.79)$$

and

$$R_{12} = \frac{1}{k}\sin(kl) + d\cos(kl) \quad (2.80)$$

Then relation (2.71) becomes for n measurements:

$$= \begin{bmatrix} \sigma_{11}(1)_1 \\ \sigma_{11}(1)_2 \\ \vdots \\ \sigma_{11}(1)_i \\ \vdots \\ \sigma_{11}(1)_n \end{bmatrix} \begin{bmatrix} \{\cos(k_1l) - k_1d\sin(k_1l)\}^2 & 2\{(\cos(k_1l) - k_1d\sin(k_1l)) * (\frac{1}{k_1}\sin(k_1l) + d\cos(k_1l))\} & \{\frac{1}{k_1}\sin(k_1l) + d\cos(k_1l)\}^2 \\ \{\cos(k_2l) - k_2d\sin(k_2l)\}^2 & 2\{(\cos(k_2l) - k_2d\sin(k_2l)) * (\frac{1}{k_2}\sin(k_2l) + d\cos(k_2l))\} & \{\frac{1}{k_2}\sin(k_2l) + d\cos(k_2l)\}^2 \\ \vdots & \vdots & \vdots \\ \{\cos(k_il) - k_id\sin(k_il)\}^2 & 2\{(\cos(k_il) - k_id\sin(k_il)) * (\frac{1}{k_i}\sin(k_il) + d\cos(k_il))\} & \{\frac{1}{k_i}\sin(k_il) + d\cos(k_il)\}^2 \\ \vdots & \vdots & \vdots \\ \{\cos(k_nl) - k_nd\sin(k_nl)\}^2 & 2\{(\cos(k_nl) - k_nd\sin(k_nl)) * (\frac{1}{k_n}\sin(k_nl) + d\cos(k_nl))\} & \{\frac{1}{k_n}\sin(k_nl) + d\cos(k_nl)\}^2 \end{bmatrix} \begin{bmatrix} \sigma_{11}(0) \\ \sigma_{12}(0) \\ \sigma_{22}(0) \end{bmatrix}$$

$$\vec{\sigma}_{11}(1) = \tilde{R} \vec{\sigma}(0). \quad (2.81)$$

This system of equations is inverted to yield

$$\vec{\sigma}(0) = \begin{bmatrix} \sigma_{11}(0) \\ \sigma_{12}(0) \\ \sigma_{22}(0) \end{bmatrix} \quad (2.82)$$

The geometric emittance is given by:

$$\epsilon_x = \sqrt{\sigma_{11}(0)\sigma_{22}(0) - \sigma_{12}^2(0)} \quad (2.83)$$

The normalized emittance is given by:

$$\epsilon_x = \beta\gamma \sqrt{\sigma_{11}(0)\sigma_{22}(0) - \sigma_{12}^2(0)} \quad (2.84)$$

Therefore all that is required for the determination of the normalized emittance is the beam energy and the information contained in $\vec{\sigma}(0)$ from the quadrupole scan which requires the beam halfwidths from the screen and the corresponding lattice settings.

2.8 Numerical Analysis Considerations

In the quadrupole scans performed at the GTF ten measurements of the beam size were made, $n=10$ in equation (2.81) above. This was done to significantly vary the size of the beam in order to provide more information about the behavior of the beam. This enables an increase in the precision of the determination of $\vec{\sigma}(0)$ [34]. The

system of equations in (2.81) is then overdetermined, 10 equations and 3 unknowns. Overdetermined systems can be solved by the general method of least squares fitting using the so called normal equations[35],[36]. However, while mathematically elegant, the normal equations are susceptible to round off error when applied to problems solved by computer. According to [36] they should only be used for the "easy" least squares problems, and the preferred method involves QR decomposition. For this reason I utilized the "slash" operator of MatLab[37] to invert the system (2.81) and all similar systems presented in the following chapters since this routine utilizes QR decomposition.

Chapter 3

Simulations

In this chapter simulations will be presented to illustrate the quadrupole scan technique using Gaussian distributions. The simulations will be used to demonstrate how the quadrupole scan technique yields accurate results for beam distributions that are symmetric as well as asymmetric in transverse dimensions. Simulations will be presented which demonstrate that the quadrupole scan technique can yield incorrect results when rotations of the distribution are included.

3.1 Generation Of The Distributions

In order to generate a six dimensional distribution of particles I utilized Monte Carlo methods discussed in [38] to form Gaussian distributions in the six dimensions x , x' , y , y' , z and p_z with widths which are representative of those of the GTF. While one of the goals of the GTF is to produce non-Gaussian beams, the beams generated at the GTF were formed from Gaussian beams by clipping and stretching Gaussians as discussed in the Chap. 1. So the underlying spatial and temporal laser beam distributions are Gaussian. Further the assumption is made that the electron beam distribution generated from the photocathode is similar to the laser distribution. The transverse and longitudinal momentum of the electron beam are assumed to have Gaussian distributions. The values for the half widths or sigmas of the x and y distributions of the beam were taken to be in the range of hundreds of microns, and

the half widths or sigmas for the x' and y' distributions were taken to be in the range of hundreds of microradians as was found in the measurements presented in Chap. 7. The energy spread was also assumed to be Gaussian with a spread of .1% which was measured using the GTF spectrometer. Since the energy spread of the real beam was small (.1%) the effect of chromatic aberration was not included in the simulations.

In order to generate a Gaussian distribution of the form:

$$F(x) = \frac{1}{\sqrt{2\pi}\sigma} \exp\left(\frac{-x^2}{2\sigma^2}\right) \quad (3.1)$$

using Monte Carlo methods, the distribution above is treated as a probability distribution. Then the probability that a particle will lie within the range x to dx is given by:

$$F(x)dx = \frac{1}{\sqrt{2\pi}\sigma} \exp\left(\frac{-x^2}{2\sigma^2}\right) dx. \quad (3.2)$$

Next the c.d.f. or cumulative distribution function, $c(r)$, is formed where:

$$c(r) = \int_0^r F(x)dx. \quad (3.3)$$

Now $c(\infty) = 1$ since $F(x)$ is a normalized probability function and so $0 \leq c < 1$. And $dc = F(x)dx$ is the probability of finding a value between x and dx . Now if r is uniformly distributed on the interval $0 \leq r < 1$ and if c is a randomly selected value from that interval, then $0 \leq c < 1$. Since r is uniformly distributed, c is uniformly distributed. The probability of finding a value in the range dc is Pdc and since c is uniformly distributed $Pdc = dc$. The probability of finding a value in the range dx is $F(x)dx = dc$ and $dc = Pdc$. Then we can set $r = c(x)$ and then solving for x we obtain:

$$x = c^{-1}(r). \quad (3.4)$$

Since

$$\begin{aligned} c(r) &= \int_0^r F(x) dx \\ &= \int_0^r \frac{1}{\sqrt{2\pi}\sigma} \exp\left(\frac{-x^2}{2\sigma^2}\right) dx \\ &= \frac{1}{2} \operatorname{erf}\left(\frac{x}{\sqrt{2\sigma^2}}\right). \end{aligned}$$

then,

$$c^{-1}(r) = \frac{1}{2} \operatorname{erf}^{-1}\left(\frac{x}{\sqrt{2\sigma^2}}\right) \quad (3.5)$$

Now since $-1 \leq \operatorname{erf}(s) < 1$ then $-1/2 \leq c(x) < 1/2$. And if the random variable r is in the range $0 < r < 1$ then $c(x) = (r - 1/2)$. And finally,

$$x = \frac{1}{2} \sqrt{2\sigma^2} \operatorname{erf}^{-1}\left[\frac{(r - \frac{1}{2})}{\sqrt{2\sigma^2}}\right] \quad (3.6)$$

or,

$$x = \sqrt{2}\sigma \operatorname{erf}^{-1}\left[\frac{(r - \frac{1}{2})}{\sqrt{2\sigma^2}}\right] \quad (3.7)$$

The above technique was used to generate the x, x', y, y', E and z distributions by filling a $6 \times N$ vector where N is the number of particles used. All of the simulations presented utilized 10,000 particles this was chosen since this is usually the number of particles used in PARMELA [46] simulations. The distribution was taken to describe

the beam after it had exited the linac and as it entered the quadrupole doublet used to measure the emittance. In the simulations presented the transverse and longitudinal dimensions of the beam were considered uncoupled so only the transverse dimensions of the beam were. The energy distribution was only used to normalize the emittance. Also since the energy spread of the real beam from the photoinjector was very small, .1% , chromatic effects are also ignored.

3.2 Simulation With A Symmetric Beam

The emittance of the initial distribution was determined by calculating the moments of the initial distribution contained in the $4 \times N$ vector, $X(0)$. The distribution is then propagated through the system for each setting of quadrupole q2 by performing the multiplication:

$$X(1) = RX(0) \tag{3.8}$$

Referring to Fig. 1.2, the transfer matrix, R , of this section of the beam line is of the form:

$$R = R_{d2}R_{q2}R_{d1}R_{q1} \tag{3.9}$$

is matrix formed by multiplying the transfer matrices of the beam line elements from the entrance of q1 to the YAG screen where the beam size measurements were made. The horizontal width of the distribution was determined by calculating the RMS width of the horizontal projection of the beam distribution. This is the same method that is used in the actual measurements. The first quadrupole of the doublet, q1, which was horizontally defocusing was kept at a fixed strength and the second quadrupole, q2, which was horizontally focusing was varied. Ten settings we used as in the measurements. Using the quadrupole scan algorithm derived above the

emittance of the beam is then calculated.

Starting with the initial parameters:

$$\begin{aligned} \sigma_x = \sigma_y = 0.2 \text{ mm} \quad \sigma_{x'} = \sigma_{y'} = 0.2 \text{ mrad} \\ \sigma_z = 2.0 \text{ ps} \quad E = 30 \text{ MeV} \quad \delta E = .03 \text{ MeV} \end{aligned}$$

The initial normalized emittance of the distribution is:

$$\epsilon_x = 2.38 \text{ mm mrad}$$

The normalized emittance obtained from the quadrupole scan technique is:

$$\epsilon_{x\text{quadscan}} = 2.38 \text{ mm mrad}$$

demonstrating the validity of the procedure used. Plots of the original distributions in $x - y$ and $x - x'$ are show in Fig. 3.1 and Fig 3.2 below:

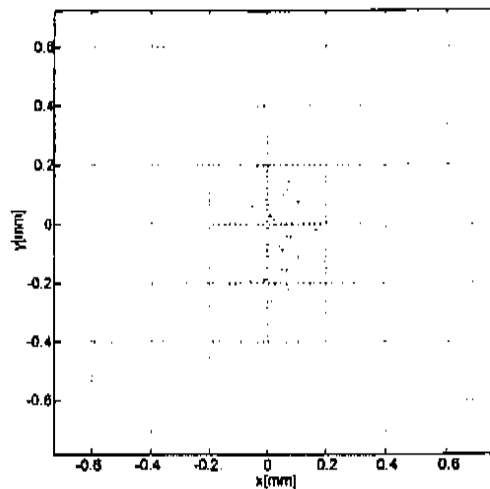


Figure 3.1: Initial x-y distribution for symmetric distribution

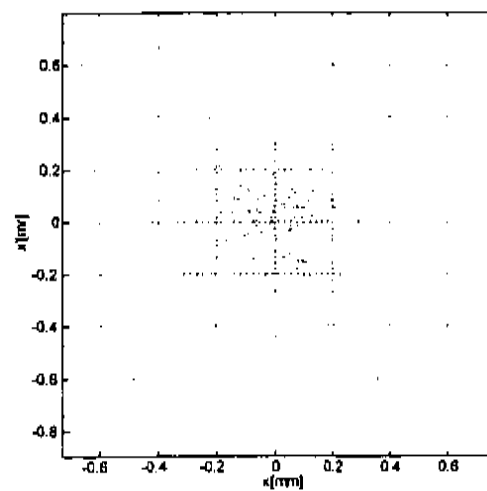


Figure 3.2: Initial $x-x'$ distribution for symmetric distribution

Plots of the distributions at the screen location for three different q_2 strengths are presented in Table 3.1 on the next page.

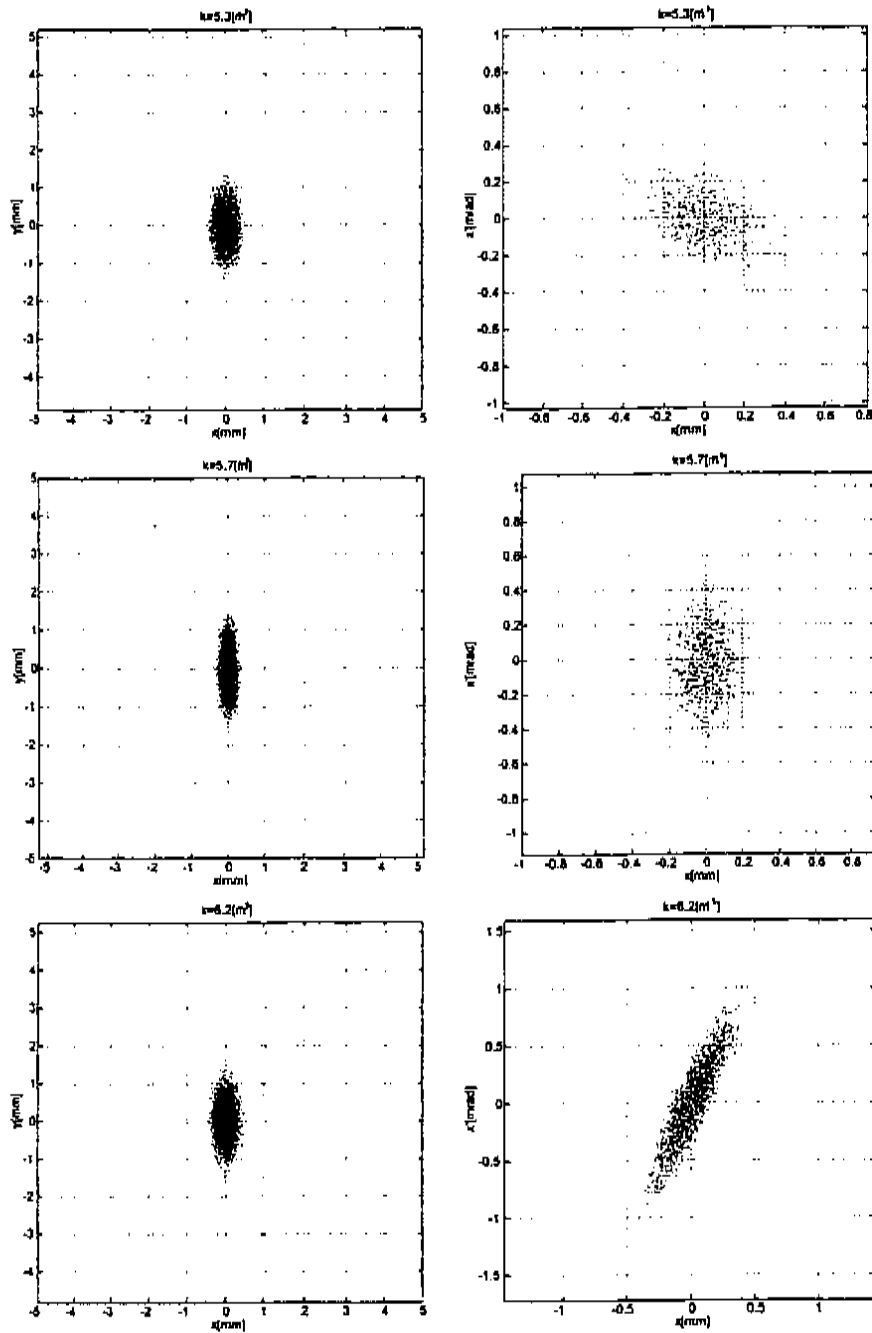
Table 3.1: Plot of x - y and x - x' distributions for three different q_2 strengths

Fig. 3.3 below is a plot of the beam size versus q_2 strength which shows how the beam width is brought through a minimum.

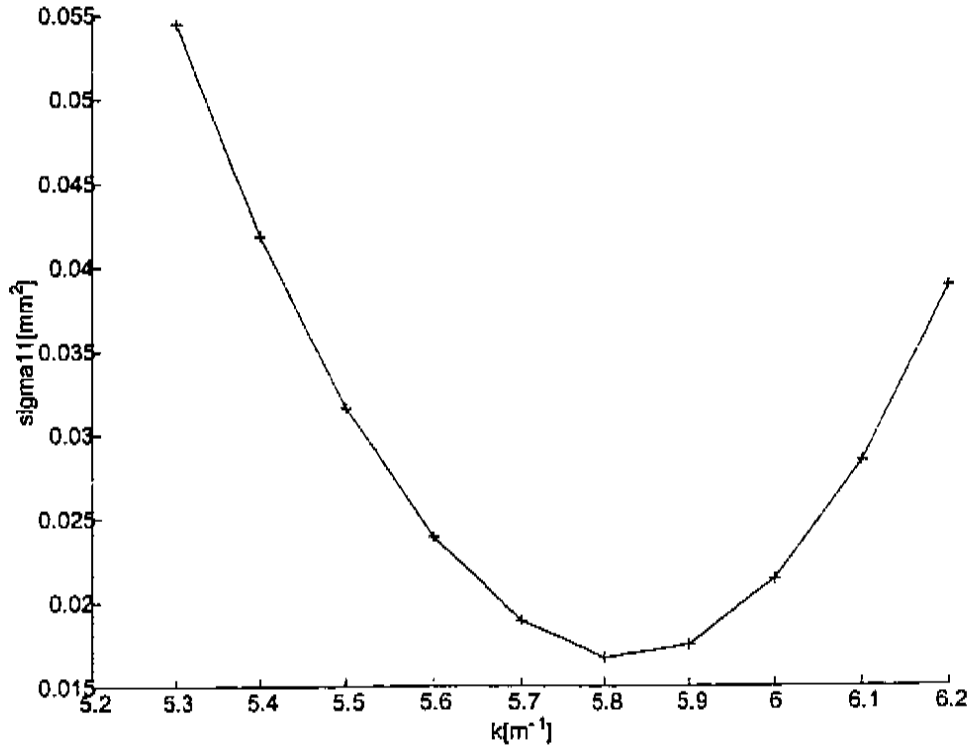


Figure 3.3: Square of beam half width vs q_2 strength for symmetric distribution

The agreement between the initial distribution and the calculated value is expected since the transforms for quadrupoles and drifts which were used throughout the simulation all have $\det(R) = 1$. This ensures conservation of phase space.

3.2.1 Simulation With An Asymmetric Beam

Even astigmatic beams, those with unequal values for σ_x and σ_y and or $\sigma_{x'}$ and $\sigma_{y'}$ present no problem for the quadrupole scan technique. If we use a distribution with:

$$\begin{aligned} \sigma_x &= 0.4 \text{ mm} & \sigma_y &= 0.2 \text{ mm} & \sigma_{x'} &= 0.1 \text{ mrad} & \sigma_{y'} &= 0.2 \text{ mrad} \\ \sigma_z &= 2.0 \text{ ps} & E &= 30 \text{ MeV} & \delta E &= .03 \text{ MeV} \end{aligned}$$

The initial emittance of the distribution is:

$$\epsilon_x = 2.33 \text{ mm mrad}$$

The emittance from the quadrupole scan technique is:

$$\epsilon_{x\text{quadscan}} = 2.33 \text{ mm mrad}$$

Plots of the original distributions in $x - y$ and $x - x'$ are show in Fig. 3.4 and Fig. 3.5 below:

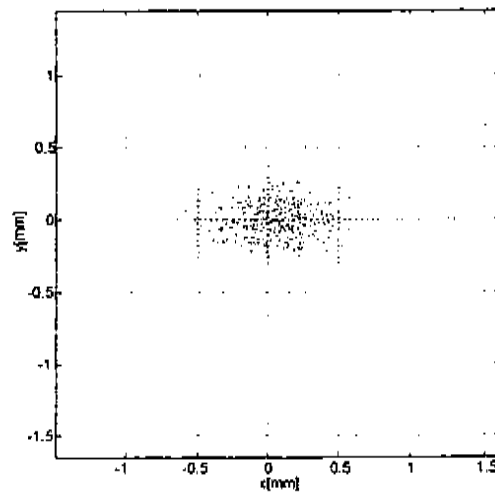


Figure 3.4: Initial x-y distribution for asymmetric distribution

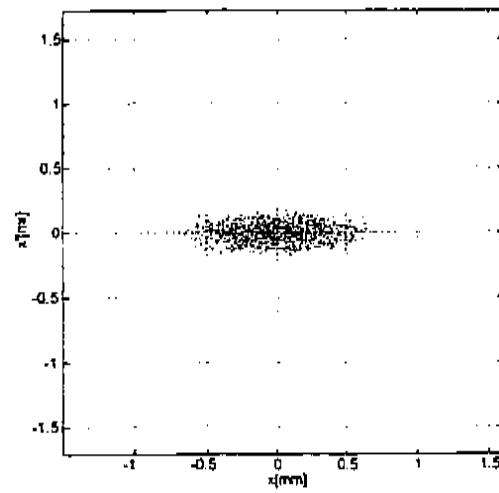


Figure 3.5: Initial $x-x'$ distribution for asymmetric distribution

Plots of the distributions at the screen location for three different q^2 strengths are presented in Table 3.2 on the next page.

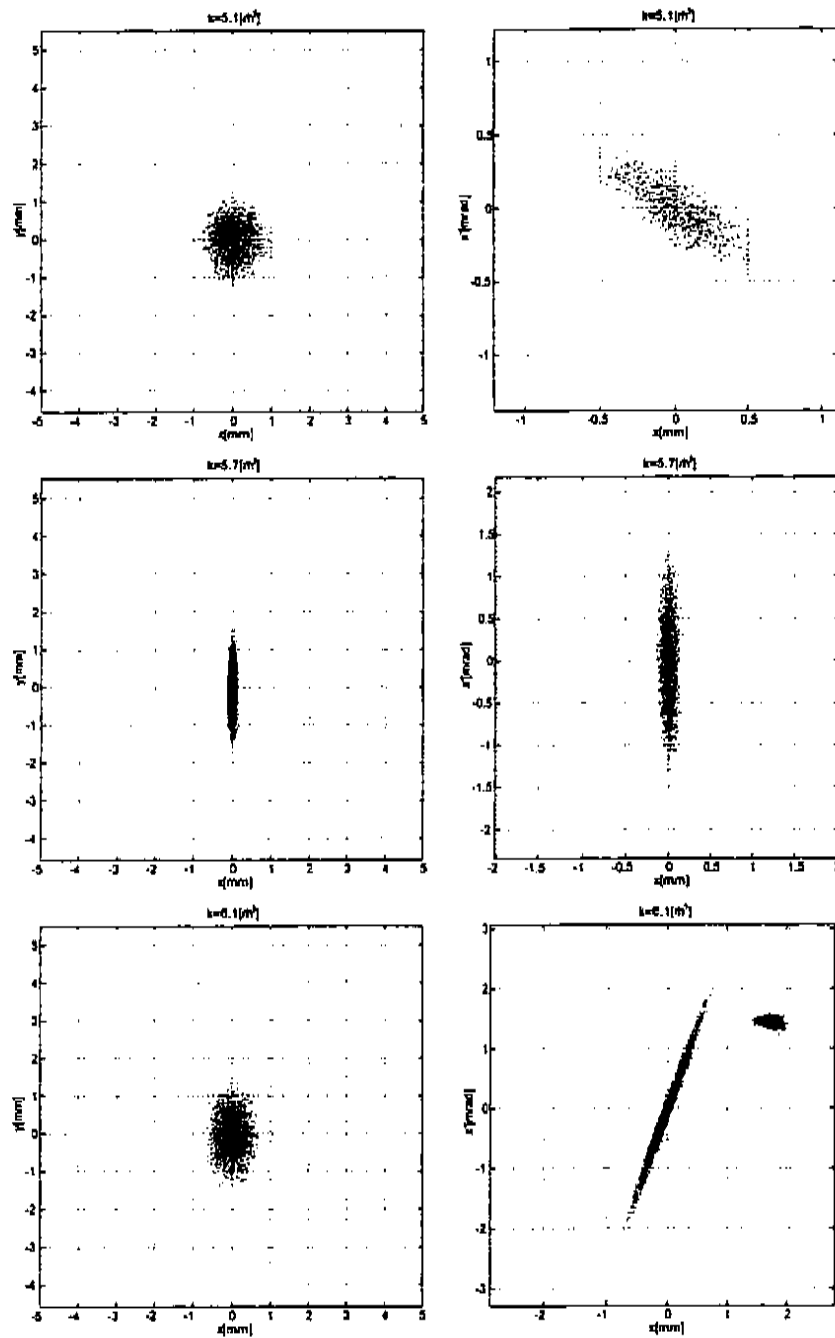


Table 3.2: Plots of x - y and x - x' distributions for asymmetric beam for three different q_2 strengths

Fig. 3.6 below is a plot of the beam size versus q_2 strength which shows how the beam width is brought through a minimum.

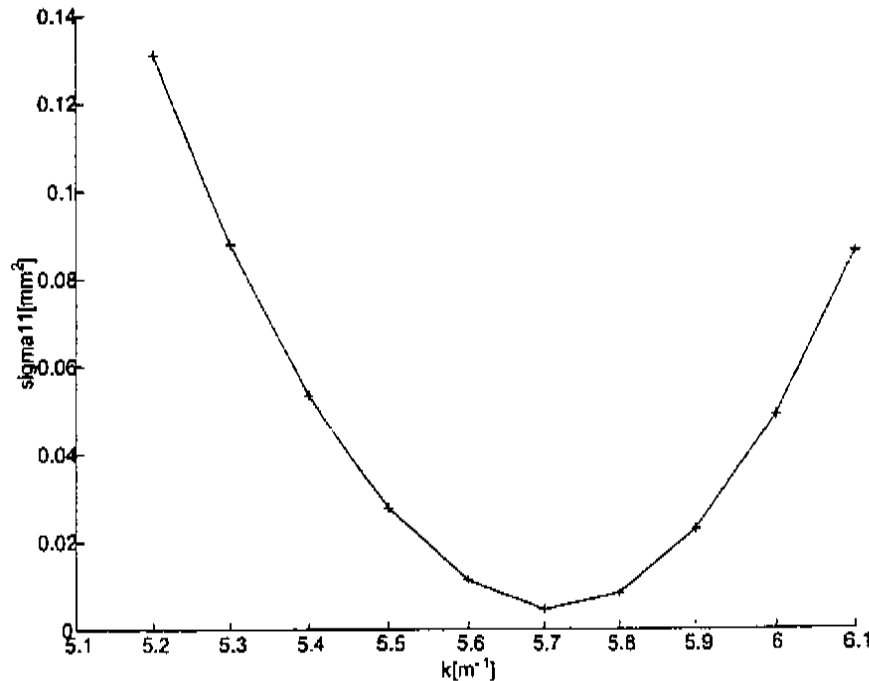


Figure 3.6: Square of beam half width vs q_2 strength for asymmetric distribution

From the $x - x'$ plots the shearing action of the quadrupole and drift combination is apparent. That is the beam distribution shears from left to right due to the drift and depending on its orientation when exiting the quadrupole the beam distribution will end up with a different $x - x'$ correlation when it reaches the screen location. By measuring $\sqrt{\sigma_{11}}$ of the distribution at various strengths of the quadrupole q_2 we are able to determine the area occupied by the beam. Also apparent is the lack of any tilt or correlation in the $x - y$ plots. Notice that even with an astigmatic beam the quadrupole scan technique accurately yields the horizontal emittance of the beam.

However, in the emittance compensated photoinjector a solenoid is used to focus the beam as it exists the gun. Unlike a quadrupole, the solenoid is focusing in both planes and unlike a quadrupole the solenoid rotates the beam. There are rotations at the entrance and exit of the solenoid. These rotations introduce a coupling between

the transverse coordinates of the beam which is dependent on the strength of the solenoid. In the next section a rotation will be included in the simulations and it will be shown that the quadrupole scan technique can yield unreliable results due to the coupling from the solenoid. Coupling of the transverse dimensions of the beam can also be produced by rotated beam line elements such as quadrupole magnets and by higher order modes in RF cavities.

3.3 Solenoidal Magnets And Coupling

The first order transform matrix for a solenoid from the Transport manual [32] is presented below:

$$R_{\text{Solenoid}} = \begin{bmatrix} C^2 & SC/k & SC & S^2/k & 0 & 0 \\ -kSC & C^2 & -kS^2 & SC & 0 & 0 \\ -SC & -S^2/k & C^2 & SC/k & 0 & 0 \\ kS^2 & -SC & -kSC & C^2 & 0 & 0 \\ 0 & 0 & 0 & 0 & 1 & 0 \\ 0 & 0 & 0 & 0 & 0 & 1 \end{bmatrix} \quad (3.10)$$

where

$$C = \cos(kL)$$

$$S = \sin(kL)$$

L = the effective length of the solenoid

$k = \left| \frac{B(0)}{2B\rho_0} \right|$, $B(0)$ is the field inside the solenoid and $2B\rho_0$ is the momentum of the central trajectory

This transform is for the full six-dimensional transform which utilizes a six-dimensional vector to describe a particle. The fifth entry of the particle vector denoted by l , is the path length difference between the central trajectory and the current particle. The sixth entry is the fractional momentum deviation between the current particle and the central trajectory $\Delta p/p$ denoted by δ . Clearly the transformation for the solenoid only couples the transverse coordinates of the particles. It is

pointed out in the TRANSPORT manual[32] that the transverse components can be decoupled by rotating the transverse coordinates about the z axis by an angle $-kL$. Now the transform for a rotation of the transverse coordinates is given by:

$$R_{\text{Rotation}} = \begin{bmatrix} C & 0 & S & 0 & 0 & 0 \\ 0 & C & 0 & S & 0 & 0 \\ -S & 0 & C & 0 & 0 & 0 \\ 0 & -S & 0 & C & 0 & 0 \\ 0 & 0 & 0 & 0 & 1 & 0 \\ 0 & 0 & 0 & 0 & 0 & 1 \end{bmatrix} \quad (3.11)$$

where $C = \cos(\alpha)$, $S = \sin(\alpha)$ and α is the angle of rotation about the z-axis.

Then if the transverse coordinates following the solenoid are rotated through an angle $\alpha = -kL$ we have:

$$R_{\text{Rotation}}(\alpha) R_{\text{Solenoid}} = \begin{bmatrix} C & S/k & 0 & 0 & 0 & 0 \\ -kS & C & 0 & 0 & 0 & 0 \\ 0 & 0 & C & S/k & 0 & 0 \\ 0 & 0 & -kS & C & 0 & 0 \\ 0 & 0 & 0 & 0 & 1 & 0 \\ 0 & 0 & 0 & 0 & 0 & 1 \end{bmatrix} \quad (3.12)$$

The transformation above does not couple the transverse or the longitudinal coordinates of the beam. Also the focusing in both planes of the solenoid is clear. The decoupling appears simple enough but one would have to determine the rotation angle for each solenoid setting which is used. And it would have to be incorporated into the measurement technique in order to decouple the transverse coordinates so that the measured emittance would be a conserved quantity. This is true since according to Lejeune[3] if two dimensions of the beam are coupled then only the four dimensional phase is conserved. Also according to Ripkin's theorem for coupled beams[39] if there

is coupling in the transverse dimensions of the beam the projected emittance is of "limited use." And the projected emittance is what is measured in the quadrupole scan. The last point is shown in the simulations presented below.

3.3.1 Simulations With Coupling

Since the rotation transform only couples the transverse dimensions of the beam I will again only use the four dimensional form of the beam transformation in the simulations. In order to incorporate rotation of the beam in the simulations an additional matrix is multiplied on the right of equation (3.9).

$$R = R_{d2}R_{q2}R_{d1}R_{q1}R_{rot} \quad (3.13)$$

The beam is propagated through the above system and the projected horizontal width is measured at the screen location for ten different strengths of q_2 . The quadrupole scan formalism is used to determine the second moments of the beam from which the horizontal emittance is then calculated

3.3.2 Astigmatic Beam

To illustrate the effects of coupling of the transverse dimensions of the beam on the quadrupole scan technique I begin with the distribution from the end of section 3.2.1:

$$\begin{aligned} \sigma_x &= 0.4 \text{ mm} & \sigma_y &= 0.2 \text{ mm} \\ \sigma_{x'} &= 0.1 \text{ mrad} & \sigma_{y'} &= 0.2 \text{ mrad} \\ \sigma_z &= 2.0 \text{ ps} & E &= 30 \text{ MeV} & \delta E &= .03 \text{ MeV} \end{aligned}$$

The initial horizontal emittance of the distribution is:

$$\epsilon_x = 2.33 \text{ mm mrad}$$

And the emittance calculated at the screen by the quadrupole scan is:

$$\epsilon_{x\text{quadscan}} = 2.33 \text{ mm mrad}.$$

If the distribution is rotated through an angle of $\alpha = \pi/4$ by applying the rotation matrix before the distribution is propagated through the quadrupole doublet the calculated horizontal emittance is:

$$\epsilon_{x\text{quadscan}_{\alpha=\pi/4}} = 2.94 \text{ mm mrad} \quad (3.14)$$

As shown in Table 3.3 the distributions at the screen now become:

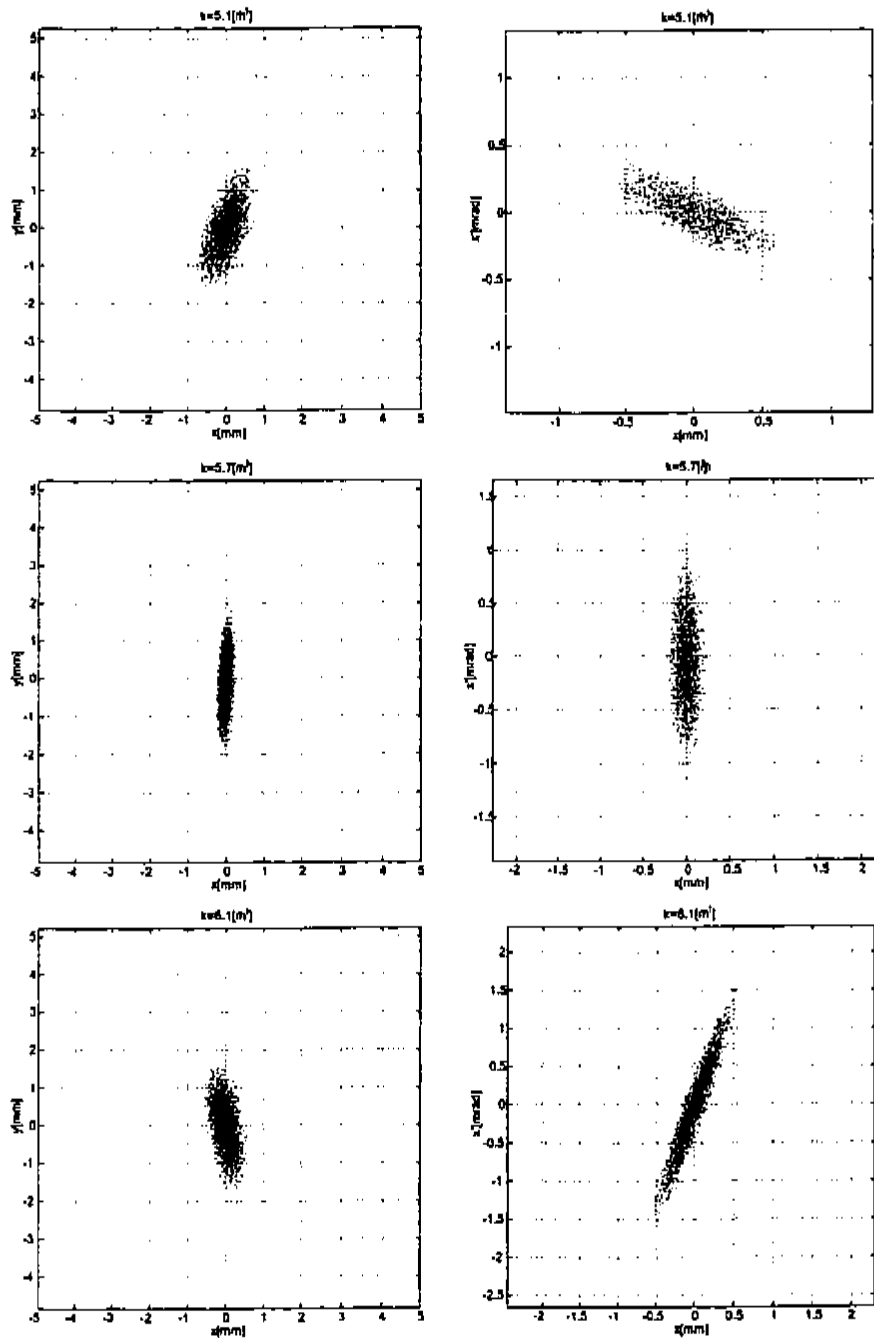


Table 3.3: Plots of x - y and x - x' distributions for three different q_2 strengths for rotated asymmetric beam

Below is a plot, Fig. 3.7, of the beam size versus q_2 strength which shows how the beam width is brought through a minimum.

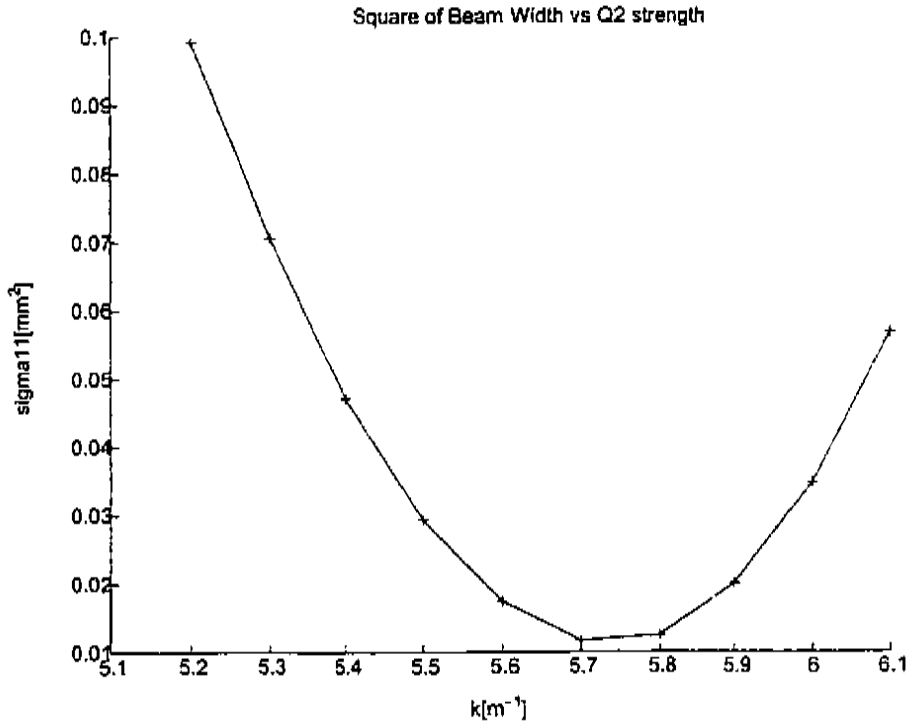


Figure 3.7: Square of beam half width vs q_2 strength for rotated asymmetric distribution

In Fig. 3.7 above, there is nothing in the plot which would indicate any anomaly. And the $x - x'$ phase space in Table 3.3 behaves as it did in the cases where there was no rotation of the beam before it was sent into the doublet. However, the $x - y$ space now shears, there is a visible tilt in the beam which changes as the quadrupole strength is changed. The shear is quite noticeable and the beam distribution crosses the y -axis. This correlation was not present in the simulations for the previous beams (no rotation) even for the astigmatic beams. This behavior is seen in the experimental data presented in the Chap. 7 and was a motivation for this study of the effects of rotations on the quadrupole scan technique. A series of background subtracted images from the YAG screen of a quadrupole scan performed at the GTF the details of which are discussed in detail in Chap. 7 are presented in Fig. 3.8 below.

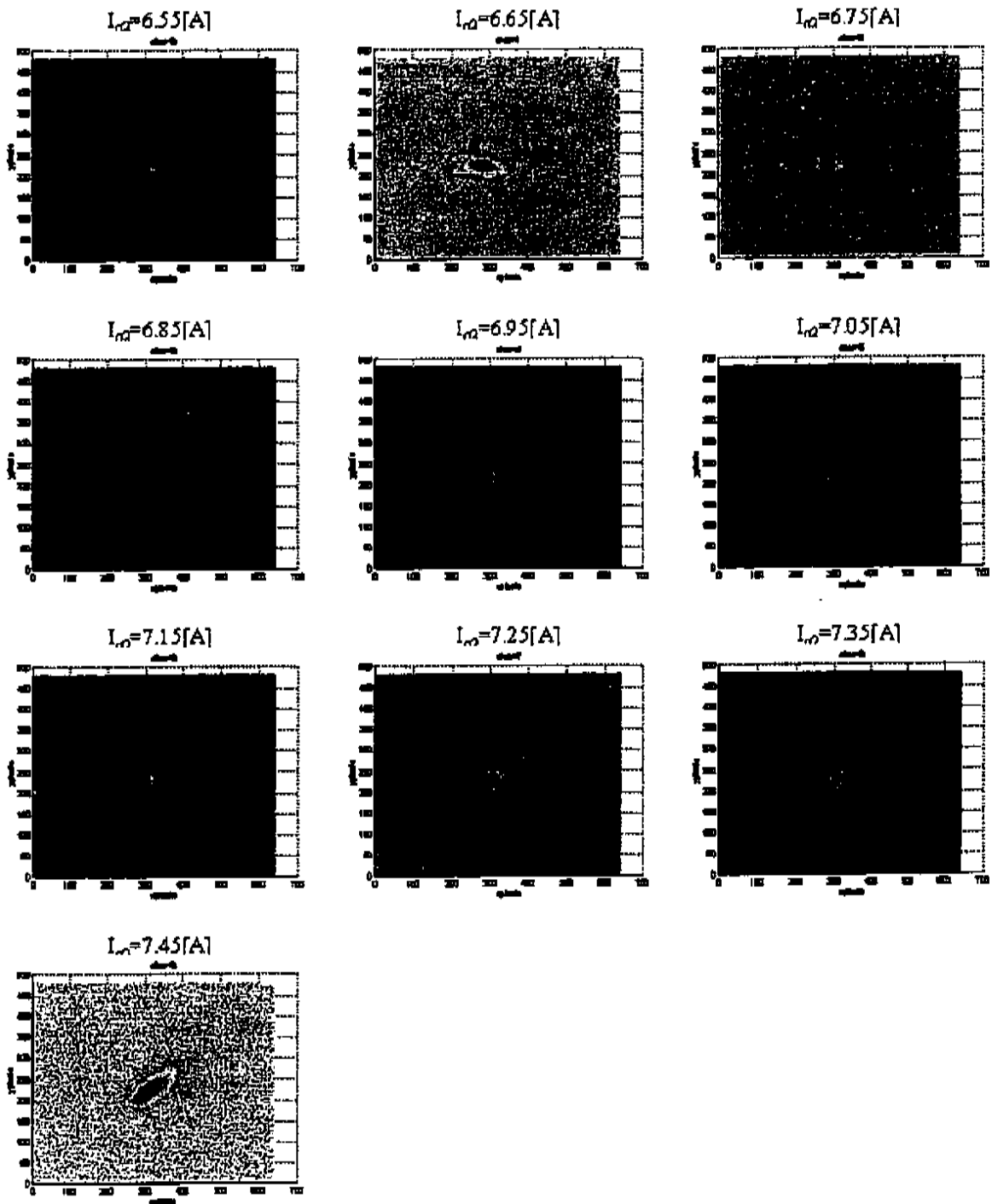


Figure 3.8: Images of the beam from a quadrupole scan at the GTF the horizontal and vertical axes are x and y pixel number respectively

Each image was taken at a particular quadrupole strength denoted in amperes used to energize the quadrupole q2. The horizontal and vertical axes are x and y pixel number respectively. Clearly there is a shearing or rotation of the beam in $x - y$ space as the strength of q2 is changed. There is a definite $x - y$ coupling or correlation which changes as the strength of q2 is changed. The $x - y$ coupling was not present in the quadrupole scans from section 3.2 where the beam distributions were symmetric and asymmetric. Once a rotation is performed on the distribution the $x - y$ correlation becomes evident. This is discussed in great detail in the following sections and chapters.

Returning to the simulations, depending on the values used in the generation of distribution for the simulation, the variation in the emittance calculated with the quadrupole can be even more severe. The beam used above has initial normalized emittances of:

$$\epsilon_x = 2.33 \text{ mm mrad} \text{ and } \epsilon_y = 2.38 \text{ mm mrad} .$$

Next I use a distribution in the simulation with :

$$\begin{array}{lll} \sigma_x & = & 0.2 \text{ mm} \quad \sigma_y = 0.4 \text{ mm} \\ \sigma_{x'} & = & 0.2 \text{ mrad} \quad \sigma_{y'} = 0.3 \text{ mrad} \\ \sigma_z & = & 2.0 \text{ ps} \quad E = 30 \text{ MeV} \quad \delta E = .03 \text{ MeV} \end{array}$$

with initial normalized emittances of:

$$\epsilon_x = 2.34 \text{ mm mrad} \text{ and } \epsilon_y = 7.09 \text{ mm mrad} .$$

For the case of no rotation the calculated normalized emittance is:

$$\epsilon_{x\text{quadscan}} = 2.33 \text{ mm mrad}.$$

For the case where the beam is rotated by an angle of $\alpha = \pi/4$ about the z axis I obtain:

$$\epsilon_{x\text{quadscan}_{\alpha=\pi/4}} = 4.74 \text{ mm mrad}.$$

Now if I rotate the beam through the angles $0 \leq \alpha \leq \pi$ in steps of $\pi/20$ and calculate the projected emittance from the quadrupole scan I obtain values as shown in Fig. 3.9:

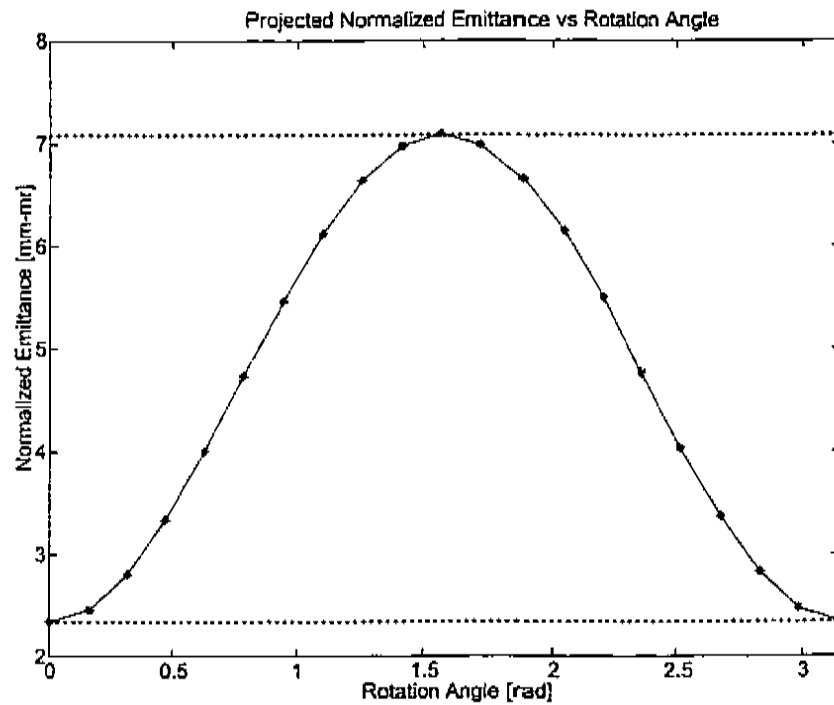


Figure 3.9: Projected normalized emittance vs rotation angle for asymmetric beam

The horizontal dotted lines are the initial emittances $\epsilon_{xi} = 2.34 \text{ mm mrad}$ and $\epsilon_{yi} = 7.09 \text{ mm mrad}$.

The emittance calculated using the quadrupole scan technique is clearly dependent on the rotation angle which effects the amount of coupling in the transverse dimensions of the beam. Therefore the projected horizontal emittance is not a conserved quantity under the influence of a rotation. In order to understand this recall that the beam occupies a region of six dimensional phase space. We choose to project out the various dimensions of the beam such as the $x - x'$, $y - y'$ and $z - z'$ when we make projection measurements. For example a typical quadrupole scan is a sampling of the projected $x - x'$ space. The rotation alters the $x - x'$ phase space.

To visualize this projection, picture viewing the shadow of an egg. The shadow represents the $x - x'$ area formed by projecting out the other dimensions. If there is a light source located vertically above a plane surface and an egg is held between the light source and the plane, the shadow of the egg will be formed on the plane surface. Now since the egg is approximately an ellipsoid, there are two different axes of the egg depending on the orientation. I choose to call the minor axis of the egg that which contains the axis of minimum length. And the major axis that which contains the maximum length. The area of the shadow is a function of the orientation of the egg. It can be made to vary between a minimum when the egg is held so that its minor axis is parallel to the plane of the shadow. Then the shadow cast is a circle with the minimum possible shadow area. If the egg is oriented so that the major axis is parallel to the plane of the shadow, the shadow cast will be an ellipse which has the maximum possible shadow area. The projected area can be any value between these two extremes depending on the orientation of the egg. The conserved quantity in the above experiment is the volume of the egg, it is constant regardless of the orientation of the egg. If the egg is replaced with a ball then the shadow cast will be a circle with constant area regardless of the orientation. From this area one can infer the radius of the ball and hence its volume. To do the same with the egg one would need to know the dimensions of the shadow and the orientation of the egg to determine the volume of the egg. This is the case of the asymmetric distribution, we cannot rely on the projected quantities since they are not conserved for all orientation of an asymmetric distribution.

3.3.3 Simulations With Symmetric Beams

One could argue that the beam is perfectly round in four dimensional phase space and therefore immune to the effects of the rotation of the beam. The projection of a sphere is a circle no matter how it is rotated. This is true and is shown below by performing the same simulation as above but with the first distribution of this chapter. Starting with the initial parameters:

$$\begin{aligned} \sigma_x &= \sigma_y = 0.2 \text{ mm} & \sigma_{x'} &= \sigma_{y'} = 0.2 \text{ mrad} \\ \sigma_z &= 2.0 \text{ ps} & E &= 30 \text{ MeV} & \delta E &= .03 \text{ MeV} \end{aligned}$$

The initial horizontal emittance of the distribution is:

$$\epsilon_x = 2.38 \text{ mm mrad}$$

The emittance from the quadrupole scan technique is:

$$\epsilon_{x\text{quadscan}} = 2.38 \text{ mm mrad}$$

Now the distribution is rotated through an angle of $\alpha = \pi/4$ by applying the rotation matrix before it is propagated through the quadrupole doublet. The horizontal emittance from the quadrupole scan technique is:

$$\epsilon_{x\text{quadscan}_{\alpha=\pi/4}} = 2.38 \text{ mm mrad}$$

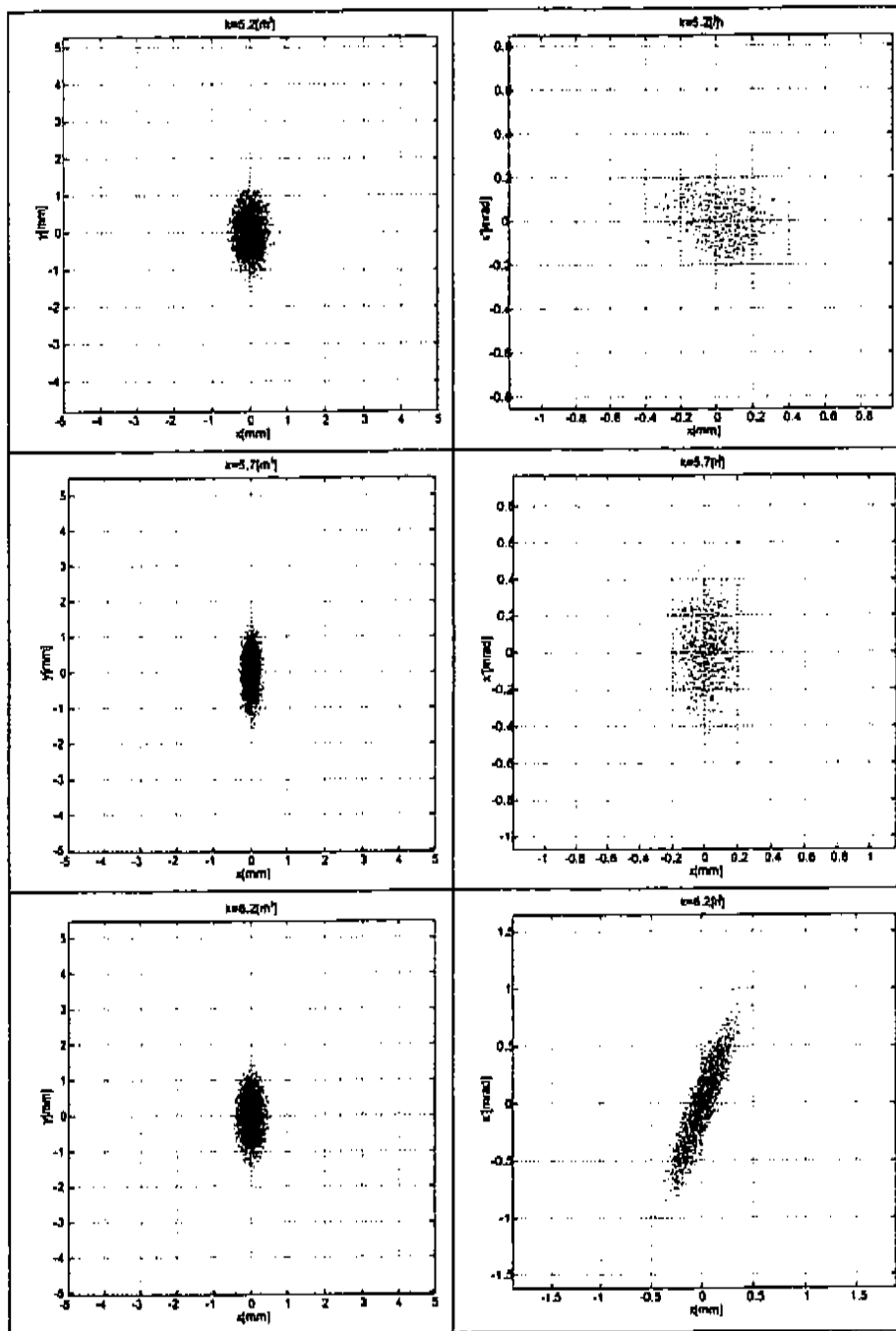


Table 3.4: Plots of x - y and x - x' distributions for symmetric beam rotated for three different q_2 strengths

The distributions at the screen are shown in Table 3.4 above. Notice that there is no apparent correlation in the $x - y$ distributions.

Now if I rotate the beam through the angles $0 \leq \alpha \leq \pi$ in steps of $\pi/20$ and measure the projected emittance from the quadrupole scan I obtain:

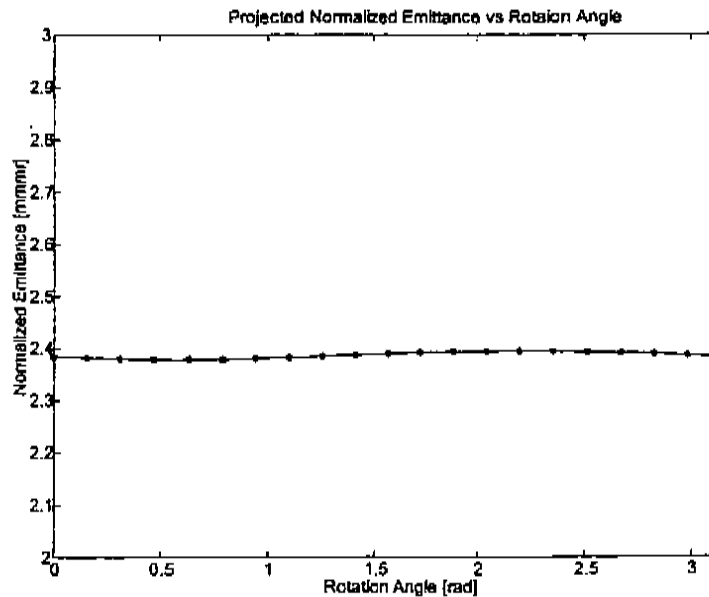


Figure 3.10: Projected normalized emittance vs rotation angle for symmetric beam

This shows that the values for the projected emittance from a quadrupole scan in which the distribution is subject to a rotation is reliable if the distribution is symmetric in four dimensions. However, that is a fairly stringent requirement and how would one go about proving the beam is symmetric in four dimensional phase space? Also notice there is a small fluctuation in the values for the emittance with rotation angle which is due to presence of small amounts of correlations in the initial distribution that occur in the distribution despite the specification of symmetry in the variables used to generate the distribution. This is discussed in greater detail in the next chapter. The variation in the graph above would be considered negligible in the laboratory environment.

3.3.4 Simulations With Bi-Symmetric Beams

One could also argue that the beam makes a round spot at the entrance to the quadrupole doublet and is symmetric. But that only ensures symmetry in the $x - y$ dimensions of the beam. What of the x' and y' dimensions? I repeat the previous simulation but make:

$$\begin{aligned} \sigma_x &= \sigma_y = 0.2 \text{ mm} \\ \sigma_{x'} &= 0.2 \text{ mrad} & \sigma_{y'} &= 0.4 \text{ mrad} \\ \sigma_z &= 2.0 \text{ ps} & E &= 30 \text{ MeV} & \delta E &= .03 \text{ MeV} \end{aligned}$$

The initial normalized emittances of the distribution are:

$$\begin{aligned} \epsilon_x &= 2.39 \text{ mm mrad} \\ \epsilon_y &= 4.81 \text{ mm mrad} \end{aligned}$$

The emittance from the quadrupole scan technique with no rotation of the beam is:

$$\epsilon_{\text{xquadscan}} = 2.39 \text{ mm mrad}$$

Now the distribution is rotated through an angle of $\alpha = \pi/4$ by applying the rotation matrix before it is propagated through the quadrupole doublet. The horizontal emittance calculated from the quadrupole scan techniques is:

$$\epsilon_{\text{xquadscan}_{\alpha=\pi/4}} = 3.71 \text{ mm mrad} .$$

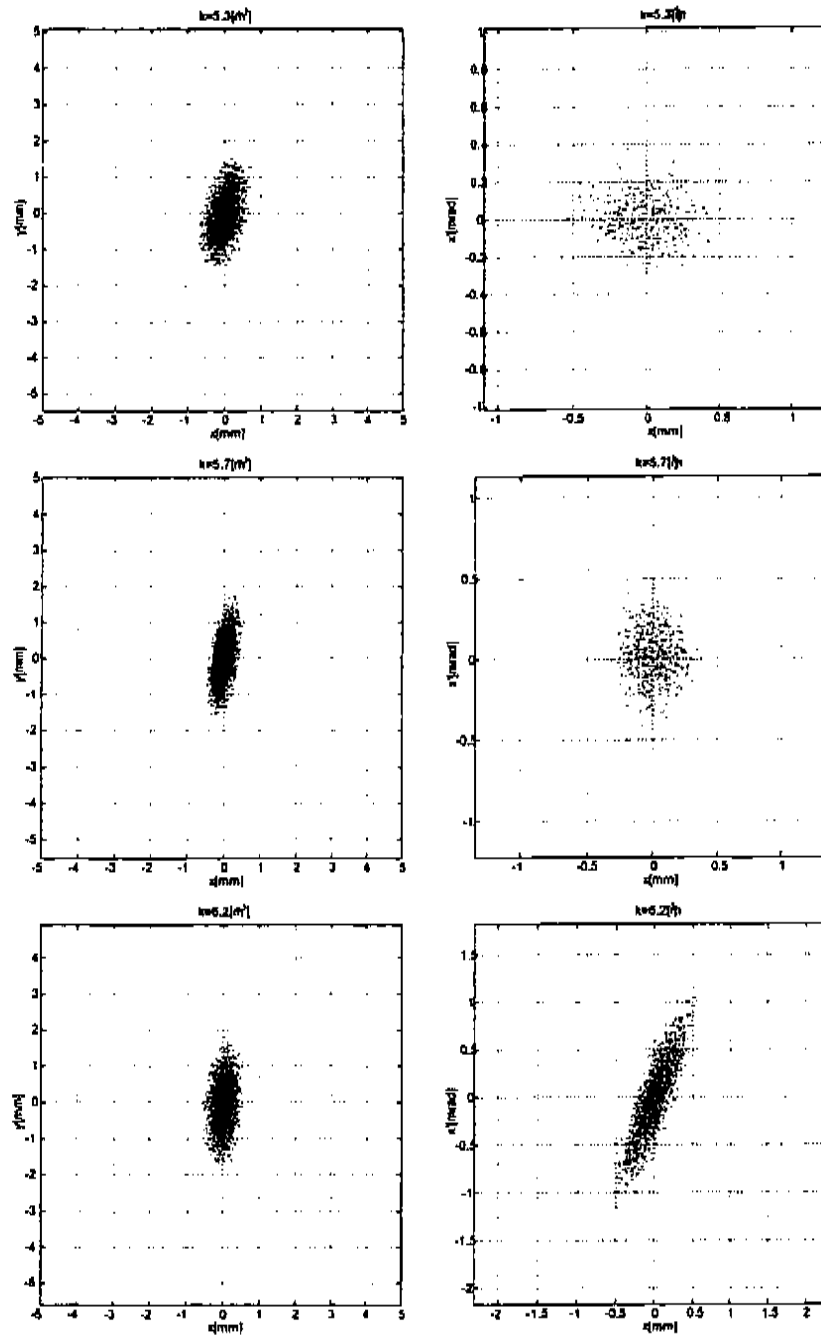


Table 3.5: Plot of x - y and x - x' distributions for bi-symmetric beam rotated for three different q_2 strengths

The distributions at the screen are shown in Table 3.5 above. Again there is a correlation in the $x - y$ plot.

Now if I rotate the beam through the angles $0 \leq \alpha \leq \pi$ and calculate the projected emittance from the quadrupole scan I obtain Fig 3.11:

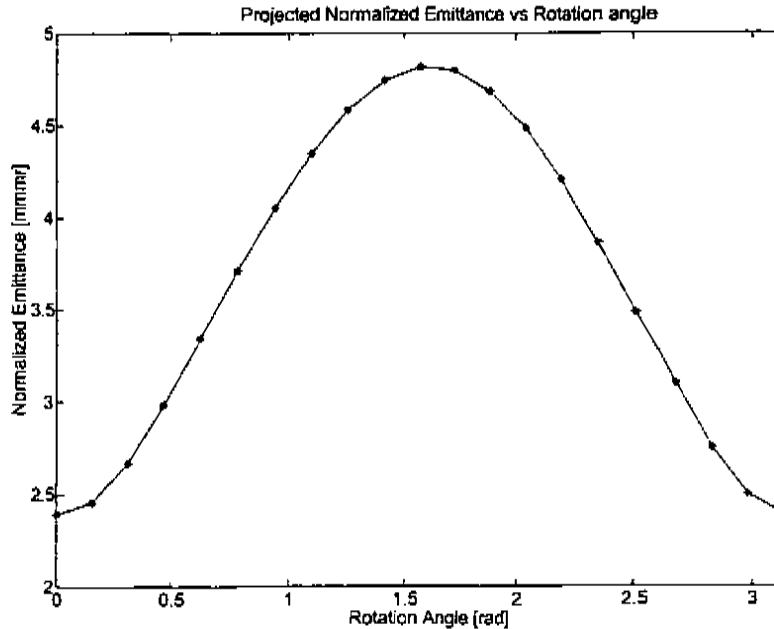


Figure 3.11: Projected normalized emittance vs rotation angle for bi-symmetric distribution

Even though the initial $x - y$ distribution is round the projected emittance is dependent on the angle of rotation. So unless the distribution is symmetric in four dimensions before it enters the doublet the projected emittance is dependent on the angle of rotation about the z axis.

In a photoinjector the laser may produce a beam pulse that has an asymmetric distribution and also the cathode surface may have a nonuniform quantum efficiency which results in an uneven production of electrons in the photo-election process[40] and thus generate an asymmetric electron beam from the cathode. Other sources of asymmetric electron beam may be higher order modes in the RF gun and in the solenoid itself. Any of which can lead to an asymmetric distribution which is rotated

by the solenoid. And as shown above this can lead to a projected emittance which is a function of rotation angle.

I will show in the next chapter that the conserved quantity in the presence of rotations is the four dimensional volume of phase space occupied by the beam. This volume is formed by the squares of the maximum extents of transverse components of the beam $\sigma_{11} = (x_{\max})^2$, $\sigma_{22} = (x'_{\max})^2$, $\sigma_{33} = (y_{\max})^2$ and $\sigma_{44} = (y'_{\max})^2$ with the inclusion of all possible couplings σ_{12} , σ_{13} , σ_{14} , σ_{23} , σ_{24} and σ_{34} . Recall one must include σ_{12} to correctly calculate of the projected emittance $\epsilon_n = \beta\gamma\sqrt{\sigma_{11}\sigma_{22} - \sigma_{12}^2}$. I will show that the couplings σ_{12} , σ_{13} , σ_{14} , σ_{23} , σ_{24} and σ_{34} must be included to form the conserved quantity, the four dimensional volume occupied by the beam in phase space.

Chapter 4

Four Dimensional Trace Space Analysis

In this chapter the formalism for four dimensional trace space analysis is developed which enables the determination of the four dimensional volume occupied by the beam in trace space. First the two dimensional trace space analysis is presented as a motivation for the development of the four dimensional analysis. Next the four dimensional uncoupled trace space is presented as a further step in the progression of the development of the four dimensional analysis. Finally the full coupled four dimensional trace space analysis is presented.

4.1 Two Dimensional Coupling

From the previous chapter it was clear that in the presence of rotations for distributions which are not symmetric in four dimensions there was a correlation in the $x - y$ space. This correlation complicates the question of what the beam width is since the beam is tilted in $x - y$ space. The projected width of a beam with a non-zero $x - y$ correlation is larger than if the beam were upright. This is similar to the situation of the two dimensional analysis of $x - x'$ space. The beam may have a correlation between x and x' and a projection is taken to determine the width of the beam. The two dimensional trace space diagram where $1 := x$ and $2 := x'$ from the Chap. 3 is

reproduced in Fig. 4.1 below:

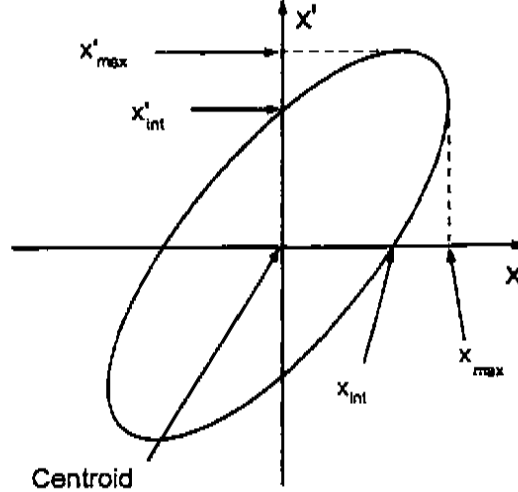


Figure 4.1: Ellipse surrounding beam distribution in trace space

The square of the projected half width of the beam $\sigma_{11} = x_{\max}^2$ is a function of the tilt of the phase ellipse. We desire to determine the area of the ellipse and use the projected quantities σ_{11} and σ_{22} to calculate it. We must also consider the correlation between the x and x' dimensions by inclusion of σ_{12} in the equation for the area of the ellipse which is given by:

$$A = \pi \sqrt{\det(\sigma)} = \pi \sqrt{\sigma_{11}\sigma_{22} - \sigma_{12}^2} = \pi \epsilon_x \quad (4.1)$$

The area calculated in the manner above is constant for any orientation of the ellipse by inclusion of the effect of the coupling of the $x - x'$ coordinates. From the diagram we see that if the area is calculated without the correlation term we obtain:

$$\tilde{A} = \pi \sqrt{\sigma_{11}\sigma_{22}} = \pi \sqrt{\text{trace}(\sigma)} \quad (4.2)$$

$\tilde{A} = \pi \sqrt{\sigma_{11}\sigma_{22}}$ is the area of an upright ellipse with axis equal to $\sqrt{\sigma_{11}}$ and $\sqrt{\sigma_{22}}$ and so the area \tilde{A} is greater than A if σ_{12} is nonzero. So the coupling term σ_{12} must be included in the calculation of the area of the phase ellipse unless it can be proven to

be zero.

Another relation involving the correlation and the projection is given by equation (2.55):

$$x_{int} = +\sqrt{\sigma_{11}(1 - r_{12}^2)} \quad (4.3)$$

which gives the width of the distribution along the x -axis, x_{int} , in terms of the projected width σ_{11} and the correlation coefficient:

$$r_{12} = \frac{\sigma_{12}}{\sqrt{\sigma_{11}\sigma_{22}}} \quad (4.4)$$

If there is no correlation in the beam then $r_{12} = 0$ and $x_{int} = +\sqrt{\sigma_{11}} = x_{max}$. If $r_{12} \neq 0$ then $x_{max} > x_{int}$ and the apparent enlargement of the projected width must be taken into account by inclusion of the correlation in the beam. If $\sigma_{13} \neq 0$ in $x - y$ space then $r_{13} = \frac{\sigma_{13}}{\sqrt{\sigma_{11}\sigma_{33}}} \neq 0$ and there is an apparent enlargement in the projected width of the beam $x_{max} = \sqrt{\sigma_{11}} > x_{int} = +\sqrt{\sigma_{11}(1 - r_{13}^2)}$. Therefore one must determine how to account for this correlation in the beam in determining the projected emittance.

4.2 Four Dimensional Beam Matrix With Partial Coupling

In order to advance toward the full four dimensional volume first consider four dimensional trace space with coupling only in the $x - x'$ and $y - y'$ subspaces the four dimensional sigma matrix becomes:

$$\sigma_{4D-PC} = \begin{bmatrix} \sigma_{11} & \sigma_{12} & 0 & 0 \\ \sigma_{12} & \sigma_{22} & 0 & 0 \\ 0 & 0 & \sigma_{33} & \sigma_{34} \\ 0 & 0 & \sigma_{34} & \sigma_{44} \end{bmatrix} \quad (4.5)$$

where $1 := x$, $2 := x'$, $3 := y$ and $4 := y'$. This is the usual form for the four

dimensional sigma matrix since the transforms for drifts and quadrupoles do not contain any terms which lead to coupling between the transverse x and y degrees of freedom of the beam. The four dimensional transforms for a drift and a focusing quadrupole are given below [32]:

$$R_{\text{Drift}} = \begin{bmatrix} 1 & d & 0 & 0 \\ 0 & 1 & 0 & 0 \\ 0 & 0 & 1 & d \\ 0 & 0 & 0 & 1 \end{bmatrix} \quad (4.6)$$

where d is the length of the drift

$$R_{\text{Focusing quad}} = \begin{bmatrix} \cos(kL) & (1/k)\sin(kL) & 0 & 0 \\ -k\sin(kL) & \cos(kL) & 0 & 0 \\ 0 & 0 & \cosh(kL) & (1/k)\sinh(kL) \\ 0 & 0 & k\sinh(kL) & \cosh(kL) \end{bmatrix} \quad (4.7)$$

where L is the effective length of the quadrupole and k is the strength of the quadrupole.

This shows that a focusing quadrupole is focusing in the horizontal plane and defocusing in the vertical plane. A defocusing quadrupole is represented by:

$$R_{\text{Defocusing quad}} = \begin{bmatrix} \cosh(kL) & (1/k)\sinh(kL) & 0 & 0 \\ k\sinh(kL) & \cosh(kL) & 0 & 0 \\ 0 & 0 & \cos(kL) & (1/k)\sin(kL) \\ 0 & 0 & -k\sin(kL) & \cos(kL) \end{bmatrix} \quad (4.8)$$

Any combination of the above transforms formed by multiplication will also have no coupling of the transverse dimensions x and y . So when the four dimensional sigma matrix is transformed as described in the last chapter:

$$\sigma(1)_{4\text{D-PC}} = R\sigma(0)_{4\text{D-PC}}R^t \quad (4.9)$$

where PC denotes 'partial coupling.' The coupling elements of the sigma matrix

above which are shown as equal to zero remain equal to zero.

For the transforms presented above $\det(R) = 1$ and $\det(R^t) = 1$. Since the determinant of a product of transforms is equal to the product of the determinants of the individual transforms we have $\det(R) = \det(R^t) = 1$ for the transformation formed by any combination of drifts and quadrupoles. Taking the determinant of both sides of the previous equation above we have:

$$\begin{aligned} \det(\sigma(1)_{4D-PC}) &= \det(R\sigma(0)_{4D-PC}R^t) \\ &= \det(R)\det(\sigma(0)_{4D-PC})\det(R^t) \\ &= \det(\sigma(0)_{4D-PC}) \end{aligned} \quad (4.10)$$

Which demonstrates the conservation of $\det(\sigma_{4D-PC})$ between two locations of a beam line if the transforms relating the two locations have the property that $\det(R) = 1$ and $\det(R^t) = 1$. Now the volume of the 4-dimensional ellipsoid defined by σ_{4D-PC} is [41]:

$$\begin{aligned} V_{4D-PC} &= \left[\frac{\pi^2}{\Gamma(3)} \right] \sqrt{\det(\sigma_{4D-PC})} \\ &= \left[\frac{\pi^2}{2} \right] \sqrt{\det(\sigma_{4D-PC})} \end{aligned} \quad (4.11)$$

So the volume of the four dimensional trace space is conserved. Notice that:

$$\begin{aligned} \det(\sigma_{4-D}) &= [\sigma_{11}\sigma_{22} - \sigma_{12}^2][\sigma_{33}\sigma_{44} - \sigma_{34}^2] \\ &= \epsilon_x^2 \epsilon_y^2 \end{aligned} \quad (4.12)$$

so that,

$$V_{4-D} = \frac{\pi^2}{2} \epsilon_x \epsilon_y \quad (4.13)$$

This is the form of the denominator in the definition for beam brightness from Chap.

1:

$$B = \frac{I}{\frac{\pi^2}{2} \epsilon_x \epsilon_y} \quad (4.14)$$

where I is the peak current. So the brightness is conserved for system where there is no coupling between the transverse dimensions.

4.3 Four Dimensional Beam Matrix With Full Coupling

Now if we include coupling between all four of the dimensions of the beam, the sigma matrix becomes:

$$\sigma_{4-D} = \begin{bmatrix} \sigma_{11} & \sigma_{12} & \sigma_{13} & \sigma_{14} \\ \sigma_{12} & \sigma_{22} & \sigma_{23} & \sigma_{24} \\ \sigma_{13} & \sigma_{23} & \sigma_{33} & \sigma_{34} \\ \sigma_{14} & \sigma_{24} & \sigma_{34} & \sigma_{44} \end{bmatrix} \quad (4.15)$$

where the new elements are assumed to be symmetric:

$$\sigma_{ij} = \sigma_{ji} \quad (4.16)$$

And these new elements are calculated as before:

$$\sigma_{ij} = \frac{\iiint\int u_i u_j \rho(i, j) dx dx' dy dy'}{\iiint\int \rho(i, j) dx dx' dy dy'} \quad (4.17)$$

where $i, j = 1, 2, 3, 4$ and $u_1 = x$, $u_2 = x'$, $u_3 = y$ and $u_4 = y'$. The correlation coefficients are then:

$$r_{ij} = \frac{\sigma_{ij}}{\sqrt{\sigma_{ii} \sigma_{jj}}} \quad (4.18)$$

where $i \neq j$.

Now from Lawson[2] and Lejeune[3] the four dimensional volume is the conserved quantity in the presence of coupling of the transverse dimensions. One can also use the same arguments used previously by taking the determinant of the relation for the transformation of the four dimensional beam matrix from one location to another along the beam line:

$$\begin{aligned}
 \det(\sigma(1)) &= \det(R\sigma(0)R^t) \\
 &= \det(R)\det(\sigma(0))\det(R^t) \\
 &= \det(\sigma(0))
 \end{aligned} \tag{4.19}$$

Again this demonstrates the conservation of $\det(\sigma)$ between two locations of the beam line provided the transforms relating the two locations have the property that $\det(R) = 1$ and $\det(R^t) = 1$. Recall the transform for a rotation of the transverse coordinates is given by:

$$R_{\text{Rotation}} = \begin{bmatrix} C & 0 & S & 0 & 0 & 0 \\ 0 & C & 0 & S & 0 & 0 \\ -S & 0 & C & 0 & 0 & 0 \\ 0 & -S & 0 & C & 0 & 0 \\ 0 & 0 & 0 & 0 & 1 & 0 \\ 0 & 0 & 0 & 0 & 0 & 1 \end{bmatrix} \tag{4.20}$$

where $C = \cos(\alpha)$, $S = \sin(\alpha)$ and α is the angle of rotation about the z-axis. Note that the determinant of the full 6-D and the 4-D submatrix are both equal to 1. So by using the 6-D or 4-D formalism we are guaranteed to have $\det(\sigma(1)) = \det(\sigma(0))$ which demonstrates the conservation of the 6 and 4 dimensional volumes. However the 2-D analysis with a rotation fails to conserve $\det(\sigma_{2-D})$. In the presence of rotations if one only considers the $x - x'$ space then only the 11, 12, 21 and 22 elements of the transformation matrices and the beam matrix are used in modeling the beam. If only the 11, 12, 21 and 22 elements of the rotation transform are used

one obtains the transform for a rotation for $x - x'$ space:

$$R_{\text{Rotation}_{x-x'}} = \begin{bmatrix} \cos(\alpha) & 0 \\ 0 & \cos(\alpha) \end{bmatrix} \quad (4.21)$$

Clearly the determinant of this matrix is only equal to 1 if $\alpha = 0$, or there is NO rotation. If $\alpha = \pm\pi$, $\sin(\pi) = 0$ and the rotation transform does not produce coupling between the transverse dimensions.

If there are no rotations and if the 11,12, 21, and 22 or the 33, 34, 43 and 44 elements for the four dimensional transforms for the drift or quadrupoles are used to form two dimensional matrices $R_{2 \times 2}$ then we have $\det(R_{2 \times 2}) = 1$. So the areas of the $x - x'$ and $y - y'$ subspaces are conserved and can be treated separately when there is no rotation of the beam. This is clearly not true when rotations are involved. Interestingly in the situation for a four dimensionally symmetric beam where the projected emittance seems unaffected by a rotation, conservation of the $x - x'$ area is NOT guaranteed. Only the volume of the four dimensional ellipsoid is constant under rotation of the beam.

Again the four dimensional volume is given by:

$$\begin{aligned} V_{4-D} &= \left[\frac{\pi^2}{\Gamma(3)} \right] \sqrt{\det(\sigma_{4-D})} \\ &= \left[\frac{\pi^2}{2} \right] \sqrt{\det(\sigma_{4-D})} \end{aligned} \quad (4.22)$$

but now we consider the possibility that the additional coupling terms $\sigma_{13}, \sigma_{14}, \sigma_{23}, \sigma_{24}$ may be non-zero. Finally the brightness of the beam with coupling of the transverse dimensions is given by[42]:

$$B = \frac{I}{V_{4-D}} \quad (4.23)$$

Where V_{4-D} is the volume given by the relation above, this form of the brightness is conserved in the presence of coupling of the transverse dimensions of the beam. This relation for the volume reduces to the uncoupled case when the coupling terms are

set to zero. Expanding $\det(\sigma_{4-D})$, collecting terms and identifying $\sqrt{\sigma_{11}\sigma_{22} - \sigma_{12}^2} = \epsilon_x$ and $\sqrt{\sigma_{33}\sigma_{44} - \sigma_{34}^2} = \epsilon_y$, we obtain:

$$\begin{aligned} \det(\sigma_{4-D}) = & \epsilon_x^2 \epsilon_y^2 \\ & + (\sigma_{13}\sigma_{21} - \sigma_{11}\sigma_{23})(\sigma_{23}\sigma_{44} - \sigma_{34}\sigma_{24}) + (\sigma_{11}\sigma_{24} - \sigma_{14}\sigma_{12})(\sigma_{23}\sigma_{34} - \sigma_{33}\sigma_{24}) \\ & + (\sigma_{12}\sigma_{23} - \sigma_{13}\sigma_{22})(\sigma_{13}\sigma_{44} - \sigma_{34}\sigma_{14}) + (\sigma_{14}\sigma_{22} - \sigma_{12}\sigma_{24})(\sigma_{13}\sigma_{34} - \sigma_{33}\sigma_{14}) \\ & + (\sigma_{13}\sigma_{24} - \sigma_{14}\sigma_{23})(\sigma_{13}\sigma_{24} - \sigma_{23}\sigma_{14}). \end{aligned} \quad (4.24)$$

The above equation reduces to the uncoupled case:

$$\det(\sigma_{4-D}) = \epsilon_x^2 \epsilon_y^2 \quad (4.25)$$

only when all of the coupling terms σ_{13} , σ_{14} , σ_{23} and σ_{24} are equal to zero. Also in the event the coupling terms σ_{12} and σ_{34} can also be made to be zero the four dimensional ellipsoid is “upright” and any projected dimension is free of the effects from correlations which lead to a lengthening of dimensions.

4.4 Measuring The Four Dimensional Trace Space Volume

Clearly if all of the elements of the four dimensional beam matrix could be determined the volume could be formed and we would have a conserved quantity. Also knowledge of all of the couplings would give an insight into the orientation of the beam in four dimensional trace space. How does one go about determining the elements?

4.4.1 Horizontal Information

Following the analysis of the previous chapter we begin with the relation for transforming the beam matrix from one location to another along the beamline:

$$\sigma(1)_{4-D} = R\sigma(0)_{4-D}R^t \quad (4.26)$$

and again we form a relation for the $\sigma(1)_{11}$ term on the left. However, now R and $\sigma(0)_{4-D}$ are 4 dimensional. Again we multiply out the right side of the above relation and form the following relation:

$$\sigma(1)_{11} = \widetilde{R}_1 \vec{\sigma}(0)_{4-D} \quad (4.27)$$

where $\sigma(1)_{11}$ is a scalar, $\vec{\sigma}(0)_{4-D}$ is a vector and \widetilde{R}_1 is a 10×1 matrix. Due to the symmetry of the beam matrix σ_{4-D} there are now ten terms to determine instead of three in the two dimensional case. So the vector on the right of the above relation becomes:

$$\vec{\sigma}(0)_{4-D} = \begin{bmatrix} \sigma(0)_{11} \\ \sigma(0)_{12} \\ \sigma(0)_{13} \\ \sigma(0)_{14} \\ \sigma(0)_{22} \\ \sigma(0)_{23} \\ \sigma(0)_{24} \\ \sigma(0)_{33} \\ \sigma(0)_{34} \\ \sigma(0)_{44} \end{bmatrix} \quad (4.28)$$

From Carey[43] if only first order terms are considered equation (4.27) can be rewritten as:

$$\sigma(1)_{11} = \sum R_{1i}R_{1j}\sigma(0)_{ij} \quad (4.29)$$

where $i, j = 1, 2, 3, 4$ and R_{1i} is the i^{th} element from the first row of the transformation matrix R . It is instructive to show the full form of the above relation:

$$\begin{aligned} \sigma(1)_{11} = & [R_{11}^2\sigma(0)_{11} + 2R_{11}R_{12}\sigma(0)_{12} + 2R_{11}R_{13}\sigma(0)_{13} + 2R_{11}R_{14}\sigma_{14}(0) \\ & + R_{12}^2\sigma_{22}(0) + 2R_{12}R_{13}\sigma_{23}(0) + 2R_{12}R_{14}\sigma_{24}(0) + R_{13}^2\sigma_{33}(0) \\ & + 2R_{13}R_{14}\sigma_{34}(0) + R_{14}^2\sigma_{44}(0)] \end{aligned} \quad (4.30)$$

For a quadrupole scan the values for the quadrupoles and the drift distance are well known and the rotation angle is unknown. Since all of the details of the possible asymmetry and rotation are not known at this time I choose to only use a transform of the form:

$$R = R_{d2}R_{q2}R_{d1}R_{q1} \quad (4.31)$$

in the relation for $\sigma(1)_{11}$. Note that this transform does not include any element that would introduce rotation. This is the transformation for the beamline starting at the entrance to the quadrupole doublet and ending at the screen location. This portion is chosen since I choose to model any coupling between the transverse dimensions of the beam as occurring before the quadrupole doublet. I believe this is reasonable since the solenoid which contains rotations at its entrance and exit is located upstream of the doublet. And the quadrupoles of the doublet are mounted on the same precision rails and so should not be rotated with respect to each other. A transform of this form has $R_{13} = R_{14} = 0$ since these terms are zero in the transformations for drifts and quadrupoles. Then the equation (4.30) above becomes:

$$\begin{aligned} \sigma(1)_{11} = & [R_{11}^2\sigma(0)_{11} + 2R_{11}R_{12}\sigma(0)_{12} + 0 \cdot \sigma(0)_{13} + 0 \cdot \sigma_{14}(0) + R_{12}^2\sigma_{22}(0) \\ & + 0 \cdot \sigma_{23}(0) + 0 \cdot \sigma_{24}(0) + 0 \cdot \sigma_{33}(0) + 0 \cdot \sigma_{34}(0) + 0 \cdot \sigma_{44}(0)] \end{aligned} \quad (4.32)$$

or,

$$\sigma(1)_{11} = [R_{11}^2 \sigma(0)_{11} + 2R_{11}R_{12} \sigma(0)_{12} + R_{12}^2 \sigma_{22}(0)] \quad (4.33)$$

And in a more compact form,

$$\sigma(1)_{11} = \widetilde{R}_1 \vec{\sigma}(0)_{4-D}. \quad (4.34)$$

In the relation above the only nonzero terms are those involving $\sigma(0)_{11}$, $\sigma(0)_{12}$ and $\sigma(0)_{22}$ which is the same as the previous two dimensional case. So now \widetilde{R}_1 for a set of n measurements has the form:

$$\begin{bmatrix} (R_{11}^2)_1 & (2R_{11}R_{12})_1 & 0 & 0 & (R_{12}^2)_1 & 0 & 0 & 0 & 0 & 0 \\ (R_{11}^2)_2 & (2R_{11}R_{12})_2 & 0 & 0 & (R_{12}^2)_2 & 0 & 0 & 0 & 0 & 0 \\ (R_{11}^2)_3 & (2R_{11}R_{12})_3 & 0 & 0 & (R_{12}^2)_3 & 0 & 0 & 0 & 0 & 0 \\ \vdots & \vdots & \vdots & \vdots & \vdots & \vdots & \vdots & \vdots & \vdots & \vdots \\ (R_{11}^2)_i & (2R_{11}R_{12})_i & 0 & 0 & (R_{12}^2)_i & 0 & 0 & 0 & 0 & 0 \\ \vdots & \vdots & \vdots & \vdots & \vdots & \vdots & \vdots & \vdots & \vdots & \vdots \\ (R_{11}^2)_n & (2R_{11}R_{12})_n & 0 & 0 & (R_{12}^2)_n & 0 & 0 & 0 & 0 & 0 \end{bmatrix} \quad (4.35)$$

Clearly there are only three independent columns in the above matrix. Therefore there are not enough independent columns and the matrix is rank deficient and so is not invertible[44].

4.4.2 Vertical Information

If the same process is repeated for $\sigma(1)_{33}$, the square of the width of the y projection, one obtains a matrix \widetilde{R}_3 in which only the last three columns that are non-zero. This is seen from the expansion of (4.29) for $\sigma(1)_{33}$:

$$\begin{aligned} \sigma(1)_{33} = & [R_{31}^2\sigma(0)_{11} + 2R_{31}R_{32}\sigma(0)_{12} + 2R_{31}R_{33}\sigma(0)_{13} + 2R_{31}R_{34}\sigma(0)_{14} \\ & + R_{32}^2\sigma(0)_{22} + 2R_{32}R_{33}\sigma(0)_{23} + 2R_{32}R_{34}\sigma(0)_{24} + R_{33}^2\sigma(0)_{33} \\ & + 2R_{33}R_{34}\sigma(0)_{34} + R_{34}^2\sigma(0)_{44}] \end{aligned} \quad (4.36)$$

Since there is no coupling included in the R transfer matrix $R_{31} = R_{32} = R_{41} = 0$

$$\begin{aligned} \sigma(1)_{33} = & [0 \cdot \sigma(0)_{11} + 0 \cdot \sigma(0)_{12} + 0 \cdot \sigma(0)_{13} + 0 \cdot \sigma(0)_{14} + 0 \cdot \sigma(0)_{22} + 0 \cdot \sigma(0)_{23} \\ & + 0 \cdot \sigma(0)_{24} + R_{33}^2\sigma(0)_{33} + 2R_{33}R_{34}\sigma(0)_{34} + R_{34}^2\sigma(0)_{44}] \end{aligned} \quad (4.37)$$

or,

$$\sigma(1)_{33} = [R_{33}^2\sigma_{33}(0) + 2R_{33}R_{34}\sigma_{34}(0) + R_{34}^2\sigma_{44}(0)] \quad (4.38)$$

And in a more compact form,

$$\sigma(1)_{33} = \widetilde{R}_3\sigma(0). \quad (4.39)$$

The only nonzero terms are those involving $\sigma(0)_{33}$, $\sigma(0)_{34}$ and $\sigma(0)_{44}$. And so the matrix for \widetilde{R}_3 becomes:

$$\begin{bmatrix}
 0 & 0 & 0 & 0 & 0 & 0 & 0 & (R_{33}^2)_1 & (2R_{33}R_{34})_1 & (R_{34}^2)_1 \\
 0 & 0 & 0 & 0 & 0 & 0 & 0 & (R_{33}^2)_2 & (2R_{33}R_{34})_2 & (R_{34}^2)_2 \\
 0 & 0 & 0 & 0 & 0 & 0 & 0 & (R_{33}^2)_3 & (2R_{33}R_{34})_3 & (R_{34}^2)_3 \\
 \vdots & \vdots & \vdots & \vdots & \vdots & \vdots & \vdots & \vdots & \vdots & \vdots \\
 0 & 0 & 0 & 0 & 0 & 0 & 0 & (R_{33}^2)_i & (2R_{33}R_{34})_i & (R_{34}^2)_i \\
 \vdots & \vdots & \vdots & \vdots & \vdots & \vdots & \vdots & \vdots & \vdots & \vdots \\
 0 & 0 & 0 & 0 & 0 & 0 & 0 & (R_{33}^2)_n & (2R_{33}R_{34})_n & (R_{34}^2)_n
 \end{bmatrix} \quad (4.40)$$

where the subscripts after the right closing parenthesis indicate the measurement number.

We can combine the two vectors $\sigma(1)_{11}$ and $\sigma(1)_{33}$ into a single vector of length $2n \times 1$ where n is the total number of measurements and combine the two matrices, \widetilde{R}_1 and \widetilde{R}_3 , into one $2n \times 10$ matrix but there would still only be six independent columns. If only a $2n \times 6$ matrix is formed it could be inverted to determine σ_{11} , σ_{12} , σ_{22} , σ_{33} , σ_{34} and σ_{44} but we do not have enough information to determine all ten of the elements of the four dimensional beam matrix. Another set of independent relations is needed to determine all of the ten elements.

4.4.3 Correlation Information

Only the $x - y$ space is available in the experimental process. The two projected widths of the beam have been used to this point. What has been left unexplored is the information about the correlation between the x and y dimensions of the beam. In the case of $x - x'$ space the correlation σ_{12} between x and x' must be determined indirectly through the quadrupole scan measurement process. In $x - y$ space we can calculate it directly from the $x - y$ distribution for each of the measurements by using the relation (2.46) with 2 replaced by 3 and x' replaced by y :

$$\sigma_{13} = \widetilde{xy} = \frac{\iint xy\rho(x,y)dx dy}{\iint \rho(x,y)dx dy} \quad (4.41)$$

where $\rho(x, y)$ is the distribution at the screen location. Again σ_{13} is calculated about the centroid of the distribution which is given by the first moments of the distribution. In the actual measurements of the electron beam, $\rho(x, y)$ is the intensity distribution from a CCD camera for example. Notice that σ_{11} , σ_{33} and σ_{13} comprise all of the second moment information that can be taken from a two-dimensional image of the beam. Normally information about σ_{13} is lost since projections are used to determine $\sigma_{11} = x_{\max}^2$ and $\sigma_{33} = y_{\max}^2$ as shown in the Fig. 4.2 below.

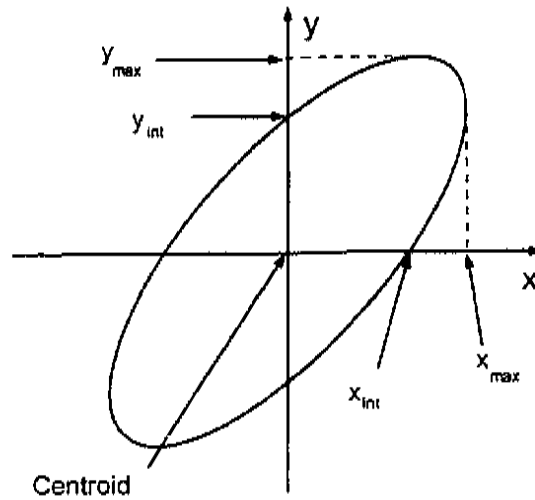


Figure 4.2: Ellipse surrounding beam distribution in x-y space

If equation (4.29) is used to form the relation for the measured $\sigma(1)_{13}$ we have:

$$\sigma(1)_{13} = \sum R_{1k} R_{3l} \sigma_{kl}(0) \quad (4.42)$$

where $k, l = 1, 2, 3, 4$ and when expanded becomes:

$$\begin{aligned}
\sigma(1)_{13} = & [R_{11}R_{31}\sigma(0)_{11} + (R_{11}R_{32} + R_{12}R_{31})\sigma(0)_{12} + (R_{11}R_{33} + R_{13}R_{31})\sigma(0)_{13} \\
& + (R_{11}R_{34} + R_{14}R_{31})\sigma(0)_{14} + R_{12}R_{32}\sigma(0)_{22} + (R_{12}R_{33} + R_{13}R_{32})\sigma(0)_{23} \\
& + (R_{12}R_{34} + R_{14}R_{32})\sigma(0)_{24} + R_{13}R_{33}\sigma(0)_{33} + (R_{13}R_{34} + R_{14}R_{33})\sigma(0)_{34} \\
& + R_{34}R_{34}\sigma(0)_{44}] \tag{4.43}
\end{aligned}$$

Since there is no coupling in the transform chosen for the quadrupole scan, R , the terms $R_{13} = R_{14} = R_{23} = R_{24} = R_{31} = R_{32} = R_{41} = R_{42} = 0$. Taking this in to account the above relation becomes:

$$\begin{aligned}
\sigma(1)_{13} = & [0 \cdot \sigma(0)_{11} + 0 \cdot \sigma(0)_{12} + R_{11}R_{33}\sigma(0)_{13} + R_{11}R_{34}\sigma(0)_{14} \\
& + 0 \cdot \sigma(0)_{22} + R_{12}R_{33}\sigma(0)_{23} + R_{12}R_{34}\sigma(0)_{24} + 0 \cdot \sigma(0)_{33} \\
& + 0 \cdot \sigma(0)_{34} + 0 \cdot \sigma(0)_{44}] \tag{4.44}
\end{aligned}$$

or

$$\sigma(1)_{13} = [R_{11}R_{33}\sigma(0)_{13} + R_{11}R_{34}\sigma(0)_{14} + R_{12}R_{33}\sigma(0)_{23} + R_{12}R_{34}\sigma(0)_{24}]. \tag{4.45}$$

And in a more compact form,

$$\sigma(1)_{13} = \widetilde{R}_{13}\sigma(0) \tag{4.46}$$

From equation (4.45) the only nonzero terms that contribute to the $\sigma(1)_{13}$ that is measured at the screen location are those involving $\sigma(0)_{13}$, $\sigma(0)_{14}$, $\sigma(0)_{23}$, and $\sigma(0)_{24}$. As will be shown in the next chapter for a typical quadrupole scan the terms $R_{11}R_{33}$, $R_{11}R_{34}$, $R_{12}R_{33}$ and $R_{12}R_{34}$ are nonzero except at one point in the quadrupole scan. Therefore if nonzero $\sigma(1)_{13}$ is measured on the screen during a quadrupole scan one can conclude that the input beam has some amount of coupling due only to the terms $\sigma(0)_{13}$, $\sigma(0)_{14}$, $\sigma(0)_{23}$, or $\sigma(0)_{24}$. The point is that nonzero $\sigma(1)_{13}$ is NOT due

to the values at the doublet entrance of $\sigma(0)_{11}$, $\sigma(0)_{22}$, $\sigma(0)_{33}$, $\sigma(0)_{44}$ or the other couplings $\sigma(0)_{12}$, and $\sigma(0)_{34}$. This is important since it means that nonzero $\sigma(1)_{13}$ and nonzero correlation coefficient r_{13}

$$r_{13} = \frac{\sigma_{13}}{\sqrt{\sigma_{11}\sigma_{33}}} \quad (4.47)$$

obtained in the measurement of a beam during a quadrupole scan indicates the presence of coupling between the transverse dimensions of the beam due to ANY one of the elements $\sigma(0)_{13}$, $\sigma(0)_{14}$, $\sigma(0)_{23}$, or $\sigma(0)_{24}$. And as shown in the previous section if there is coupling between the transverse dimensions of the beam the projected emittance is NOT a conserved quantity. Also since r_{13} is normalized then $|r_{13}| \leq 1$ and it provides a convenient measure of the amount of correlation in the beam. Values of $|r_{13}|$ for a quadrupole scan that are close to one indicate a strong transverse coupling in the beam and a value of zero indicates no transverse coupling in the beam.

Returning to the matrix for \widetilde{R}_{13} we have:

$$\widetilde{R}_{13} = \begin{bmatrix} 0 & 0 & (R_{11}R_{33})_1 & (R_{11}R_{34})_1 & 0 & (R_{12}R_{33})_1 & (R_{12}R_{34})_1 & 0 & 0 & 0 \\ 0 & 0 & (R_{11}R_{33})_2 & (R_{11}R_{34})_2 & 0 & (R_{12}R_{33})_2 & (R_{12}R_{34})_2 & 0 & 0 & 0 \\ 0 & 0 & (R_{11}R_{33})_3 & (R_{11}R_{34})_3 & 0 & (R_{12}R_{33})_3 & (R_{12}R_{34})_3 & 0 & 0 & 0 \\ \vdots & \vdots & \vdots & \vdots & \vdots & \vdots & \vdots & \vdots & \vdots & \vdots \\ 0 & 0 & (R_{11}R_{33})_i & (R_{11}R_{34})_i & 0 & (R_{12}R_{33})_i & (R_{12}R_{34})_i & 0 & 0 & 0 \\ \vdots & \vdots & \vdots & \vdots & \vdots & \vdots & \vdots & \vdots & \vdots & \vdots \\ 0 & 0 & (R_{11}R_{33})_n & (R_{11}R_{34})_n & 0 & (R_{12}R_{33})_n & (R_{12}R_{34})_n & 0 & 0 & 0 \end{bmatrix} \quad (4.48)$$

Now if we combine all of the information from the horizontal, vertical and $x - y$ correlation we can form a system with relations for all of the ten elements of the initial beam matrix. We combine the measured values for $\sigma(1)_{11}$, $\sigma(1)_{33}$ and $\sigma(1)_{13}$ obtained from a set of n measurements into a $3n \times 1$ vector, $\sigma(1)$, and form a $3n \times 10$

matrix, \widetilde{R} , from the matrices \widetilde{R}_1 , \widetilde{R}_3 , and \widetilde{R}_{13} we have the system of equations:

$$\vec{\sigma}(1) = \widetilde{R}\vec{\sigma}(0) \quad (4.49)$$

where $\vec{\sigma}(0)$ is the 1×10 dimensional vector containing the initial values for the beam matrix that we want to solve for.

Then the full system has the form:

$$\begin{bmatrix} \sigma_{11}(1)_1 \\ \vdots \\ \sigma_{11}(1)_n \\ \sigma_{33}(1)_1 \\ \vdots \\ \sigma_{33}(1)_n \\ \sigma_{13}(1)_1 \\ \vdots \\ \sigma_{13}(1)_n \end{bmatrix} = \begin{bmatrix} (R_{11}^2)_1 & (2R_{11}R_{12})_1 & 0 & 0 & (R_{12}^2)_1 \\ \vdots & \vdots & \vdots & \vdots & \vdots \\ (R_{11}^2)_n & (2R_{11}R_{12})_n & 0 & 0 & (R_{12}^2)_n \\ 0 & 0 & 0 & 0 & 0 \\ \vdots & \vdots & \vdots & \vdots & \vdots \\ 0 & 0 & 0 & 0 & 0 \\ 0 & 0 & (R_{11}R_{33})_1 & (R_{11}R_{34})_1 & 0 \\ \vdots & \vdots & \vdots & \vdots & \vdots \\ 0 & 0 & (R_{11}R_{33})_n & (R_{11}R_{34})_n & 0 \end{bmatrix} \begin{bmatrix} 0 & 0 & 0 & 0 & 0 \\ \vdots & \vdots & \vdots & \vdots & \vdots \\ 0 & 0 & 0 & 0 & 0 \\ 0 & 0 & (R_{33}^2)_1 & (2R_{33}R_{34})_1 & (R_{34}^2)_1 \\ \vdots & \vdots & \vdots & \vdots & \vdots \\ 0 & 0 & (R_{33}^2)_n & (2R_{33}R_{34})_n & (R_{34}^2)_n \\ (R_{12}R_{33})_1 & (R_{12}R_{34})_1 & 0 & 0 & 0 \\ \vdots & \vdots & \vdots & \vdots & \vdots \\ (R_{12}R_{33})_n & (R_{12}R_{34})_n & 0 & 0 & 0 \end{bmatrix} \begin{bmatrix} \sigma_{11}(0) \\ \sigma_{12}(0) \\ \sigma_{13}(0) \\ \sigma_{14}(0) \\ \sigma_{22}(0) \\ \sigma_{23}(0) \\ \sigma_{24}(0) \\ \sigma_{33}(0) \\ \sigma_{34}(0) \\ \sigma_{44}(0) \end{bmatrix}$$

$$\vec{\sigma}(1) = \widetilde{R}\vec{\sigma}(0) \quad (4.50)$$

Now the matrix R has sufficient rank for inversion since there are now ten independent

columns and so the calculation:

$$\vec{\sigma}(0) = \tilde{R}^{-1} \vec{\sigma}(1) \quad (4.51)$$

can be performed to obtain $\vec{\sigma}(0)$ which contains the ten elements of the four dimensional beam matrix σ_{4-D} . And finally the four dimensional volume can be calculated using:

$$V_{4-D} = \left(\frac{\pi^2}{2}\right) \sqrt{\det[\sigma_{4-D}(0)]}. \quad (4.52)$$

4.5 Normalization

As discussed in the previous chapter use of the canonical momenta p_x , p_y and p_z of the particles guarantees conservation of regions of phase space if there is a change in energy of the beam or if one wishes to compare two beams at different energies. The quantities measured in the laboratory are the direction tangents $x' = \frac{p_x}{p_z}$ and $y' = \frac{p_y}{p_z}$ and the relationship linking the quantities is:

$$p_x = \beta\gamma mcx' \quad (4.53)$$

$$p_y = \beta\gamma mcy' \quad (4.54)$$

From equations (4.24) and (4.52) with $\epsilon_x = \sqrt{\sigma_{11}\sigma_{22} - \sigma_{12}^2}$ and $\epsilon_y = \sqrt{\sigma_{33}\sigma_{44} - \sigma_{34}^2}$, we obtain the full expression for the four dimensional volume:

$$\begin{aligned} V_{4-D} = & \left[\frac{\pi^2}{2}\right] \{(\sigma_{11}\sigma_{22} - \sigma_{12}^2)(\sigma_{33}\sigma_{44} - \sigma_{34}^2) \\ & + (\sigma_{13}\sigma_{21} - \sigma_{11}\sigma_{23})(\sigma_{23}\sigma_{44} - \sigma_{34}\sigma_{24}) + (\sigma_{11}\sigma_{24} - \sigma_{14}\sigma_{12})(\sigma_{23}\sigma_{34} - \sigma_{33}\sigma_{24}) \\ & + (\sigma_{12}\sigma_{23} - \sigma_{13}\sigma_{22})(\sigma_{13}\sigma_{44} - \sigma_{34}\sigma_{14}) + (\sigma_{14}\sigma_{22} - \sigma_{12}\sigma_{24})(\sigma_{13}\sigma_{34} - \sigma_{33}\sigma_{14}) \\ & + (\sigma_{13}\sigma_{24} - \sigma_{14}\sigma_{23})(\sigma_{13}\sigma_{24} - \sigma_{23}\sigma_{14})\}^{1/2}. \quad (4.55) \end{aligned}$$

In this equation every occurrence of the indices 2 and 4 requires a multiplication of the factor $\beta\gamma$ to the term containing the index. For example $\sigma_{22} \rightarrow (\beta\gamma)^2\sigma_{22}$ and $\sigma_{23} \rightarrow (\beta\gamma)\sigma_{23}$ to normalize the 4-*DVol*. Therefore the normalized four dimensional volume is given by:

$$V_{4-D_n} = (\beta\gamma)^2 \left(\frac{\pi^2}{2} \right) \sqrt{\det(\sigma_{4-D})} \quad (4.56)$$

Again in first order the volume in trace space (x, x', y, y') is conserved so the normalization above may seem unnecessary. However in order to compare the V_{4-D} of beams which differ in energy one would have to use the normalized V_{4-D_n} in order to account for the effects of the different longitudinal momentum, p_z , on the quantities $x' = \frac{p_x}{p_z}$ and $y' = \frac{p_y}{p_z}$.

The formulation is complete for the method to calculate the four dimensional volume of the beam using only quantities σ_{11} , σ_{33} and σ_{13} which represent the projected beam half widths in the horizontal and vertical and the $x - y$ correlation respectively. All of these quantities can be determined in the laboratory. Further it was shown that if $\sigma_{13} \neq 0$ in a quadrupole scan there is coupling between the transverse coordinates of the beam at the doublet entrance. Also the quantity $r_{13} = \frac{\sigma_{13}}{\sqrt{\sigma_{11}\sigma_{33}}}$ with the property $|r_{13}| \leq 1$, provides a normalized quantity which indicates the degree of coupling in the beam. In the next chapter this algorithm will be tested with the distributions from the previous chapter which presented problems for the 1 - *D* quadrupole scan in which only the horizontal information of the beam was utilized.

Chapter 5

Simulations With Coupling

In this chapter simulations will be presented to demonstrate the concept of calculating four dimensional trace space by calculating the quantities $\sqrt{\sigma_{11}}$, $\sqrt{\sigma_{33}}$ and σ_{13} at the screen location which represent the widths of the projections of the horizontal and vertical dimensions of the beam and correlation between those dimensions respectively. First the simulation method is discussed. Then the distributions from Chap. 3 will be used to demonstrate the calculation of the four dimensional volume and comparisons with the projected quantities will be made.

5.1 Simulation Method

The simulation process is as follows, first the initial distribution is generated as described in Chap. 3. Then the four dimensional beam matrix elements are determined by calculating the moments of the distribution. Although no correlations are intentionally introduced, statistically there will be some amount of correlation present in the beam therefore all of the correlations are calculated. Next the normalized four dimensional volume of the initial distribution is computed by calculating:

$$V_{4-D_0} = \frac{\pi^2}{2} (\beta\gamma)^2 \sqrt{\det\sigma(0)_{4-D}} \quad (5.1)$$

Where $\sigma(0)_{4-D}$ is the four-dimensional beam matrix for the initial distribution. The normalized horizontal and vertical emittances are calculated using:

$$\epsilon_{x0} = \pi\beta\gamma\sqrt{\sigma_{11}(0)\sigma_{22}(0) - \sigma_{12}^2(0)} \quad (5.2)$$

and

$$\epsilon_{y0} = \pi\beta\gamma\sqrt{\sigma_{33}(0)\sigma_{44}(0) - \sigma_{34}^2(0)} \quad (5.3)$$

where the elements in the square roots are those of the four dimensional beam matrix for the initial distribution. Next the beam is propagated through the system formed by the transformation from Chap. 3 eq (3.13):

$$R_{prop} = R_{d2}R_{q2}R_{d1}R_{q1}R_{rot} \quad (5.4)$$

by multiplying the initial vector $X(0)$ by this transformation

$$X(1) = R_{prop}X(0) \quad (5.5)$$

Then at the screen location, denoted (1), the following quantities $\sqrt{\sigma_{11}}$, $\sqrt{\sigma_{33}}$ and σ_{13} which are the widths of the projections of the horizontal and vertical dimensions of the beam and correlation between those dimensions are calculated. This is repeated for each of the ten, $n = 10$, different strengths of q_2 in the quadrupole scan. Next the 30×1 vector $\vec{\sigma}(1)$ containing the quantities σ_{11} , σ_{33} and σ_{13} for each measurement is formed as in relation (4.50) of the previous chapter.

The matrix \tilde{R} containing the elements of the transformation matrix R_{calc} at each measurement as given in relation (4.50) is formed. Where R_{calc} is given by:

$$R_{\text{calc}} = R_{d2}R_{q2}R_{d1}R_{q1} \quad (5.6)$$

and it is important to note that the matrix R_{calc} DOES NOT contain a rotation since as in the actual measurements we treat any rotation as unknown so it is not included. The relation $\vec{\sigma}(1) = \tilde{R}\vec{\sigma}_{\text{calc}}$ is then inverted to give:

$$\vec{\sigma}_{\text{calc}} = \tilde{R}^{-1}\vec{\sigma}(1) \quad (5.7)$$

where $\vec{\sigma}_{\text{calc}}$ contains the ten elements of the calculated four dimensional beam matrix at the entrance to the doublet again not assuming any rotation. The calculations for the normalized four dimensional volume and projected emittances are then calculated using;

$$V_{4\text{-D}_{\text{calc}}} = \frac{\pi^2}{2}(\beta\gamma)^2\sqrt{\det\sigma_{\text{calc}}} \quad (5.8)$$

Where σ_{calc} is the four dimensional beam matrix. The horizontal and vertical emittances are calculated using:

$$\epsilon_{z\text{calc}} = \pi\beta\gamma\sqrt{\sigma_{\text{calc}11}\sigma_{\text{calc}22} - \sigma_{\text{calc}12}^2} \quad (5.9)$$

and

$$\epsilon_{y\text{calc}} = \pi\beta\gamma\sqrt{\sigma_{\text{calc}33}\sigma_{\text{calc}44} - \sigma_{\text{calc}34}^2} \quad (5.10)$$

5.2 Astigmatic Beams

The astigmatic beam from Chap. 3 clearly presented a problem with coupling and the quadrupole scan. The first beam to be analyzed with the four dimensional phase space technique has the following parameters:

$$\begin{aligned}\sigma_x &= 0.2 \text{ mm} & \sigma_y &= 0.4 \text{ mm} & \sigma_{x'} &= 0.2 \text{ mrad} & \sigma_{y'} &= 0.3 \text{ mrad} \\ \sigma_z &= 2.0 \text{ ps} & E &= 30 \text{ Mev}\end{aligned}$$

with initial normalized four dimensional volume of:

$$V_{4-D_0} = 8.29 \text{ (mm mrad)}^2$$

and normalized emittances of:

$$\epsilon_{x0} = 2.34 \text{ mm mrad} \text{ and } \epsilon_{y0} = 7.09 \text{ mm mrad}$$

The beam is rotated through the angles $0 < \alpha < \pi$ in steps of $\pi/20$ and propagated at each angle through the doublet to the screen. The vector σ_{calc} is calculated for each angle by performing a quadrupole scan at each angle. The four dimensional volume at the doublet entrance, $V_{4-D_{calc}}$, and the projected normalized emittances ϵ_{xcalc} and ϵ_{ycalc} are calculated using the relations (5.8-10) above. Also, $\frac{1}{2}\epsilon_{xcalc}\epsilon_{ycalc}$ is calculated in order to compare the values used in the uncoupled brightness relation with the four dimensional volume. Plots of the data are given in Fig. 5.1 and Fig. 5.2 below:

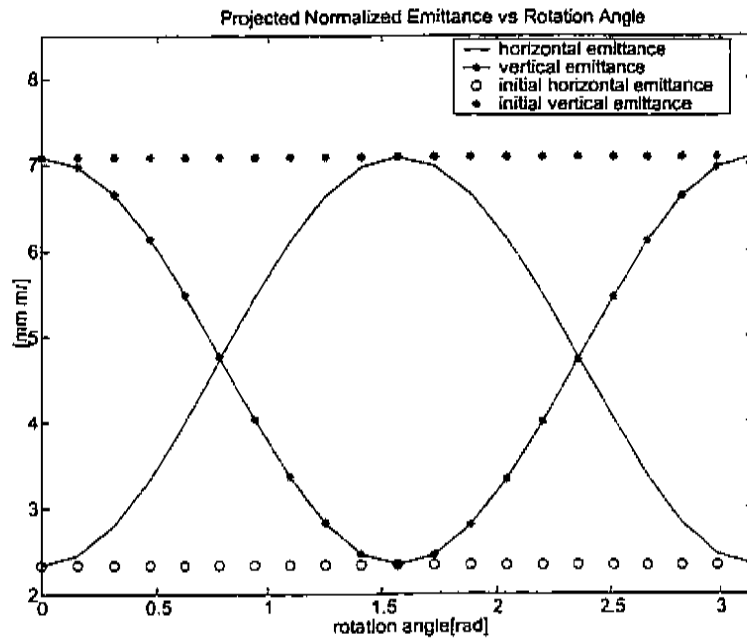


Figure 5.1: Plot of projected normalized emittances versus rotation angle for astigmatic beam

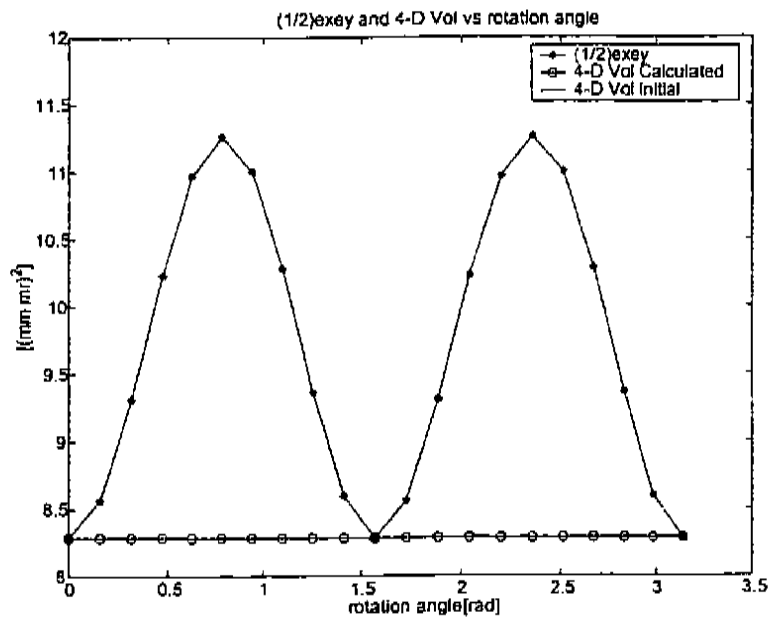


Figure 5.2: Plot of projected normalized $1/2\epsilon_x\epsilon_y$ and V_{4-D} Calculated and V_{4-D} Initial versus rotation angle for astigmatic beam

A table of the raw data is presented below:

<i>Rotation Angle</i>	$V_{4-D,Initial}$	$V_{4-D,Calculated}$	$V_{4-D,RelativeError}$
[rad]	[(mm mrad) ²]	[(mm mrad) ²]	%
0.000	8.2862	8.2862	0.000
0.157	8.2862	8.2863	0.001
0.314	8.2862	8.2864	0.003
0.471	8.2862	8.2866	0.005
0.628	8.2862	8.2868	0.007
0.785	8.2862	8.2868	0.007
0.942	8.2862	8.2868	0.007
1.100	8.2862	8.2866	0.005
1.257	8.2862	8.2864	0.003
1.414	8.2862	8.2863	0.001
1.571	8.2862	8.2862	0.000
1.728	8.2862	8.2863	0.001
1.885	8.2862	8.2864	0.003
2.042	8.2862	8.2866	0.005
2.199	8.2862	8.2868	0.007
2.356	8.2862	8.2868	0.007
2.513	8.2862	8.2868	0.007
2.670	8.2862	8.2866	0.005
2.827	8.2862	8.2864	0.003
2.985	8.2862	8.2863	0.001
3.142	8.2862	8.2862	0.000

Table 5.1: Values for 4-DVol Initial, Calculated and relative error

Where

$$V_{4-D,RelativeError} = \frac{100\% \cdot [V_{4-D,Calculated} - V_{4-D,Initial}]}{V_{4-D,Initial}} \quad (5.11)$$

Rotation Angle [rad]	$V_{4-D,Initial}$ [(mm mrad) ²]	$(\frac{1}{2}\epsilon_x\epsilon_y)_{Calculated}$ [(mm mrad) ²]	$(\frac{1}{2}\epsilon_x\epsilon_y)_{RelativeError}$ [%]
0.000	8.2862	8.287	0.01
0.157	8.2862	8.563	3.34
0.314	8.2862	9.310	12.36
0.471	8.2862	10.230	23.45
0.628	8.2862	10.972	32.41
0.785	8.2862	11.265	35.94
0.942	8.2862	11.003	32.79
1.100	8.2862	10.283	24.09
1.257	8.2862	9.366	13.03
1.414	8.2862	8.599	3.77
1.571	8.2862	8.287	0.01
1.728	8.2862	8.563	3.34
1.885	8.2862	9.310	12.36
2.042	8.2862	10.230	23.45
2.199	8.2862	10.972	32.41
2.356	8.2862	11.265	35.94
2.513	8.2862	11.003	32.79
2.670	8.2862	10.283	24.09
2.827	8.2862	9.366	13.03
2.985	8.2862	8.599	3.77
3.142	8.2862	8.287	0.01

Table 5.2: Values for 4-DVol Initial, $1/2\epsilon_x\epsilon_y$ calculated and the relative error between them

And for the data in the table above:

$$\left(\frac{1}{2}\epsilon_x\epsilon_y\right)_{RelativeError} = \frac{100\% \cdot [(\frac{1}{2}\epsilon_x\epsilon_y)_{Calculated} - V_{4-D,Initial}]}{V_{4-D,Initial}} \quad (5.12)$$

It is quite clear that if the beam has couplings introduced by a rotation, the calculated four dimensional volume is conserved in comparison to the values of ϵ_x, ϵ_y and $\frac{1}{2}\epsilon_x\epsilon_y$. The difference between the initial and calculated 4-D volume is less than .01% in all cases. This difference is due to the finite number of particles, 10,000, used in the simulations. The simulations were repeated with 20,000 and 50,000 particles.

Each time the distributions are generated they are slightly different due to the use of the random generator, so the initial 4 - D volume, $V_{4-D,Initial}$, changes slightly. Plots for the relative errors are given in Fig. 5.3 and Fig. 5.4 below:

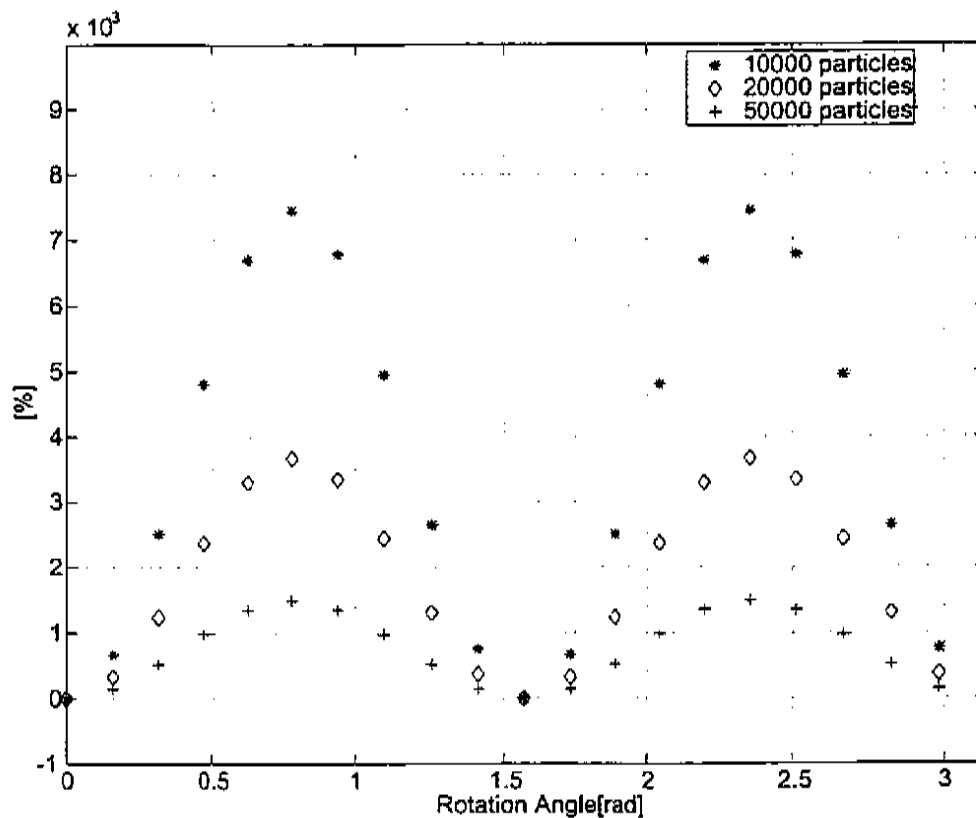


Figure 5.3: $V_{4-D,RelativeError}$ for different number of particles

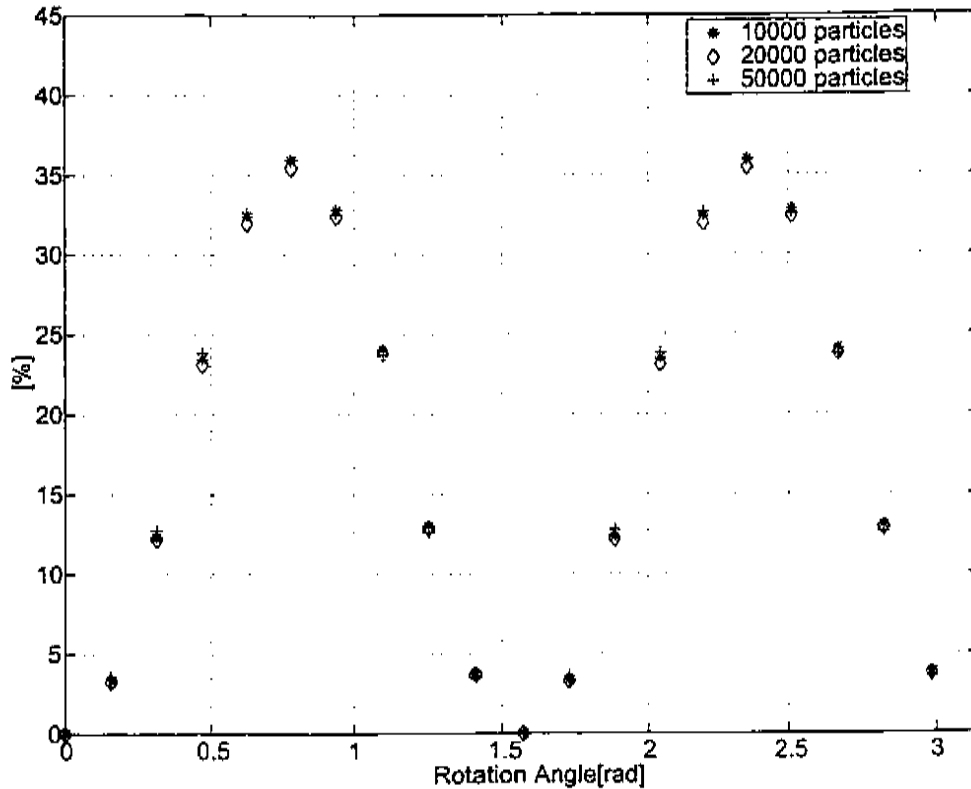


Figure 5.4: $\frac{1}{2}\epsilon_x\epsilon_y$ Relative Error for different number of particles

In the first plot, Fig. 5.3, the percent relative error for the calculated 4-D volume is reduced by the use of more particles in the simulation. In the second plot, Fig. 5.4, the percent relative error for $\frac{1}{2}\epsilon_x\epsilon_y$ is not reduced by the use of more particles. Therefore the percent relative error for the 4-D volume or the difference between the 4-D volume calculated using information from the quadrupole scans and the initial 4-D volume can be made arbitrarily small by the use of more particles in the simulations. And once again it should be noted that in the determination of the calculated four dimensional volume there is no assumption of a rotation. While the calculated four dimensional volume remains constant for each rotation angle, the individual elements of the vector $\vec{\sigma}_{\text{calc}}$ fluctuate with the angle of rotation. This is seen in a plot of the ten elements for three different rotation angles, Fig. 5.5, the line connecting the values is to guide the eye.

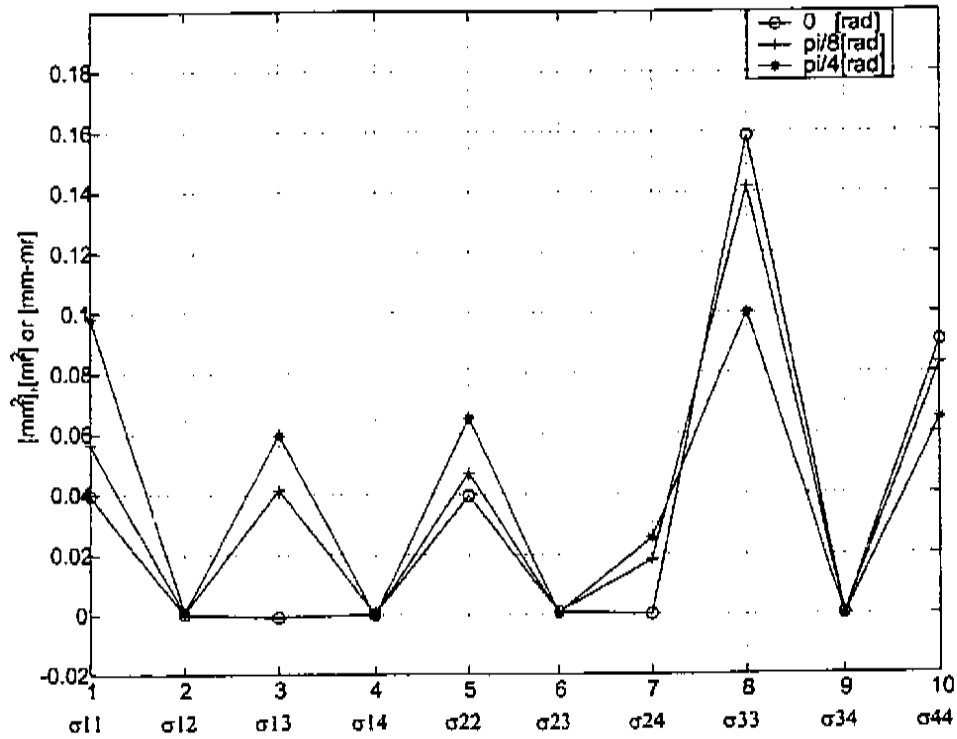


Figure 5.5: Values for the Calculated Sigma Vector for three rotation angles

Rotation	σ_{11} [mm ²]	σ_{12} [mm mrad]	σ_{13} [mm ²]	σ_{14} [mm mrad]	σ_{22} [mrad ²]
InitialDist	3.9631E-02	2.1852E-04	-8.5616E-04	2.1684E-04	3.9533E-02
0.0	3.9631E-02	2.1852E-04	-8.5616E-04	2.1684E-04	3.9533E-02
$\pi/8$	5.6456E-02	6.3308E-04	4.1471E-02	2.1852E-04	4.7073E-02
$\pi/4$	9.8286E-02	7.9149E-04	5.9505E-02	-4.0150E-04	6.5157E-02

Rotation	σ_{23} [mm mrad]	σ_{24} [mrad ²]	σ_{33} [mm ²]	σ_{34} [mm mrad]	σ_{44} [mrad ²]
InitialDist	9.7442E-04	8.5890E-05	1.5865E-01	1.7309E-04	9.0609E-02
0.0	9.7442E-04	8.5890E-05	1.5865E-01	1.7309E-04	9.0609E-02
$\pi/8$	7.8390E-04	1.8117E-02	1.4183E-01	-2.4147E-04	8.3068E-02
$\pi/4$	3.5608E-04	2.5535E-02	9.9999E-02	-3.9988E-04	6.4985E-02

Table 5.3: Individual Sigma Vector elements for the initial distribution and for the calculated values at various rotation angles

Notice that for zero rotation the elements σ_{13} , σ_{14} , σ_{23} and σ_{24} are all small but nonzero. This is because statistically there is always some amount of correlation between the various dimensions of the beam. In the creation of the initial distribution no correlations are intentionally introduced. However, they are calculated and are nonzero. The rotation even reduces some of the correlation as in the case of σ_{23} . Of the elements σ_{13} , σ_{14} , σ_{23} and σ_{24} , the elements σ_{13} and σ_{24} change by the greatest amount, this is due to the asymmetry between σ_x and σ_y , as well as that between $\sigma_{x'}$ and $\sigma_{y'}$ in the initial non-rotated distribution. This will be shown analytically at the end of this chapter.

On the next two pages quadrupole scan plots for σ_{11} , σ_{33} , σ_{13} and τ_{13} versus q^2 strength for rotation angles of 0 , $\pi/8$ and $\pi/4$ are presented in Tables 5.4 and 5.5. In the plots for σ_{13} and τ_{13} the effect of rotation on coupling strength is evident as an increase in the range of values for both σ_{13} and correlation coefficient τ_{13} . Since the range of $|\tau_{13}| = \frac{\sigma_{13}}{\sqrt{\sigma_{11}\sigma_{33}}} \leq 1$ due to the normalization by σ_{11} and σ_{33} , examination of the plots for τ_{13} allows one to easily compare the effects of the coupling. Also evident by the change of sign in the plots of σ_{13} and τ_{13} for rotation angles of $\pi/8$ and $\pi/4$ is that the beam crosses the y axis during the quadrupole scan.

The plots for σ_{11} and σ_{33} versus q^2 strength from the quadrupole scans contain additional information about the beam. In the plot of sigma 11, σ_{11} , versus quadrupole q^2 strength the minimum value in each plot becomes greater as the rotation angle is increased. This indicates a larger emittance with increasing rotation angle as is calculated and shown in the plots of Table 5.4. This also indicates an asymmetry in the beam. Since the initial distribution has $\epsilon_{x0} = 2.34$ mm mrad and $\epsilon_{y0} = 7.09$ mm mrad the rotation is presenting a larger horizontal emittance to the doublet up to $\pi/2$. This is also seen in the calculated values for σ_{11} in Table 5.3. The opposite is true for the vertical. The vertical emittance at the doublet entrance decreases for increasing rotation angle up to the angle of $\pi/2$. While the minimum value for the plot of σ_{33} versus quadrupole q^2 strength does decrease with rotation angle, it does not pass through a minimum and rise again. In fact since q^2 is vertically defocusing it would be expected that σ_{33} would increase with increasing q^2 strength. The decrease

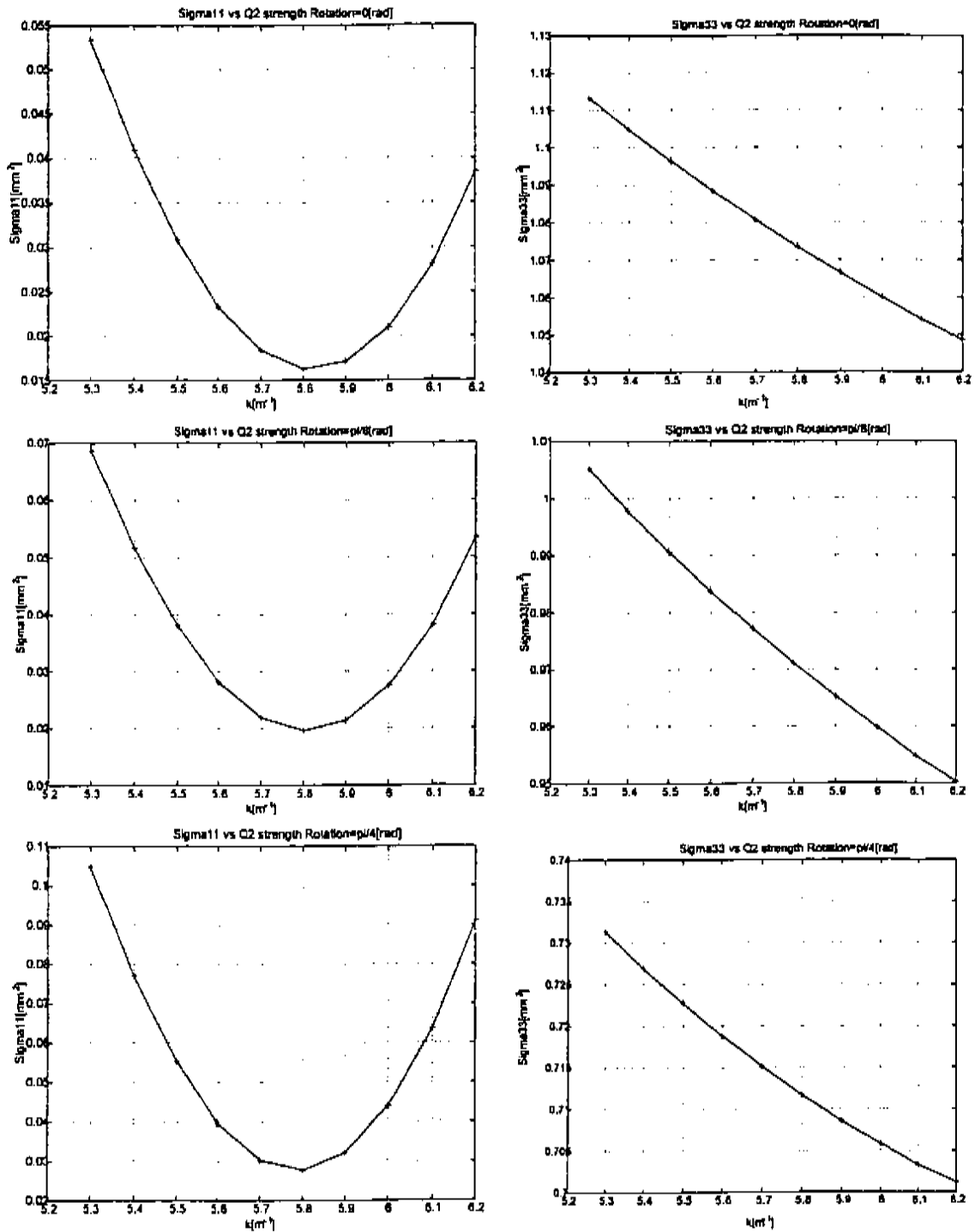


Table 5.4: Plots of σ_{11} and σ_{33} versus q_2 strength for three different rotation angles

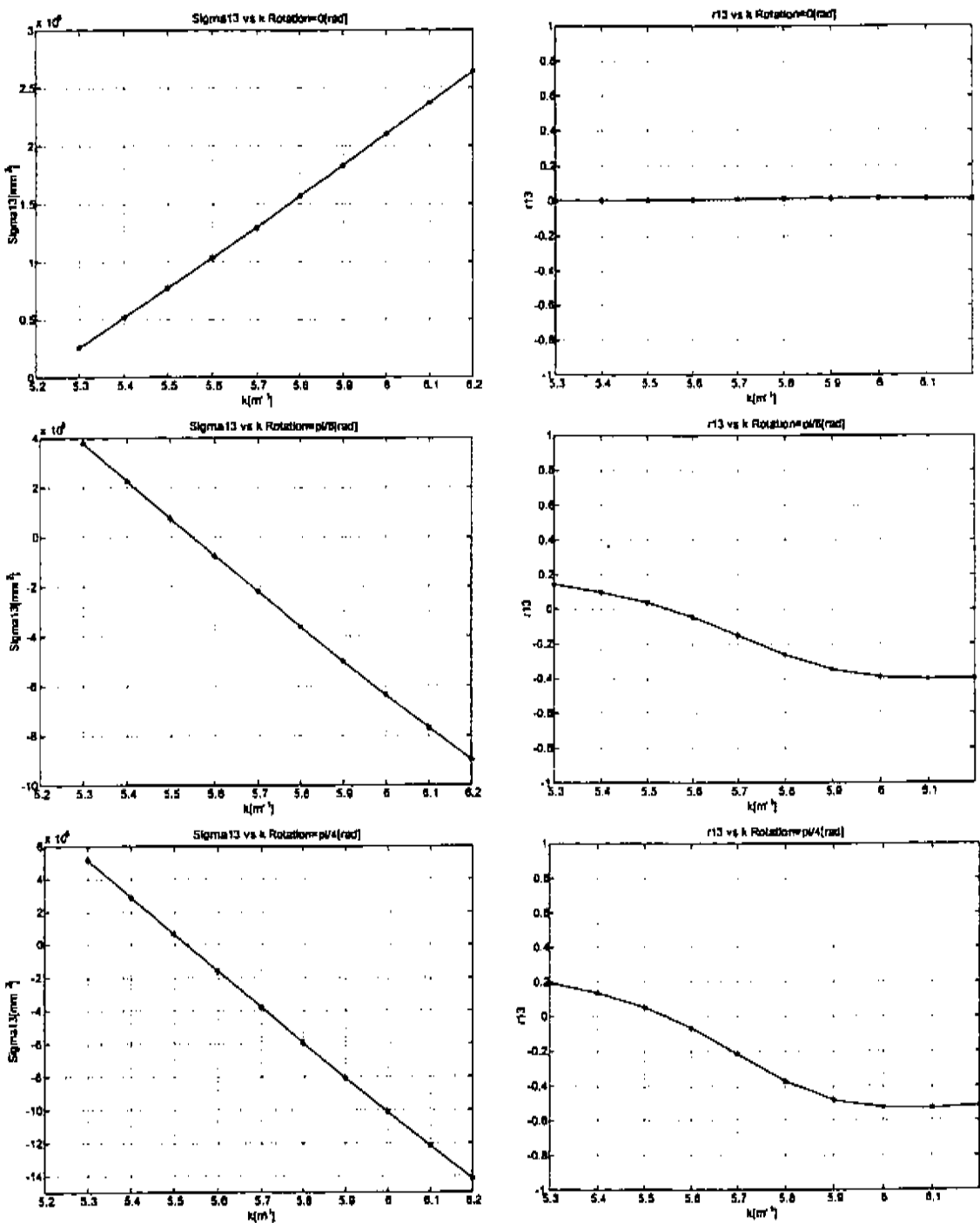


Table 5.5: Plots of σ_{13} and r_{13} versus q_2 strength for three different rotation angles

in σ_{33} with increasing q_2 strength indicates that the beam is strongly vertically focusing as it enters q_2 . The choice of $k_2 = 6[m^{-1}]$ and starting value of $k_1 = 5.2[m^{-1}]$ were made setting by adjusting the quadrupoles so that a nice spot is formed at the screen location as was done for the measurements made in the lab. The information about the vertical focusing is not available from the projected horizontal width of the beam which is measured in the traditional quadrupole scan.

In the plots of r_{13} for the three rotation angles $0, \pi/8$ and $\pi/4$, Table 5.5, the maximum value of $|r_{13}|$ increases with rotation angle. From the plot below, Fig. 5.6, there is a nonzero r_{13} for no rotation of the initial distribution. The maximum value for $|r_{13}|$ is more than an order of magnitude less than the maximum $|r_{13}|$ for the other two rotation angles as shown in Table 5.5. The nonzero r_{13} in the zero rotation case is due to nonzero correlations in the initial distribution.

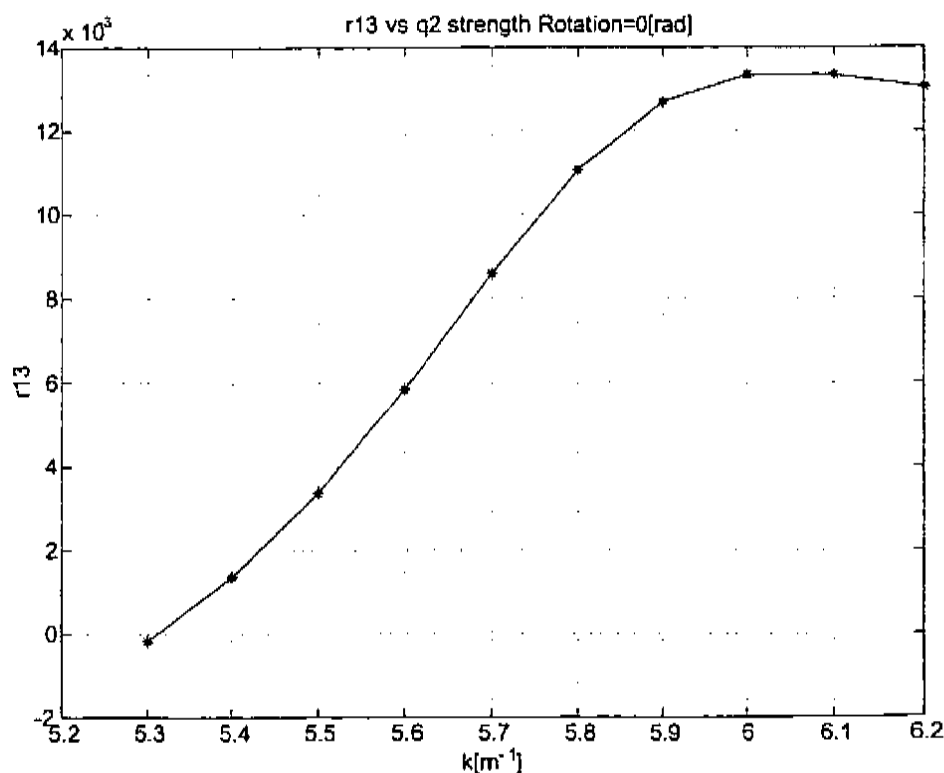


Figure 5.6: Plot of r_{13} versus q_2 strength for no rotation of the beam

The increase in $|r_{13}|$ with rotation angle is shown in a plot of r_{13} versus q_2 strength for rotation angle from 0 to $\pi/4$ in steps of $\pi/20$ presented in Fig. 5.7 below.

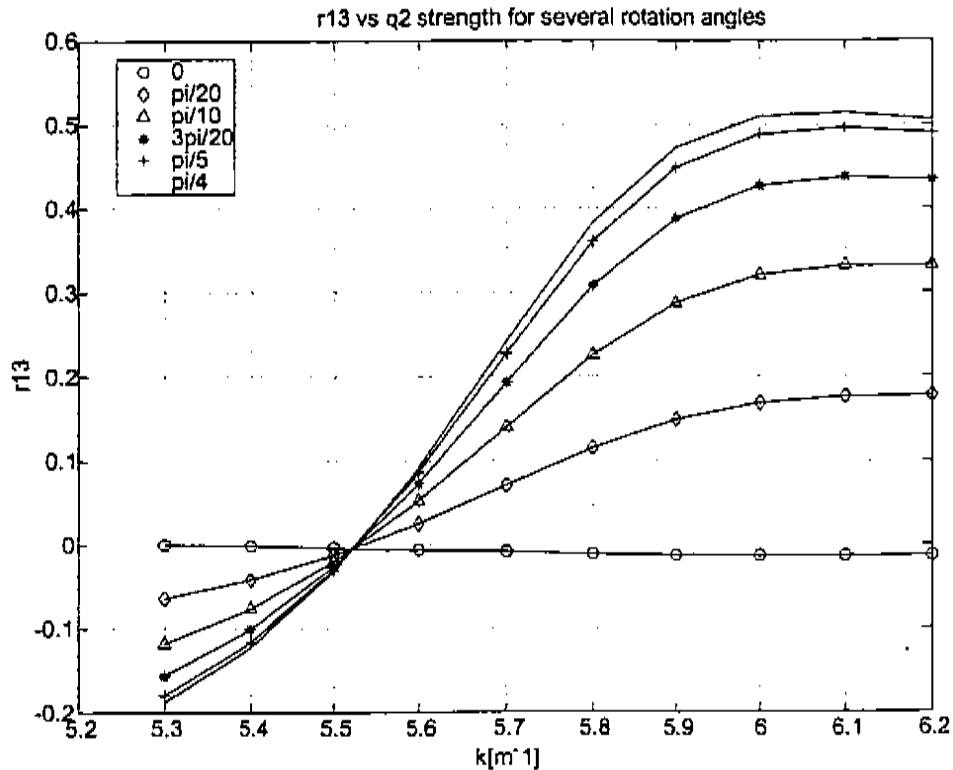
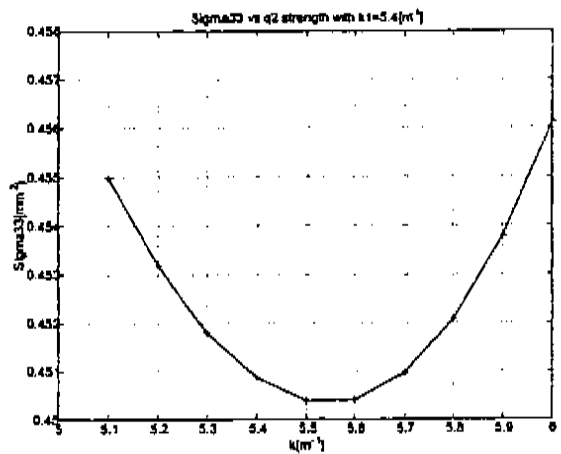
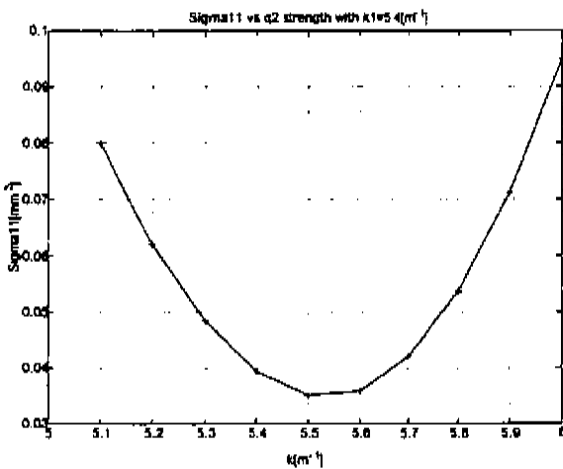
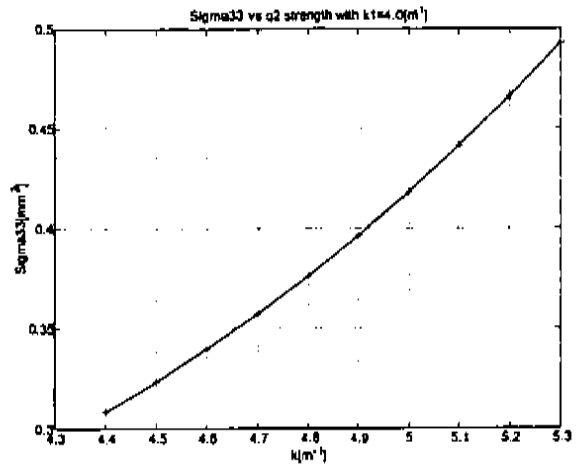
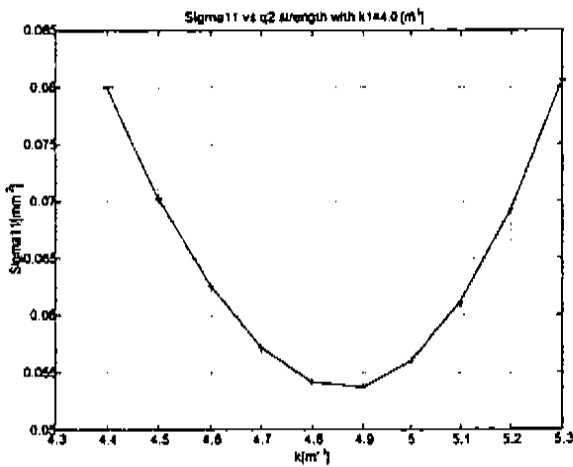


Figure 5.7: Plot of r_{13} versus q_2 strength for different rotation angles

5.3 Variation Of Doublet Parameters

As another test of the algorithm the above simulations are repeated with the rotation angle fixed at $\pi/4$ and using different values for k_1 and k_2 of the quadrupoles of the doublet. This demonstrates the insensitivity of the algorithm to the lattice settings. In the first case the first quadrupole, q_1 , is fixed at $k_1 = 3.8[m^{-1}]$ and the second quadrupole, q_2 , is varied from $k_2 = 4.3$ to $5.3[m^{-1}]$. In the second case q_1 is fixed at $k_1 = 5.4[m^{-1}]$ and q_2 is varied from $k_2 = 5.0$ to $6.0[m^{-1}]$. In the last case the q_1 is

fixed at $k_1 = 6.0[m^{-1}]$ and q_2 is varied from $k_2 = 5.2$ to $6.2[m^{-1}]$. Plots of σ_{11} , σ_{33} , σ_{13} and τ_{13} versus q_2 strength and values for ϵ_x , ϵ_y , $\frac{1}{2}\epsilon_x\epsilon_y$ and the four dimensional volume for the three cases are presented in Tables 5.6-5.8 below.



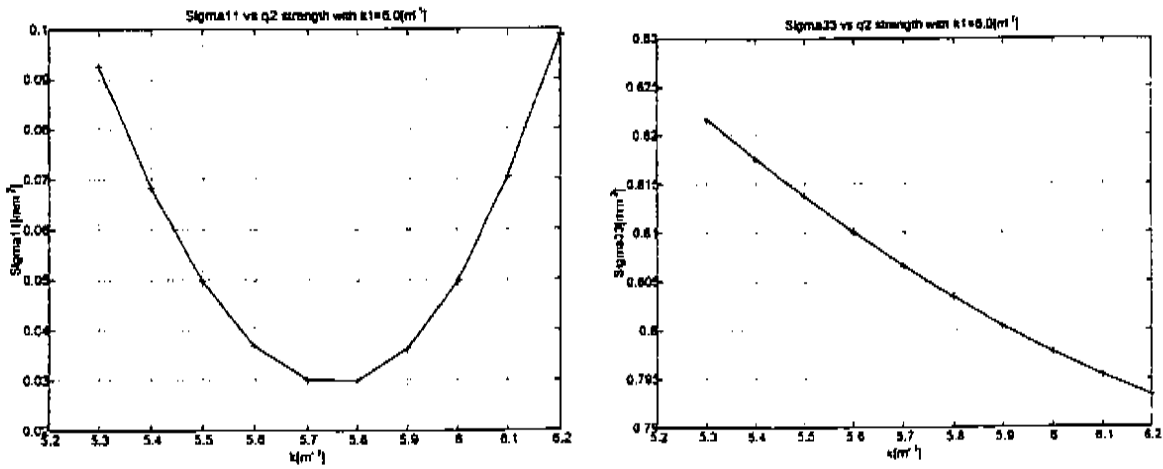
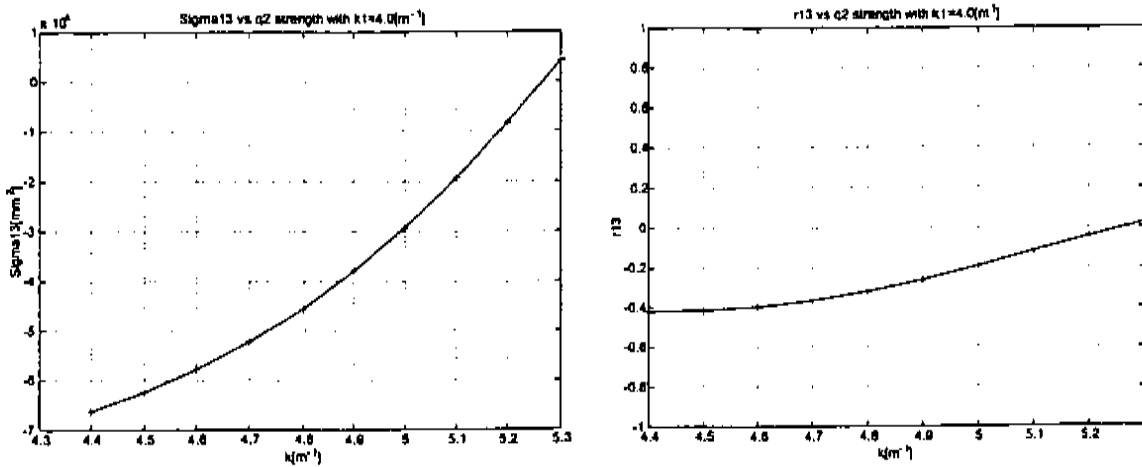


Table 5.6: Plots of sigma11 and sigma33 versus q2 strength for three different doublet parameters



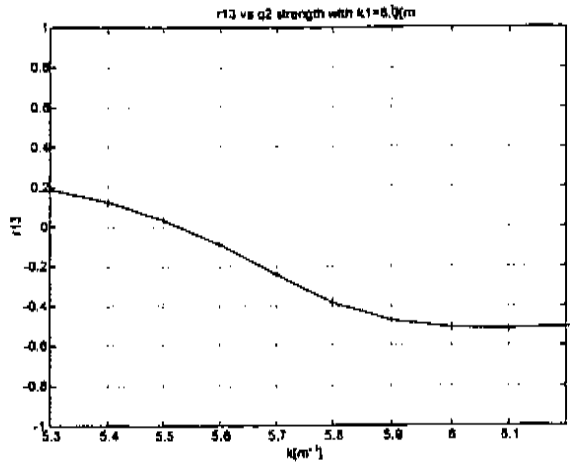
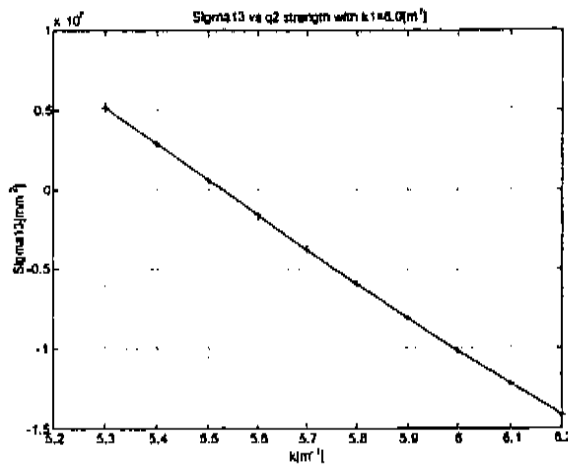
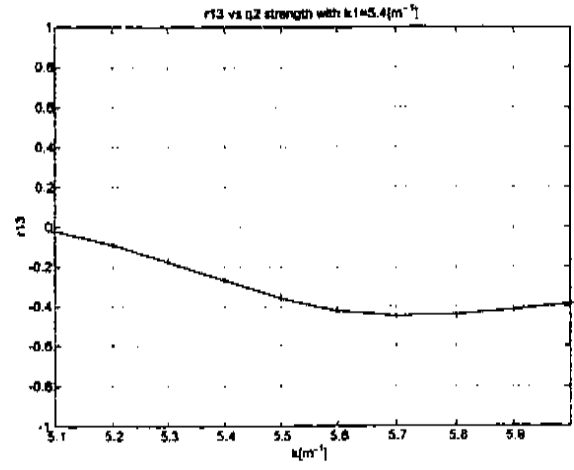
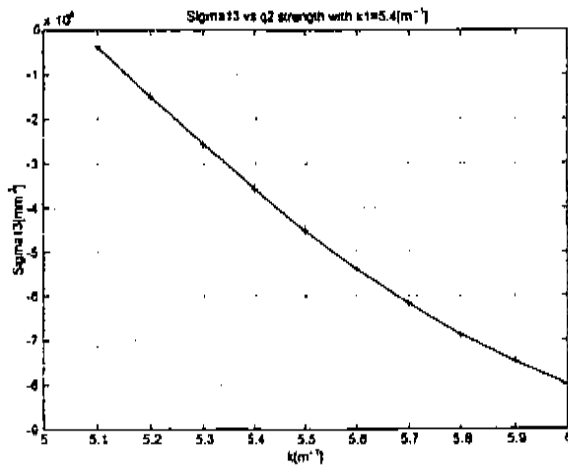


Table 5.7: Plots of sigma13 and r13 versus q2 strength for three different doublet parameters

$k1$	ϵ_x	ϵ_y	$\frac{1}{2}\epsilon_x\epsilon_y$	$V_{4-D,Initial}$
$[m^{-1}]$	$[\text{mm mrad}]$	$[\text{mm mrad}]$	$[(\text{mm mrad})^2]$	$[(\text{mm mrad})^2]$
3.8	4.729	4.764	11.2647	8.2862
5.4	4.729	4.764	11.2647	8.2862
6.0	4.729	4.764	11.2647	8.2862

$k1$	$V_{4-D,Calc}$	$V_{4-D,Initial}$
$[m^{-1}]$	$[(\text{mm mrad})^2]$	$[(\text{mm mrad})^2]$
3.8	8.2868	8.2862
5.4	8.2868	8.2862
6.0	8.2868	8.2862

Table 5.8: Projected and 4-DVol quantities for three different doublet parameters

The initial normalized emittances of the distribution are $\epsilon_{x0} = 2.34$ mm mrad and $\epsilon_{y0} = 7.09$ mm mrad. The rotation angle is fixed at $\pi/4$ for all of the quadrupole scans. In all cases the beam is brought through a minimum in the horizontal as is typical for a horizontal quadrupole scan. Depending on the value for the first quadrupole in the doublet, $q1$, the vertical beam projection is increasing, passes through a minimum or is decreasing for the scan of $q2$. And although the shapes of the curve in the plot for r_{13} versus $q2$ strength, Table 5.7, are different for each plot, r_{13} is still nonzero which reflects the coupling present in the beam from the rotation of $\pi/4$. The beam shears in each case but only in the last case does it clearly shear through the y -axis as is evident by the change of sign in the plot of r_{13} versus $q2$ strength. Although the beam behaves differently for each sequence of plots above, the calculated vector

$$\vec{\sigma}_{calc} = \tilde{R}^{-1} \vec{\sigma}(1)$$

is the same for all conditions. This is evident from the values in the table above since all were calculated from $\vec{\sigma}_{calc}$. This is also expected since the input beam to the doublet is not changed only the doublet values are different. The values for ϵ_x , ϵ_y and $\frac{1}{2}\epsilon_x\epsilon_y$ also remain constant for each of the different lattice conditions since the rotation of the initial beam is not changed. And the value for $\frac{1}{2}\epsilon_x\epsilon_y$ is greater than the V_{4-D} as expected due to the presence of nonzero r_{13} in the quadrupole scans. So

the algorithm is not dependent on a particular configuration of the doublet. The method accurately reproduces the initial four dimensional volume under rotation and for different configurations of the doublet strength.

5.4 Determination Of The Initial Rotation Of The Beam

The algorithm can also be used to determine the rotation angle of the input beam. Recall the vector $\vec{\sigma}_{\text{calc}}$ which contains the ten elements used to determine the four dimensional volume is found from the relation (5.7):

$$\vec{\sigma}_{\text{calc}} = \tilde{R}^{-1} \vec{\sigma}(1)$$

where the matrix \tilde{R} is formed from the elements of the transform $R_{\text{calc}} = R_{d2} R_{q2} R_{d1} R_{q1}$. And $\sigma(1)$ is formed from the measured values σ_{11} , σ_{33} and σ_{13} at the screen location. A rotation transform with rotation angle, α_1 , is now included in the transform $R_{\text{calc}} = R_{d2} R_{q2} R_{d1} R_{q1} R_{\text{rot1}}$. The values σ_{11} , σ_{33} and σ_{13} at the screen are calculated for each quadrupole q2 setting of the quadrupole scan as before but this is now done at each value of the new rotation angle, α_1 , in the range $0 < \alpha_1 < \pi$ for some initial unknown fixed value of rotation of the initial beam, α_0 . Now the values for $\frac{1}{2}\epsilon_x\epsilon_y$ and the four dimensional volume are plotted and one obtains the following, Fig. 5.8 and Fig. 5.9 below.

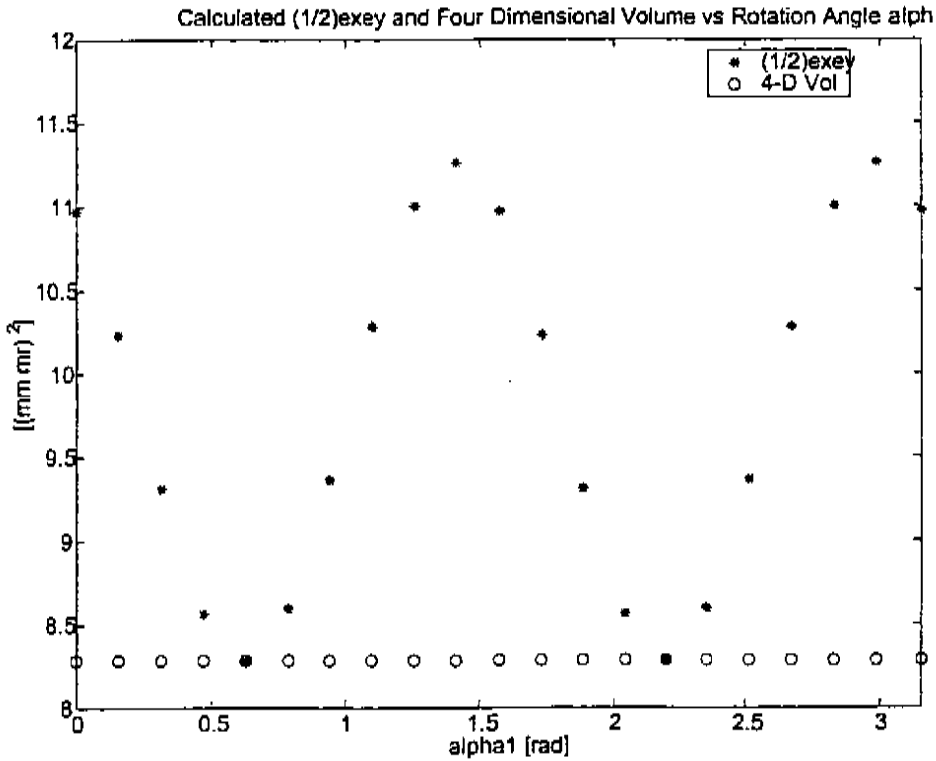


Figure 5.8: Calculated $1/2\epsilon_x\epsilon_y$ and V_{4-D} versus rotation angle α_1

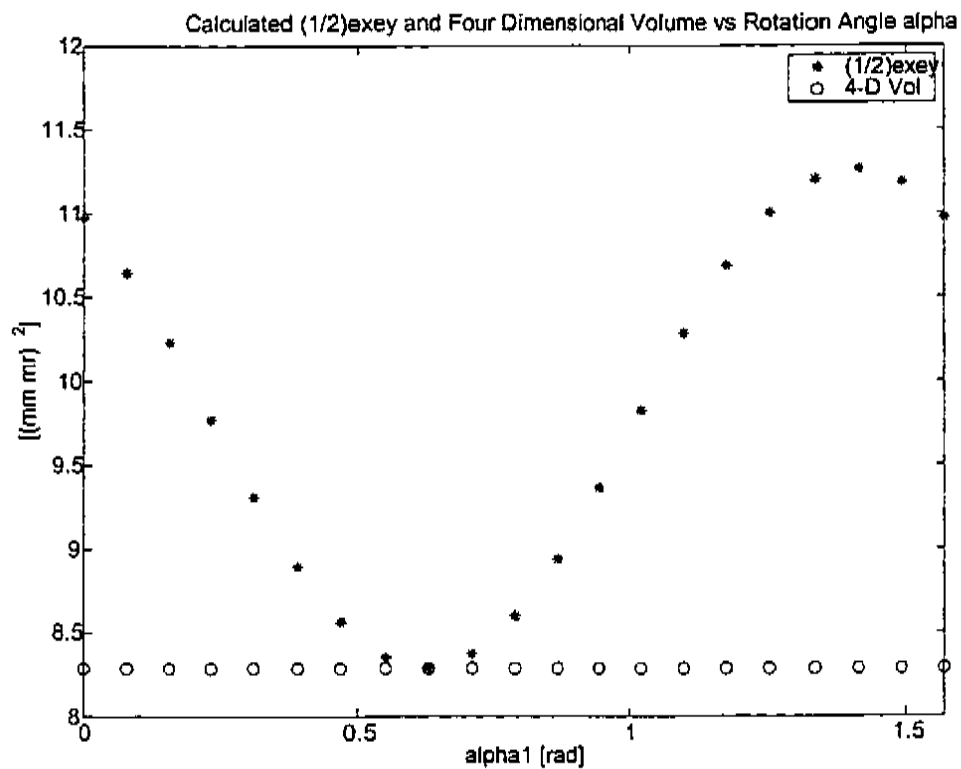


Figure 5.9: Calculated $1/2\epsilon_x\epsilon_y$ and V_{4-D} versus rotation angle α change of horizontal scale

The rotation angle α_1 was varied in steps of $\pi/20$ in the first plot, Fig. 5.8, and the rotation angle α_1 was varied in steps of $\pi/40$ in the last plot, Fig. 5.9, for more detail. The values for $\frac{1}{2}\epsilon_x\epsilon_y$ and the four dimensional volume are equal when the couplings introduced by the rotation are zero. In the first plot, Fig. 5.8, the values for $\frac{1}{2}\epsilon_x\epsilon_y$ and the four dimensional volume coincide at two places $4\pi/20 = \pi/5$ and $14\pi/20 = 7\pi/10$, the two values are separated by $\pi/2$. The initial rotation of the beam was $\alpha_0 = \pi/5$. The additional rotation of $\pi/2$ from $\alpha_0 = \pi/5$ yields $\alpha_0 = 7\pi/10$, represents an interchange of the pairs x, y and x', y' along with a mirror about the y and y' axes. So the determination of the orientation of the axes with respect to the initial distribution is not complete. While the values for the four dimensional volumes are the same regardless of rotation, the values for ϵ_x , ϵ_y and $\frac{1}{2}\epsilon_x\epsilon_y$ are dependent on the rotation of the beam. The values for the four dimensional volumes, $\frac{1}{2}\epsilon_x\epsilon_y$, ϵ_x and ϵ_y are presented in Table 5.9 below.

α_0 [rad]	$\pi/5$	$\pi/5$	$\pi/5$	$7\pi/10$
α_1 [rad]	0	$\pi/5$	$7\pi/10$	0
$V_{4-D,Initial}[(\text{mm mrad})^2]$	8.29	8.29	8.29	8.29
$V_{4-D,Calc}[(\text{mm mrad})^2]$	8.29	8.29	8.29	8.29
$\frac{1}{2}\epsilon_x\epsilon_y[(\text{mm mrad})^2]$	10.97	8.29	8.29	10.97
ϵ_x [mm mrad]	4.00	2.34	7.09	5.49
ϵ_y [mm mrad]	5.49	7.09	2.34	4.00

Table 5.9: Table of values for projected and 4-DVol

There are two possible values for the angle α_1 that lead to the condition $\frac{1}{2}\epsilon_x\epsilon_y = V_{4-D}$. In order to determine the correct value for α_1 , the measurement is repeated with $\alpha_1 = 0$. The sign of $\sigma(0)_{13}$ will give the orientation of the initial beam. If $\sigma(0)_{13} > 0$ then $0 < \alpha_0 < \pi/2$ since the initial distribution lies in the first and third quadrants of the initial $x - y$ space and $x \times y \geq 0$ for each of the particles in the distribution. If $\sigma(0)_{13} < 0$ then $\pi/2 < \alpha_0 < \pi$ since the initial distribution lies in the second and fourth quadrants and $x \times y \leq 0$ for each of the particles in the distribution. These concepts are demonstrated in Fig. 5.10 which contains the ten values of the vector σ_{calc} for four cases. The plots for the first three entries of the legend, $\alpha_0 = \pi/5$ with $\alpha_1 = 0$, $\alpha_1 = \pi/5$ and $\alpha_1 = 7\pi/10$ represent the situations where the initial rotation

is $\alpha_0 = \pi/5$ and the “guessed” rotations are $\alpha_1 = 0, \pi/5$ and $7\pi/10$. The last plot $\alpha_0 = 7\pi/10$ with $\alpha_1 = 0$ represents an initial rotation of $\alpha_0 = 7\pi/10$ and a rotation guess of $\alpha_1 = 0$.

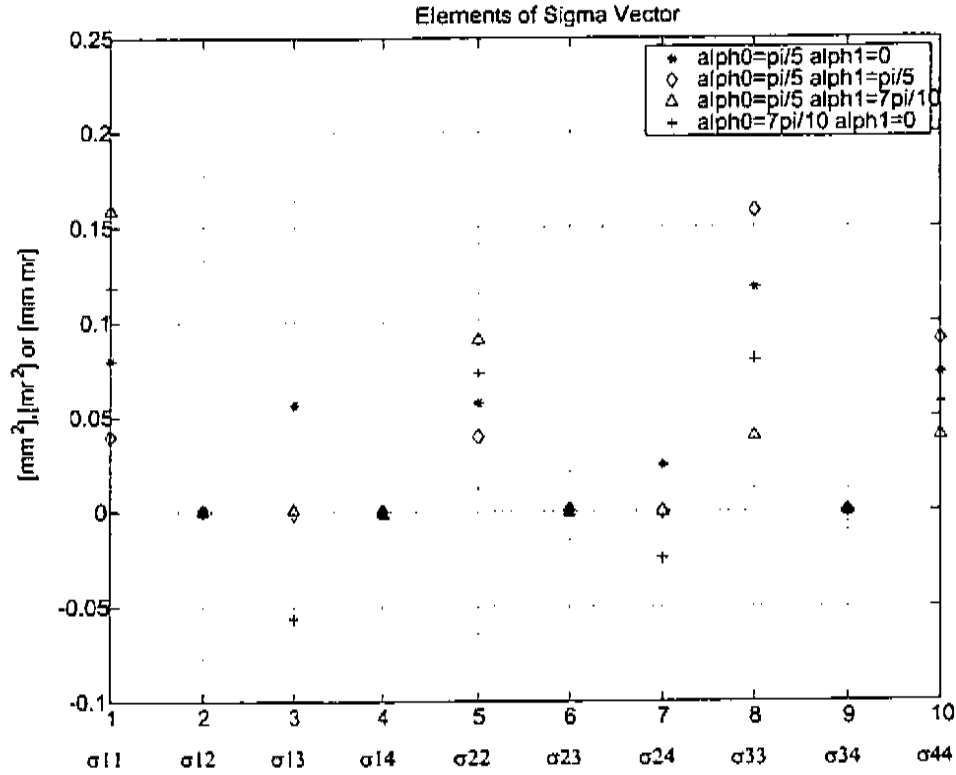


Figure 5.10: Elements of the sigma vector

In Fig. 5.10 the data for the cases $\alpha_0 = \pi/5$ with $\alpha_1 = \pi/5$ and $\alpha_1 = 7\pi/10$ show the minimization of elements σ_{13} , σ_{14} , σ_{23} and σ_{24} . Element σ_{13} is positive for the case of $\alpha_0 = \pi/5$ with $\alpha_1 = 0$ which indicates that the beam is initially rotated by an angle in the range $0 < \alpha_0 < \pi/2$ therefore $\alpha_0 = \pi/5$. Also shown is the case where the beam is initially rotated by an angle of $\alpha_0 = 7\pi/10$ (the other possible initial orientation) and with $\alpha_1 = 0$ this initial distribution yields an element σ_{13} which is negative. So by sweeping an initial rotation α_1 in the transformation $R_{calc} = R_{d2}R_{q2}R_{d1}R_{q1}R_{rot1}$ used to calculate the initial ten elements of the vector $\vec{\sigma}_{calc}$ and checking the sign of σ_{13} for the case where $\alpha_1 = 0$, the initial angle of

rotation of the beam can be determined. This angle could be useful in the use of skew quadrupoles which can rotate the beam and therefore reduce the effects of the coupling that are presented to the next magnetic element such as a quadrupole or even an to an undulator.

This is similar to transforming to the Larmor frame[45]. While this may seem a straightforward calculation, in the case of the photoinjector one needs to know the beam energy at the exit of the gun, the solenoid strength and know exactly where the astigmatism in the beam occurs. For example if the astigmatism is due to the laser one would need to know the orientation of the beam on the cathode. Further complications are the possibility of non-uniformity of the cathode emission, higher order modes in the gun and in the solenoid itself. Also both of the methods are based on a single rotation to decouple the transverse dimensions of the beam. If there are other coupling effects present before the rotation, the coupling elements may not all be nulled by changing to the rotated frame. And for non-rotationally symmetric beams with transverse coupling, transforming to the Larmor frame does not guarantee that Liouville's theorem is satisfied for the projected emittances. For such beams Liouville's theorem only holds true for the 4-D volume[45].

5.5 Symmetric Distribution

Rotation of beams which are not symmetric has been shown to produce undesirable results in the traditional quadrupole scan. Next the approximately four dimensionally symmetric distribution from Chap. 3 is used in the simulations. Starting with the initial parameters:

$$\begin{aligned} \sigma_x &= \sigma_y = 0.2 \text{ mm} & \sigma_{x'} &= \sigma_{y'} = 0.2 \text{ mrad} & \sigma_z &= 2.0 \text{ ps} \\ E &= 30 \text{ MeV} & \sigma_E &= .03 \text{ MeV} \end{aligned}$$

with initial normalized four dimensional volume of:

$$V_{4-D_0} = 2.837 \text{ [mm mrad]}^2$$

and normalized emittances of:

$$\epsilon_{x0} = 2.370 \text{ mm mrad} \text{ and } \epsilon_{y0} = 2.385 \text{ mm mrad}$$

and,

$$\frac{1}{2}\epsilon_{x0}\epsilon_{y0} = 2.837 \text{ [mm mrad]}^2$$

More significant figures are utilized to show the slight difference in the emittances which is due to slight asymmetry in the transverse dimensions of the beam which is unavoidable since a perfectly symmetry beam would be impossible to generate using a finite number of particles. Again the beam is rotated through the angles $0 < \alpha < \pi$ in steps of $\pi/20$ and propagated at each angle through the doublet to the screen. The vector $\vec{\sigma}_{\text{calc}} = \tilde{R}^{-1}\vec{\sigma}(1)$ is calculated for each angle by performing a quadrupole scan at each angle. The four dimensional volume at the doublet entrance, $V_{4-D,\text{calc}}$, and the projected normalized emittances $\epsilon_{x\text{calc}}$ and $\epsilon_{y\text{calc}}$ are calculated using the relations (5.8-10) above. Also, $\frac{1}{2}\epsilon_{x\text{calc}}\epsilon_{y\text{calc}}$ is calculated in order to compare the values used in the uncoupled Brightness relation with the four dimensional volume. Plots of the data are given in Fig. 5.11 and Fig. 5.12 below:

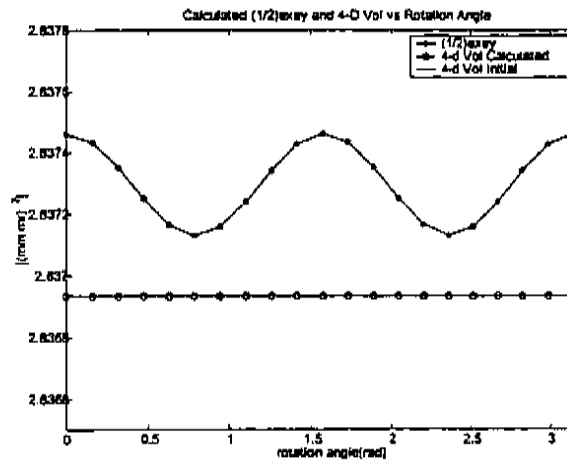


Figure 5.11: Plot $1/2\epsilon_x\epsilon_y$, V_{4-D} calc and initial versus rotation angle

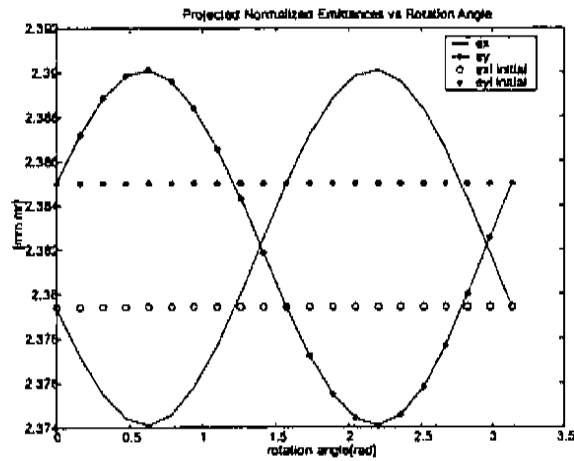


Figure 5.12: Plot ϵ_x and ϵ_y versus rotation angle

Rotation Angle [rad]	$V_{4-D,Initial}$ [(mm mrad) ²]	$V_{4-D,Calculated}$ [(mm mrad) ²]	ΔV_{4-D} % delta
0.000	2.8369	2.8369	0.0000
0.157	2.8369	2.8369	0.0000
0.314	2.8369	2.8369	0.0000
0.471	2.8369	2.8369	0.0000
0.628	2.8369	2.8369	0.0000
0.785	2.8369	2.8369	0.0000
0.942	2.8369	2.8369	0.0000
1.100	2.8369	2.8369	0.0000
1.257	2.8369	2.8369	0.0000
1.414	2.8369	2.8369	0.0000
1.571	2.8369	2.8369	0.0000
1.728	2.8369	2.8369	0.0000
1.885	2.8369	2.8369	0.0000
2.042	2.8369	2.8369	0.0000
2.199	2.8369	2.8369	0.0000
2.356	2.8369	2.8369	0.0000
2.513	2.8369	2.8369	0.0000
2.670	2.8369	2.8369	0.0000
2.827	2.8369	2.8369	0.0000
2.985	2.8369	2.8369	0.0000
3.142	2.8369	2.8369	0.0000

Table 5.10: Values for 4-DVol initial, calculated and their relative error for different rotation angles for symmetric distribution

Rotation Angle [rad]	$V_{4-D,Initial}$ [(mm mrad) ²]	$(\frac{1}{2}\epsilon_x\epsilon_y)_{Calculated}$ [(mm mrad) ²]	$\Delta (\frac{1}{2}\epsilon_x\epsilon_y)_{Calculated}$ % delta
0.000	2.8369	2.8375	0.0186
0.157	2.8369	2.8374	0.0176
0.314	2.8369	2.8374	0.0147
0.471	2.8369	2.8373	0.0111
0.628	2.8369	2.8372	0.0082
0.785	2.8369	2.8371	0.0069
0.942	2.8369	2.8372	0.0079
1.100	2.8369	2.8372	0.0107
1.257	2.8369	2.8373	0.0143
1.414	2.8369	2.8374	0.0173
1.571	2.8369	2.8375	0.0186
1.728	2.8369	2.8374	0.0176
1.885	2.8369	2.8374	0.0147
2.042	2.8369	2.8373	0.0111
2.199	2.8369	2.8372	0.0082
2.356	2.8369	2.8371	0.0069
2.513	2.8369	2.8372	0.0079
2.670	2.8369	2.8372	0.0107
2.827	2.8369	2.8373	0.0143
2.985	2.8369	2.8374	0.0173
3.142	2.8369	2.8375	0.0186

Table 5.11: Values for 4-DVol initial and 1/2exey calculated and their relative error for different rotation angles for symmetric distribution

Rotation Angle [rad]	ϵ_x Calculated [mm mrad]	ϵ_y Calculated [mm mrad]
0.000	2.3794	2.3850
0.157	2.3772	2.3872
0.314	2.3755	2.3888
0.471	2.3744	2.3899
0.628	2.3741	2.3901
0.785	2.3746	2.3896
0.942	2.3758	2.3884
1.100	2.3777	2.3866
1.257	2.3800	2.3843
1.414	2.3825	2.3819
1.571	2.3850	2.3794
1.728	2.3872	2.3772
1.885	2.3888	2.3755
2.042	2.3899	2.3744
2.199	2.3901	2.3741
2.356	2.3896	2.3746
2.513	2.3884	2.3758
2.670	2.3866	2.3777
2.827	2.3843	2.3800
2.985	2.3819	2.3825
3.142	2.3794	2.3850

Table 5.12: Values for ϵ_x and ϵ_y for different rotation angles for symmetric distribution

From the data above in Tables 5.10-5.12 it is clear that values calculated using projected quantities are not constant with respect to rotation. As was pointed out in the previous chapter there is no guarantee of conservation for projected quantities in the transformations of phase space when rotations are involved. Any asymmetry in the distribution will lead to differences between the four dimensional volume which is the conserved quantity and $\frac{1}{2}\epsilon_x\epsilon_y$ which is calculated from projected values. For the case of the distribution which is approximately symmetric in four dimensional space the deviations are quite small. And in the laboratory environment the differences would be considered insignificant. The data below, Fig. 5.13 and Table 5.13, for the initial distribution indicate small but nonzero values for the couplings along with a slight asymmetry in the transverse dimensions of the beam. These nonzero couplings and asymmetries lead to the variation in the projected quantities. A plot, Fig. 5.13, and table, Table 5.13, for the calculated sigma vector for three different rotation angle are presented below.

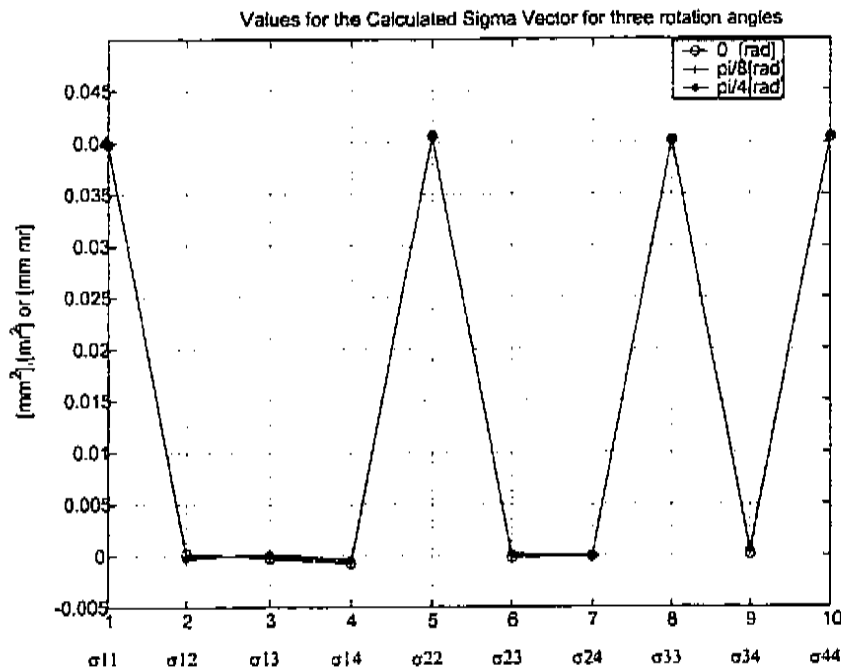


Figure 5.13: Values for calculated sigma vector for three different rotation angles for symmetric distribution

<i>Rotation</i>	σ_{11} [mm ²]	σ_{12} [mm mrad]	σ_{13} [mm ²]	σ_{14} [mm mrad]
<i>InitialDist</i>	3.9886E-02	2.4972E-04	-2.3182E-04	-7.2891E-04
0.0	3.9886E-02	2.4972E-04	-2.3182E-04	-7.2891E-04
$\pi/8$	3.9771E-02	-6.7296E-05	-4.5794E-05	-6.4027E-04
$\pi/4$	3.9822E-02	-2.2880E-04	1.6705E-04	-3.5343E-04
<i>Rotation</i>	σ_{22} [mrad ²]	σ_{23} [mm mrad]	σ_{24} [mrad ²]	
<i>InitialDist</i>	4.0643E-02	-1.2506E-04	-2.5189E-05	
0.0	4.0643E-02	-1.2506E-04	-2.5189E-05	
$\pi/8$	4.0603E-02	-3.6426E-05	-7.0553E-05	
$\pi/4$	4.0543E-02	2.5041E-04	-7.4587E-05	
<i>Rotation</i>	σ_{33} [mm ²]	σ_{34} [mm mrad]	σ_{44} [mrad ²]	
<i>InitialDist</i>	4.0220E-02	1.4670E-04	4.0494E-02	
0.0	4.0220E-02	1.4670E-04	4.0494E-02	
$\pi/8$	4.0335E-02	4.6376E-04	4.0534E-02	
$\pi/4$	4.0285E-02	6.2526E-04	4.0594E-02	

Table 5.13: Values for sigma vector for initial distribution and three different rotation angles for symmetric distribution

Although the projected values are not conserved, if the asymmetries in the distribution and the couplings are small then the projected quantities are approximately conserved. In order for both of these conditions to be true the projected emittances should be approximately equal, $\sigma_{11} \sim \sigma_{33}$, $\sigma_{22} \sim \sigma_{44}$, $\sigma_{12} \sim \sigma_{34}$, this reduces the effects due to asymmetries in the distribution. Also the strength of the couplings σ_{13} , σ_{14} , σ_{23} and σ_{24} should be small. Both of which lead to an approximately four dimensionally symmetric beam. From Fig. 5.3 above the $\sigma_{11} \sim \sigma_{33}$, $\sigma_{22} \sim \sigma_{44}$, $\sigma_{12} \sim \sigma_{34}$ and the other couplings σ_{13} , σ_{14} , σ_{23} and σ_{24} are small. These requirements will be demonstrated analytically in section 5.7. The effect of the couplings can be inferred from a plot of r_{13} versus quadrupole strength. In the plot $|r_{13}| \ll 1$ for any of the strengths of q2 and for any of the rotation angles.

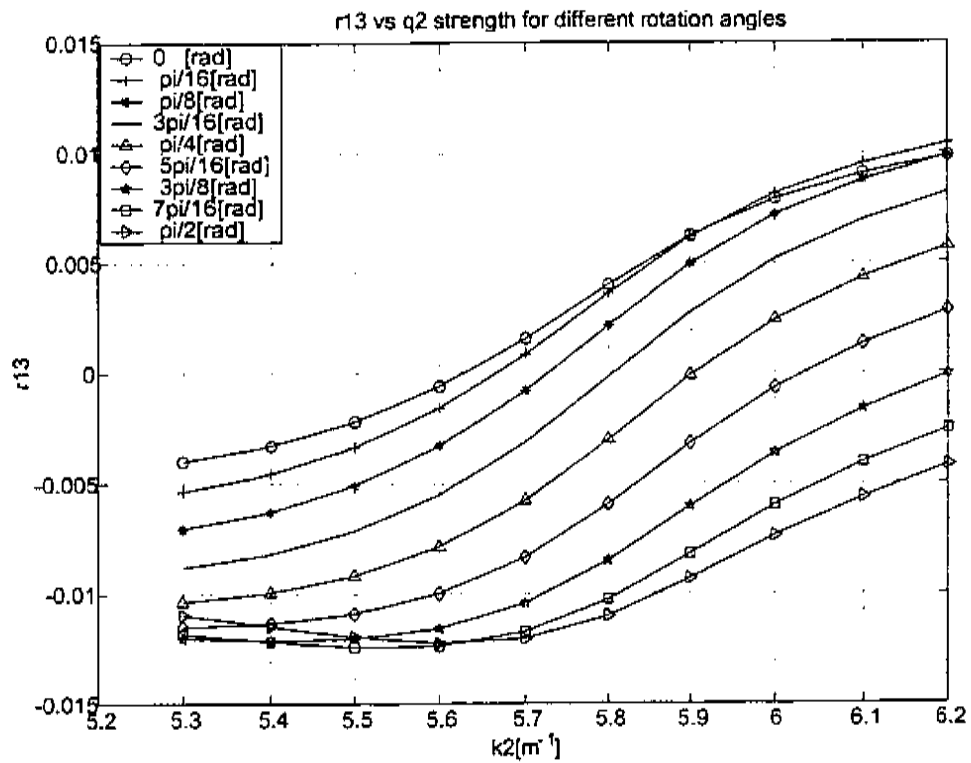


Figure 5.14: Plot r_{13} versus q_2 strength for different rotation angles for symmetric distribution

5.6 Simulations With Bi-Symmetric Beams

The next simulation is for the case of the bi-symmetric distribution which is symmetric in $x - y$ space but asymmetric in $x' - y'$ space. I repeat the previous simulation but make:

$$\begin{aligned} \sigma_x &= \sigma_y = 0.2 \text{ mm} & \sigma_{x'} &= 0.2 \text{ mrad} & \sigma_{y'} &= 0.4 \text{ mrad} \\ \sigma_z &= 2.0 \text{ ps} & E &= 30 \text{ MeV} & \sigma_E &= .03 \text{ MeV} \end{aligned}$$

with initial normalized four dimensional volume of:

$$V_{4-D_0} = 5.74 \text{ [mm mrad]}^2$$

and normalized emittances of:

$$\epsilon_{x0} = 2.39 \text{ mm mrad}, \epsilon_{y0} = 4.81 \text{ mm mrad} \text{ and } \frac{1}{2}\epsilon_{x0}\epsilon_{y0} = 5.75 \text{ [mm mrad]}^2 \quad (5.13)$$

Again the beam is rotated through the angles $0 < \alpha < \pi$ in steps of $\pi/20$ and propagated at each angle through the doublet to the screen. The vector $\vec{\sigma}_{calc}$ is calculated for each angle by performing a quadrupole scan at each angle. The calculated four dimensional volume at the doublet entrance, $V_{4-D,Calc}$, and the projected normalized emittances ϵ_{xcalc} and ϵ_{ycalc} are calculated using the relations (5.8-10) above. Also, $\frac{1}{2}\epsilon_{xcalc}\epsilon_{ycalc}$ is calculated in order to compare the values used in the uncoupled brightness relation with the four dimensional volume. Plots of the data are given in Figs 5.15 and 5.16 below:

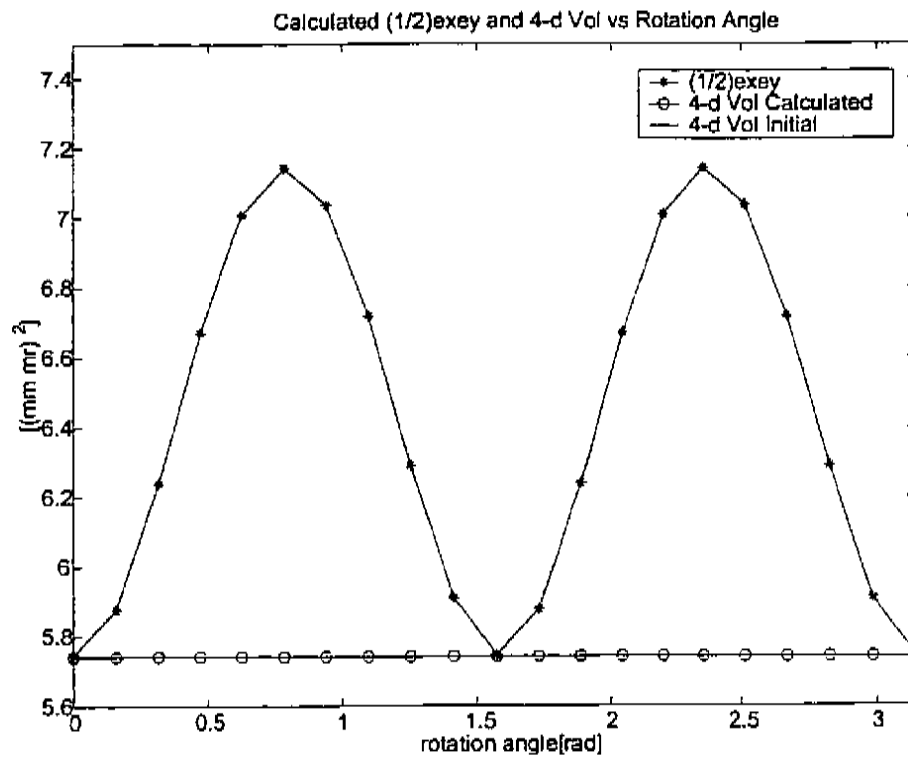


Figure 5.15: Plot $1/2\epsilon_{xy}$ and 4-DVol calculated and initial for different rotation angles for bi-symmetric distribution

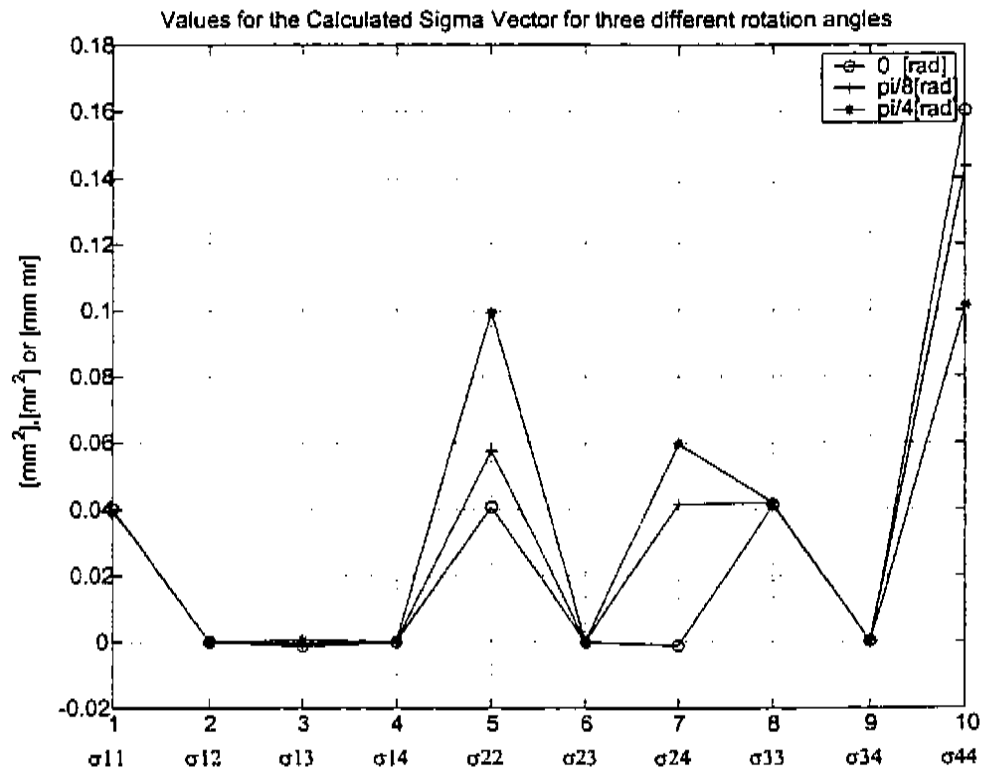


Figure 5.16: Plot calculated sigma vector elements for three different rotation angles for bi-symmetric distribution

<i>Rotation</i>	$\sigma_{11}[\text{mm}^2]$	$\sigma_{12}[\text{mm mrad}]$	$\sigma_{13}[\text{mm}^2]$	$\sigma_{14}[\text{mm mrad}]$
<i>InitialDist</i>	$4.0197E-02$	$1.0688E-04$	$-1.2269E-03$	$6.1049E-05$
0.0	$4.0197E-02$	$1.0689E-04$	$-1.2269E-03$	$6.1049E-05$
$\pi/8$	$3.9493E-02$	$1.0701E-04$	$-4.7241E-04$	$1.5302E-04$
$\pi/4$	$3.9529E-02$	$1.7212E-04$	$5.5877E-04$	$2.1797E-04$

<i>Rotation</i>	$\sigma_{22}[\text{mrad}^2]$	$\sigma_{23}[\text{mm mrad}]$	$\sigma_{24}[\text{mrad}^2]$
<i>InitialDist</i>	$4.0706E-02$	$-1.5274E-04$	$-1.0314E-03$
0.0	$4.0706E-02$	$-1.5274E-04$	$-1.0314E-03$
$\pi/8$	$5.7462E-02$	$-6.0773E-05$	$4.1479E-02$
$\pi/4$	$9.9373E-02$	$4.1780E-06$	$5.9692E-02$

<i>Rotation</i>	$\sigma_{33}[\text{mm}^2]$	$\sigma_{34}[\text{mm mrad}]$	$\sigma_{44}[\text{mrad}^2]$
<i>InitialDist</i>	$4.1315E-02$	$3.2903E-04$	$1.6010E-01$
0.0	$4.1315E-02$	$3.2906E-04$	$1.6010E-01$
$\pi/8$	$4.2019E-02$	$3.2895E-04$	$1.4335E-01$
$\pi/4$	$4.1983E-02$	$2.6383E-04$	$1.0144E-01$

Table 5.14: Elements of sigma vector for initial distribution and three different rotation angles for bi-symmetric distribution

The asymmetry in the x' and y' dimensions of the initial beam is reflected in the values for σ_{22} and σ_{44} in the initial distribution. This asymmetry drives σ_{24} as the rotation angle is increased as evidenced by the increase in the value for σ_{24} with rotation angle while in comparison the changes in the other couplings σ_{13} , σ_{14} and σ_{23} with increase in rotation angle are almost negligible. The couplings σ_{13} , σ_{14} and σ_{23} are initially small and the rotation does not increase the already small couplings. This will be shown analytically the next section. The effects of increasing the amount of rotation applied to the distribution before the quadrupole doublet is seen as an increase in the value for σ_{13} as is evident in the plot Fig 5.17 below. Note that the only curve which passes through zero is the one for no rotation. This is due to the small nonzero couplings present in the initial distribution. The other curves do not pass through zero since the dominant coupling in the beam is due to the asymmetry in the x' and y' dimensions of the beam which drives the σ_{24} coupling. In the propagation of the rotated beam through the quadrupole doublet the σ_{24} coupling is multiplied by a term which does not pass through zero as the scanning quadrupole, q2, is changed. This will be shown in detail in the next section.

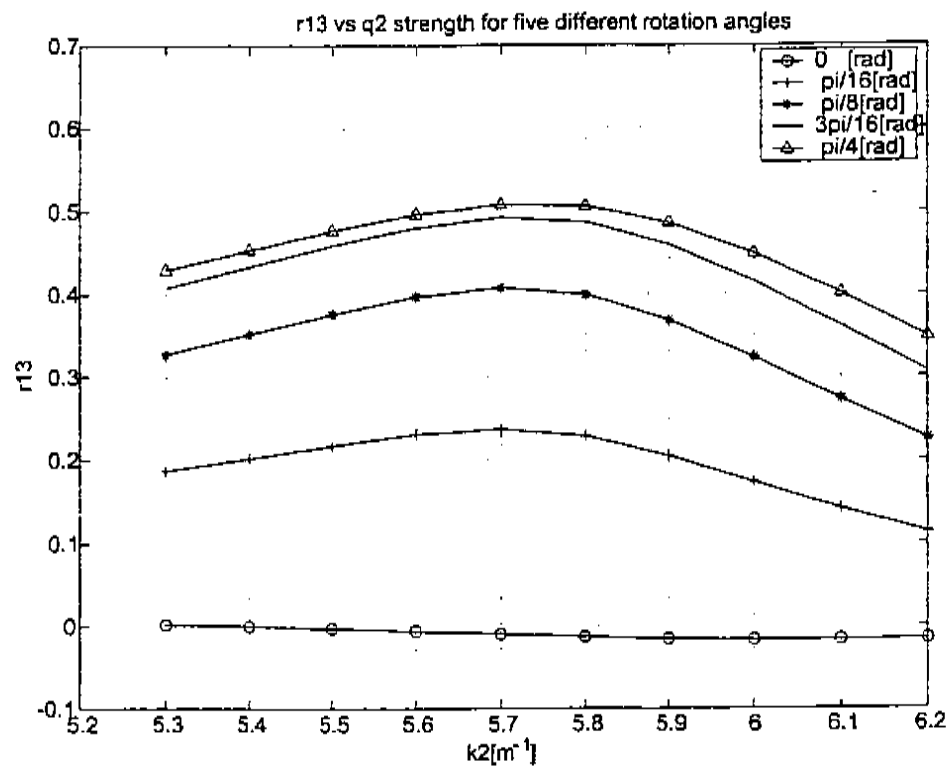


Figure 5.17: Plot r_{13} versus q_2 strength for different rotation angles for bi-symmetric distributions

5.7 Characterization Of σ_{13} And r_{13}

The quadrupole scan allows one to measure the $x - y$ correlation, $\sigma_{13}(1)$, in the beam. Knowledge of $\sigma_{13}(1)$ in the beam is important since nonzero $x - y$ correlation measured in a quadrupole scan indicates the presence of one or more of the correlations $\sigma_{13}(0)$, $\sigma_{14}(0)$, $\sigma_{23}(0)$ and $\sigma_{24}(0)$ in the beam at the input to the doublet. If these correlations are nonzero then the projected emittances, ϵ_x and ϵ_y , are not conserved and only the V_{4-D} is a conserved quantity. The correlation $\sigma_{13}(1)$ which is measured at the screen location is determined by the initial values for the correlations $\sigma_{13}(0)$, $\sigma_{14}(0)$, $\sigma_{23}(0)$ and $\sigma_{24}(0)$ at the input to the doublet and the lattice settings for the doublet. From Chap. 4 equation (4.45), $\sigma_{13}(1)$ at the screen location is given by:

$$\sigma_{13}(1) = [R_{11}R_{33}\sigma_{13}(0) + R_{11}R_{34}\sigma_{14}(0) + R_{12}R_{33}\sigma_{23}(0) + R_{12}R_{34}\sigma_{24}(0)]. \quad (5.14)$$

Where R_{ij} are the ij elements of the transfer matrix R for the beam line between the doublet entrance and the screen given by:

$$R = R_{d2}R_{q2}R_{d1}R_{q1} \quad (5.15)$$

No rotation of the beam is assumed in the quadrupole scan measurement process. The only parameter that changes during a quadrupole scan is the strength of the focusing quadrupole, $q2$, located before the drift section, $d2$, which precedes the screen where the moments $\sigma_{11}(1)$, $\sigma_{33}(1)$ and $\sigma_{13}(1)$ of the distribution are determined. A plot of the elements of the transfer matrix for the parameters used in the simulations is given in Fig. 5.18 below.

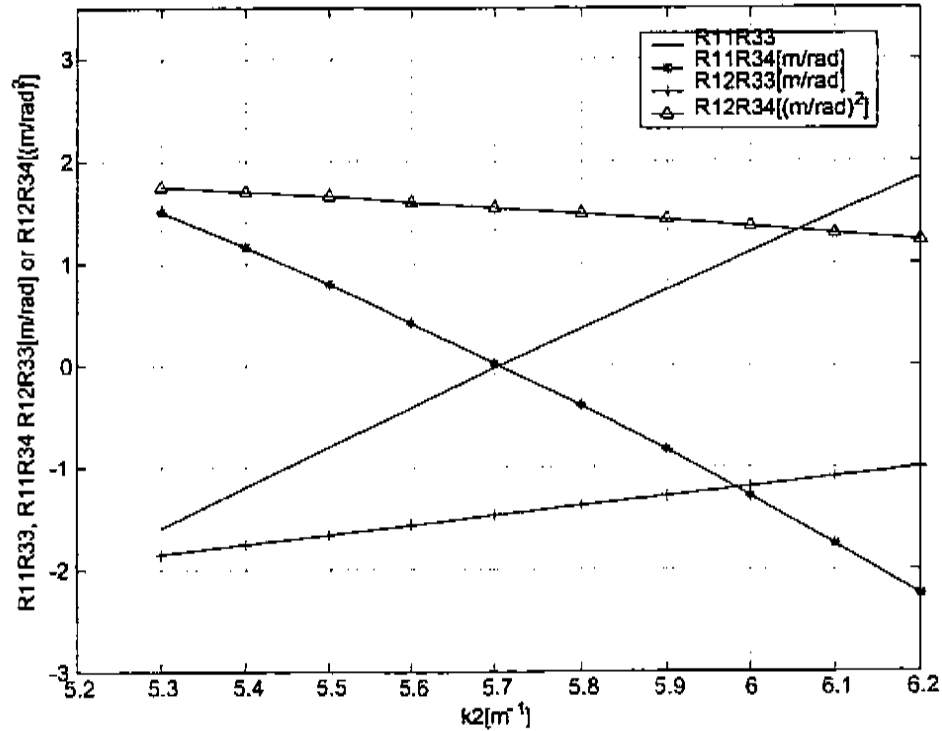


Figure 5.18: Plot of elements of the transfer matrix used in the simulations

For the lattice settings chosen, if there is only $\sigma_{13}(0)$ or $\sigma_{14}(0)$ present in the beam the correlation $\sigma_{13}(1)$ will pass linearly through zero during the quadrupole scan. If there is only $\sigma_{23}(0)$ or $\sigma_{24}(0)$ present in the beam the correlation $\sigma_{13}(1)$ will not pass through zero for the lattice settings chosen. In the initial beam there is always a small amount of all of these couplings. But as shown in the simulation for the symmetric beam case for rotation angles $0 \leq \alpha \leq \pi$, $|\tau_{13}| \ll 1$ or the correlation $\sigma_{13}(1)$ at the screen location is weak. So these initial statistical correlations are fairly weak. In comparison, the asymmetric beams where $\sigma_x \neq \sigma_y$ and/or $\sigma_{x'} \neq \sigma_{y'}$ the correlations are strong since $|\tau_{13}|$ became as large as .5 for rotation angles $0 \leq \alpha \leq \pi$. This is also seen in the values for the transverse couplings in the plots for the sigma vectors, Figs 5.5 and 5.16. Therefore, asymmetries in the initial beam before rotation of the beam can lead to significant amounts of the correlations $\sigma_{13}(0)$, $\sigma_{14}(0)$, $\sigma_{23}(0)$ and $\sigma_{24}(0)$ at the input to the doublet. And the presence of correlations $\sigma_{13}(i)$, $\sigma_{14}(i)$, $\sigma_{23}(i)$ and

$\sigma_{24}(i)$ that are large enough in the initial beam can also lead to correlations $\sigma_{13}(0)$, $\sigma_{14}(0)$, $\sigma_{23}(0)$ and $\sigma_{24}(0)$ at the input to the doublet.

Therefore in order to eliminate the couplings $\sigma_{13}(0)$, $\sigma_{14}(0)$, $\sigma_{23}(0)$ and $\sigma_{24}(0)$ in the beam at the input to the quadrupole doublet, asymmetries and the presence of the couplings $\sigma_{13}(i)$, $\sigma_{14}(i)$, $\sigma_{23}(i)$ and $\sigma_{24}(i)$ in the initial beam before the rotation should be eliminated. This can be seen by transforming the elements of the sigma matrix through the rotation to the doublet entrance using the relation:

$$\sigma_{ij}(0) = \sum R_{ik} R_{jl} \sigma_{kl}(i) \quad k, l = 1, 2, 3, 4 \quad (5.16)$$

where $\sigma_{ij}(0)$ is the ij element of the sigma matrix at the doublet entrance, R_{ik} is the ik element of the rotation transform and $\sigma_{kl}(i)$ is the kl element of the sigma matrix for the initial distribution.

The transform for a rotation of the transverse coordinates is given by:

$$R(\text{rotation}) = \begin{bmatrix} C & 0 & S & 0 \\ 0 & C & 0 & S \\ -S & 0 & C & 0 \\ 0 & -S & 0 & C \end{bmatrix} \quad (5.17)$$

where $C = \cos(\alpha)$, $S = \sin(\alpha)$ and α is the angle of rotation about the z-axis. Expanding equation (5.16) above for $\sigma_{13}(0)$ gives:

$$\begin{aligned} \sigma_{13}(0) = & [R_{11}R_{31}\sigma_{11}(i) + (R_{11}R_{32} + R_{12}R_{31})\sigma_{12}(i) + (R_{11}R_{33} + R_{13}R_{31})\sigma_{13}(i) \\ & + (R_{11}R_{34} + R_{14}R_{31})\sigma_{14}(i) + R_{12}R_{32}\sigma_{22}(i) + (R_{12}R_{33} + R_{13}R_{32})\sigma_{23}(i) \\ & + (R_{12}R_{34} + R_{14}R_{32})\sigma_{24}(i) + R_{13}R_{33}\sigma_{33}(i) + (R_{13}R_{34} + R_{14}R_{33})\sigma_{34}(i) \\ & + R_{34}R_{34}\sigma_{44}(i)] \end{aligned} \quad (5.18)$$

Substituting the values for the elements of the transform matrix for the rotation into

the above relation gives:

$$\sigma_{13}(0) = [(-CS)\sigma_{11}(i) + (C^2 - S^2)\sigma_{13}(i) + (SC)\sigma_{33}(i)]$$

$$\sigma_{13}(0) = [CS(\sigma_{33}(i) - \sigma_{11}(i)) + (C^2 - S^2)\sigma_{13}(i)] \quad (5.19)$$

where $C = \cos(\alpha)$, $S = \sin(\alpha)$ and α is the angle of rotation about the z-axis. In the range of rotation $\alpha = 0$ to π the contribution from $(C^2 - S^2)\sigma_{13}(i)$ is zero for two angles $\alpha = \pi/4$ and $\alpha = 3\pi/4$. In order for the $\sigma_{13}(0)$ correlation at the input to the doublet to be zero for any value of α , we must have $\sigma_{11}(i) = \sigma_{33}(i)$ and $\sigma_{13}(i) = 0$. So the initial beam must be symmetric in the x and y dimensions and have zero $\sigma_{13}(i)$ before the rotation is introduced in order for the correlation $\sigma_{13}(0) = 0$ at the doublet entrance. Alternatively, nonzero $\sigma_{13}(i)$ (for $\alpha \neq \frac{\pi}{4}$ or $\frac{3\pi}{4}$) and asymmetry in the initial transverse dimensions of the beam leads to nonzero $\sigma_{13}(0)$ correlation at the input to the doublet.

Repeating the expansion and substitution of the rotation transform matrix elements for the $\sigma_{14}(0)$ correlation yields:

$$\sigma_{14}(0) = [(-CS)\sigma_{12}(i) + (C^2)\sigma_{14}(i) + (-S^2)\sigma_{23}(i) + (SC)\sigma_{34}(i)]$$

$$\sigma_{14}(0) = [CS(\sigma_{34}(i) - \sigma_{12}(i)) + (C^2)\sigma_{14}(i) + (-S^2)\sigma_{23}(i)] \quad (5.20)$$

In order for $\sigma_{14}(0)$ to be zero for any value of α , we must have $\sigma_{12}(i) = \sigma_{34}(i)$, $\sigma_{14}(i) = 0$ and $\sigma_{23}(i) = 0$. Therefore the initial beam, before the rotation, must have the same coupling between $x - x'$ and $y - y'$. So the orientation of the phase ellipses in $x - x'$ and $y - y'$ space must be the same, not only both upright or both focusing or both defocusing, but with the same amount of correlation. And there must be no

correlation between the x and y' dimensions and the x' and y dimensions, $\sigma_{14}(i) = 0$ and $\sigma_{23}(i) = 0$.

The expansion and substitution of the rotation transform matrix elements for the $\sigma_{23}(0)$ correlation gives:

$$\sigma_{23}(0) = [(-CS)\sigma_{12}(i) + (-S^2)\sigma_{14}(i) + (C^2)\sigma_{23}(i) + (SC)\sigma_{34}(i)]$$

$$\sigma_{23}(0) = [CS(\sigma_{34}(i) - \sigma_{12}(i)) + (-S^2)\sigma_{14}(i) + (C^2)\sigma_{23}(i)] \quad (5.21)$$

In order for $\sigma_{23}(0)$ to be zero for any value of α , again we must have $\sigma_{12}(i) = \sigma_{34}(i)$, $\sigma_{14}(i) = 0$ and $\sigma_{23}(i) = 0$ in the initial beam before the rotation. The reversal of C^2 and S^2 as the coefficients for $\sigma_{14}(i)$ and $\sigma_{23}(i)$ between the two equations above further enforces the requirement that $\sigma_{14}(i) = 0$ and $\sigma_{23}(i) = 0$ in order to have $\sigma_{14}(0) = 0$ and $\sigma_{23}(0) = 0$ at the doublet entrance. Alternatively, nonzero $\sigma_{14}(i)$ and $\sigma_{23}(i)$ in the initial beam or inequality between $\sigma_{12}(i)$ and $\sigma_{34}(i)$ in the initial beam before the rotation leads to nonzero $\sigma_{14}(0)$ and $\sigma_{23}(0)$ correlations at the input to the doublet

Finally the expansion and substitution of the rotation transform matrix elements for the $\sigma_{24}(0)$ correlation yields:

$$\sigma_{24}(0) = [(-CS)\sigma_{22}(i) + (C^2 - S^2)\sigma_{24}(i) + (SC)\sigma_{44}(i)]$$

$$\sigma_{24}(0) = [CS(\sigma_{44}(i) - \sigma_{22}(i)) + (C^2 - S^2)\sigma_{24}(i)] \quad (5.22)$$

In the range of rotation $\alpha = 0$ to π the contribution from $(C^2 - S^2)\sigma_{24}(i)$ is zero for two angles $\alpha = \pi/4$ and $\alpha = 3\pi/4$. In order for $\sigma_{24}(0)$ to be zero for any value of α , we

must have $\sigma_{22}(i) = \sigma_{44}(i)$ and $\sigma_{24}(i) = 0$. So the horizontal and vertical divergences of the initial beam must be equal and there must be no correlation between the horizontal and vertical dimensions in order for $\sigma_{24}(0) = 0$ at the doublet entrance for any rotation angle.

Conditions For No Transverse Couplings After A Single Rotation

Therefore if there are to be no correlations $\sigma_{13}(0)$, $\sigma_{14}(0)$, $\sigma_{23}(0)$ and $\sigma_{24}(0)$ after a rotation of the beam, then the input beam before the rotation must be symmetric in $x - y$ space, $\sigma_{11}(i) = \sigma_{33}(i)$, and symmetric in $x' - y'$ space, $\sigma_{44}(i) = \sigma_{22}(i)$. And the $x - x'$ and $y - y'$ couplings must be equal $\sigma_{12}(i) = \sigma_{34}(i)$. This forms a requirement that is more stringent than requiring that the projected emittances be equal $\epsilon_x = \epsilon_y$. Also there must be no initial correlations $\sigma_{13}(i)$, $\sigma_{14}(i)$, $\sigma_{23}(i)$ and $\sigma_{24}(i)$ in the beam before the rotation. Such rotations are present, for example, at the entrance and exit of the emittance compensation solenoid in a photoinjector.

In addition to providing a measure of the strength of coupling terms $\sigma_{13}(0)$, $\sigma_{14}(0)$, $\sigma_{23}(0)$ and $\sigma_{24}(0)$ at the input to the doublet for the quadrupole scan, the correlation coefficient $r_{13} = \frac{\sigma_{13}(1)}{\sqrt{\sigma_{11}(1)\sigma_{33}(1)}}$ (where $|r_{13}| \leq 1$) can be used to further illustrate the points made above about the behavior of $\sigma_{13}(1)$ at the screen and the asymmetries in the initial distribution. Plots of r_{13} for quadrupole scans with input distributions that contain the following asymmetries (1) $\sigma_x \neq \sigma_y$ and $\sigma_{x'} = \sigma_{y'}$, (2) $\sigma_{x'} \neq \sigma_{y'}$ and $\sigma_x = \sigma_y$, and (3) $\sigma_x \neq \sigma_y$ and $\sigma_{x'} \neq \sigma_{y'}$ and $\epsilon_x = \epsilon_y$ were generated. These initial distributions were then subject to a rotation of $\alpha = \pi/4$ before it was propagated through the quadrupole doublet to the screen where the beam moments and the $x - y$ correlation is measured. A plot of r_{13} for case (1) $\sigma_x \neq \sigma_y$ and $\sigma_{x'} = \sigma_{y'}$ is presented below in Fig. 5.19.

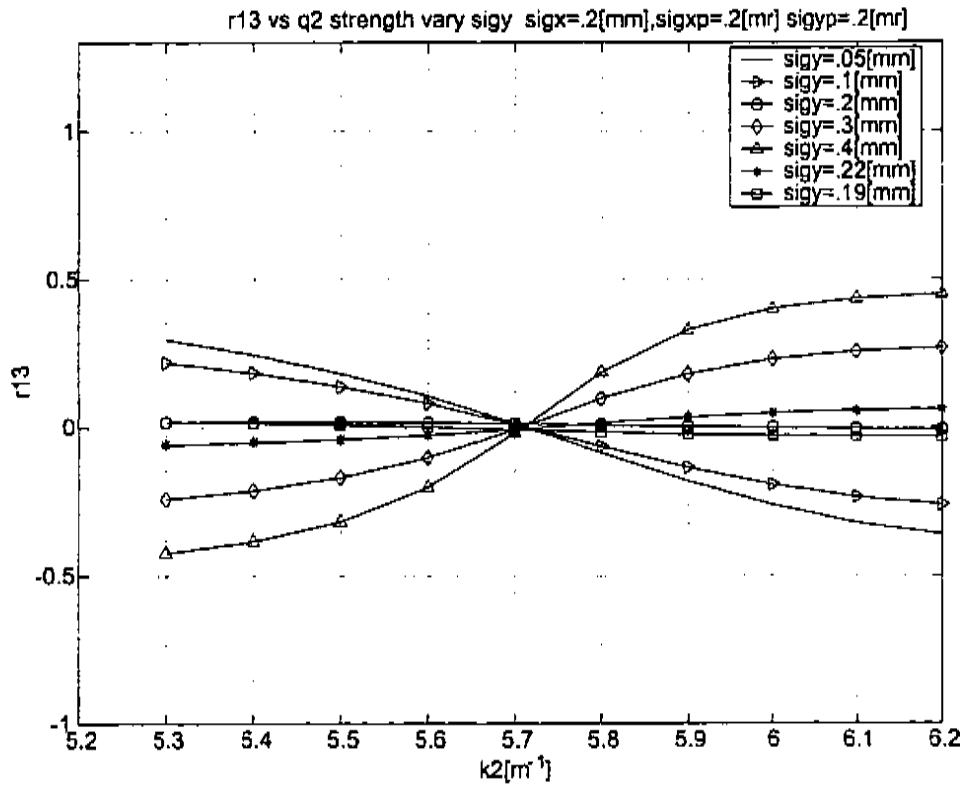


Figure 5.19: Plot of r13 versus q2 strength for $\sigma_{x'} = \sigma_{y'}$ and vary σ_y

All of the curves pass through zero at the same location which indicates the presence of only the correlations $\sigma_{13}(0)$ and $\sigma_{14}(0)$ at the entrance to the quadrupole doublet. Statistically there is a small amount of the correlations $\sigma_{12}(i)$, $\sigma_{13}(i)$, $\sigma_{14}(i)$, $\sigma_{23}(i)$, $\sigma_{24}(i)$ and $\sigma_{34}(i)$ in the initial distribution. This is seen in the nonzero values for the case of $\sigma_y = \sigma_x = .2[\text{mm}]$. As the asymmetry due to the increase in σ_y grows, $|\tau_{13}|$ increases due to the contribution from the term $CS(\sigma_{33}(i) - \sigma_{11}(i))$ of $\sigma_{13}(0) = [CS(\sigma_{33}(i) - \sigma_{11}(i)) + (C^2 - S^2)\sigma_{13}(i)]$. The increase is not from $\sigma_{14}(0) = [CS(\sigma_{34}(i) - \sigma_{12}(i)) + (C^2)\sigma_{14}(i) + (-S^2)\sigma_{23}(i)]$, $\sigma_{23}(0) = [CS(\sigma_{34}(i) - \sigma_{12}(i)) + (-S^2)\sigma_{14}(i) + (C^2)\sigma_{23}(i)]$ or $\sigma_{24}(0) = [CS(\sigma_{44}(i) - \sigma_{22}(i)) + (C^2 - S^2)\sigma_{24}(i)]$ since $\sigma_{34}(i)$, $\sigma_{12}(i)$, $\sigma_{14}(i)$ and $\sigma_{23}(i)$ are all small, $(C^2 - S^2) = 0$, and $\sigma_{44}(i) = \sigma_{22}(i)$.

A plot of r_{13} for case (2) $\sigma_{x'} \neq \sigma_{y'}$ and $\sigma_x = \sigma_y$ is presented in Fig. 5.20 below.

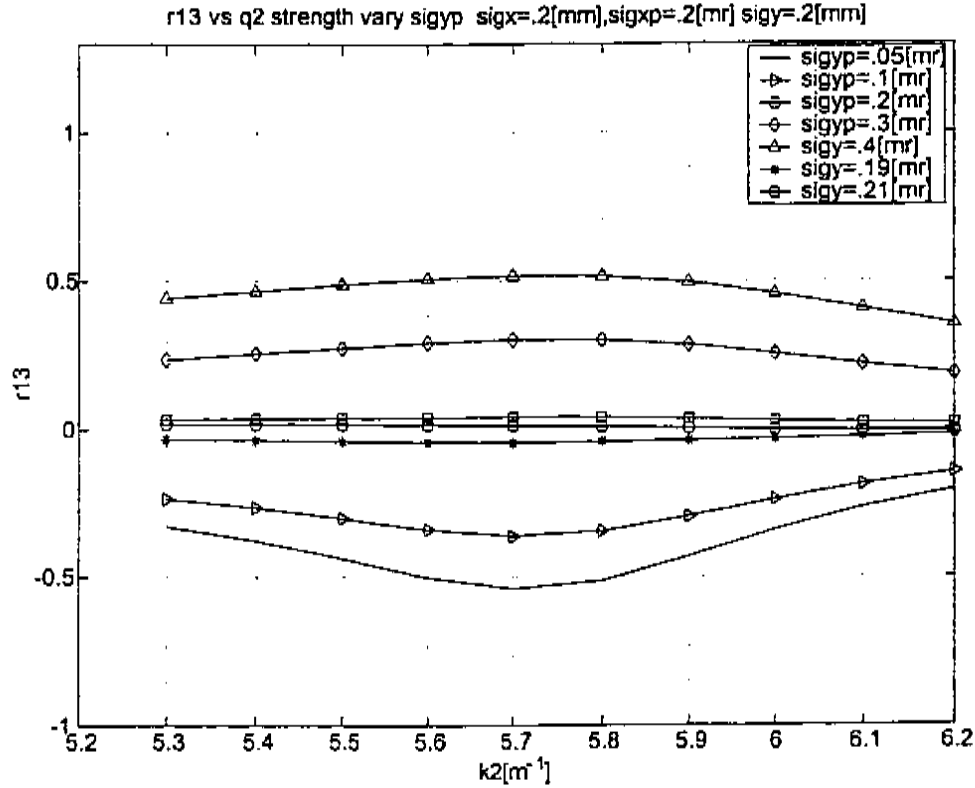


Figure 5.20: Plot of r_{13} versus q_2 strength for $\sigma_x = \sigma_y$ and vary $\sigma_{y'}$

Only the curve for the symmetric case $\sigma_{y'} = .2$ [mrad] passes through zero. This reflects the presence of a small amount of the correlations in the initial beam since $|r_{13}| \ll 1$ the correlations are very small. The other curves do not pass through zero which indicates the presence of only $\sigma_{23}(0)$ or $\sigma_{24}(0)$ at the input to the doublet. Since $\sigma_{23}(0) = [CS(\sigma_{34}(i) - \sigma_{12}(i)) + (-S^2)\sigma_{14}(i) + (C^2)\sigma_{23}(i)]$ and $\sigma_{34}(i)$, $\sigma_{12}(i)$, $\sigma_{14}(i)$ and $\sigma_{23}(i)$ are all small so $\sigma_{23}(0)$ is also small. And $\sigma_{24}(0) = [CS(\sigma_{44}(i) - \sigma_{22}(i)) + (C^2 - S^2)\sigma_{24}(i)]$ is driven by the asymmetry between $\sigma_{44}(i)$ and $\sigma_{22}(i)$, $(C^2 - S^2) = 0$.

A plot for case (3) $\sigma_x \neq \sigma_y$ and $\sigma_{x'} \neq \sigma_{y'}$ and $\epsilon_x = \epsilon_y$ is presented in Fig. 5.21 below.

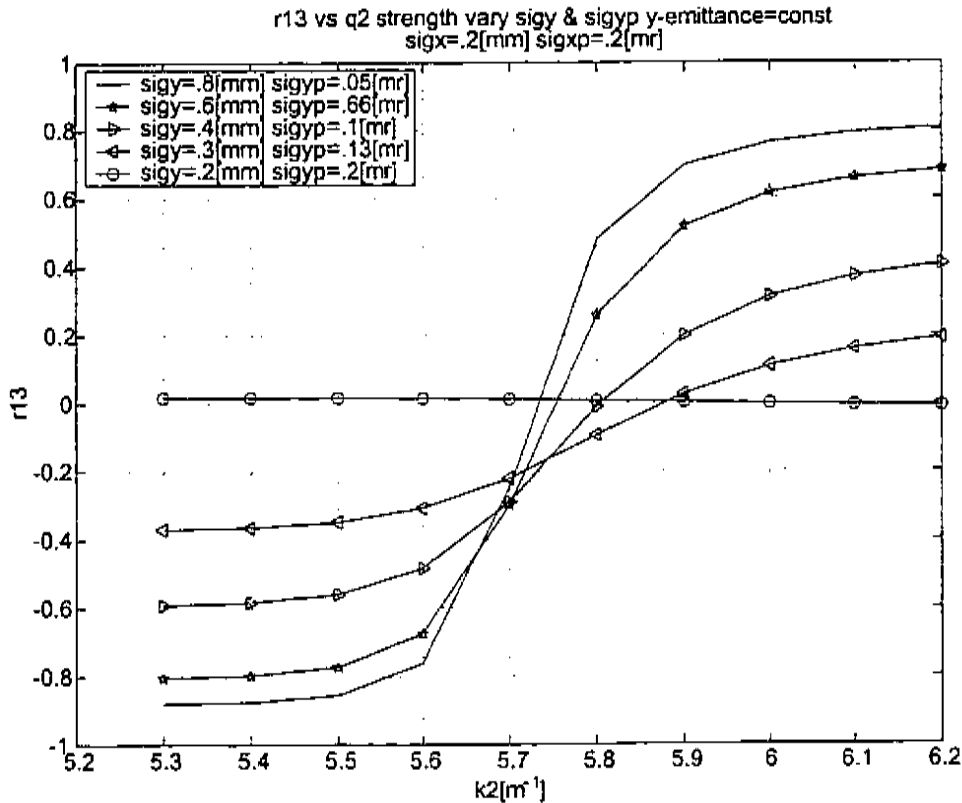


Figure 5.21: Plot of r_{13} versus q_2 strength vary σ_y and $\sigma_{y'}$ with ϵ_y constant

From this plot it is clear that although $\epsilon_x = \epsilon_y$ for all of the curves, only the curve for which $\sigma_x = \sigma_y$ and $\sigma_{x'} = \sigma_{y'}$ has the property that $|r_{13}| \ll 1$. For the other curves $r_{13} = \frac{\sigma_{13}(1)}{\sqrt{\sigma_{11}(1)\sigma_{33}(1)}} \neq 0$ since $\sigma_{13}(1) \neq 0$ and therefore ϵ_x and ϵ_y are not conserved quantities. Also, the curves do not pass through zero at the same location which indicates the presence of both correlations $\sigma_{13}(0)$ and $\sigma_{24}(0)$ at the input to the doublet for the quadrupole scan. The asymmetry between σ_x and σ_y drives $\sigma_{13}(0)$, and the asymmetry between $\sigma_{x'}$ and $\sigma_{y'}$ drives $\sigma_{24}(0)$ as shown above. The curves pass through zero due to the presence of $\sigma_{13}(0)$ and $\sigma_{24}(0)$ adds a nonzero offset which shifts the zero crossing of the curves. This is similar to what is seen in the experimental data presented in the last chapter.

Chapter 6

PARMELA Simulations

In order to further explore the effects of coupling on the quadrupole scan technique PARMELA[46] simulations were performed. PARMELA is a particle-pushing computer code which can simulate particle dynamics from the cathode, through the gun and solenoid, accelerate the particles through a traveling wave accelerator section and through various beamline elements. PARMELA can also simulate space charge effects which cause the electrons in the beam to repel each other. From the previous chapters asymmetries in the distribution before rotations lead to excitations of the transverse coupling terms σ_{13} , σ_{14} , σ_{23} and σ_{24} . Since the absolute source of the asymmetry in the distribution is unknown I chose to study asymmetries in the transverse dimensions of the laser on the cathode. The asymmetries were simulated using distributions on the cathode that had a fixed horizontal RMS width, σ_x , and different vertical RMS widths, σ_y . The simulations show the excitation of the σ_{13} correlation and the r_{13} correlation coefficient with the increase in asymmetry in the initial distribution. Also since PARMELA tracks the full six dimensional distribution the additional transverse-longitudinal couplings are evaluated. The couplings are small giving an indication that the effects due to transverse and longitudinal couplings are minimal for the accelerator parameters chosen for the simulations.

6.1 Simulation Parameters

The simulations were conducted using conditions similar to those used in the creation of the experimental data presented in the next chapter. The longitudinal distribution of the laser pulse was Gaussian with a 3 ps FWHM that generated 200 pC of charge at a laser injection phase of 60 degrees. The fields in the gun were chosen to be 140 MV/m peak value (or 50 MV average value) that was the estimated value for the experimental data. The linac phase was set to produce the smallest possible energy spread .1% and the linac gradients were set to produce a 30 MeV beam as measured using the spectrometer after the linac. In the experimental data the transverse profile of the laser was Gaussian with $\sigma_r = 1.0$ mm clipped at $r = 1.0$ mm using an aperture. And finally the solenoid settings for the experimental data ranged from 140 to 150 A.

At this time a few points about using PARMELA with asymmetric distributions must be made. This is not an typical method of using PARMELA. All of the standard input options set up distributions for the user that are radially symmetric. I used the 'input 4' option of the code which allows the specification of the six coordinates of a particle. However, as the acronym of PARMELA, Phase And Radial Motion in Electron Linear Accelerators indicates the code calculates radial motion. Also, the standard space charge routine of the code utilizes cylindrically symmetric space charge meshing, a three dimensional mesh is available but it is 'very slow' and 'very noisy' according to the author[46]. I chose the basic space charge mesh due to its speed and ease of use. And the code only calculates the ϵ_x , ϵ_y and ϵ_z it assumes no transverse coupling effects in the calculations of the emittances. Therefore the calculations for the data presented in this thesis were made by using the six dimensional distribution output. Also the code utilizes off axis expansions for the fields in the linac, this means that the field strengths on the longitudinal axis are used to calculate the field strengths at locations away from the axis. I did not investigate the implications of these effects with an asymmetric distribution since I only believe that a true three-dimensional code would correctly address these issues. I used PARMELA since it is widely used in simulating particle beams and believe that general trends can be observed in the simulations that are of interest. Specifically the increase or decrease

in a quantity is relevant but the exact value of the quantity must be taken with the above caveats.

6.2 Asymmetric Distribution on the Cathode

Using the Monte Carlo methods discussed in previous chapters distributions with $\sigma_x = 1.0$ mm RMS, $\sigma_z = 1.27$ ps RMS (3 ps FWHM RMS) and $\sigma_y = 1.0, 1.25, 1.5, 1.75$ and 2.0 mm RMS were generated. The other dimensions of the beam $\sigma_{x'}$, $\sigma_{y'}$, E_0 and σ_{E_0} can also be specified (z_0 is specified by the injection phase.) In order to specify the $\sigma_{x'}$ and $\sigma_{y'}$, the initial or thermal emittance of the beam at the cathode must be estimated. To determine the thermal emittance of the beam I utilized a derivation from the thesis of David Reis[47], a graduate student from the University of Rochester who was instrumental in the construction of the GTF especially the first laser system. Reis' analysis includes the UV photon energy, 4.7eV, the Fermi energy of the electrons in the cathode, 7 eV, the work function of the copper cathode which is the energy required to liberate an electron from Fermi sea of the copper, approximately 4.5 eV. The analysis also includes the Shottky effect which is the lowering the of the work function value for the copper cathode due to the electric fields present in the gun. For a Gaussian distribution with $\sigma_x = 1.0$ mm and a field level in the gun of 140 MV/m the thermal emittance is $\epsilon_{th} = .19$ mm mrad. Assuming no $x - x'$ correlation and inverting with $\sigma_x = 1.0$ mm gives $\sigma_{x'} = .19$ mrad RMS. I further assumed $\sigma_{y'} = \sigma_{x'} = .19$ mrad RMS. The initial energy of the beam was taken as $E_0 = .65$ eV from the difference between the energy of the UV photons and the Shottky lowered work function and a energy spread of $\sigma_{E_0} = .1E_0$ or 10 percent of the initial energy was arbitrarily chosen. The generated distributions were launched with the conditions given in the previous section. The solenoid was set to provide the field strength of 2.18 KG corresponding to 145 A, or the middle of the range used in the experimental data. Note that the tails of the distributions were not clipped since this would require an elliptic aperture. Therefore the emittances are rather large for the asymmetric distributions.

The six dimensional distribution at the first quadrupole of the doublet was then

dumped and used as input to the algorithm presented in the previous chapters. The algorithm first calculates the initial sigma vector, $\vec{\sigma}(0)_{\text{Initial}}$, by calculating the transverse moments and correlations in the beam distribution. The initial 4-dimensional volume, $V_{4-D,\text{Initial}}$, and the horizontal and vertical emittances, $\epsilon_{x\text{Initial}}$ and $\epsilon_{y\text{Initial}}$, are then calculated from the elements of the sigma vector $\vec{\sigma}(0)_{\text{Initial}}$. These quantities are denoted as "initial" values in reference to those calculated from the quadrupole scan technique. The quadrupole scan is performed by varying the strength of $q2$ which is the second or focusing quadrupole of the doublet. The moments of the horizontal and vertical projections and the $x - y$ correlation in the beam at the screen are calculated for each setting of $q2$. These results along with the lattice settings, the values for $q1$ and $q2$, are used to form the relation $\vec{\sigma}(1) = \tilde{R} \vec{\sigma}(0)_{\text{Calc}}$ which is inverted to give the initial sigma vector $\vec{\sigma}(0)_{\text{Calc}}$. The calculated 4-dimensional volume, $V_{4-D,\text{Calc}}$, and the horizontal and vertical emittances, $\epsilon_{x\text{Calc}}$ and $\epsilon_{y\text{Calc}}$, are determined from the elements of the sigma vector $\vec{\sigma}(0)_{\text{Calc}}$.

6.3 Quantities From The Distribution At The Doublet Entrance

In this section I present quantities which were determined from the distribution at the quadrupole doublet entrance. Since I change the vertical dimensions of the beam on the cathode the 4-dimensional volume and emittances become larger as the beam dimensions on the cathode are changed. The purpose of these simulations is to show the excitations of the transverse coupling terms σ_{13} , σ_{14} , σ_{23} and σ_{24} with the asymmetry of the beam on the cathode. This is evident in the components of the initial sigma vector calculated from the distribution at the entrance to the quadrupole doublet.

In Fig. 6.1 the coupling terms σ_{13} , σ_{14} , σ_{23} and σ_{24} increase with the asymmetry of the distribution at the doublet entrance. This is due to the combination of the asymmetry in the distribution on the cathode and the coupling effects of the rotations from the entrance and exit of the solenoid. The rotations also influence the values of the terms σ_{11} , σ_{22} , σ_{33} and σ_{44} . If there was no rotation of the beam only σ_{33} would

increase with the increase of the vertical width of the beam on the cathode.

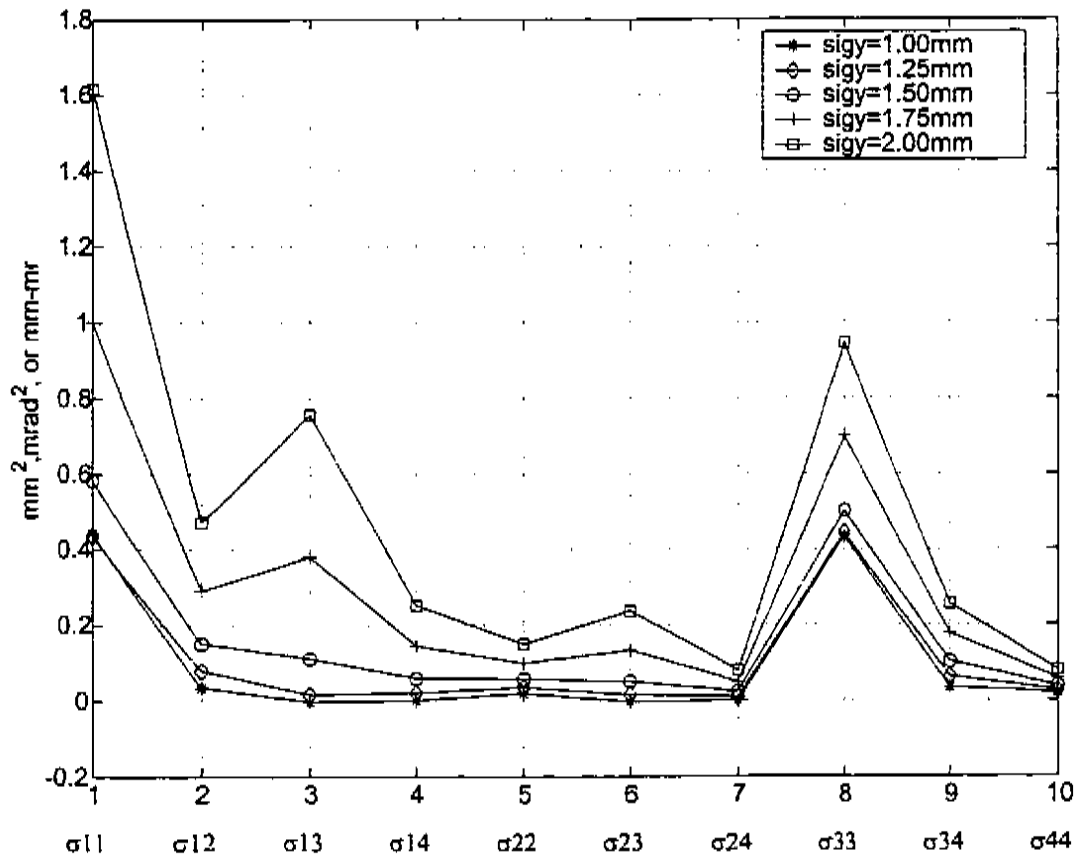


Figure 6.1: Initial sigma vector elements at the doublet entrance for asymmetric distributions on the cathode

Next a plot of the correlation coefficients for the transverse dimensions of the beam r_{12} , r_{13} , r_{14} , r_{23} , r_{24} and r_{34} is presented in Fig. 6.2. The correlation coefficients $r_{ij} = \frac{\sigma_{ij}}{\sqrt{\sigma_{ii}\sigma_{jj}}}$ $i \neq j$ have the property that $|r_{ij}| \leq 1$ this allows one to estimate the magnitude of the couplings and so estimate their effects. The correlation coefficients r_{12} and r_{34} indicate the coupling between $x - x'$ and $y - y'$ respectively. They are nonzero due to focusing of the solenoid. For the symmetric distribution at the cathode these correlation coefficients are equal as expected since the beam is symmetric. Recall these coupling do not influence the deviation between the 4 dimensional volume, V_{4-D} , and $\frac{1}{2}\epsilon_x\epsilon_y$. The values of the correlation coefficients r_{13} , r_{14} , r_{23} and r_{24} can

indicate a deviation between the V_{4-D} and $\frac{1}{2}\epsilon_x\epsilon_y$. These correlation coefficients are all approximately zero for the symmetric distribution $\sigma_y = \sigma_x = 1.00$ mm. Indicating a negligible amount of coupling in the beam. Recall there is always a small amount of correlation in the distribution. However, as shown in the table below, the relative difference between the $V_{4-D,Initial}$ and $(\frac{1}{2}\epsilon_x\epsilon_y)_{Initial}$ of .04% implies the effect of the correlations is negligible. Increasing σ_y leads to an increase in the asymmetry of the initial distribution at the doublet entrance and so the 4 dimensional volume increases. As the asymmetry in the distribution on the cathode is increased, the values for the correlation coefficients r_{13} , r_{14} , r_{23} and r_{24} grow. And the increase in the difference between the $V_{4-D,Initial}$ and $(\frac{1}{2}\epsilon_x\epsilon_y)_{Initial}$ reflects the increase in asymmetry in the distribution on the cathode. This information is contained in Table 6.1.

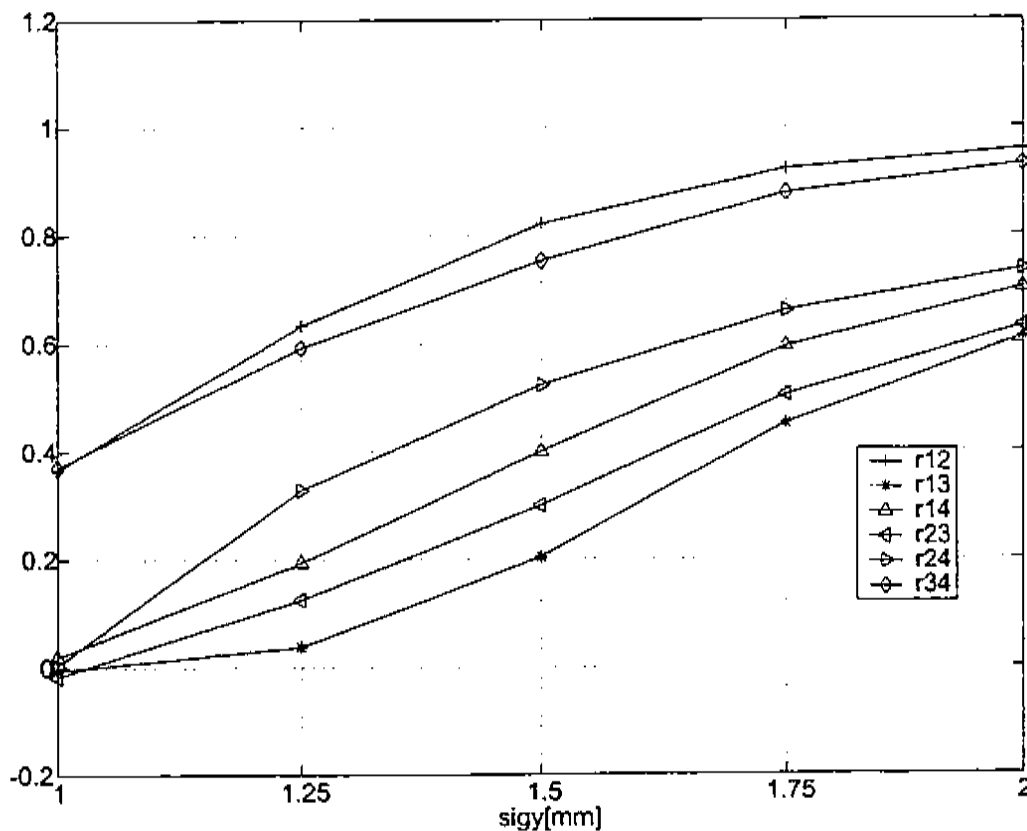


Figure 6.2: Correlation coefficients at the doublet entrance as a function of asymmetry in the initial distributions on the cathode

6.3. QUANTITIES FROM THE DISTRIBUTION AT THE DOUBLET ENTRANCE 147

Cathode Distribution σ_x [mm]	1.00	1.00	1.00	1.00	1.60
Cathode Distribution σ_y [mm]	1	1.25	1.50	1.75	2.00
$V_{4-D,Initial}[(\text{mm} - \text{mrad})^2]$	12.934	13.342	13.523	14.843	16.101
$(\frac{1}{2}\epsilon_x\epsilon_y)_{Initial}[(\text{mm} - \text{mrad})^2]$	12.939	14.200	16.133	20.222	24.434
%Relative Error V_{4-D} vs $\frac{1}{2}\epsilon_x\epsilon_y$	0.037	6.437	19.301	36.238	51.757
$\epsilon_{zInitial}$ [mm - mrad]	5.060	5.625	6.128	7.134	8.280
$\epsilon_{zInitial}$ [mm - mrad]	5.114	5.049	5.265	5.669	5.902

Table 6.1: Normalized 4-D Volume vs projected quantities at doublet entrance for asymmetric distributions on cathode

Since the six dimensions of the particles of the beam distribution are available, the remaining correlation coefficients r_{15} , r_{16} , r_{25} , r_{26} , r_{35} , r_{36} , r_{45} , and r_{46} that characterize the couplings between the transverse and longitudinal dimensions of the beam may be calculated. The longitudinal coordinates are denoted as $5 = E$ and $6 = \phi$, and represent the longitudinal half width of the energy distribution of the beam and the half width of the phase distribution of the beam respectively. These are the 5 and 6 variables that are used in PARMELA. Recall that if the correlation coefficients r_{13} , r_{14} , r_{23} and r_{24} are small the quantity $\frac{1}{2}\epsilon_x\epsilon_y$ is an approximately conserved quantity. This is true since nonzero r_{13} , r_{14} , r_{23} and r_{24} indicate nonzero σ_{13} , σ_{14} , σ_{23} and σ_{24} respectively. These coupling terms must all be zero in order to have $V_{4-D} = \frac{1}{2}\epsilon_x\epsilon_y$. By extension to six dimensions, the correlation coefficients r_{15} , r_{16} , r_{25} , r_{26} , r_{35} , r_{36} , r_{45} , and r_{46} give an indication of the deviation of the V_{4-D} from being a conserved quantity. This occurs if the assumption of no coupling between the transverse and longitudinal dimensions of the beam is violated. In which case the six dimensional volume is the new conserved quantity. In future work I hope to explore the six dimensional volume of the beam. For now I restrict the discussion to the four dimensional space since this space is accessible with the information available from a standard quadrupole scan. I digress to 6 dimensions since that information is available in PARMELA simulations.

As was shown in the case of a 4 dimensionally symmetric beam there will always be a small amount of the couplings σ_{13} , σ_{14} , σ_{23} and σ_{24} in the beam distribution. The same is true for the 6 dimensional case but the degree of couplings can be estimated using the property that $|r_{ij}| \leq 1$ for the correlation coefficients. Note that

the correlation r_{56} indicates the correlation between the longitudinal dimensions of the beam similar to r_{12} and r_{34} for the transverse dimensions and so does not relate to a deviation of the V_{4-D} from being a conserved quantity. A plot and table of the correlation coefficients r_{15} , r_{16} , r_{25} , r_{26} , r_{35} , r_{36} , r_{45} , and r_{46} is given in Fig. 6.3 below.

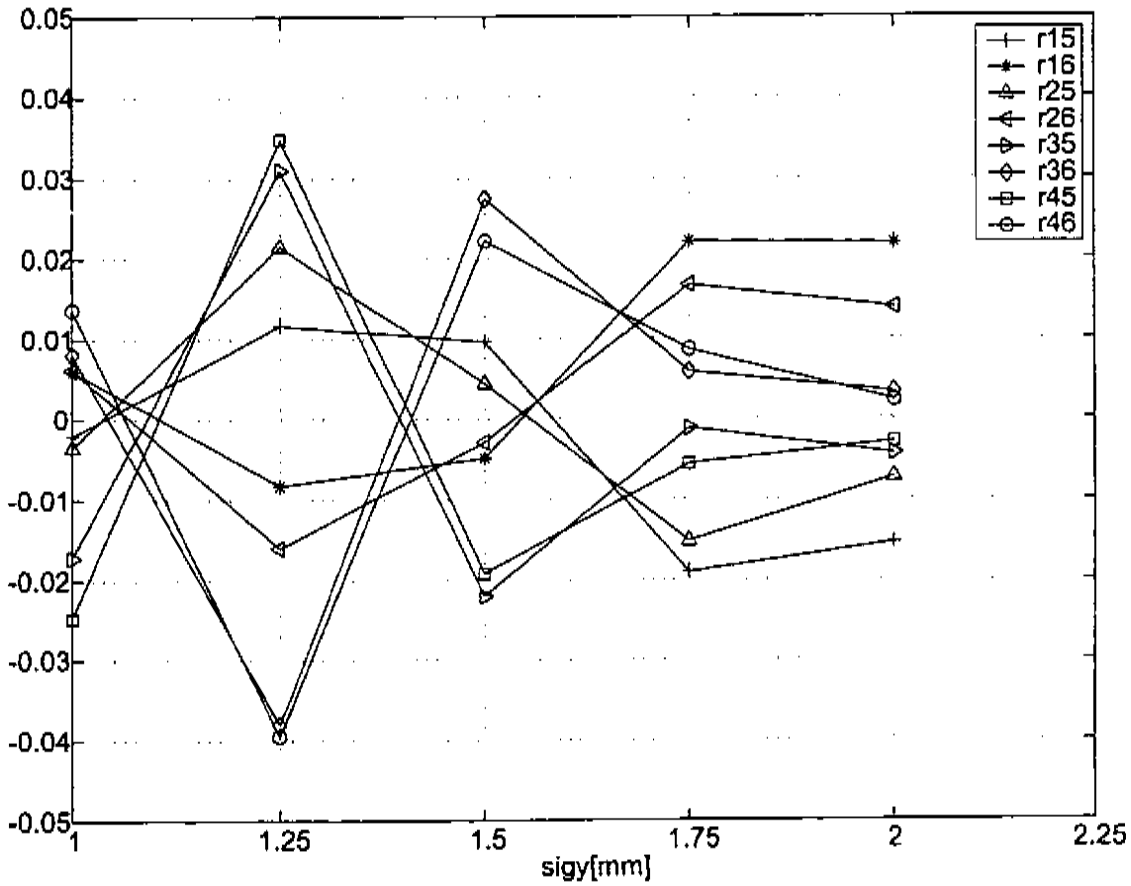


Figure 6.3: Transverse-longitudinal correlation coefficients as a function of asymmetry in the initial distributions on the cathode

6.3. QUANTITIES FROM THE DISTRIBUTION AT THE DOUBLET ENTRANCE 149

Cathode Distribution σ_x [mm]	1.00	1.00	1.00	1.00	1.00
Cathode Distribution σ_y [mm]	1.00	1.25	1.50	1.75	2.00
r_{15}	-0.00207	0.01163	0.00959	-0.01903	-0.01541
r_{16}	0.006	-0.00828	-0.00487	0.02206	0.02186
r_{25}	-0.00355	0.02142	0.00432	-0.0152	-0.00726
r_{26}	0.00616	-0.01602	-0.00291	0.01662	0.01383
r_{35}	-0.0172	0.03095	-0.02204	-0.00121	-0.00436
r_{36}	0.00808	-0.03809	0.02745	0.00581	0.00325
r_{45}	-0.02474	0.03476	-0.01922	-0.00559	-0.00289
r_{46}	0.01362	-0.03948	0.02216	0.00862	0.00225
r_{56}	-0.87518	-0.86671	-0.87637	-0.86189	-0.84687

Table 6.2: Transverse-Longitudinal Correlation coefficients for asymmetric distributions on the cathode

As indicated in Fig. 6.3 and the Table 6.2 above the correlation coefficients r_{15} , r_{16} , r_{25} , r_{26} , r_{35} , r_{36} , r_{45} , and r_{46} are all much less than one. This provides an indication that the four dimensional volume is close to being a conserved quantity since the couplings between the transverse and the longitudinal dimensions are weak. Also there is no clear correlation between the increase in the transverse asymmetry in the beam and the correlation coefficients r_{15} , r_{16} , r_{25} , r_{26} , r_{35} , r_{36} , r_{45} , and r_{46} . Unlike the clear trend in the correlation coefficients r_{13} , r_{14} , r_{23} , and r_{24} with the increase in the asymmetry in the initial distribution. This indicates that there is no clear coupling between the transverse and longitudinal dimensions of the beam.

For comparison a plot of all of the correlation coefficients is presented in Fig. 6.4 below. From this plot it is clear that the correlation coefficients r_{15} , r_{16} , r_{25} , r_{26} , r_{35} , r_{36} , r_{45} , and r_{46} that characterize the coupling between the transverse and longitudinal dimensions of the beam are the smallest. Therefore of all of the couplings these will have the least effect if they are ignored.

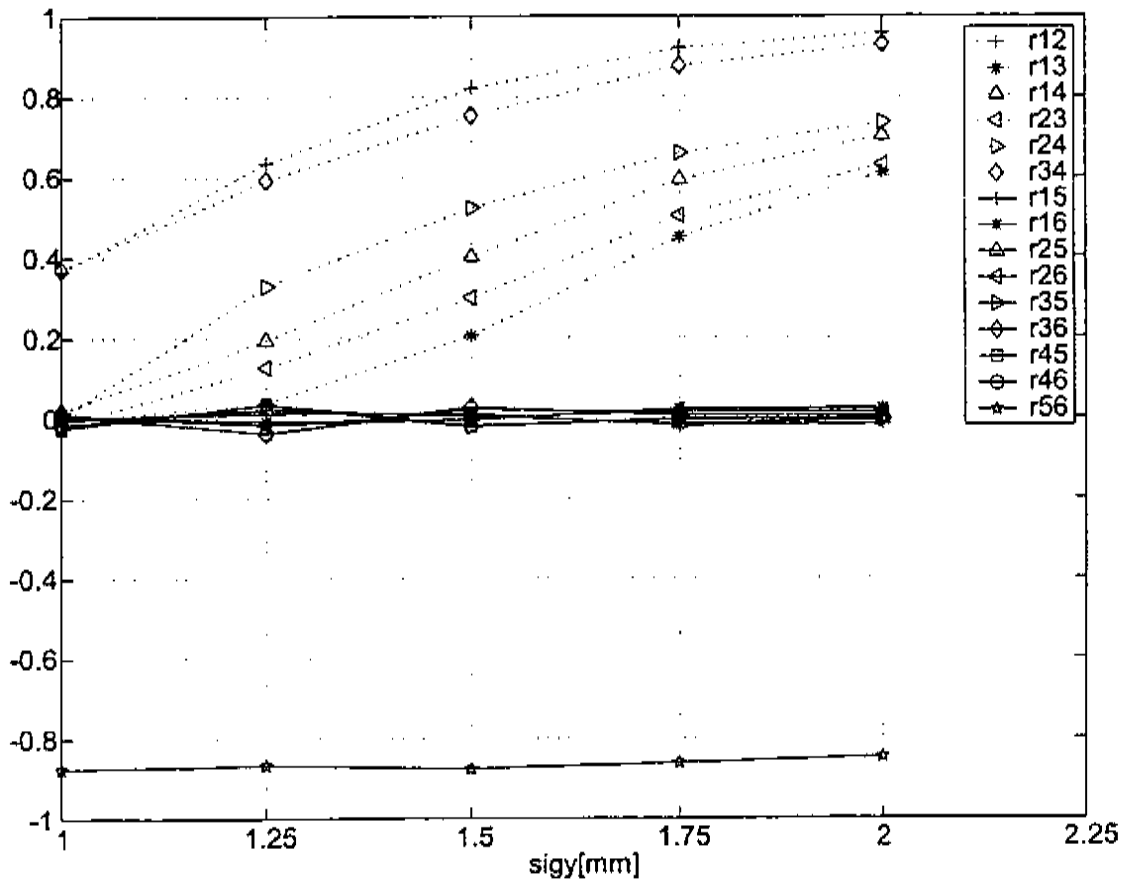


Figure 6.4: All correlation coefficients as a function of asymmetry in the initial distributions on the cathode

6.4 Quantities From 4-D Quadrupole Scan

In the laboratory environment the six dimensional distribution information is not available. In the laboratory the moments for the horizontal and vertical projections and the $x - y$ correlation of the electron beam distribution on the screen for each of the quadrupole settings of a quadrupole scan are available. From this information the correlation coefficient $r_{13} = \frac{\sigma_{13}}{\sqrt{\sigma_{11}\sigma_{33}}}$ can be formed. In this section the six dimensional distribution was used as input to the quadrupole scan algorithm developed and discussed earlier. Recall the algorithm performs a quadrupole scan using the second quadrupole, $q2$, of the doublet. The moments of the projected horizontal and vertical distributions and the $x - y$ correlation at the screen location are calculated for each setting of $q2$. The quantities σ_{11} , σ_{33} , σ_{13} and r_{13} versus k (the strength of $q2$) are plotted in Figs. 6.5-6.8 below.

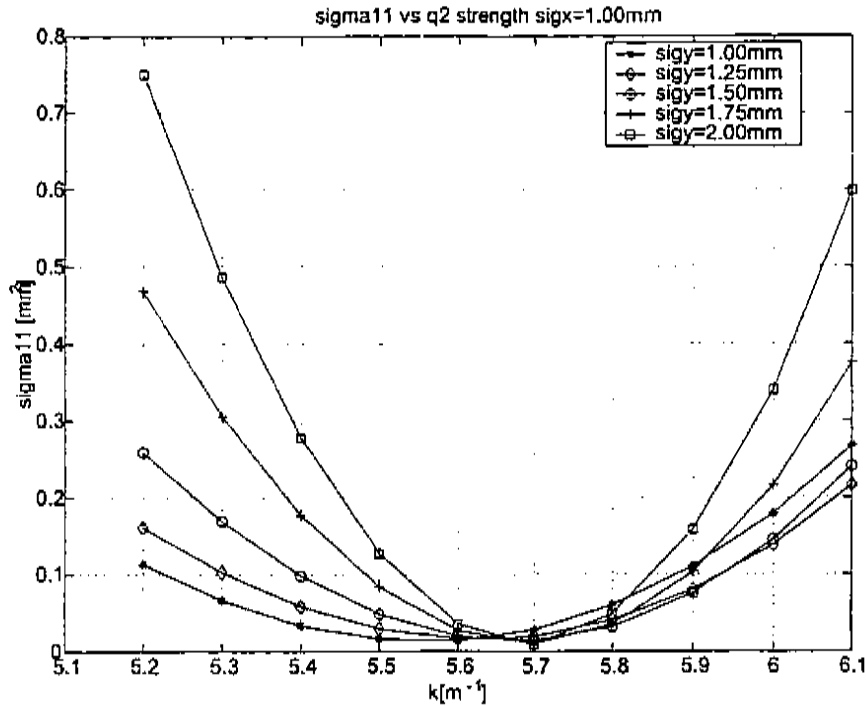


Figure 6.5: Sigma11 vs q2 strength for different asymmetry in the initial distribution on the cathode

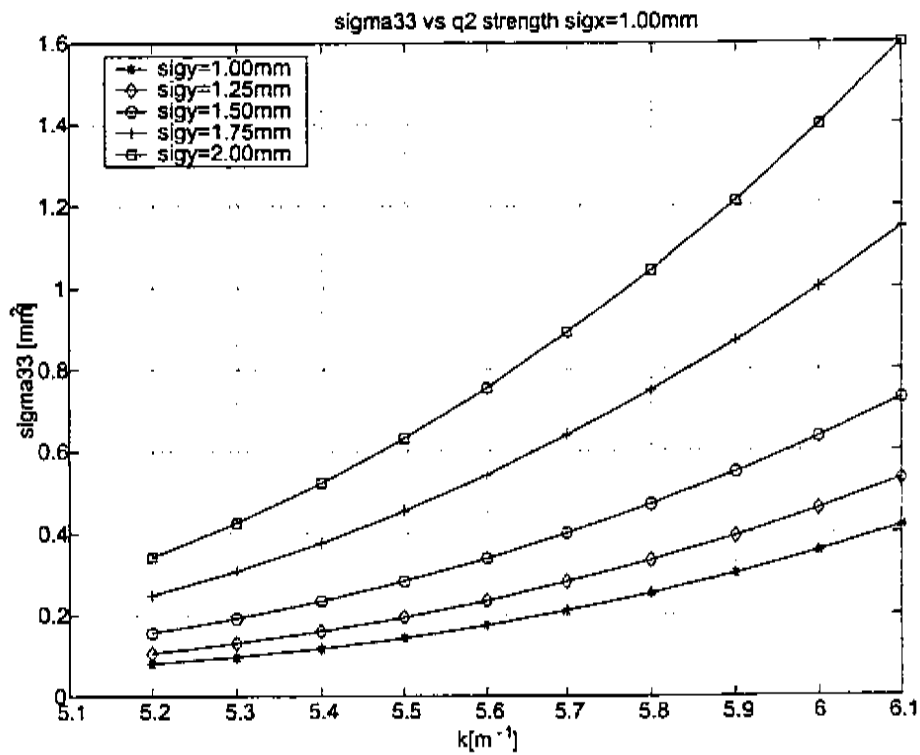


Figure 6.6: Sigma33 vs q2 strength for different asymmetry in the initial distributions on the cathode

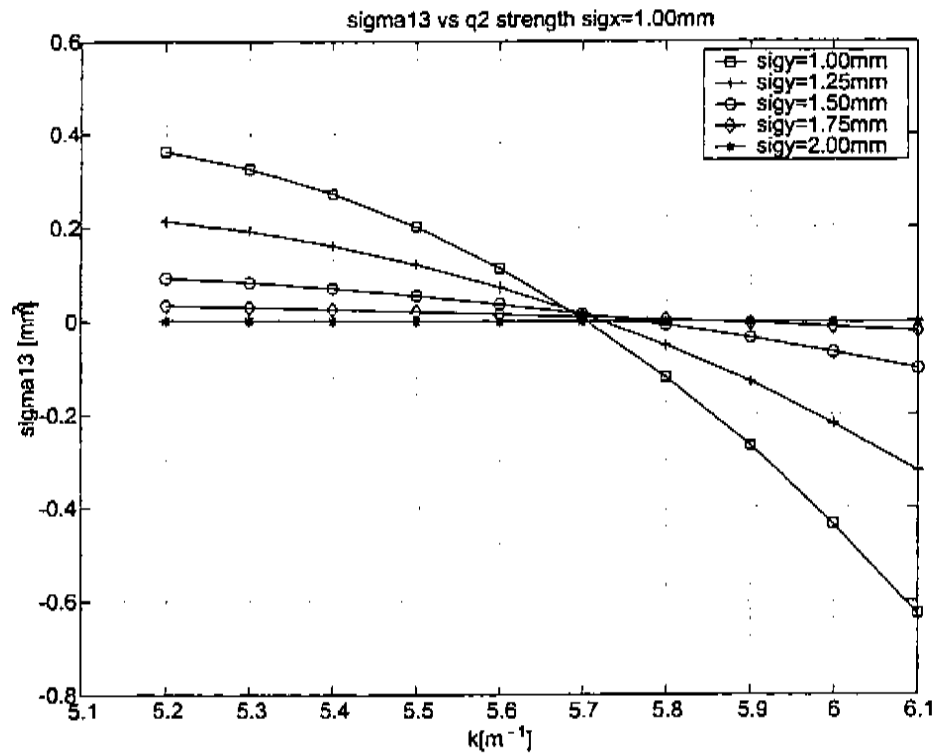


Figure 6.7: Sigma13 vs q2 strength for different asymmetry in the initial distributions on the cathode

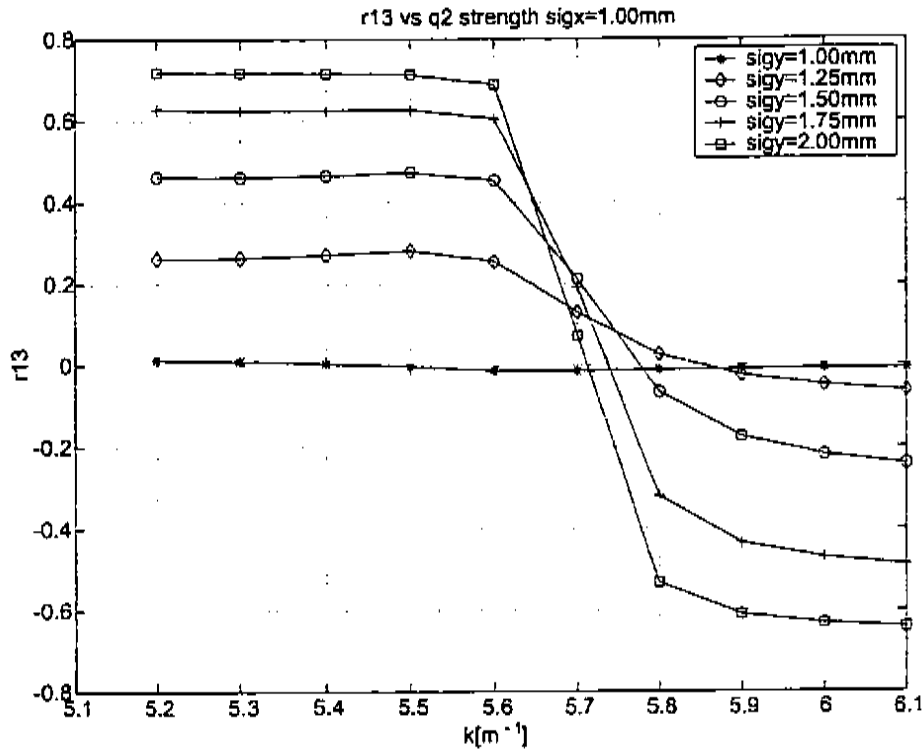


Figure 6.8: r_{13} vs q_2 strength for different asymmetry in the initial distributions on the cathode

The plots for the horizontal and vertical projections, Figs 6.5 and 6.6 behave as expected. As the symmetry of the initial beam on the cathode is increased the projected emittances increase. For the horizontal projections the curves become steeper as the asymmetry is increased, the flatter the curve the lower the emittance. And similarly for the vertical dimension. As shown in previous chapters nonzero $x - y$ correlation, σ_{13} , at the screen in a quadrupole scan is an indication of the presence of coupling in the beam at the quadrupole doublet entrance. In the plot of the σ_{13} correlation versus q_2 strength, σ_{13} increases as the asymmetry in the initial beam is increased. The correlation coefficient r_{13} also increases as the asymmetry of the initial distribution increases and $|r_{13}| \leq 1$ as expected. Therefore the σ_{13} and r_{13} are both clear indicators of the strength of the coupling in the input beam of the quadrupole scan. Also evident from both plots is that the beam becomes upright or

Cathode Distribution σ_x [mm]	1.00	1.00	1.00	1.00	1.00
Cathode Distribution σ_y [mm]	1.00	1.25	1.50	1.75	2.00
$V_{4-D,Initial}[(\text{mm mrad})^2]$	12.934	13.342	13.523	14.843	16.101
$V_{4-D,Calc}[(\text{mm mrad})^2]$	12.934	13.340	13.518	14.829	16.070
$(\frac{1}{2}\epsilon_x\epsilon_y)_{Calc}[(\text{mm mrad})^2]$	12.939	14.200	16.133	20.222	24.434
ϵ_{xCalc} [mm mrad]	5.060	5.625	6.128	7.134	8.280
ϵ_{yCalc} [mm mrad]	5.114	5.049	5.265	5.669	5.902
%error V_{4-D}	0.003	0.012	0.035	0.097	0.188
%error $(\frac{1}{2}\epsilon_x\epsilon_y)_{Calc}$	0.037	6.437	19.301	36.238	51.757

Table 6.3: Normalized 4-DVol initial, calculated and projected quantities for asymmetric distributions on cathode

crosses through the vertical during the quadrupole scan since both plots pass through zero. The plots of σ_{11} and σ_{33} versus $q2$ strength also show the effects of the rotation. While only the vertical dimension of the initial beam on the cathode is changed, both the horizontal and vertical dimensions of the quadrupole scans increase with increasing vertical width of the initial beam on the cathode.

In Table 6.3 above the values for the initial normalized V_{4-D} calculated from the initial six dimensional distribution at the doublet entrance are by denoted $V_{4-D,Initial}$. The normalized V_{4-D} and associated projected quantities calculated from the second moments of the screen from the quadrupole scan are denoted $V_{4-D,Calc}$, $(\frac{1}{2}\epsilon_x\epsilon_y)_{Calc}$, ϵ_{xCalc} and ϵ_{yCalc} . And the relative errors are calculated using the following relations:

$$\begin{aligned} \%error V_{4-D} &= 100\% \frac{(V_{4-D,Initial} - V_{4-D,Calc})}{V_{4-D,Initial}} \\ \%error (\frac{1}{2}\epsilon_x\epsilon_y)_{Calc} &= 100\% \frac{(\frac{1}{2}\epsilon_x\epsilon_y)_{Calc} - V_{4-D,Initial}}{V_{4-D,Initial}} \end{aligned}$$

The two 4 dimensional volume calculations agree quite well as shown by the quantity %error V_{4-D} . In comparison the quantity %error $(\frac{1}{2}\epsilon_x\epsilon_y)_{Calc}$ shows a clear difference between the four dimensional volume at the quadrupole doublet entrance, $V_{4-D,Initial}$, and the quantity $(\frac{1}{2}\epsilon_x\epsilon_y)_{Calc}$. The difference increases with asymmetry in the initial distribution on the cathode. This series of simulations demonstrates the ability of

the algorithm to reliably reproduce the 4 dimensional volume at the entrance to the quadrupole doublet using only information available at the screen of the quadrupole scan.

Finally I generated distributions in which the σ_x and σ_y dimensions of the beam differed by up to a factor of 1000 and there was no appreciable signs of asymmetry in the distributions at the entrance to the quadrupole doublet. There were no effects on the V_{4D} or the projected emittances. I believe this is due to the extreme acceleration of the electrons in the gun. The beam is accelerated from .65 eV at the cathode to about 6 MeV at the gun exit so $\beta\gamma$ increases by a factor of 2×10^6 . Any reasonable asymmetry in the transverse momentum of the initial distribution on the cathode is washed out by this effect.

The simulations presented in this chapter show the excitation of the transverse coupling terms σ_{13} , σ_{14} , σ_{23} and σ_{24} and the corresponding correlation coefficients r_{13} , r_{14} , r_{23} and r_{24} with the increase of the asymmetry of the initial beam distribution on the cathode. This is expected since, as shown in the previous chapter, asymmetry in the beam before a rotation leads to excitation of the transverse coupling coefficients. Also shown is that with respect to the transverse correlation coefficients the transverse-longitudinal correlation coefficients are negligible for changes in the asymmetry of the initial distribution on the cathode. This indicates that the 4-D volume is approximately conserved for the system parameters chosen. Finally the simulations demonstrate that the 4-D volume measurement algorithm can reliably reproduce the initial 4-D volume at the entrance to the quadrupole doublet regardless of the transverse coupling in the incident beam.

Chapter 7

Measurements

In this chapter I will discuss electron beam measurements made at the GTF facility. The particular laser and accelerator system parameters used in the measurements are discussed first. The raw results are presented which clearly show the presence of large values for the correlation coefficient r_{13} indicating the presence of strong coupling in the electron beam. Therefore the projected emittances are non-conserved quantities as shown in previous chapters. The data reduction technique to enable the determination of all of the moments of the data at the screen is discussed. The reduction of the data presented unforeseen problems due to the real world limitations on the resolution of the measurement system. A solution to this problem is found by including additional information about the 4-D distribution. The reduced data for measurements of the electron beam are presented for five different solenoid settings and show the variation in the non-conserved quantities ϵ_x , ϵ_y and $\frac{1}{2}\epsilon_x\epsilon_y$ and the conservation of the four dimensional volume, V_{4-D} , within the uncertainty of the measurement process. Also the relation $V_{4-D} \leq \frac{1}{2}\epsilon_x\epsilon_y$ is shown for all of the data. This implies that the electron beam is up to 10 times brighter than would be found using the non-conserved quantities.

7.1 System Parameters

The system parameters include those from both the laser and accelerator systems. The goal for the GTF laser system was to produce a UV laser pulse with transverse profile which was as close to uniform as possible and a longitudinal distribution of 10ps "flat top" FWHM and sufficient UV energy to produce InC of charge from the copper cathode. Due to a combination of low quantum efficiency of the copper cathode and financial constraints on laser system development these goals were never met. The amount of available UV from the laser is a function of the output energy of the regenerative amplifier, the conversion efficiency of the two nonlinear crystals which convert the IR into green and the green into UV, the amount of shaping of the longitudinal and transverse distributions which is performed on the laser pulses and the transport losses of the system from the laser room to the cathode. The laser system produced beams which are Gaussian in both transverse and longitudinal dimensions. Transverse shaping of the laser pulse consisted of spatial filtering and passing the resulting beam through an aperture to "clip the tails" of the Gaussian distribution. Longitudinal shaping consisted of varying the amount of compression after the regenerative amplifier.

Typically the laser was optimized to produce the maximum amount of UV energy. This meant a compromise between the goals of a uniform beam both transverse and longitudinal and the laser system constraints. The regenerative amplifier output was limited to 8 mJ to prevent optical damage to the amplifier. In order to maximize the conversion efficiency of the nonlinear crystals, a beam with small transverse and longitudinal dimensions is required. A telescope was used to reduce the transverse dimensions of the IR beam, $\sigma_r < 1.0$ mm, that was presented to the first nonlinear crystal which produced a green beam with similar transverse dimensions. The output from the first crystal entered the second crystal directly with no mirrors or lenses in between the crystals. The second crystal produced a UV beam with similar transverse dimensions. The telescope and crystal orientations were tuned to produce the largest amount of UV without damaging the crystals. After the second crystal another telescope was used to reduce the UV beam to a small focus where a .4 mm diameter

pinhole was placed to spatially filter the UV. Another telescope was used to produce a collimated beam with $\sigma_r = 1.0$ mm. A 2.0 mm diameter aperture was used to remove the tails of the distribution. The aperture was relay imaged to cathode. In order to reduce the longitudinal dimensions of the beam the compressor was set for maximum compression. This produced a UV pulse of 3 ps FWHM measured with a model FS300 Hadland Steak camera. After the transport system, 120 μ J of energy was available at the laser table in linac vault. From an emittance compensation view point, the electron beam pulse should be a 10 ps flat top[1]. By changing the amount of compression of the IR pulse its length can be increased. But any lengthening of the pulse drastically reduced the amount of UV produced by the nonlinear crystals.

The transversely spatially filtered and clipped UV pulse was directed onto the cathode at normal incidence by using an mirror in vacuum upstream of the emittance compensation solenoid. In order to determine if the UV pulse was injected at the desired RF phase in the gun a Shottky scan was utilized. This consists varying the injection phase of the UV until photoelectrons are produced from the gun as detected by either a Faraday cup or toroid located after the solenoid. The injection phase is changed so that the amount of photoelectrons emitted from the gun is reduced until no photoelectrons are emitted from the gun. This phase is the "zero crossing" which occurs when the photoelectrons from the UV pulse are emitted at the wrong RF phase for acceleration and thus do not exit the gun. The injection phase is then raised from the zero crossing to 60° . The choice of 60° believed to produce the best emittance[48]. The level of the RF fields in the gun was set as high as possible in order to accelerate the beam to relativistic velocities as quickly as possible to reduce the effects of space charge[49]. The peak fields in the gun were estimated to be about 140 MV/m as measured by a field probe. This produced an electron beam with an energy of about 6 MeV at the injection phase of 60° . The goal was to produce 1 nC of charge, however due to low quantum efficiency of the cathode and the available UV pulse energy only 200 pC could be produced at the desired gun injection phase for the experimental data presented. The solenoid at the gun exit focuses the beam before it is injected into the single 3-m SLAC linac section. The linac gradient was set to produce an electron beam with an energy of 30 MeV and the linac was phased

to produce the minimum energy spread of 0.1%. Both quantities were measured on the spectrometer after the linac.

The data presented in this thesis consists of a small fraction of what was collected over many runs. The majority of data was very problematic due to difficulties with the cathode, the laser or both. In the interest of generating 1nC of charge the original cathode was laser cleaned as discussed in detail in reference[40]. Unfortunately this led to a cathode with many small pits and uneven emission. The replacement cathode was not perfect either. During the final stages of machining and polishing of the copper surface a small mound was left in the mechanical center of the cathode from the machining process. The defect was clearly visible to the naked eye. It was determined that this imperfection was not a problem from an RF point of view and due to time constraints the cathode was installed. A common philosophy regarding defects in photon optics such as mirrors and lenses is: "if you can't see it don't worry about it, if you can see it replace it" [50]. Unfortunately this was not followed and the result was that if the laser was aligned on the defect of the cathode for certain quadrupole settings the defect produced an electron beam with a hole in the center from lack of charge. This effect was clearly visible on the YAG screen. An image of the beam with the effect is presented below. In the image dark regions represent the lack of electrons and light regions represent the presence of electrons. Clearly there is no beam in the center of the ring.

If the laser was moved horizontally partially off of the center of defect the electron beam distribution became non uniform, the hole moved to the side of the electron beam distribution which produced an unsymmetrical distribution. If the center of the laser spot on the cathode was moved horizontally about one beam diameter, 1 mm, from the center of the defect the effect of distorting the uniformity of the electron beam was minimized. Ideally one would run with the laser aligned on the electrical center of the cathode in order to avoid non-uniformities in the accelerating fields in the gun. Due to the defect this was not possible. The data presented in this thesis consists of five quadrupole scans performed with the center of laser spot one beam diameter horizontally off of the mechanical center of the cathode. The quadrupole scans were performed at the following solenoid currents 140, 142, 145, 147 and 150



Figure 7.1: Image of beam illustrating the cathode defect

amperes. The solenoid current was changed in order to determine the optimum setting for attempted emittance compensation. The range of the solenoid current was limited. If the current to the solenoid was too low or high, there was loss of charge in the transport system due to under focusing or over focusing of the electron beam. The practical range for the solenoid current was about ten amperes.

7.2 Data Collection Method

The emittance of the electron beam was measured using the quadrupole scan technique discussed in previous chapters. Between the linac and spectrometer there is a quadrupole doublet (which consists of a pair of quadrupoles separated by a drift space), a drift section and screen that were used to measure the emittance. The first quadrupole of the doublet, q_1 , was horizontally de-focusing. The second quadrupole, q_2 , was horizontally focusing and was used as the scanning quadrupole. A screen could be remotely inserted into the electron beam path to form an image of the electron beam. The screen consisted of a YAG crystal .5mm thick mounted normal

to the electron beam axis. The YAG crystal produces visible light when struck by electrons. A polished aluminum reflector mounted at 45° to the electron beam axis immediately followed the YAG crystal. The reflector directed the light produced from the crystal downwards through a view port from the vacuum of the beamline to air outside of the beamline. The light was then reflected by a 45° mirror to a Pulnix TM-7 8-bit CCD camera that produced an image size of 640×480 pixels. The camera was equipped with a VZM-750 variable zoom microscope objective from Edmunds scientific. The microscope objective produced high magnification and a flat field of view of the image from the YAG screen. The intensity of the image of the electron beam that was sent to the CCD imager of the camera was regulated by a set of remotely controlled crossed polarizers. This eliminated the depth-of-field variation encountered with variable aperture systems used in typical camera lens systems.

The video signals from the camera were fed by RG58 75 Ohm cable into an 8-bit DT-3152 Data Translation frame grabber. The camera and frame grabber both required 75 Ohm termination. The camera and the frame grabber were synchronized to the electron beam by triggering them both using timing signals from the laser timing system. The camera and frame grabber system was calibrated by taking an image of one of a series of 1.00 mm diameter fiducial holes that were machined into the edge of the YAG crystal holder and determining the number of pixels across the diameter of the hole in the horizontal and vertical directions. For the data presented here there were 75 pixels for 1.00 mm or $13.3 \mu\text{m}$ per pixel in both the horizontal and vertical dimensions. I conservatively estimated the resolution of the system to be three pixels or $40 \mu\text{m}$.

The quadrupole scans required optimization of the electron beam. This was achieved by first adjusting the strength of q_1 and q_2 to produce a small spot that was as round and as uniform as possible on the YAG screen. Then q_2 was tuned so that the beam could be brought through a horizontal minimum for the quadrupole scan. In order to avoid aberrations in the quadrupole fields, the electron beam should pass through the center of the quadrupoles. If the beam trajectory is not along the magnetic center of the quadrupole the beam spot on the screen will not remain in the same position as the strength of the quadrupole is changed. In order to center

the beam through the quadrupoles steering coils upstream were adjusted while the strength of each of the quadrupoles was varied and the beam was viewed on the YAG screen. When the beam remained as close to stationary as possible for variations in the strength of q_1 and q_2 separately, both quadrupoles were standardized to remove the effects of hysteresis. The standardization was accomplished by ramping the current to the quadrupoles from zero to ten amperes and back down to zero amperes ten times. The quadrupoles were adjusted again to produce the smallest uniform spot and the values for the currents were noted. The quadrupoles were standardized again and returned to the previously noted values. If no more optimizations were deemed necessary images of the smallest spot were examined with the frame grabber for saturation effects in the image.

Saturation in the pixel values of the camera occurs when the intensity of the image of the electron beam is $\geq 255 = 2^8 - 1$. The value of 255 is the maximum of the 0–255 grey scale range of values for the 8-bit frame grabber and camera. If the image from the camera is saturated all values of intensity that are greater than or equal to that value which is mapped into 255 are set to 255 by the analog-to-digital, A/D, converter of the frame grabber. If this occurs there is loss of intensity resolution and since the width of the spot is calculated using the intensity of the image, saturation will lead to erroneous results for the width of the beam spot. The brightest spot in the image occurs when the beam is focused to the smallest possible spot. The polarizers and frame grabber A/D maximum voltage level for the camera signal, or reference value, are adjusted so that the brightest setting of the quadrupole scan has a peak value less than 255. Then the quadrupole scan will be free of saturation since the beam spot is larger and the intensity of the image is less bright at quadrupole settings above and below that which produces the brightest beam image. A "lineout" or single line through the brightest part of the image is examined for saturation using the frame grabber software. A sample of such a lineout is presented below. In the lineout the maximum value is less than 255 so the system is not saturated. The frame grabber A/D converter has two other features, a gain and offset. The gain is an amplification factor used in the A/D conversion to enable magnification of low signal levels. For all of the measurements the gain was set to zero, i.e. there was no

gain applied since there was usually plenty of signal available from the camera. The offset is used to establish the low range of the camera signal or the voltage level that is mapped to zero. If this level is set too high the baseline of the image will appear totally flat. For example in the lineout below if the offset were set such that voltages corresponding to 50 on the grey scale were zero then all values less than 50 will be mapped into zero by the A/D. This would result in a flat line for values less than or equal to 50, and lead to a truncation of the low voltage part of the image. Ideally the offset is adjusted so that there is a small amount of noise from the camera present in the edges of image away from the beam spot. In the lineout below the vertical axis corresponds to the intensity of the signal and the horizontal axis is the pixel number. The reference level could have been set slightly lower, this would increase the span of the A/D converter or the usable range. However, the image was clearly not saturated and the low voltage end of the image was not truncated as evidenced by the noise floor.

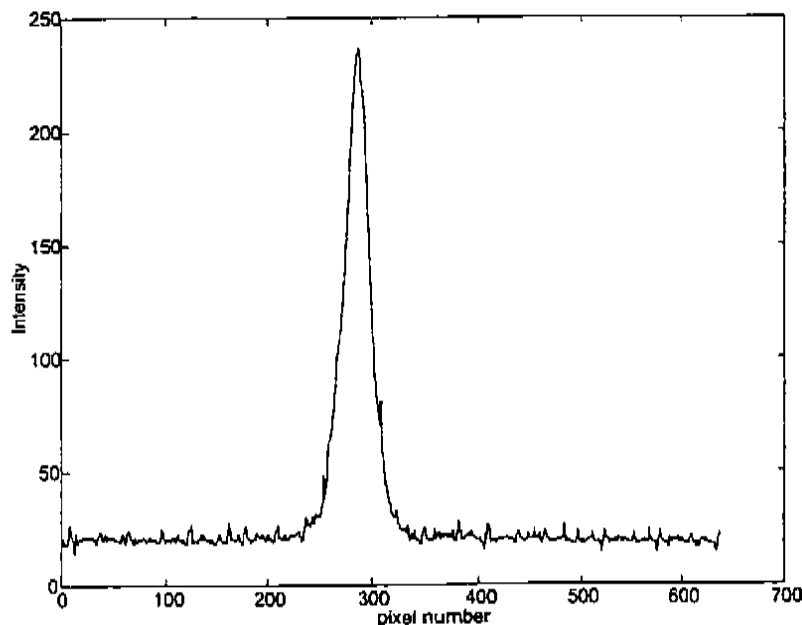


Figure 7.2: Line out through the peak in a typical image of the beam (background not subtracted). Horizontal axis is pixel number and vertical axis is intensity.

Once the polarizers and A/D values were properly set quadrupole 2, q2, was standardized again. The current was raised from zero to .5 amperes below the value that produced the smallest spot on the screen. Five images of the screen were taken with the laser on and one with the laser off, forming five shot images and one background image. The current in q2 was raised by .1 ampere and again five shot images and one background image were taken. This process was repeated for ten .1 ampere steps of the current of q2. The gun phase, linac phase, beam energy after the linac and photoelectron charge were checked before each quadrupole scan. This was repeated for five solenoid currents. The solenoid was changed in order to determine the optimum setting for emittance compensation. There were limitations to the range of the solenoid currents. If the current to the solenoid was too low or high, there was loss of charge in the transport system due to under focusing or over focusing. The practical range for the solenoid current was about ten amperes. For the data presented the solenoid was set at the following settings: 140, 142, 145, 147 and 150 amperes.

7.3 Data Reduction Technique

The first and second moments of the horizontal and vertical projections and the $x - y$ correlation of the electron beam distribution must be determined in order to calculate the four dimensional trace space volume of the electron beam which is being measured. Calculation of the moments and $x - y$ correlation of the electron beam distribution requires the determination of the portion of the image that represents the photoelectron distribution. Three effects must be taken into account in analyzing the images of the screen formed by the electron beam.

First the distribution of electrons which strike the screen contain electrons which are generated from the copper surfaces of the gun and linac section by the accelerating fields present in these RF structures. This current known as "dark current" is present regardless of the presence of the laser pulse on the cathode. Some of the charge generated by the large electric fields in the gun is lost in the gun and linac because it may be of the wrong energy and phase to be accelerated and transported to the screen. A portion of the dark current will make it to the screen and this charge must

be excluded from the photocurrent. During the quadrupole scan five shots, images of the screen are taken with the laser on, and one background, the laser off, are taken at each of the quadrupole settings. The background images contain the dark current. To exclude the dark current from the measurements, the background image is subtracted from the corresponding shot images when the data is analyzed. This is effective under the condition that the dark current is constant during the measurement process.

The only violation of this assumption that was observed during the measurements occurred when there was a breakdown of the fields in the gun or linac that produces an arc which leads to a release of an increased amount of dark current. When an arc is generated in the gun there is an increase in the RF power reflected back to the klystron which feeds the gun, there is also an increased amount of charge released into the accelerator system. Machine and personnel protection systems connected to the accelerator detect the increase in reflected power and charge and respond by removing the triggers to the klystrons effectively shutting off the RF power to the system. To restore the RF power the system must be manually reset and the phases for laser injection to the gun and the linac must be re-established. If this occurred during a quadrupole scan the scan would be terminated and the measurement would be restarted from the initial values.

The second effect that must be considered when analyzing the experimental data is due to radiation produced during the operation of the accelerator. Pixels in the CCD imager of the camera that are exposed to radiation can become saturated or close to saturated, they will have noticeably larger intensity values than their nearest neighbors. Shielding the camera with lead reduces the occurrence of these "hot pixels" but they cannot be completely eliminated. In order to eliminate these pixels the background subtracted image is searched for pixels which are more than 5 times the intensity of each of the eight nearest neighbors or were equal to 255. For pixels along the boundary of the image the five nearest neighbors are utilized. When a pixel is found which satisfies the criterion it is set to the linear average of its nearest neighbors.

The third effect is due to the random noise in the CCD camera itself. The determination of the lower value of the A/D conversion discussed above required a baseline of noise to ensure that the distribution was not improperly truncated. The random

nature of the noise leads to nonzero values after background subtraction in the regions of the image where there is no charge present as seen in Figs 7.3 and 7.4. Pixels that return negative values after the background subtraction process are set to zero. The nonzero values for the pixels in the region outside that portion of the image that is due to the photocurrent lead to increase in the values of the calculated RMS widths. The equation for the calculation of the second moment of the distribution is:

$$\sigma_{ii} = \tilde{i}^2 = \frac{\sum_x \sum_y (i - \tilde{i})^2 I(x, y)}{\sum_x \sum_y I(x, y)} \quad i = x \text{ or } y. \quad (7.1)$$

Where (\tilde{x}, \tilde{y}) is the location of the centroid of the beam distribution. Any of the positive non-zero values for $I(x, y)$ of the image contribute to the sums. The factor $(i - \tilde{i})^2$ provides a weight that increases quadratically with distance the first moment of the distribution or centroid, \tilde{i} . The positive non-zero values due to random noise in the regions where there is no beam, known as "outliers", can contribute strongly to the second moment of the distribution. For example for a distribution centered in the 640x480 pixel CCD imager, with centroid location (320, 240), a pixel with intensity say $I = 250$ located 1 pixel from the centroid will contribute $(i - \tilde{i})^2 I(x, y) = (1)^2(250) = 250$ to the sum. A pixel at the horizontal edge of the image with intensity of say $I = 1$ will contribute $(i - \tilde{i})^2 I(x, y) = (640 - 320)^2(1) = 102,400$ to the sum. This is a factor of 410 times larger contribution to the second moment for the smallest possible non-zero pixel intensity. Clearly one would desire to include only non-zero pixels that represent the electron beam and not random noise in the image. Two solutions to the problems of outliers are available if only the moments of the projections are desired. Fitting the projected data to a Gaussian distribution would solve this problem but since the laser is specifically shaped to be non-Gaussian I believe the assumption of a Gaussian distribution not to be guaranteed true. Also, if only the moments for the projections of the horizontal and vertical dimensions were to be determined, the outliers in the projections could be eliminated by estimating where to set the projected distributions to zero. This process is also known as clipping the tails of

the distribution. However the $x - y$ correlation is desired and the calculation of this moment requires the full two dimensional distribution and so cannot be obtained from the projections. And the $x - y$ correlation is also susceptible to the problem of outliers.

In order to fulfill the need to calculate the $x - y$ correlation, an algorithm to clip out the distribution above a particular threshold intensity value was developed. The basic concept is to treat the intensity plot of the image as a three dimensional distribution similar to a mountain peak rising from a flat plateau. If intensity is associated with altitude then there exist unique closed contour lines for the various values intensity or altitudes around the peak in the distribution down to the level of the plateau. This is true provided the distribution does not have valleys located in the interior. The goal is to identify the intensity value for the plateau and use this value to locate the corresponding contour line nearest the edge of the peak in the distribution. Once this is accomplished the pixels outside of the chosen contour line are set to zero and the threshold intensity is subtracted off from the pixels in the interior of the contour line. This algorithm is accomplished as follows. The beam does not fill the image so the intensity values in a strip that is 20 pixels wide around the edges of the image is averaged to determine the threshold value. Next the routine to determine the contour line is called. First the peak or mode in the distribution is found and the vertical index is held constant and the horizontal index is increased until the threshold intensity is found, this starting pixel location is logged. Next this location is treated as the center and proceeding in a clockwise direction the eight nearest neighbors are sampled to find the next occurrence of the threshold value. There must always be at least one pixel that exceeds the threshold value in the nearest neighbors to keep the contour line next to the peak in the distribution. The pixel that is found to have the threshold value is logged and forms the new center and the above process is repeated. In this way a contour line corresponding to the threshold value is followed around the distribution until the starting pixel is located and the process is stopped. Next all of the pixels outside of the contour line are set to zero and the threshold value is subtracted from the pixels inside the contour line. The subtraction of the threshold value is done since I believe only values above the threshold or noise floor

are relevant to the calculations of the beam distribution moments. Trying to estimate the distribution below the noise floor would be impossible. Typically the threshold value is small < 15 for all of the data. A typical background subtracted image at the setting of q_2 which produced the smallest spot in the quadrupole scan is presented in Fig. 7.3. The vertical axis is pixel intensity, the horizontal axis (x) is on the right with a range of 1 to 640 and the vertical axis (y) is on the left with range of 1 to 480.

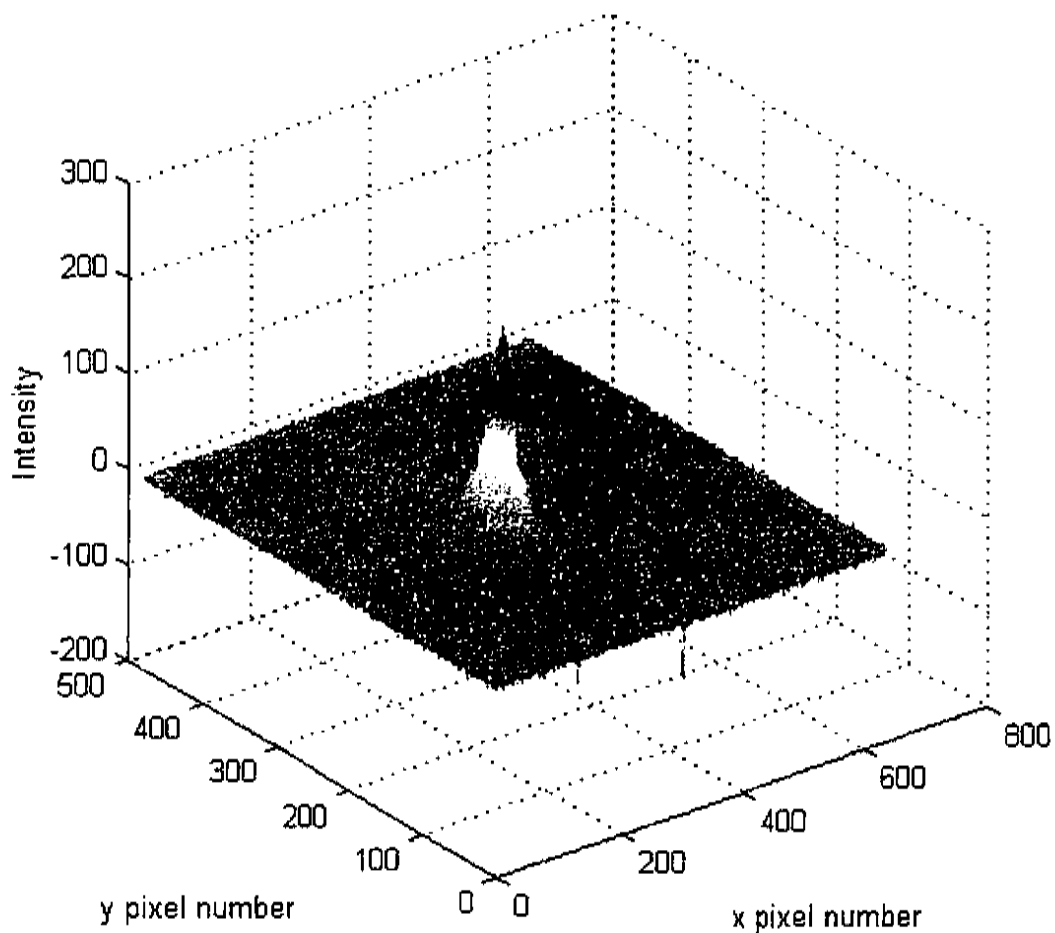


Figure 7.3: Typical background subtracted image of the electron beam

In order to show the effects discussed above the image in Fig. 7.3 above is rotated so that it is now viewed along the horizontal axis. Note this is a rotated view NOT a projection of the image. The hot pixels are noticeable at the horizontal pixel location

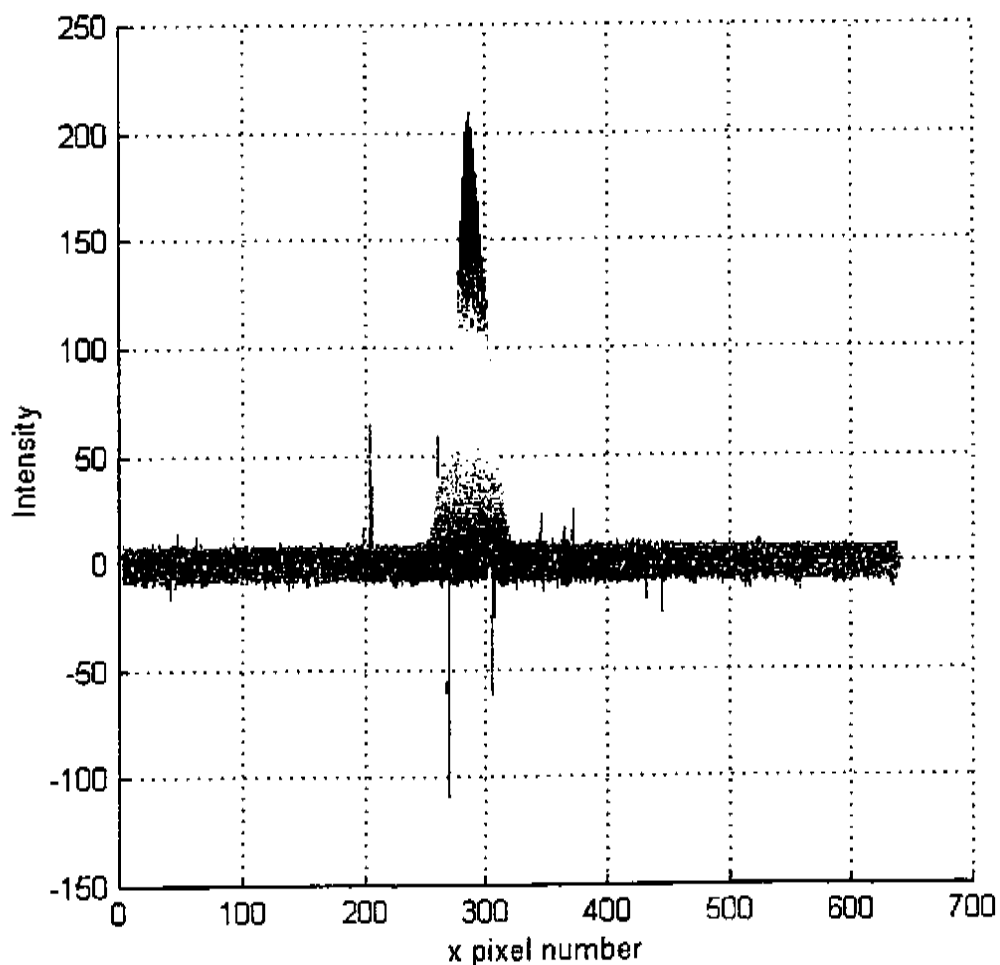


Figure 7.4: Typical background subtracted image of the electron beam rotated view 200 and two around 270 and 305 in the background image which are negative in the background subtracted image due to the subtraction process. The noise floor is approximately centered about zero so there is no large noise floor or pedestal in the background subtracted image.

Next the first and second moments of the projections are determined and the $x - y$ correlation is calculated. The first moments are calculated using the following relation for the horizontal projection:

$$\bar{x} = \frac{\sum_{i=1}^{640} \sum_{j=1}^{480} x_i I(x_i, y_j)}{\sum_{i=1}^{640} \sum_{j=1}^{480} I(x_i, y_j)} \quad (7.2)$$

and for the vertical projection:

$$\bar{y} = \frac{\sum_{j=1}^{480} \sum_{i=1}^{640} y_j I(x_i, y_j)}{\sum_{j=1}^{480} \sum_{i=1}^{640} I(x_i, y_j)} \quad (7.3)$$

where $I(x_i, y_j)$ is the intensity at the location x_i and y_j of the image. The second moments and the $x - y$ correlation are calculated about the centroid in the distribution located at (\bar{x}, \bar{y}) as in previous chapters using the following relation

$$\sigma_{ij} = ij = \frac{\iint (i - \bar{i})(j - \bar{j}) \rho(i, j) di dj}{\iint \rho(i, j) di dj} \quad (7.4)$$

with integration replaced by summation where $i, j = x$ or y .

For the horizontal dimension the relation becomes:

$$\sigma_{11} = \bar{x}^2 = \frac{\sum_{i=1}^{640} \sum_{j=1}^{480} (x_i - \bar{x})^2 I(x_i, y_j)}{\sum_{i=1}^{640} \sum_{j=1}^{480} I(x_i, y_j)} \quad (7.5)$$

For the vertical dimension the relation becomes:

$$\sigma_{33} = \tilde{y}^2 = \frac{\sum_{j=1}^{480} \sum_{i=1}^{640} (y_j - \tilde{y})^2 I(x_i, y_j)}{\sum_{j=1}^{480} \sum_{i=1}^{640} I(x_i, y_j)} \quad (7.6)$$

For the x-y correlation the relation becomes:

$$\sigma_{13} = \tilde{x}\tilde{y} = \frac{\sum_{i=1}^{640} \sum_{j=1}^{480} (x_i - \tilde{x})(y_j - \tilde{y}) I(x_i, y_j)}{\sum_{i=1}^{640} \sum_{j=1}^{480} I(x_i, y_j)} \quad (7.7)$$

In each of the quadrupole scans five images of the beam with the laser on and one image with the laser off are taken at each of the ten quadrupole settings. Therefore there are 50 background subtracted images for each of the quadrupole scans. The values for σ_{11} , σ_{33} and σ_{13} are calculated for each of the 50 background subtracted images. The average and standard deviation of the five values σ_{11} , σ_{33} and σ_{13} at each quadrupole setting are calculated. The ten averaged values of $\bar{\sigma}_{11}$, $\bar{\sigma}_{33}$ and $\bar{\sigma}_{13}$ are used in the calculation of the four dimensional volume and the standard deviations are used in the error analysis.

This information is organized into a system of equations which is solved to determine the initial elements of the beam matrix as discussed in Chap. 4. The screen location is denoted as (1) and the quadrupole doublet entrance is denoted (0). The averaged values from the screen location, $\bar{\sigma}_{11} = \sigma(1)_{11}$, $\bar{\sigma}_{33} = \sigma(1)_{33}$ and $\bar{\sigma}_{13} = \sigma(1)_{13}$ that are obtained from a set of 10 measurements are arranged into a 30×1 vector, $\vec{\sigma}(1)$. The elements of the transform matrix which represents the beam line from the quadrupole doublet entrance to the screen are used and form a 30×10 matrix, \vec{R} , from the matrices \vec{R}_1 , \vec{R}_3 , and \vec{R}_{13} . Then the system of equations:

$$\vec{\sigma}(1) = \vec{R} \vec{\sigma}(0) \quad (7.8)$$

is formed, where $\vec{\sigma}(0)$ is the 1×10 dimensional vector containing the initial values for the beam matrix at the input to the quadrupole doublet. Then the full system has

the form:

$$\begin{bmatrix} \sigma_{11}(1)_1 \\ \vdots \\ \sigma_{11}(1)_{10} \\ \sigma_{33}(1)_1 \\ \vdots \\ \sigma_{33}(1)_{10} \\ \sigma_{13}(1)_1 \\ \vdots \\ \sigma_{13}(1)_{10} \end{bmatrix} = \begin{bmatrix} (R_{11}^2)_1 & (2R_{11}R_{12})_1 & 0 & 0 & (R_{12}^2)_1 \\ \vdots & \vdots & \vdots & \vdots & \vdots \\ (R_{11}^2)_{10} & (2R_{11}R_{12})_{10} & 0 & 0 & (R_{12}^2)_{10} \\ 0 & 0 & 0 & 0 & 0 \\ \vdots & \vdots & \vdots & \vdots & \vdots \\ 0 & 0 & 0 & 0 & 0 \\ 0 & 0 & (R_{11}R_{33})_1 & (R_{11}R_{34})_1 & 0 \\ \vdots & \vdots & \vdots & \vdots & \vdots \\ 0 & 0 & (R_{11}R_{33})_{10} & (R_{11}R_{34})_{10} & 0 \\ \\ 0 & 0 & 0 & 0 & 0 \\ \vdots & \vdots & \vdots & \vdots & \vdots \\ 0 & 0 & 0 & 0 & 0 \\ 0 & 0 & (R_{33}^2)_1 & (2R_{33}R_{34})_1 & (R_{34}^2)_1 \\ \vdots & \vdots & \vdots & \vdots & \vdots \\ 0 & 0 & (R_{33}^2)_{10} & (2R_{33}R_{34})_{10} & (R_{34}^2)_{10} \\ (R_{12}R_{33})_1 & (R_{12}R_{34})_1 & 0 & 0 & 0 \\ \vdots & \vdots & \vdots & \vdots & \vdots \\ (R_{12}R_{33})_{10} & (R_{12}R_{34})_{10} & 0 & 0 & 0 \end{bmatrix} \begin{bmatrix} \sigma_{11}(0) \\ \sigma_{12}(0) \\ \sigma_{13}(0) \\ \sigma_{14}(0) \\ \sigma_{22}(0) \\ \sigma_{23}(0) \\ \sigma_{24}(0) \\ \sigma_{33}(0) \\ \sigma_{34}(0) \\ \sigma_{44}(0) \end{bmatrix}$$

or in a more compact form:

$$\vec{\sigma}(1) = \tilde{R} \vec{\sigma}(0). \tag{7.9}$$

The system is inverted to find $\sigma(0)$

$$\vec{\sigma}(0) = \tilde{R}^{-1} \vec{\sigma}(1). \tag{7.10}$$

And finally the normalized four dimensional volume can be calculated using:

$$V_{4-D} = \frac{\pi^2}{2} (\beta\gamma)^2 \sqrt{\det\sigma_{4-D}(0)} \quad (7.11)$$

with $\gamma = \frac{E}{mc^2} + 1$ and $\beta = \sqrt{1 - \gamma^{-2}}$ where E is the beam energy.

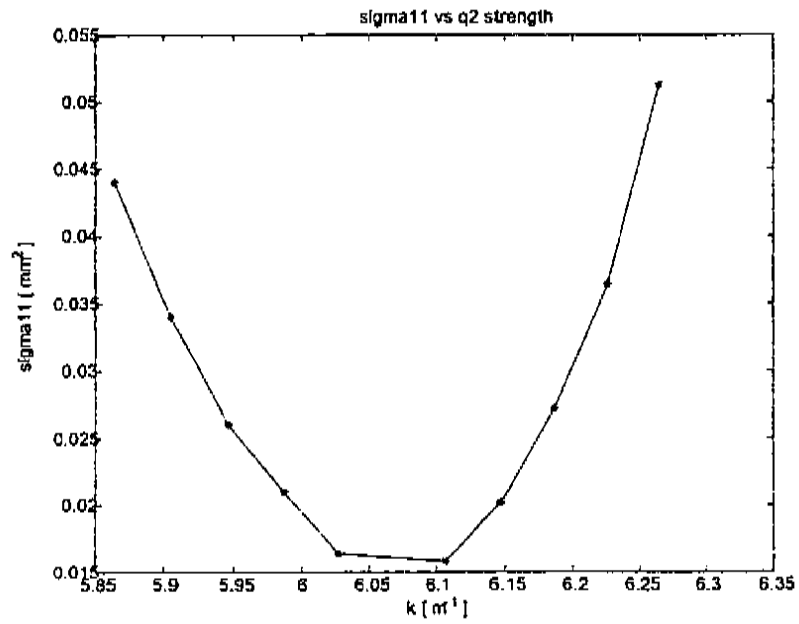
7.4 Results

A quadrupole scan was performed at the solenoid settings of 140, 142, 145, 147, and 150 amperes. The order the scans were taken was (1) 140 amperes, (2) 145 amperes, (3) 150 amperes, (4) 142 amperes, and (5) 147 amperes. The scans are denoted qs1 for 140 amperes, qs2 for 145 amperes, qs3 for 150 amperes, qs4 for 142 amperes, and qs5 for 147 amperes. The data was taken in that particular order in the search for the minimum horizontal emittance. The first three scans were evaluated and then measurements at the intermediate solenoid settings were performed. The method of analysis used a single lineout through the peak intensity of each background subtracted image to determine the width of the electron beam distribution. The single lineout method provided a quick calculation to evaluate trends in the data. After much consideration about the correlations present in the data, the method using a single slice through the data was deemed invalid. However, at the time the measurements were taken the effects of the correlation and the appropriate techniques for the analysis of the data to include correlation effects were not known.

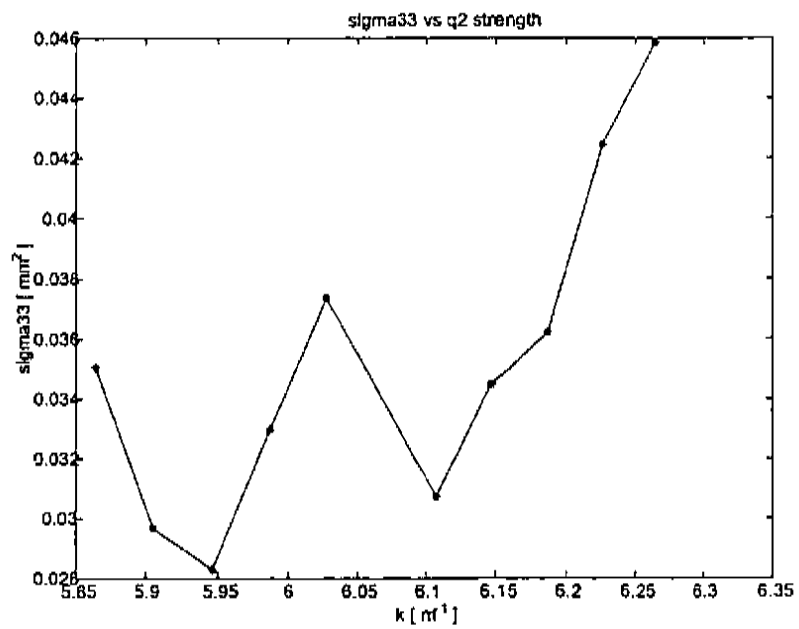
7.4.1 Raw Data

The raw data for σ_{11} , σ_{33} , σ_{13} , and r_{13} for each of the quadrupole scan is presented below.

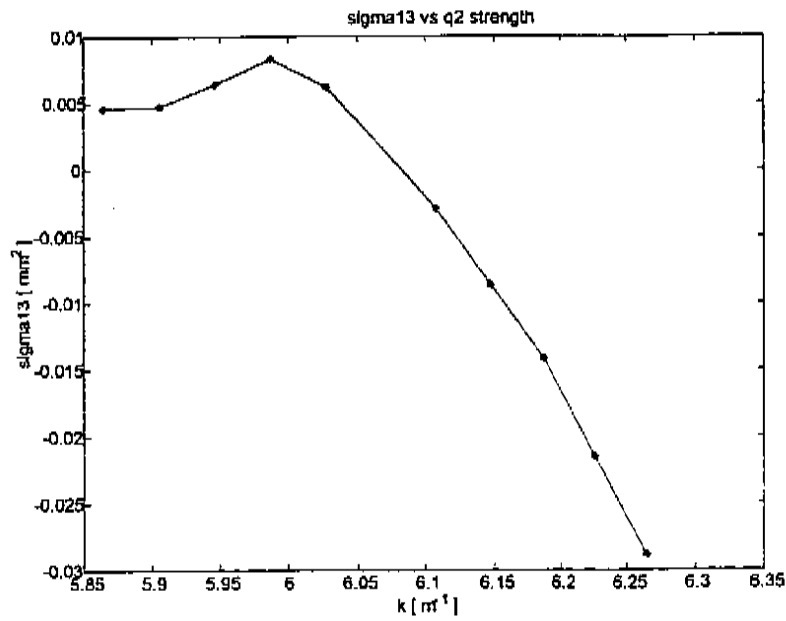
qs1 $I_{sol} = 140$ Amperes



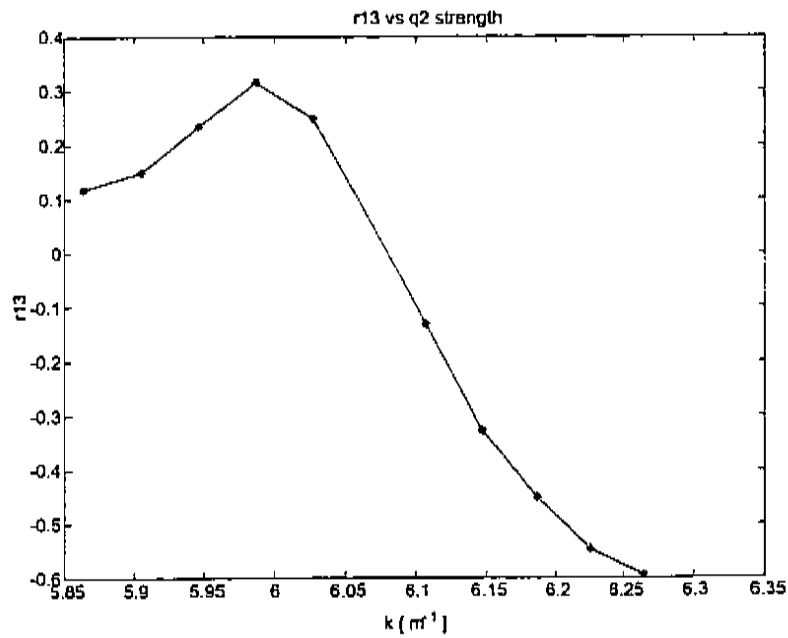
qs1 Isol=140[A] Sigma11 vs q2 strength



qs1 Isol=140[A] Sigma33 vs q2 strength

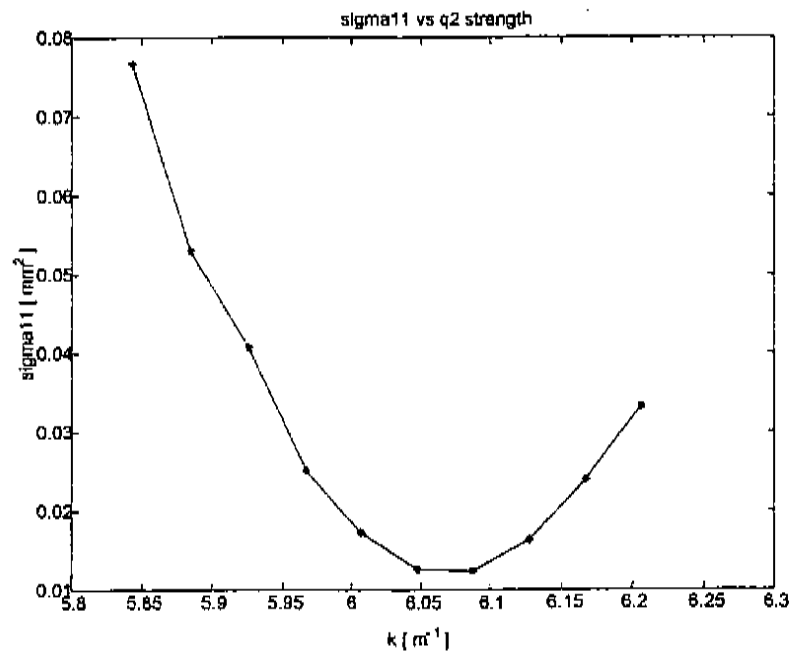


qs1 Isol=140[A] Sigma13 vs q2 strength

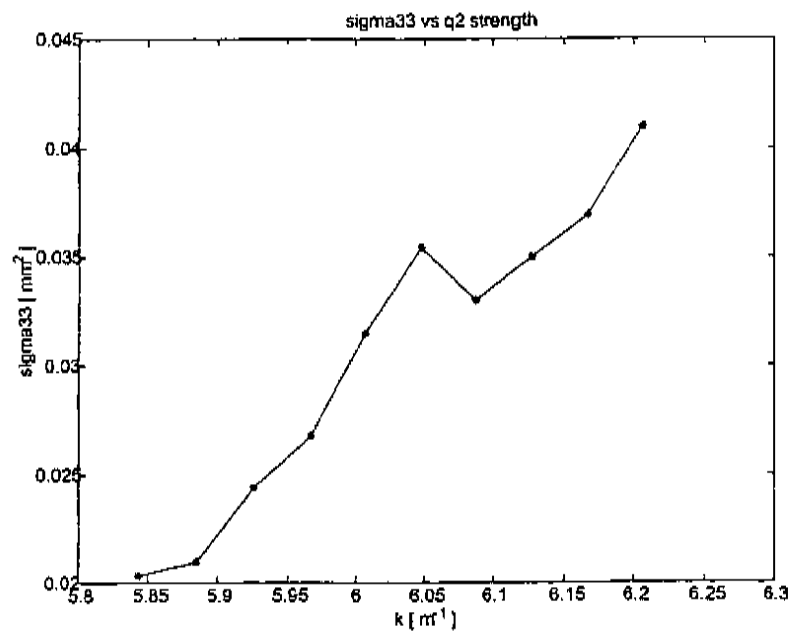


qs1 Isol=140[A] r13 vs q2 strength

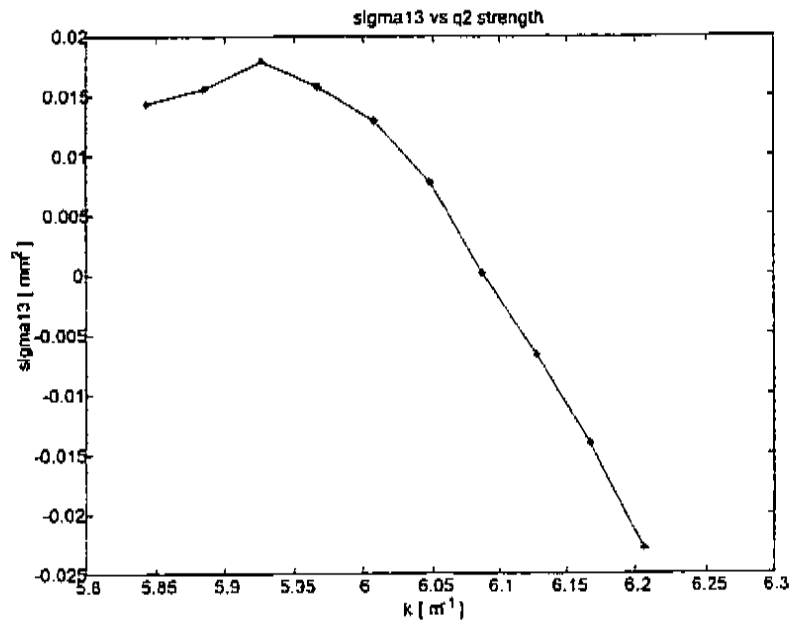
qs2 $I_{sol} = 145$ Amperes



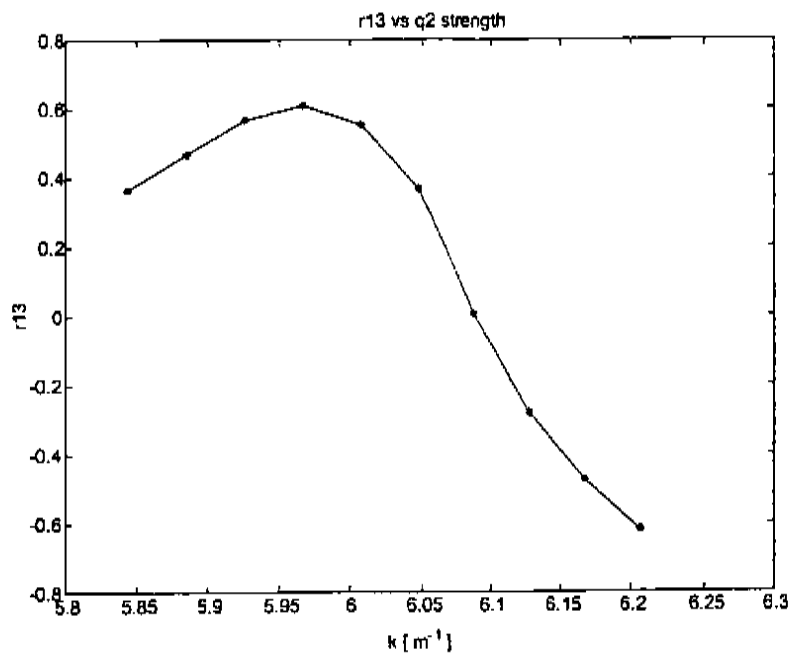
qs2 Isol=145[A] Sigma11 vs q2 strength



qs2 Isol=145[A] Sigma33 vs q2 strength

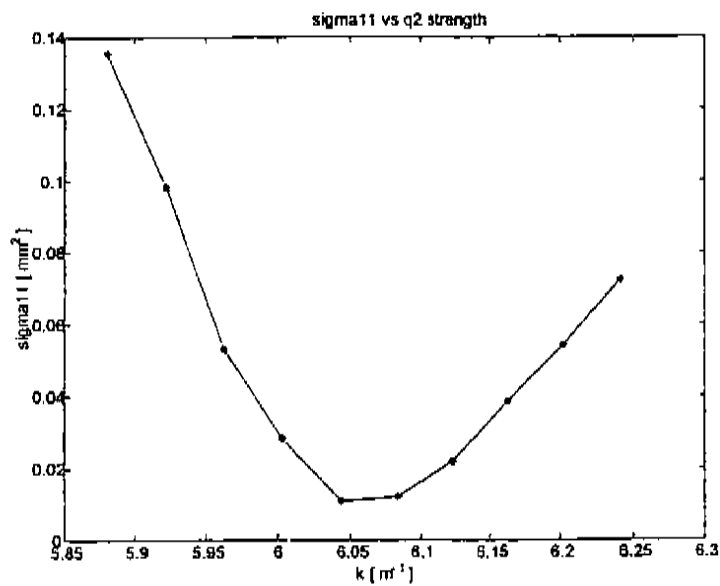


qs2 Isol=145[A] Sigma13 vs q2 strength

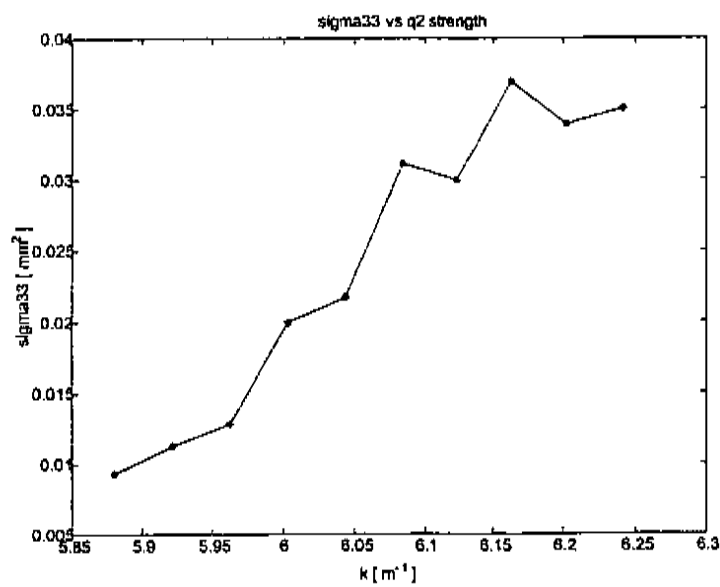


qs2 Isol=145[A] r13 vs q2 strength

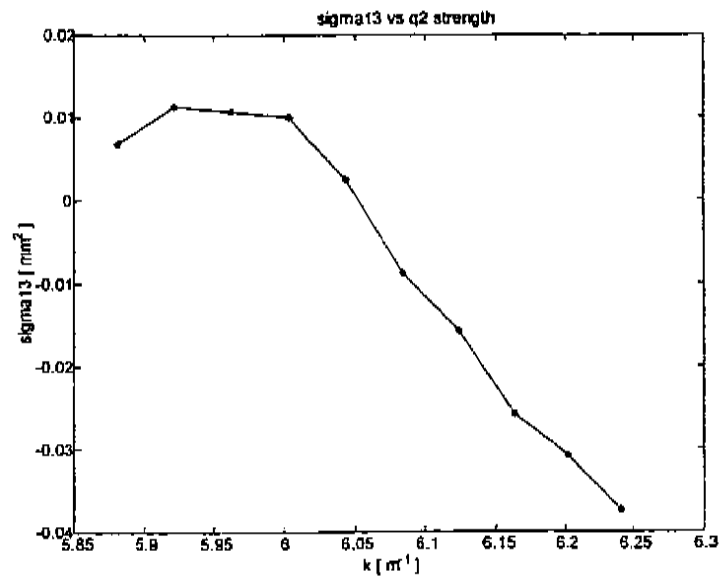
qs3 $I_{sol} = 150$ Amperes



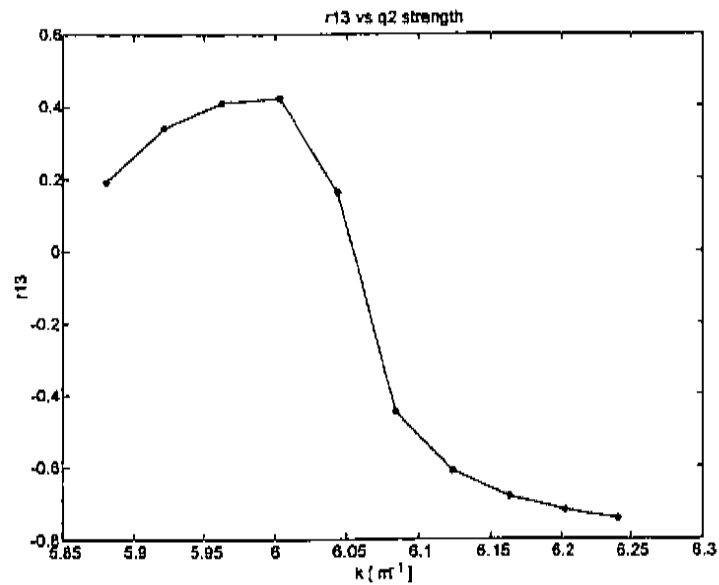
qs3 Isol=150[A] Sigma11 vs q2 strength



qs3 Isol=150[A] Sigma33 vs q2 strength

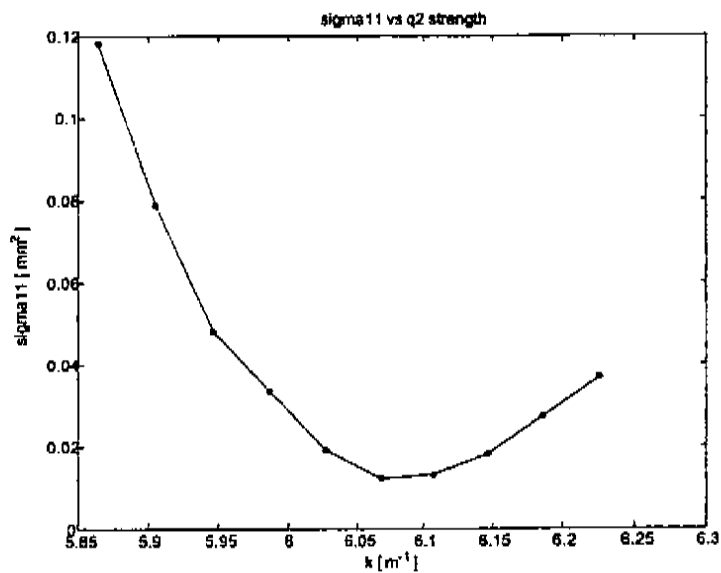


qs3 Isol=150[A] Sigma13 vs q2 strength

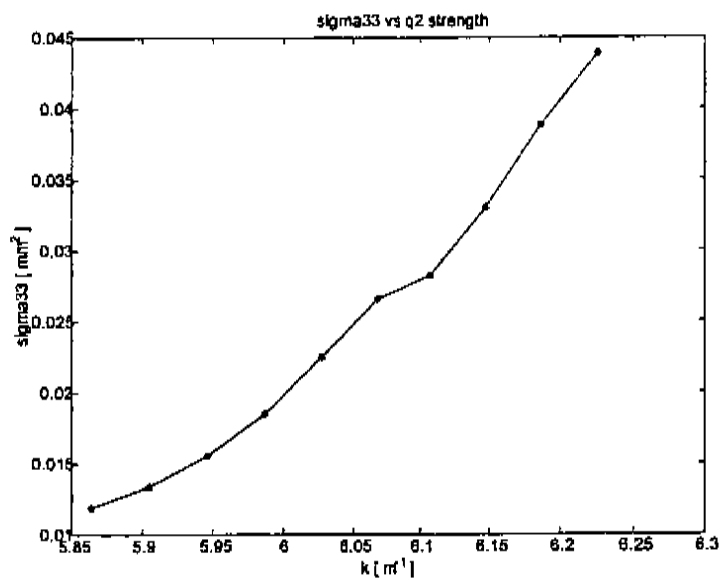


qs3 Isol=150[A] r13 vs q2 strength

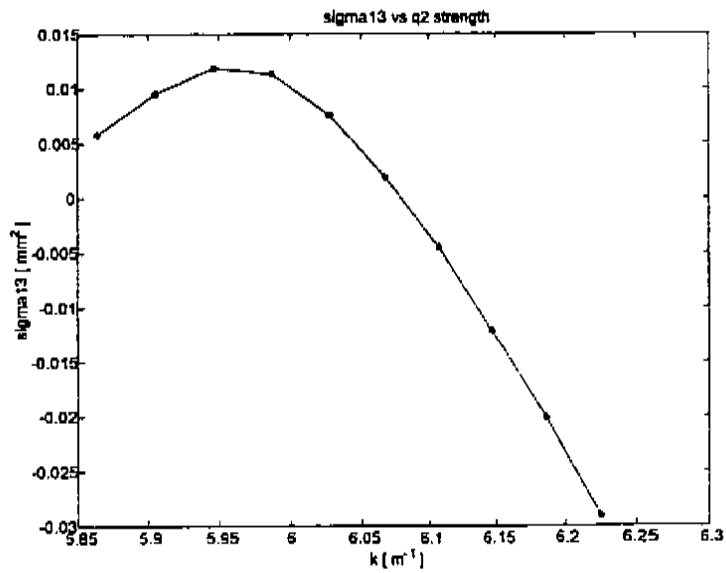
qs4 $I_{sol} = 142$ Amperes



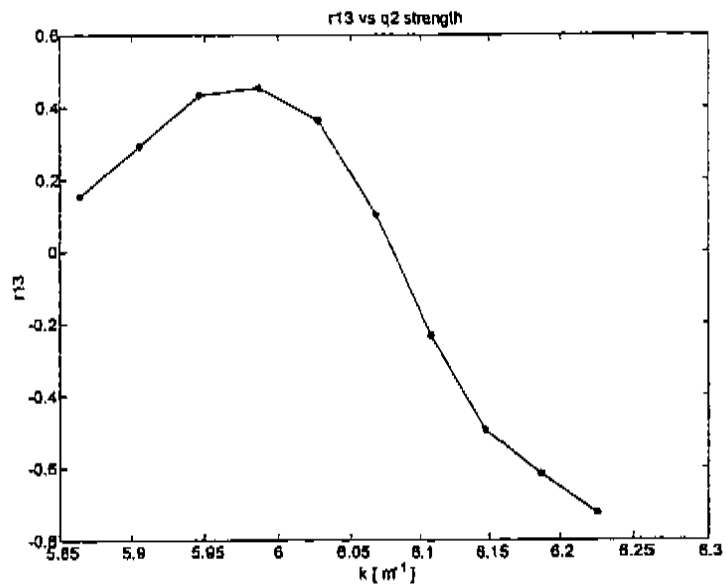
qs4 Isol=142[A] Sigma11 vs q2 strength



qs4 Isol=142[A] Sigma33 vs q2 strength

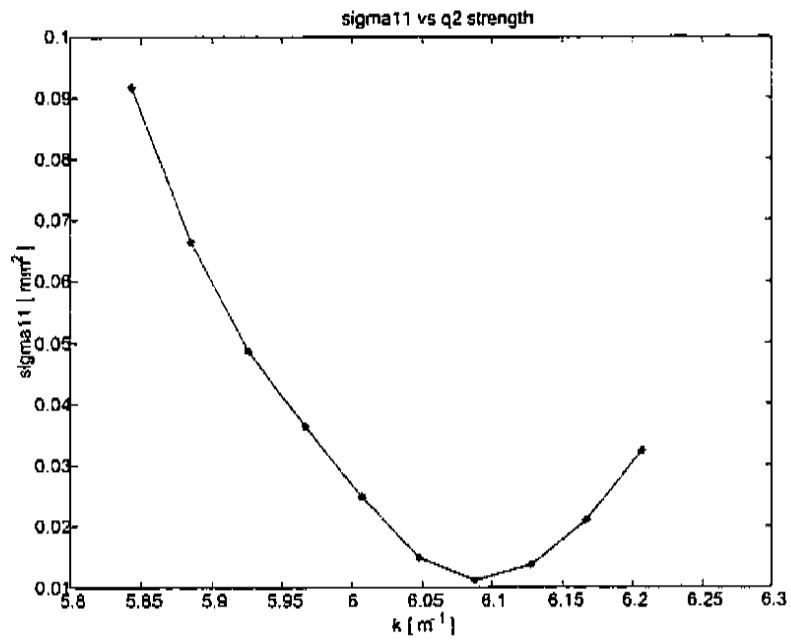


qs4 Isol=142[A] Sigma13 vs q2 strength

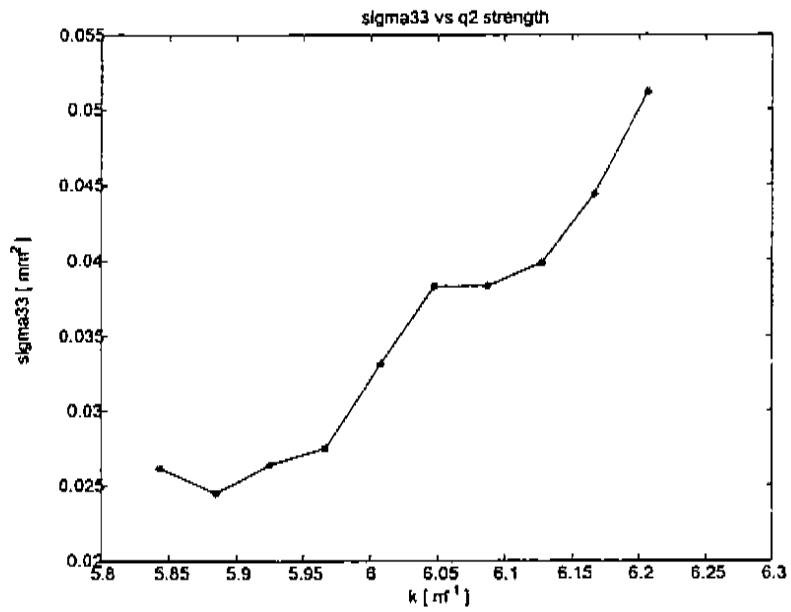


qs4 Isol=142[A] r13 vs q2 strength

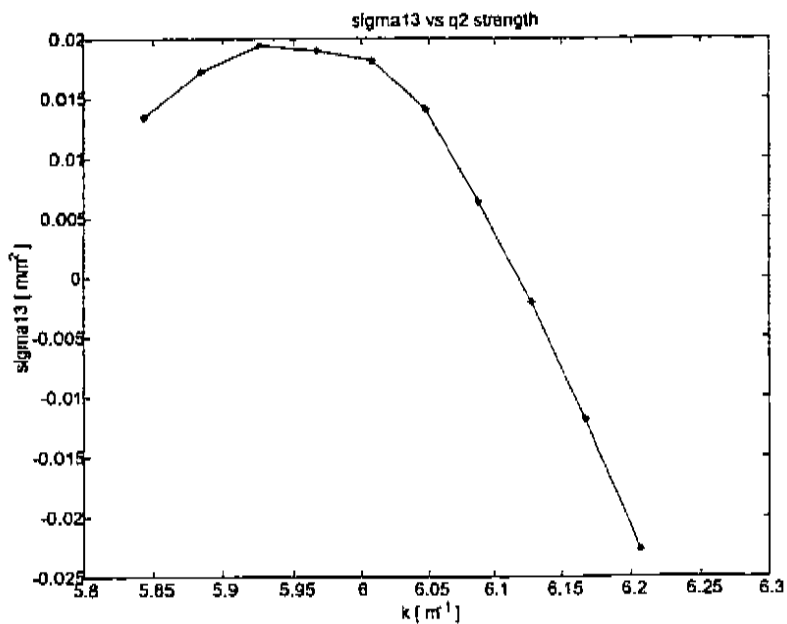
qs5 $I_{sol} = 147$ Amperes



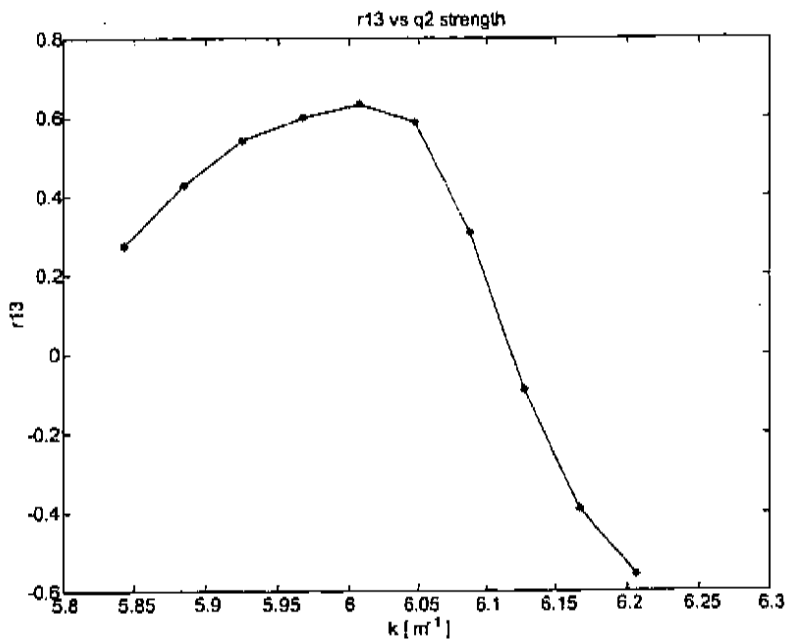
qs5 Isol=147[A] Sigma11 vs q2 strength



qs5 Isol=147[A] Sigma33 vs q2 strength



qs5 Isol=147[A] Sigma13 vs q2 strength



qs5 Isol=147[A] r13 vs q2 strength

The data for σ_{11} all pass through a minimum as expected since q2, the horizontally focusing quadrupole, was adjusted to bring the electron beam through a minimum. The σ_{33} data also follow the expected behavior from the simulations. The vertical width of the beam increases as the vertical defocusing strength of q2 is increased. There also appears to be a minimum in σ_{33} in scans qsl and qs5 similar to what was seen in the simulation of section 5.3. There is structure present in some of the plots of σ_{33} . The plots do not all vary smoothly, there is a bump in the central region of the scans. This may be due to some real structure in the beam or it may be due to the limited vertical beam size variation in the scans. The beam size varies over a smaller range in the vertical than in the horizontal as seen in difference in the scales for the σ_{11} and σ_{33} data for all of the five solenoid settings. The vertical resolution of the system is influenced by the limited range of the variation in the vertical beam widths. So this data may appear more noisy. If the vertical data is plotted on the same scale as the horizontal data the structure in the vertical data is reduced.

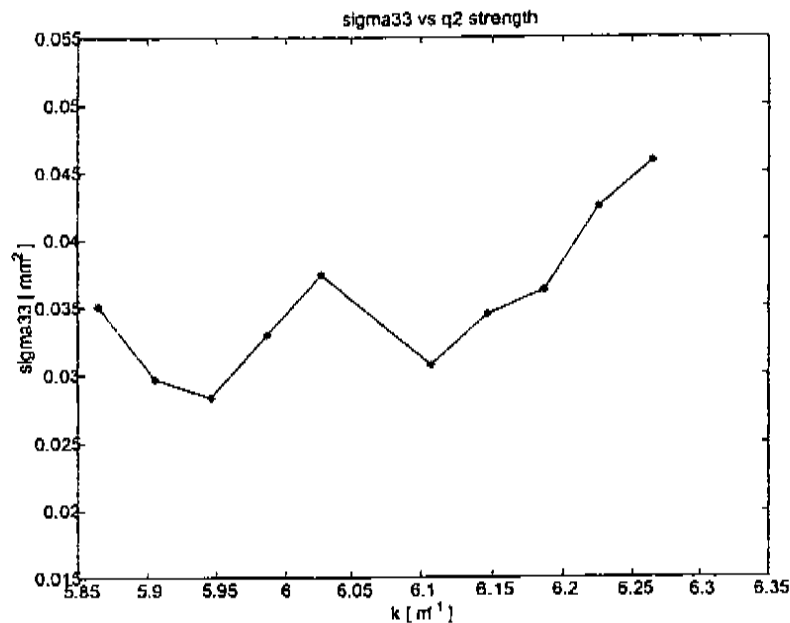


Figure 7.5: qsl Isol=140[A] Sigma33 vs q2 strength change of vertical scale

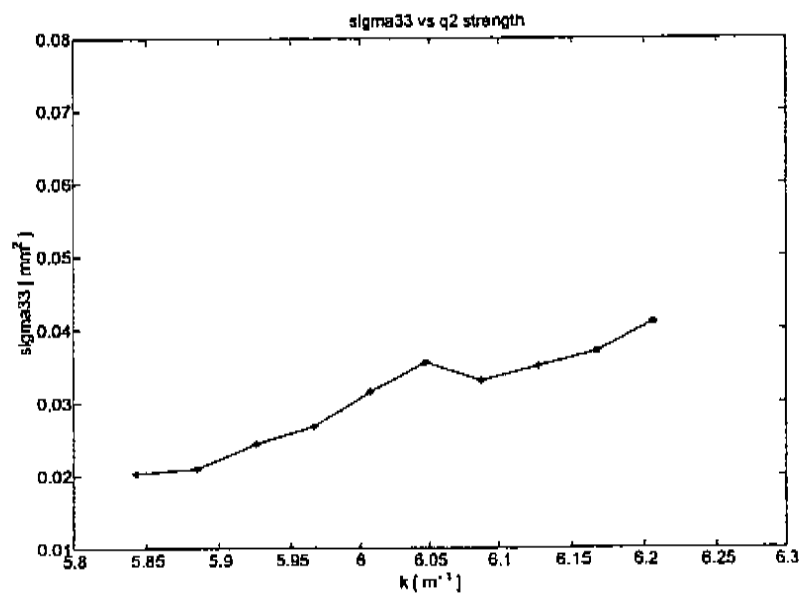


Figure 7.6: qs2 Isol=145[A] Sigma33 vs q2 strength change of vertical scale

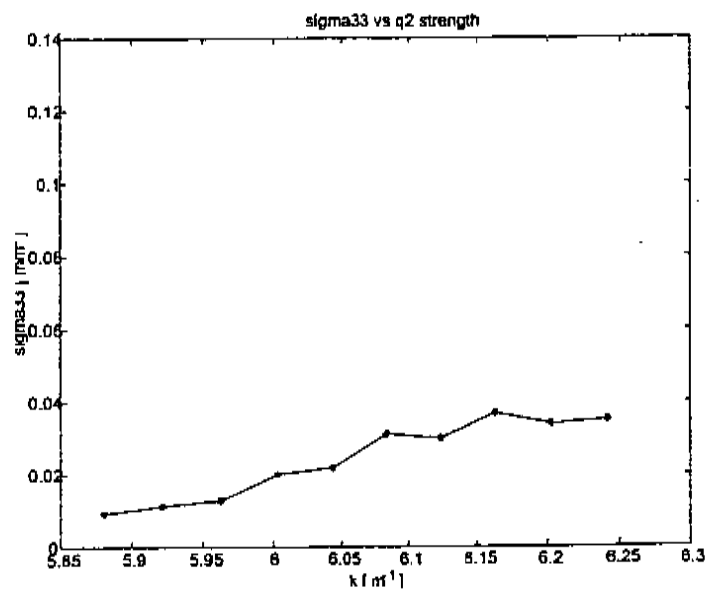


Figure 7.7: qs3 Isol=150[A] Sigma33 vs q2 strength change of vertical scale

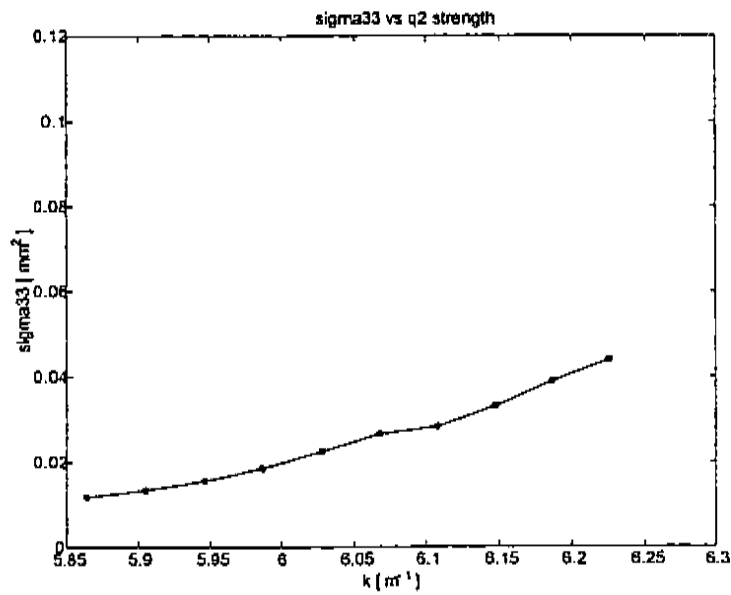


Figure 7.8: qs4 Isol=142[A] Sigma33 vs q2 strength change of vertical scale

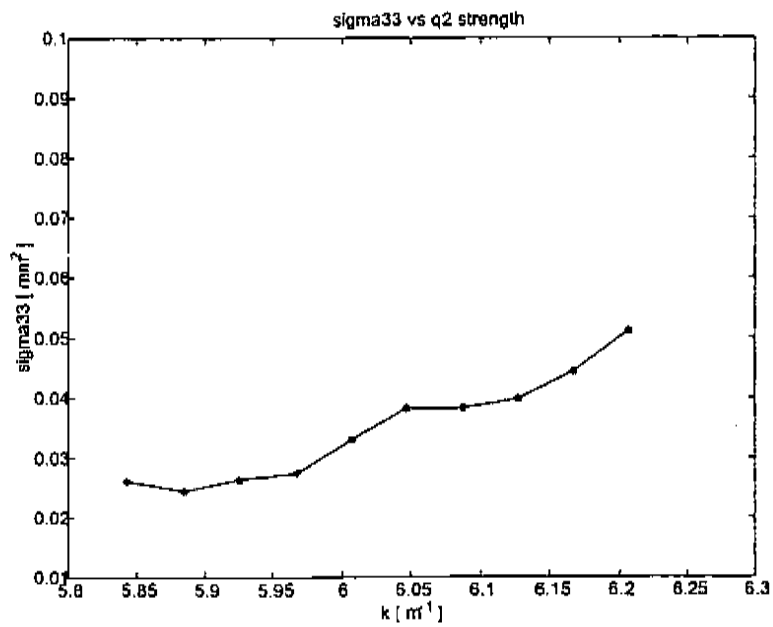


Figure 7.9: qs5 Isol=147[A] Sigma33 vs q2 strength change of vertical scale

The σ_{13} curves also behave similar to the simulations of previous chapters. The σ_{13} rise from an initial value to a maximum and then fall to zero and then they become increasingly more negative as the strength of the scanning quadrupole, q2, is increased. This occurs since initially the beam has a nonzero $x - y$ correlation which is indicated by a tilt in the beam as viewed on the screen. The tilted width, similar to the minor axis of a tilted ellipse, decreases as the strength of q2 is increased. This increases the $x - y$ correlation in the beam. The beam also rotates or more precisely shears towards the vertical axis which leads to a reduction in the value of the $x - y$ correlation. The two effects compete and there is a q2 strength which produces the largest positive value for σ_{13} . When the beam becomes perfectly upright, similar to an upright non-rotated ellipse, the $x - y$ correlation becomes zero. After the beam shears through the upright position, the sign of the $x - y$ correlation changes since the orientation of the beam distribution on the screen has changed. The beam shears further as the strength of q2 increases which leads to a larger value for the $x - y$ correlation. The plots for $r_{13} = \frac{\sigma_{13}}{\sqrt{\sigma_{11}\sigma_{33}}}$ follow the same patterns in the σ_{13} data normalized by the σ_{11} and σ_{33} data. As expected $|r_{13}| \leq 1$ for all of the plots. And the coupling between the transverse dimensions of the beam at the doublet entrance is quite strong since $|r_{13}| > 0$ and the maximum values of $|r_{13}|$ are quite large compared to the values of $|r_{13}| < 0.01$ for a 4 - D symmetric beams in the simulations of previous chapters. Therefore the coupling effects in the data should also be quite noticeable.

7.4.2 Data Reduction

Now if the data for the σ_{11} , σ_{33} , σ_{13} and the lattice settings are used in the model presented above, I obtain for qs1:

$$\begin{aligned}
 V_{4-D} &= 4.2 \times 10^{11} \text{ [(mm mr)}^2\text{]} \\
 \epsilon_x &= 5.1 \text{ [mm mr]} \\
 \epsilon_y &= 3.0 \text{ [mm mr]} \\
 \frac{1}{2}\epsilon_x\epsilon_y &= 7.5 \text{ [(mm mr)}^2\text{]}
 \end{aligned}$$

This result was quite disappointing at first since I expected to obtain a four dimensional volume such that $V_{4-D} \leq \frac{1}{2}\epsilon_x\epsilon_y$. I spent much time examining all of the data reduction routines and found no mistakes. I used simulated data at the screen location as input for the reduction routines and the values obtained for the moments of the distribution, V_{4-D} , ϵ_x , ϵ_y and $\frac{1}{2}\epsilon_x\epsilon_y$ all agreed to $< .1\%$ relative error with the simulated input values. Finally I thought about all of the digits of agreements in the simulations presented in Chap. 3,5 and 6. When working strictly on the computer where all of the simulation data is generated and analyzed, double precision was utilized. Double precision typically allows 14 digits of precision. In the measurement process used in the gathering the experimental data the number of significant figures is much less than 14 digits. In the experimental system there are at most 3 digits of precision available, the data ranges from the millimeter range, when the quadrupole is at the lowest and highest current settings, to the tens of microns, when the beam spot is at the minimum value. Or since the camera CCD imager has only 640×480 pixels there are a maximum of three digits available in the camera data in the horizontal and vertical dimensions respectively. Also the intensity of the individual pixels ranges from 0 to <255 , again three digits of range in the intensity of the camera pixels. Based on the limited precision available in the experimental data, I ran simulated data through the reduction routines limiting the data for the moments at the screen location at various numbers of digits. The input distribution had the following parameters:

$$\begin{aligned}
 \sigma_x &= .2 \text{ [mm]} \\
 \sigma_y &= .8 \text{ [mm]} \\
 \sigma_{x'} &= .2 \text{ [mr]} \\
 \sigma_{y'} &= .05 \text{ [mr]} \\
 w_0 &= 30. \text{ [MeV]}
 \end{aligned}$$

The distribution generated with the above values produced the following values for the beam that were obtained by calculating the moments and correlations in the initial beam using double precision:

$$\begin{aligned}
 V_{4-D} &= 2.77 \text{ [(mm mr)}^2\text{]} \\
 \epsilon_x &= 2.33 \text{ [mm mr]} \\
 \epsilon_y &= 2.38 \text{ [mm mr]} \\
 \frac{1}{2}\epsilon_x\epsilon_y &= 2.77 \text{ [(mm mr)}^2\text{]}
 \end{aligned}$$

Next as in the previous chapters, the beam was rotated, $\alpha = \pi/4$, and the beam was subject to a quadrupole scan and the moments and $x - y$ correlation at each quadrupole setting are calculated and the inversion method of section 7.3 is used to calculate the beam matrix at the quadrupole doublet entrance and no rotation is assumed. Using double precision in the calculations yields:

$$\begin{aligned}
 V_{4-D} &= 2.78 \text{ [(mm mr)}^2\text{]} \\
 \epsilon_x &= 4.95 \text{ [mm mr]} \\
 \epsilon_y &= 4.98 \text{ [mm mr]} \\
 \frac{1}{2}\epsilon_x\epsilon_y &= 12.34 \text{ [(mm mr)}^2\text{]}
 \end{aligned}$$

As expected the V_{4-D} is conserved and the projected emittances, ϵ_x , ϵ_y , and $\frac{1}{2}\epsilon_x\epsilon_y$ are not. Now if the moments and $x - y$ correlations obtained from the screen location are rounded to three digits the following results were obtained:

$$\begin{aligned} V_{4-D} &= 3.57 \times 10^8 \text{ [(mm mr)}^2\text{]} \\ \epsilon_x &= 4.95 \text{ [mm mr]} \\ \epsilon_y &= 5.00 \text{ [mm mr]} \\ \frac{1}{2}\epsilon_x\epsilon_y &= 12.37 \text{ [(mm mr)}^2\text{]} \end{aligned}$$

Limiting the precision of the simulated data produces similar results to those from the experimental data, large values for the V_{4-D} . So for the limited resolution of the experimental system, the inversion method does not work properly. The algorithm is sensitive to the precision of the input data. In order to try and improve the results I tried SVD, Singular Value Decomposition, and conditioning the inverted matrix in equation (7.10) above. There was no improvement, the V_{4-D} remained unchanged.

The solutions found using the limited precision in the input data are nonphysical since the relation $V_{4-D} \leq \frac{1}{2}\epsilon_x\epsilon_y$ is violated. This relation is similar to the condition $\epsilon_x = \sqrt{\sigma_{11}\sigma_{22} - \sigma_{12}^2} \leq \sqrt{\sigma_{11}\sigma_{22}}$ for horizontal trace space. The quantities V_{4-D} and ϵ_x^2 that take into account the correlations in the calculation of the volumes or areas, will be less than (or equal to if all of the correlations are zero) to those quantities which do not such as $\frac{1}{2}\epsilon_x\epsilon_y$ and $\sigma_{11}\sigma_{22}$. The condition $V_{4-D} \leq \frac{1}{2}\epsilon_x\epsilon_y$ forms a constraint on the solutions for the basis vector $\vec{\sigma}(0)$ which contains the information about the moments and correlations in the beam at the input to the quadrupole doublet:

$$\vec{\sigma}(0) = \begin{bmatrix} \sigma(0)_{11} \\ \sigma(0)_{12} \\ \sigma(0)_{13} \\ \sigma(0)_{14} \\ \sigma(0)_{22} \\ \sigma(0)_{23} \\ \sigma(0)_{24} \\ \sigma(0)_{33} \\ \sigma(0)_{34} \\ \sigma(0)_{44} \end{bmatrix} \quad (7.12)$$

That is not the only constraint on the components of the basis vector $\vec{\sigma}(0)$. From the condition that $\epsilon_x = \sqrt{\sigma_{11}\sigma_{22} - \sigma_{12}^2}$ be a real quantity since it represents an area, we must have $\sigma_{12}^2 \leq \sigma_{11}\sigma_{22}$ which implies $|r_{12}| = \left| \frac{\sigma_{12}}{\sqrt{\sigma_{11}\sigma_{22}}} \right| \leq 1$. This forms a constraint for the $x - x'$ space which is projected out of the full four dimensional space under consideration. The other possible projected spaces are: $x - y$, $x - y'$, $x' - y$, $x' - y'$ and $y - y'$ and they must also have real areas. Therefore there are five additional constraints on the components of the basis vector $\sigma(0)$: $|r_{13}| = \left| \frac{\sigma_{13}}{\sqrt{\sigma_{11}\sigma_{33}}} \right| \leq 1$, $|r_{14}| = \left| \frac{\sigma_{14}}{\sqrt{\sigma_{11}\sigma_{44}}} \right| \leq 1$, $|r_{23}| = \left| \frac{\sigma_{23}}{\sqrt{\sigma_{22}\sigma_{33}}} \right| \leq 1$, $|r_{24}| = \left| \frac{\sigma_{24}}{\sqrt{\sigma_{22}\sigma_{44}}} \right| \leq 1$, and $|r_{34}| = \left| \frac{\sigma_{34}}{\sqrt{\sigma_{33}\sigma_{44}}} \right| \leq 1$.

Therefore all of the constraints on the projected spaces are:

$$\begin{aligned} |r_{12}| &= \left| \frac{\sigma_{12}}{\sqrt{\sigma_{11}\sigma_{22}}} \right| \leq 1 \\ |r_{13}| &= \left| \frac{\sigma_{13}}{\sqrt{\sigma_{11}\sigma_{33}}} \right| \leq 1 \\ |r_{14}| &= \left| \frac{\sigma_{14}}{\sqrt{\sigma_{11}\sigma_{44}}} \right| \leq 1 \\ |r_{23}| &= \left| \frac{\sigma_{23}}{\sqrt{\sigma_{22}\sigma_{33}}} \right| \leq 1 \\ |r_{24}| &= \left| \frac{\sigma_{24}}{\sqrt{\sigma_{22}\sigma_{44}}} \right| \leq 1 \\ |r_{34}| &= \left| \frac{\sigma_{34}}{\sqrt{\sigma_{33}\sigma_{44}}} \right| \leq 1 \end{aligned}$$

Table 7.1: Constraints on the projected spaces

The variables r_{ij} where $i, j = 1, 2, 3, 4$ and $i \neq j$ are known as correlation coefficients. For the solution for qs1 which gave nonphysical results the values for the correlation coefficients are:

$$\begin{aligned}r_{12} &= 0.664 \\r_{13} &= 2.46 \times 10^4 \\r_{14} &= -3.62 \times 10^4 \\r_{23} &= -2.98 \times 10^5 \\r_{24} &= -2.94 \times 10^5 \\r_{34} &= 0.905\end{aligned}$$

The correlation coefficients r_{12} and r_{34} are both less than one and the corresponding projected areas $\epsilon_x = 5.1$ [mm mr] and $\epsilon_y = 3.0$ [mm mr] are both real. The remaining correlation coefficients violate the condition $|r| \leq 1$ and therefore violate the constraint that the respective projected areas are real. The solution found by the inversion method is not physical.

The reason the correlation coefficients r_{12} and r_{34} are both ≤ 1 while the remaining correlation coefficients are $|r_{ij}| > 1$ $ij = 13, 14, 23$ and 24 can be seen by reorganizing the system of equations (7.9).

$$\begin{bmatrix} \sigma_{11}(1)_1 \\ \vdots \\ \sigma_{11}(1)_{10} \\ \sigma_{33}(1)_1 \\ \vdots \\ \sigma_{33}(1)_{10} \\ \sigma_{13}(1)_1 \\ \vdots \\ \sigma_{13}(1)_{10} \end{bmatrix} = \begin{bmatrix} (R_{11}^2)_1 & (2R_{11}R_{12})_1 & (R_{12}^2)_1 & 0 & 0 & 0 \\ \vdots & \vdots & \vdots & \vdots & \vdots & \vdots \\ (R_{11}^2)_{10} & (2R_{11}R_{12})_{10} & (R_{12}^2)_{10} & 0 & 0 & 0 \\ 0 & 0 & 0 & (R_{33}^2)_1 & (2R_{33}R_{34})_1 & (R_{34}^2)_1 \\ \vdots & \vdots & \vdots & \vdots & \vdots & \vdots \\ 0 & 0 & 0 & (R_{33}^2)_{10} & (2R_{33}R_{34})_{10} & (R_{34}^2)_{10} \\ 0 & 0 & 0 & 0 & 0 & 0 \\ \vdots & \vdots & \vdots & \vdots & \vdots & \vdots \\ 0 & 0 & 0 & 0 & 0 & 0 \end{bmatrix}$$

$$\begin{bmatrix} 0 & 0 & 0 & 0 \\ \vdots & \vdots & \vdots & \vdots \\ 0 & 0 & 0 & 0 \\ 0 & 0 & 0 & 0 \\ \vdots & \vdots & \vdots & \vdots \\ 0 & 0 & 0 & 0 \\ (R_{11}R_{33})_1 & (R_{11}R_{34})_1 & (R_{12}R_{33})_1 & (R_{12}R_{34})_1 \\ \vdots & \vdots & \vdots & \vdots \\ (R_{11}R_{33})_{10} & (R_{11}R_{34})_{10} & (R_{12}R_{33})_{10} & (R_{12}R_{34})_{10} \end{bmatrix} \begin{bmatrix} \sigma_{11}(0) \\ \sigma_{12}(0) \\ \sigma_{22}(0) \\ \sigma_{33}(0) \\ \sigma_{34}(0) \\ \sigma_{44}(0) \\ \sigma_{13}(0) \\ \sigma_{14}(0) \\ \sigma_{23}(0) \\ \sigma_{24}(0) \end{bmatrix}$$

From this new form one can see that the solution for the terms $\sigma_{11}(0)$, $\sigma_{12}(0)$ and $\sigma_{22}(0)$ is found using information about $\sigma_{11}(1)$ or x^2 at the screen and the correlation term $\sigma_{12}(0)$ is included in the relations $\sigma_{11}(1)_i = (R_{11}^2)_i \sigma_{11}(0) + (2R_{11}R_{12})_i \sigma_{12}(0) + (R_{12}^2)_i \sigma_{22}(0)$. So the relationships include $\sigma_{11}(0)$, $\sigma_{12}(0)$ and $\sigma_{22}(0)$ and these are all of the terms used in the relation for $|\tau_{12}| = \left| \frac{\sigma_{12}(0)}{\sqrt{\sigma_{11}(0)\sigma_{22}(0)}} \right| \leq 1$. The same is true for $\sigma_{34}(0)$ and the relation $\sigma_{33}(1)_i = (R_{33}^2)_i \sigma_{33}(0) + (2R_{33}R_{34})_i \sigma_{34}(0) + (R_{34}^2)_i \sigma_{44}(0)$. So in the system of equations to be solved above both of the correlation terms are included in a relationship with the other terms in the relation for the constraints $r_{12} \leq 1$ and $r_{34} \leq 1$. This is not true for the correlations $\sigma_{13}(0)$, $\sigma_{14}(0)$, $\sigma_{23}(0)$ and $\sigma_{24}(0)$ which are solved for using the relation $\sigma_{13}(1)_i = (R_{11}R_{33})_i \sigma_{13}(0) + (R_{11}R_{34})_i \sigma_{14}(0) + (R_{12}R_{33})_i \sigma_{23}(0) + (R_{12}R_{34})_i \sigma_{24}(0)$. And the correlation coefficients are given by $|r_{13}| =$

$\left| \frac{\sigma_{13}(0)}{\sqrt{\sigma_{11}(0)\sigma_{33}(0)}} \right| \leq 1$, $|r_{14}| = \left| \frac{\sigma_{14}(0)}{\sqrt{\sigma_{11}(0)\sigma_{44}(0)}} \right| \leq 1$, $|r_{23}| = \left| \frac{\sigma_{23}(0)}{\sqrt{\sigma_{22}(0)\sigma_{33}(0)}} \right| \leq 1$, $|r_{24}| = \left| \frac{\sigma_{24}(0)}{\sqrt{\sigma_{22}(0)\sigma_{44}(0)}} \right| \leq 1$. The values for $\sigma_{13}(0)$, $\sigma_{14}(0)$, $\sigma_{23}(0)$ and $\sigma_{24}(0)$ are determined without regard for the other terms in their respective correlation coefficients. For example there is no relation between $\sigma_{13}(0)$, $\sigma_{11}(0)$ and $\sigma_{33}(0)$ in the system equations formed from the experimental data. The solutions for $\sigma_{13}(0)$, $\sigma_{11}(0)$ and $\sigma_{33}(0)$ are made without regard for each other and the respective constraint. This is not a problem with the simulation data due to the large precision (14 digits) used in the calculations.

To ensure a physical solution for the basis vector $\vec{\sigma}(0)$ the constraints must be observed in the search for the basis vector $\vec{\sigma}(0)$. In the simulations presented in the previous chapters, the determination of the basis vector $\vec{\sigma}(0)$ involved an inversion of the system $\vec{\sigma}(1) = \tilde{R}\vec{\sigma}(0)$ to produce the relation $\vec{\sigma}(0) = \tilde{R}^{-1}\vec{\sigma}(1)$. The system is over determined since there are more equations than unknowns since there are 30 equations and ten unknowns. So the solution of $\vec{\sigma}(0) = \tilde{R}^{-1}\vec{\sigma}(1)$ is found in a Least Squares sense[51]. The residual squared errors between the data and the calculated values are minimized.

$$\text{error} = \left\| \vec{\sigma}(1) - \tilde{R}\vec{\sigma}(0) \right\|^2 = \sum_{i=1}^{30} \left\{ \sigma_i(1) - \sum_{j=1}^{10} [\tilde{R}_{ij}\sigma_j(0)] \right\}^2 \quad (7.13)$$

This is the basis for the chi-square, χ^2 , algorithm which can be used to determine the values for the elements of the basis vector $\vec{\sigma}(0)$ while including the effects of the uncertainties in the measured quantities. The sum of the residual squared errors weighted by their respective uncertainty, denoted by χ^2 is calculated as follows[52]:

$$\chi^2 = \sum_{i=1}^{30} \left\{ \frac{\sigma_i(1) - \sum_{j=1}^{10} [\tilde{R}_{ij}\sigma_j(0)]}{\delta_i} \right\}^2 \quad (7.14)$$

where δ_i is the measurement error for the i^{th} data point. If all of the data points matched exactly, highly unlikely, then $\chi^2 = 0$. More likely is that each of the 30

terms, degrees of freedom, in the sum are ≤ 1 which occurs if the calculated value differs from the measured value by an amount which is $\leq \delta$ for the particular term. If this is true then $\chi^2 \leq 30$ which is considered an indication that the calculated values are a "good fit" to the measured quantities[52]. And if $\chi^2 \gg 30$ then the calculated values are considered to be a poor fit to the measured values. To normalize the χ^2 values one can divide χ^2 by the number of degrees of freedom, 30, which gives $\chi_{dof=30}^2 = \frac{\chi^2}{30}$. In this case $\chi_{dof=30}^2 \leq 1$ indicates a good fit and $\chi_{dof=30}^2 \gg 1$ indicates a poor fit to the data.

In order to implement the constraints of $V_{4-D} \leq \frac{1}{2}\epsilon_x\epsilon_y$ and the correlation coefficients constraints listed above in the search for the basis vector $\sigma(0)$, the "fmincon" nonlinear minimizer of MatLab[53] was utilized to minimize the relation for χ^2 . The mincon minimizer allows the specification of constraints to be applied during the minimization search.

To test the algorithm the simulated data from the beginning of this section with the following parameters:

$$\begin{aligned}\sigma_x &= .20 \text{ [mm]} \\ \sigma_y &= .80 \text{ [mm]} \\ \sigma_{x'} &= .20 \text{ [mr]} \\ \sigma_{y'} &= .05 \text{ [mr]} \\ w_0 &= 30.02 \text{ [MeV]}\end{aligned}$$

was utilized. The distribution produced the following values for the beam that were obtained by calculating the moments and correlations in the initial beam using double precision:

$$\begin{aligned}
 V_{4-D} &= 2.77 \text{ [(mm mr)}^2\text{]} \\
 \epsilon_x &= 2.33 \text{ [mm mr]} \\
 \epsilon_y &= 2.38 \text{ [mm mr]} \\
 \frac{1}{2}\epsilon_x\epsilon_y &= 2.77 \text{ [(mm mr)}^2\text{]}
 \end{aligned}$$

The beam distribution is rotated by $\alpha = \pi/4$ and is propagated through the quadrupole doublet and then to the screen location. The horizontally focusing quadrupole before the screen is used to perform a quadrupole scan. The results for the quadrupole scan using double precision for the horizontal and vertical moments and the $x - y$ correlation in the inversion method model yielded:

$$\begin{aligned}
 V_{4-D} &= 2.78 \text{ [(mm mr)}^2\text{]} \\
 \epsilon_x &= 4.95 \text{ [mm mr]} \\
 \epsilon_y &= 4.98 \text{ [mm mr]} \\
 \frac{1}{2}\epsilon_x\epsilon_y &= 12.34 \text{ [(mm mr)}^2\text{]}
 \end{aligned}$$

The relative error between the initial and calculated four dimensional volumes is:

$$100\% \cdot \frac{|2.7766 - 2.7747|}{2.7747} = .07\%$$

The x and y moments and $x - y$ correlation at the screen location obtained from a quadrupole scan above were rounded to three digits and the uncertainties from `qs1` were taken as the uncertainties in the data and this data was used in the χ^2 minimization algorithm presented above. The following results were obtained:

$$\begin{aligned}
V_{4-D} &= 3.00 \text{ [(mm mr)}^2\text{]} \\
\epsilon_x &= 4.94 \text{ [mm mr]} \\
\epsilon_y &= 4.99 \text{ [mm mr]} \\
\frac{1}{2}\epsilon_x\epsilon_y &= 12.34 \text{ [(mm mr)}^2\text{]}
\end{aligned}$$

The relative difference between the two four dimensional volumes is:

$$100\% \cdot \frac{|3.00 - 2.77|}{2.77} = 8.3\%$$

which is a quite reasonable error in comparison with the results using the inversion method without constrains ($V_{4-D} = 3.57 \times 10^8 \text{ [(mm mr)}^2\text{]}$.)

To determine the uncertainty in the V_{4-D} results obtained from χ^2 minimization method, a Monte Carlo method [54] was employed. If the system $\vec{\sigma}(1) = \tilde{R}\vec{\sigma}(0)$ could be inverted, the uncertainty in the V_{4-D} could be determined directly by incorporating the uncertainty in the measurements in to the system of equations [55]. However, since the system of equations cannot be reliably inverted with the limited amount of resolution available from the measurement process, the Monte Carlo method proves quite useful. The basic idea is to offset about one third of the measured values using the associated uncertainty for those measured data points to form a new set of measured values. The χ^2 minimization method is applied to the new measured values and the new basis vector $\vec{\sigma}(0)$ and associated V_{4-D} is recorded. By repeating this process the uncertainty distribution for the measurement process can be determined [54]. This was accomplished by randomly choosing three data points from each of the sets $\sigma_{11_i}(1)$, $\sigma_{33_i}(1)$ and $\sigma_{13_i}(1)$ where $i = 1, 2, 3, \dots, 10$, then the associated uncertainty, the δ_i with $i = 1, 2, 3, \dots, 30$ above, was either randomly added or subtracted to the original value and the minimization algorithm was applied to find the minimum value of χ^2 and the values for the components of the basis vector $\sigma(0)$ and the associated V_{4-D} were recorded. This process was repeated ten times for

each of the five data sets for a total of fifty trials. More trials would be desirable for better statistics but each trial took about one day. The uncertainty in the measured values was taken as a linear sum of the standard deviation in the distribution of the five images for each quadrupole setting and the three pixel resolution estimated from the calibration of the camera and frame grabber system.

The results for the five quadrupole scans are presented in the table below:

$I_{sol}[A]$	140	142	145	147	150
$V_{4-D}[(mm\ mr)^2]$	$0.73 \pm .35$	$0.72 \pm .10$	$0.61 \pm .17$	$0.72 \pm .10$	$0.80 \pm .35$
$\frac{1}{2}\epsilon_x\epsilon_y[(mm\ mr)^2]$	$7.68 \pm .18$	$5.89 \pm .20$	$5.88 \pm .23$	$9.94 \pm .16$	$5.41 \pm .41$
$\epsilon_x[mm\ mr]$	$5.06 \pm .07$	$6.59 \pm .12$	$5.63 \pm .11$	$6.09 \pm .05$	$8.54 \pm .27$
$\epsilon_y[mm\ mr]$	$3.04 \pm .04$	$1.79 \pm .06$	$2.09 \pm .05$	$3.26 \pm .03$	$1.27 \pm .08$
χ^2	24	35	25	29	69
$\chi_{dof=30}^2 = \frac{\chi^2}{30}$	0.80	1.17	0.83	0.97	2.30
r_{12}	0.67	0.90	0.83	0.85	0.93
r_{13}	0.92	0.99	0.97	0.95	0.97
r_{14}	0.99	0.96	0.98	0.99	0.90
r_{23}	0.53	0.85	0.75	0.72	0.89
r_{24}	0.63	0.82	0.83	0.84	0.81
r_{34}	0.91	0.97	0.92	0.94	0.98
$\epsilon_*[mm\ mr]$	1.21	1.20	1.10	1.20	1.27

Table 7.2: Results for all solenoid settings

In the Table 7.2 above the r_{ij} are the correlation coefficients discussed earlier and all satisfy the constraint $|r_{ij}| \leq 1$ which ensures the respective projected areas are real. Also included in the table is the quantity ϵ_* that represents the projected emittance for the calculated V_{4-D} if there were NO correlations between the transverse dimensions of the beam, $\sigma_{13} = \sigma_{14} = \sigma_{23} = \sigma_{24} = 0$, and if the transverse emittances were equal $\epsilon_x = \epsilon_y$. The quantity ϵ_* is calculated as follows. If $\sigma_{13} = \sigma_{14} = \sigma_{23} = \sigma_{24} = 0$ then $V_{4-D} = \frac{1}{2}\epsilon_x\epsilon_y$. And if $\epsilon_x = \epsilon_y = \epsilon_*$ then $V_{4-D} = 1/2\epsilon_*^2$. Solving for ϵ_* I obtain:

$$\epsilon_* = \sqrt{2 * V_{4-D}} \quad (7.15)$$

ϵ_* gives one a feel for the two dimensional trace space occupied by the beam if the measurement is free of the effects from the correlations σ_{13} , σ_{14} , σ_{23} and σ_{24} . Plots which contain the measured values for σ_{11} , σ_{33} , and σ_{13} versus q2 strength for the five solenoid settings and the calculated values that were obtained by fitting the data are presented on the following pages. The uncertainty in the measured values is represented by the vertical error bars.

*

7.4.3 qs1 Isol=140A

$$\begin{aligned}
 V_{4-D} &= 0.73 \pm .35 \text{ [(mm mr)}^2\text{]} \\
 \frac{1}{2}\epsilon_x\epsilon_y &= 7.68 \pm .18 \text{ [(mm mr)}^2\text{]} \\
 \epsilon_z &= 5.06 \pm .07 \text{ [mm mr]} \\
 \epsilon_x &= 3.04 \pm .04 \text{ [mm mr]} \\
 \epsilon_* &= 1.21 \text{ [mm mr]} \\
 \chi^2 &= 24 \\
 \frac{\chi^2}{30} &= 0.80
 \end{aligned}$$

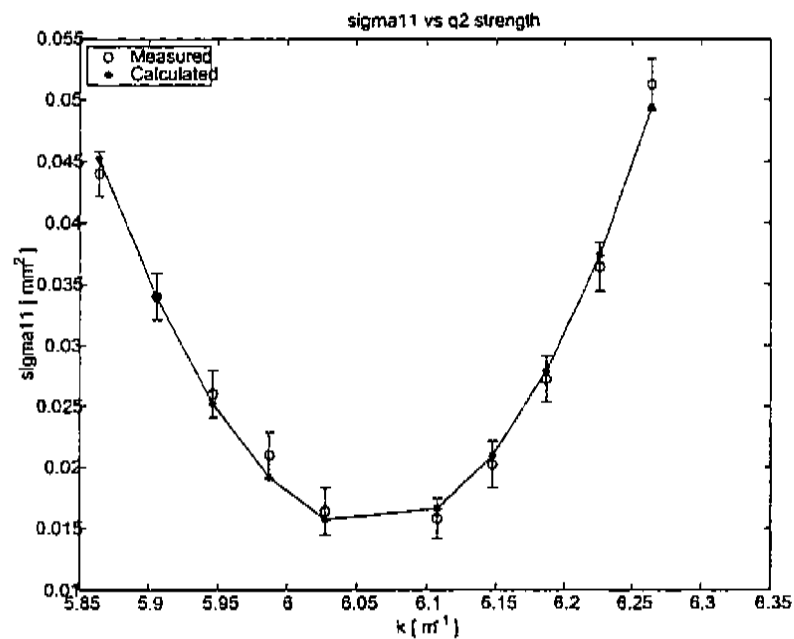


Figure 7.10: Plot qs1 sigma11 versus q2 strength measured and fit values

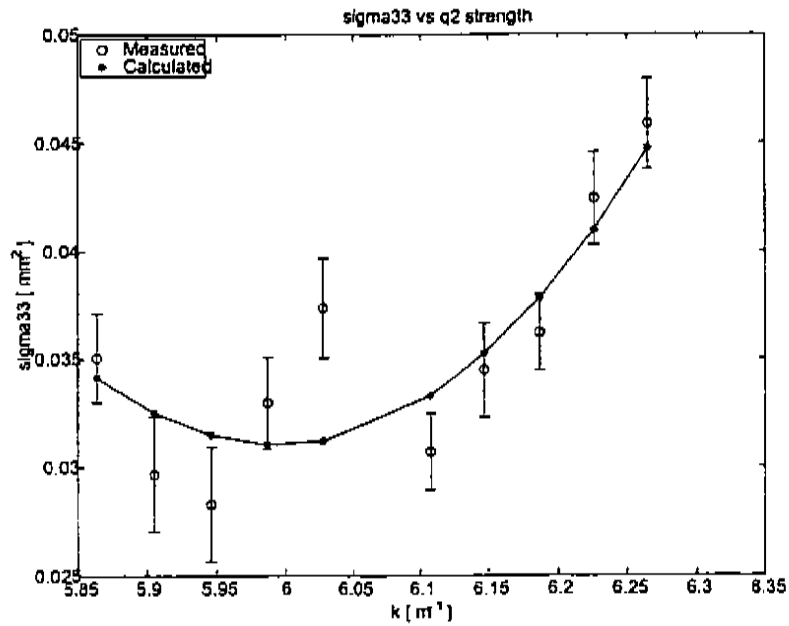


Figure 7.11: Plot qsl sigma33 versus q2 strength measured and fit values

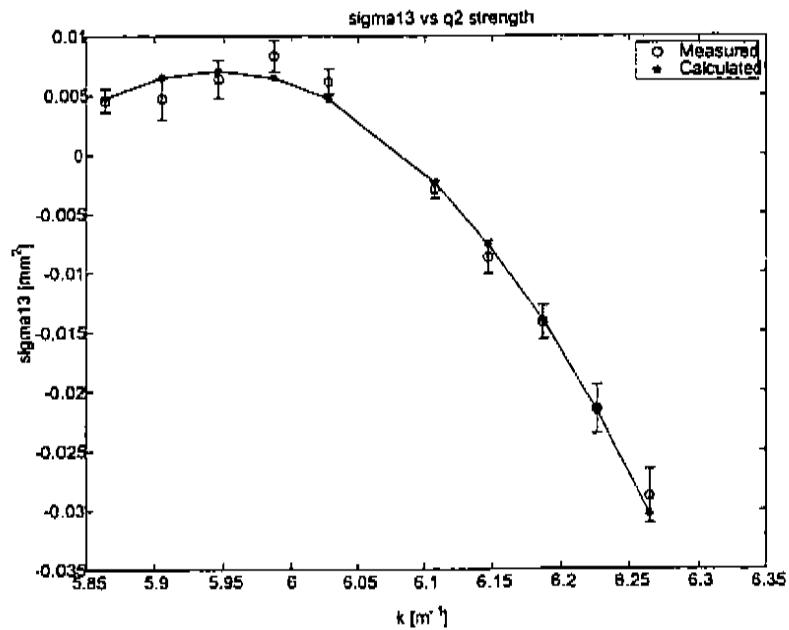


Figure 7.12: Plot qsl sigma13 versus q2 strength measured and fit values

7.4.4 qs2 Isol=145A

$$V_{4-D} = 0.61 \pm .17 \text{ [(mm mr)}^2\text{]}$$

$$\frac{1}{2}\epsilon_x\epsilon_y = 5.88 \pm .23 \text{ [(mm mr)}^2\text{]}$$

$$\epsilon_x = 5.63 \pm .11 \text{ [mm mr]}$$

$$\epsilon_x = 2.09 \pm .05 \text{ [mm mr]}$$

$$\epsilon_s = 1.10 \text{ [mm mr]}$$

$$\chi^2 = 25$$

$$\frac{\chi^2}{30} = 0.83$$

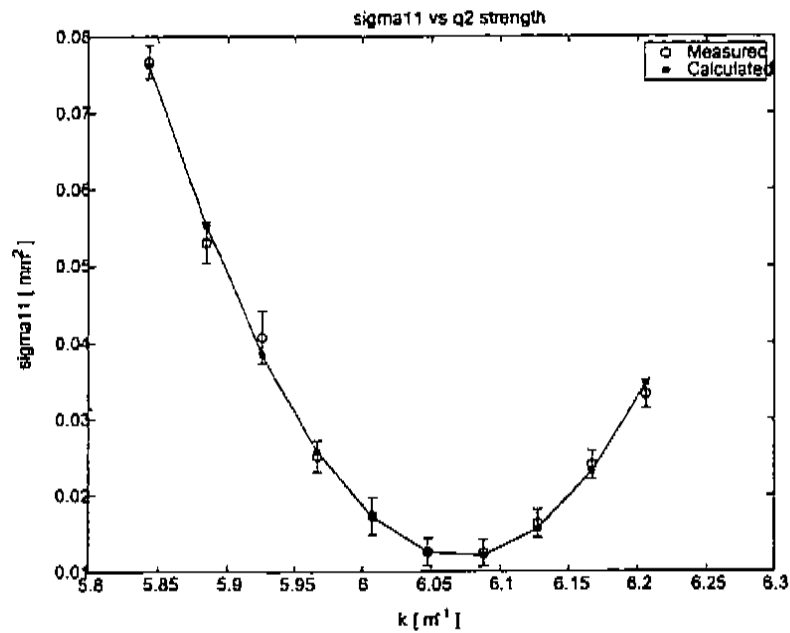


Figure 7.13: Plot qs2 sigma11 versus q2 strength measured and fit values

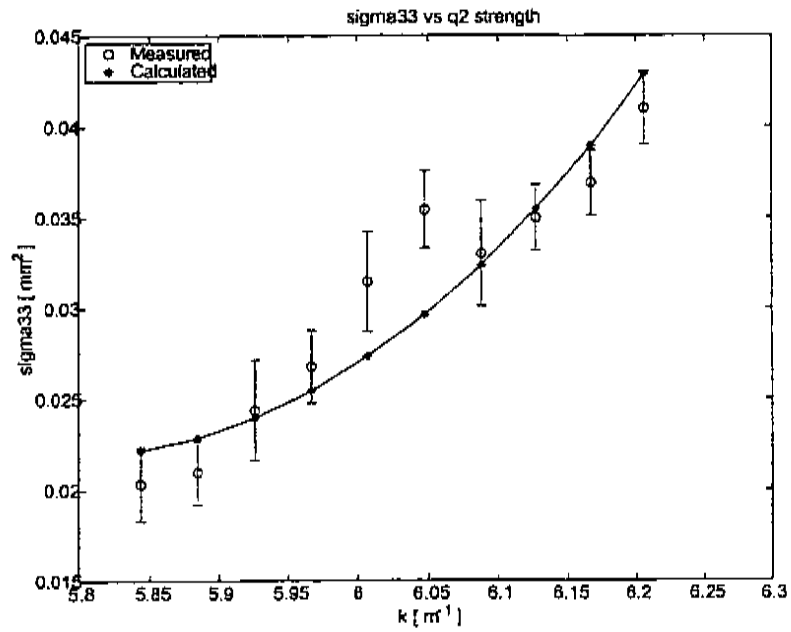


Figure 7.14: Plot qs2 sigma33 versus q2 strength measured and fit values

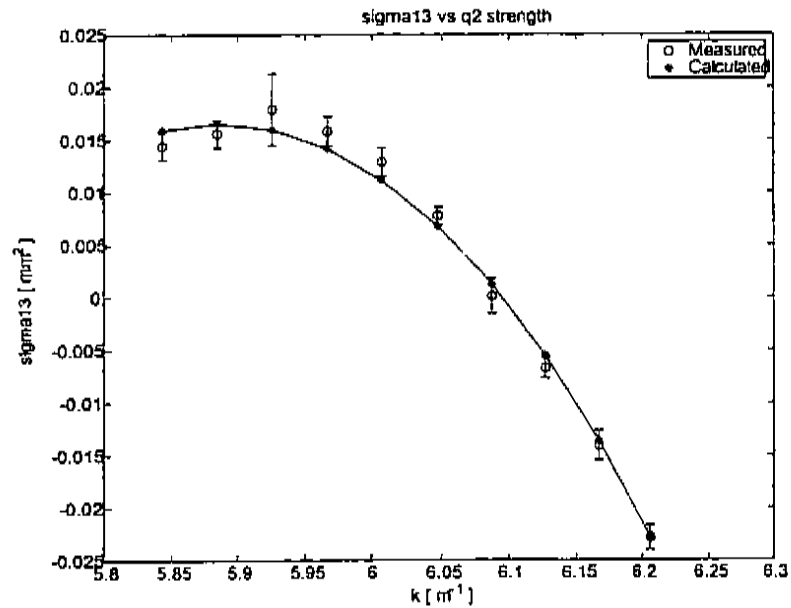


Figure 7.15: Plot qs2 sigma13 versus q2 strength measured and fit values

7.4.5 qs3 Isol=150A

$$V_{4-D} = 0.80 \pm .35 \text{ [(mm mr)}^2\text{]}$$

$$\frac{1}{2}\epsilon_x\epsilon_y = 5.41 \pm .41 \text{ [(mm mr)}^2\text{]}$$

$$\epsilon_x = 8.54 \pm .27 \text{ [mm mr]}$$

$$\epsilon_x = 1.27 \pm .08 \text{ [mm mr]}$$

$$\epsilon_* = 1.27 \text{ [mm mr]}$$

$$\chi^2 = 69$$

$$\frac{\chi^2}{30} = 2.30$$

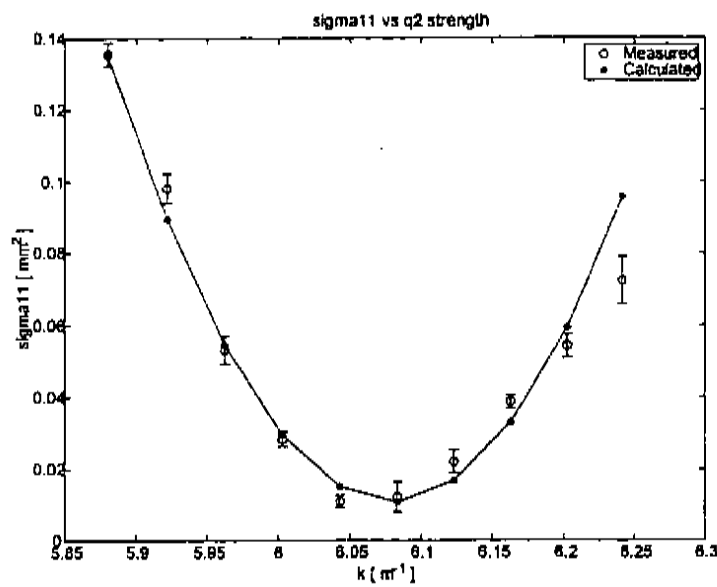
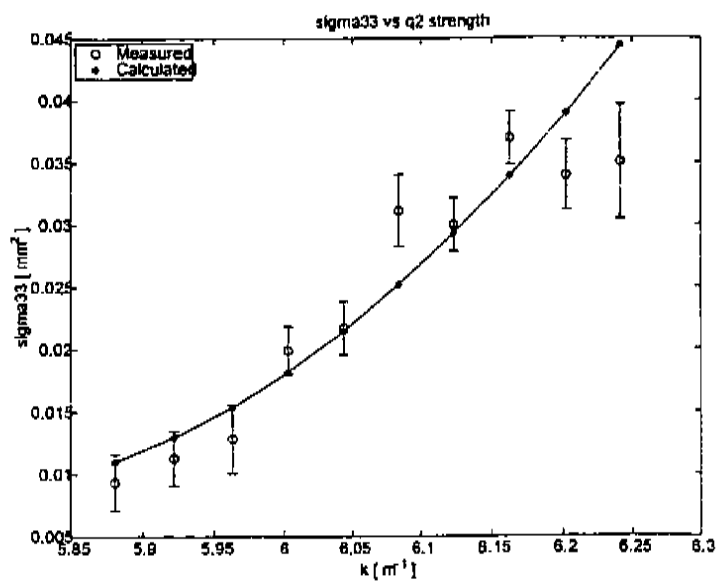
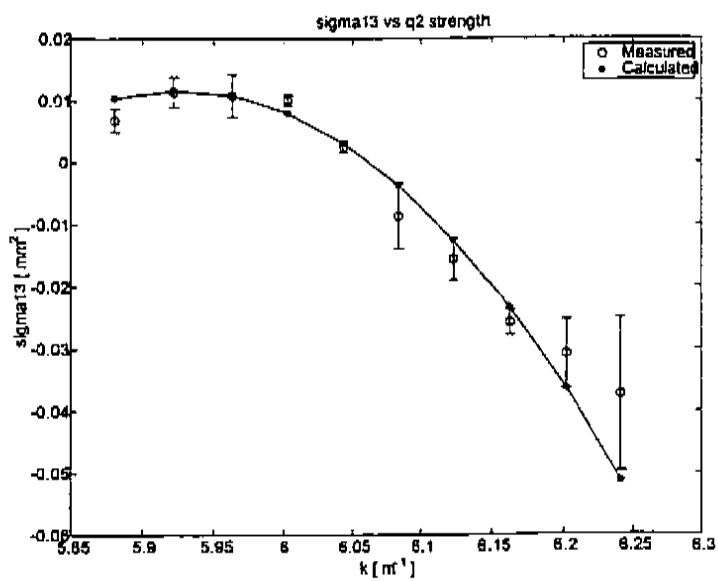


Figure 7.16: Plot qs3 sigma11 versus q2 strength measured and fit values

Figure 7.17: Plot qs_3 σ_{33} versus q_2 strength measured and fit valuesFigure 7.18: Plot qs_3 σ_{13} versus q_2 strength measured and fit values

7.4.6 qs4 Isol=142A

$$V_{4-D} = 0.72 \pm .10 \text{ [(mm mr)}^2\text{]}$$

$$\frac{1}{2}\epsilon_x\epsilon_y = 5.89 \pm .20 \text{ [(mm mr)}^2\text{]}$$

$$\epsilon_x = 6.59 \pm .12 \text{ [mm mr]}$$

$$\epsilon_z = 1.79 \pm .06 \text{ [mm mr]}$$

$$\epsilon_* = 1.20 \text{ [mm mr]}$$

$$\chi^2 = 35$$

$$\frac{\chi^2}{30} = 1.17$$

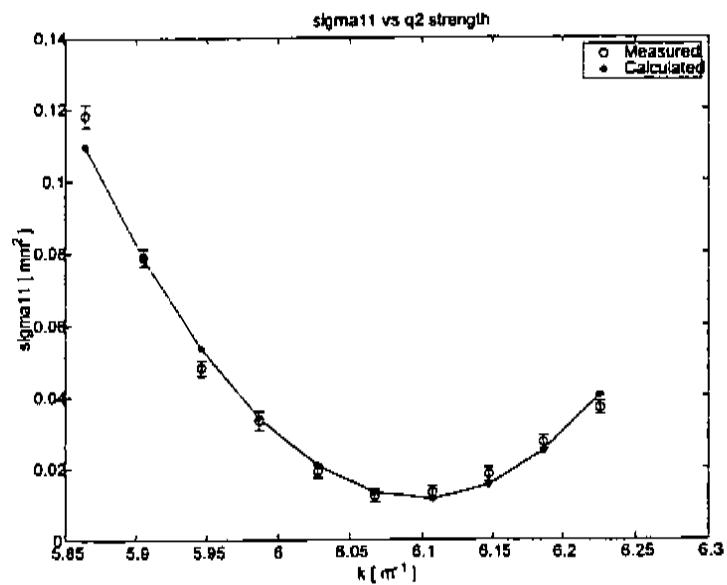


Figure 7.19: Plot qs4 sigma11 versus q2 strength measured and fit values

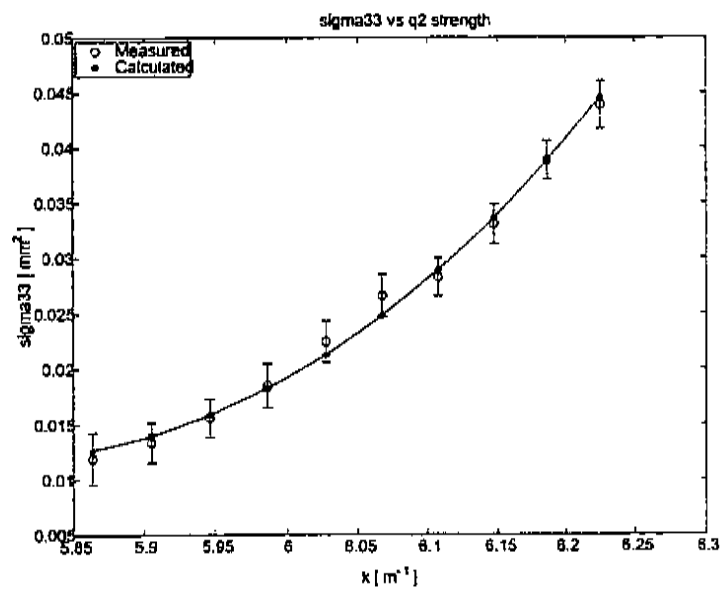


Figure 7.20: Plot qs4 sigma33 versus q2 strength measured and fit values

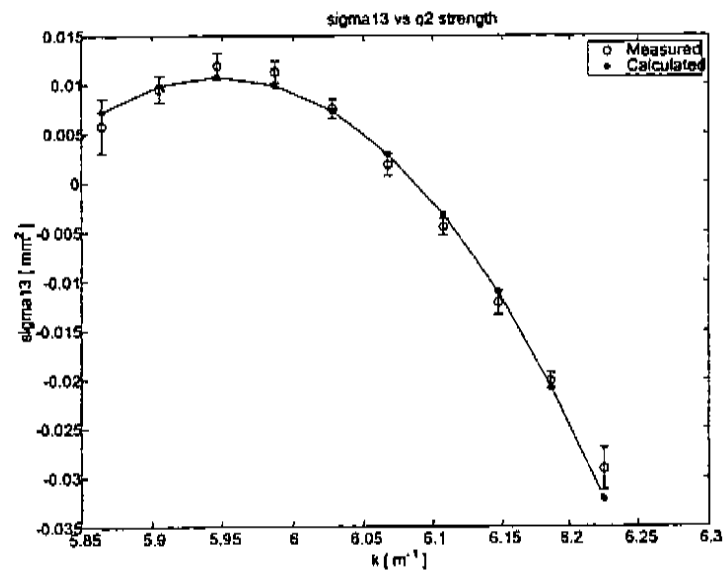


Figure 7.21: Plot qs4 sigma13 versus q2 strength measured and fit values

7.4.7 qs5 Isol=147A

$$V_{4-D} = 0.72 \pm .10 [(\text{mm mr})^2]$$

$$\frac{1}{2}\epsilon_x\epsilon_y = 9.94 \pm .16 [(\text{mm mr})^2]$$

$$\epsilon_z = 6.09 \pm .05 [\text{mm mr}]$$

$$\epsilon_x = 3.26 \pm .03 [\text{mm mr}]$$

$$\epsilon_y = 1.20 [\text{mm mr}]$$

$$\chi^2 = 29$$

$$\frac{\chi^2}{30} = 0.97$$

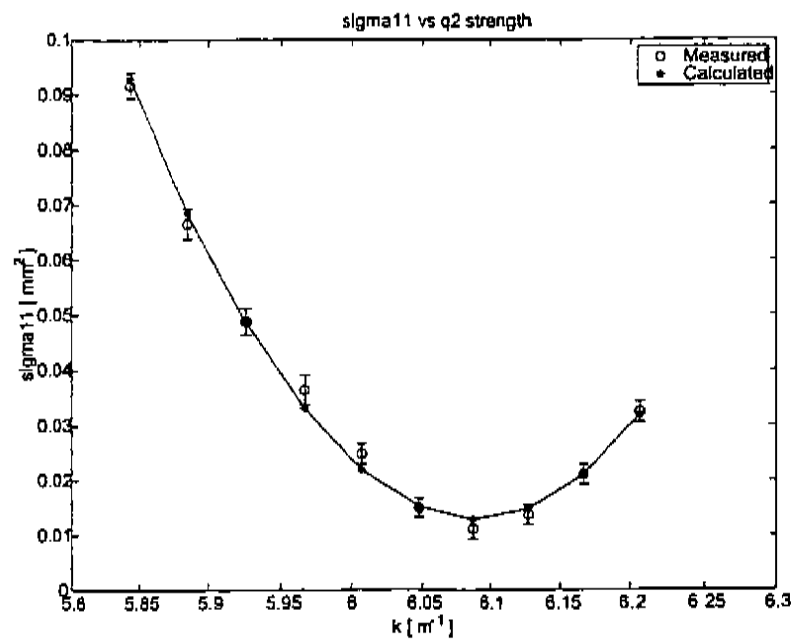


Figure 7.22: Plot qs5 sigma11 versus q2 strength measured and fit values

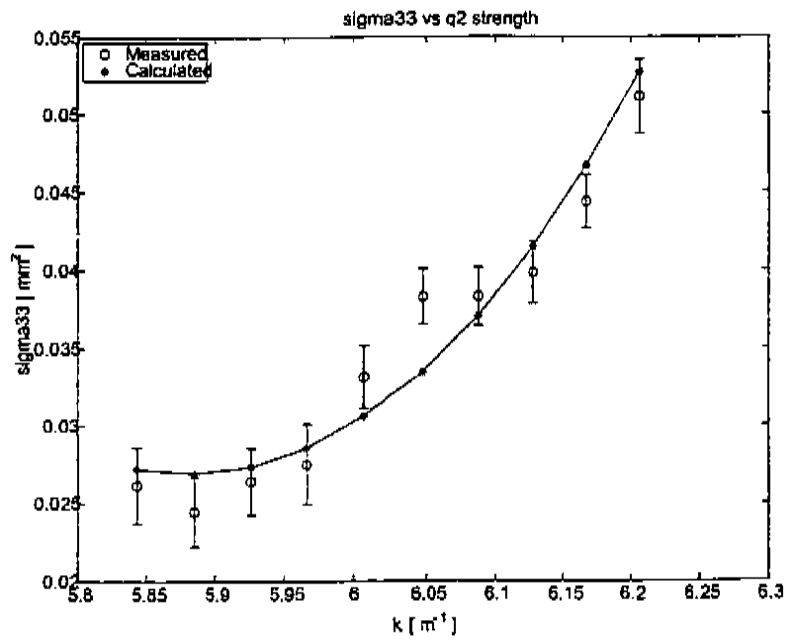


Figure 7.23: Plot qs5 sigma33 versus q2 strength measured and fit values

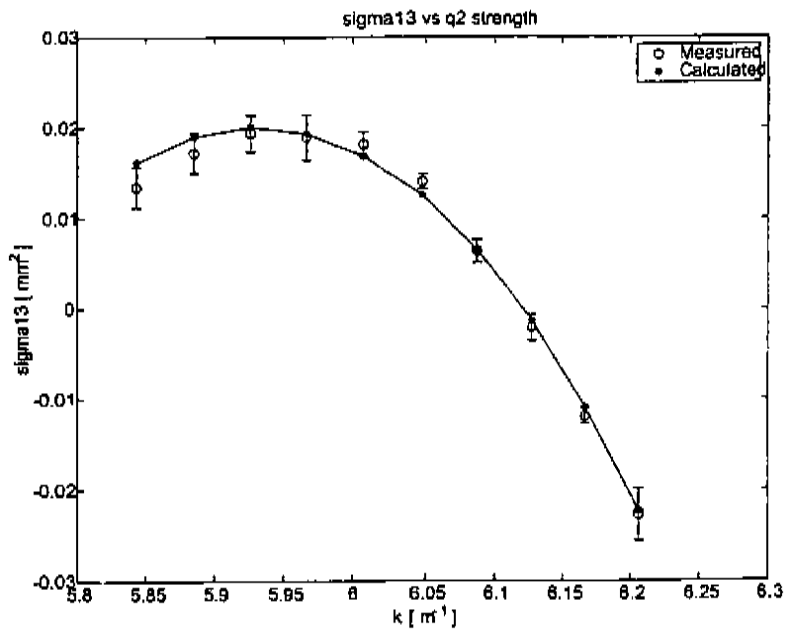


Figure 7.24: Plot qs5 sigma13 versus q2 strength measured and fit values

7.5 Discussion Of Results

All of the χ^2 fits can be considered "good fits" since $\chi_{dof=30}^2 \leq 1$ for qs1,qs2 and qs5 and $\chi_{dof=30}^2 \simeq 1$ for qs4, and $\chi_{dof=30}^2 \simeq 2$ for qs3 both of which are not $\gg 1$. In interpreting the fits one must be aware of the change of scale in the plots which influences the overall size of the error bars which are a function of the uncertainty of the associated data point. The qs3 scan was performed at the highest solenoid setting and the greater value for $\chi_{dof=30}^2 \simeq 2$ may be due to the presence of structure in the electron beam which may have been made more predominant at the higher solenoid setting. I believe this is true since in the plot for σ_{11} vs k_{q2} for qs3 the data point for the highest value of k_{q2} does not fit the calculated curve and the last two data points appear to be indicating some deviation from the expected growth in beam size as the beam is defocused. The plots for σ_{11} vs k_{q2} for the rest of the quadrupole scans show an excellent agreement between measured and calculated values. Also the error bars for the highest values of k_{q2} for all of the plots for the qs3 data are quite large, this may be due to an instability in the output of the drive laser system. This would be reflected in the error bars since the uncertainty for each data point is a sum of the fixed uncertainty of the camera and frame grabber system plus the standard deviation from the five shots of the beam which make up each data point of the plots. Also the quadrupole scans were taken in the sequence qs1 $I_{sol} = 140$ A, qs2 $I_{sol} = 145$ A, qs3 $I_{sol} = 150$ A, qs4 $I_{sol} = 142$ A, and qs5 $I_{sol} = 145$ A as discussed previously. The machine experienced an RF breakdown after qs3 which led an arc in the gun that 'tripped' the MPS (Machine Protection System.) This shuts the accelerator down by removing the RF triggers to the klystrons. There may have been some smaller arcs in the gun which may have influenced the charge distribution of the last few data points for qs3. Since the machine ran without interruption, the quadrupole scans qs1, qs2 and qs3 were performed under similar machine conditions. The quad scan qs4, $I_{sol} = 142$ A, was performed after restarting the RF system which entails re-establishing the RF levels in the gun and linac, re-phasing the laser injection to the gun and linac phase, and measuring the charge. All of those values were checked before each quadrupole scan but all of the associated systems were on at

operational levels not restarted after a machine trip. In the case of qs4 there was 180 pC produced for the what were believed to be the same RF levels and phasing, the quadrupole scans qs1, qs2 and qs3 were performed with 200 pC. This discrepancy in charge may have been due to some degradation of the efficiency of the cathode from by-products of the arcing in the gun. Or the field levels in the gun after RF recovery may have been lower than those in the previous quadrupole scans, this would lead to a lower amount of charge produced for the same laser energy. This seems unlikely since the field levels were returned to the values used in the previous quadrupole scans as determined by the field probe in the gun. The laser output as monitored by a Joule meter in the linac vault indicated the same amount of UV incident on the cathode as in the previous quadrupole scans. In order to use the same charge in qs4, I increased the output of the laser slightly. In retrospect I might have investigated this discrepancy in charge and implemented a different solution but at the time the solution of boosting the laser output seemed reasonable. Also after the completion of quadrupole scan qs4 there was a vacuum trip due to higher pressure in the gun than the MPS system set point. This also shuts the RF to the accelerator and this type of "trip" closes a valve to the gun to protect the cathode. The recovery from this trip required waiting for the ion pumps to bring the gun to an acceptable vacuum before the starting the RF to the accelerator. When the vacuum has recovered the RF system must be brought as described previously. So the quadrupole scans qs4 and qs5 were not performed at exactly the same conditions as the first three scans. However, I do not believe these differences produced significant effects in the final values for the normalized V_{4-D} in comparison with the deviation between the normalized V_{4-D} and the projected normalized quantity $\frac{1}{2}\epsilon_x\epsilon_y$. Plots of the normalized V_{4-D} versus solenoid strength and normalized V_{4-D} plus the projected normalized quantities ϵ_x , ϵ_y and $\frac{1}{2}\epsilon_x\epsilon_y$ are presented below.

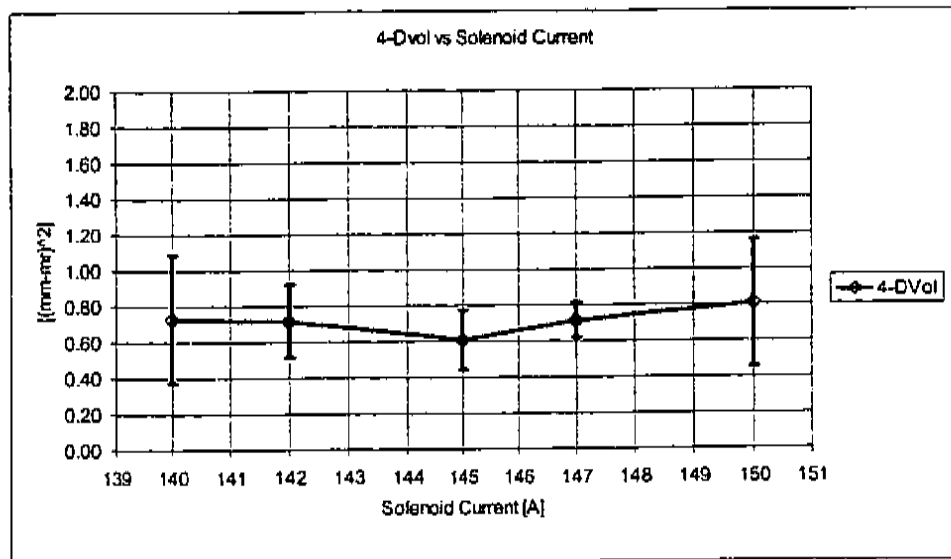


Figure 7.25: Normalized V_{4-D} vs Solenoid Strength

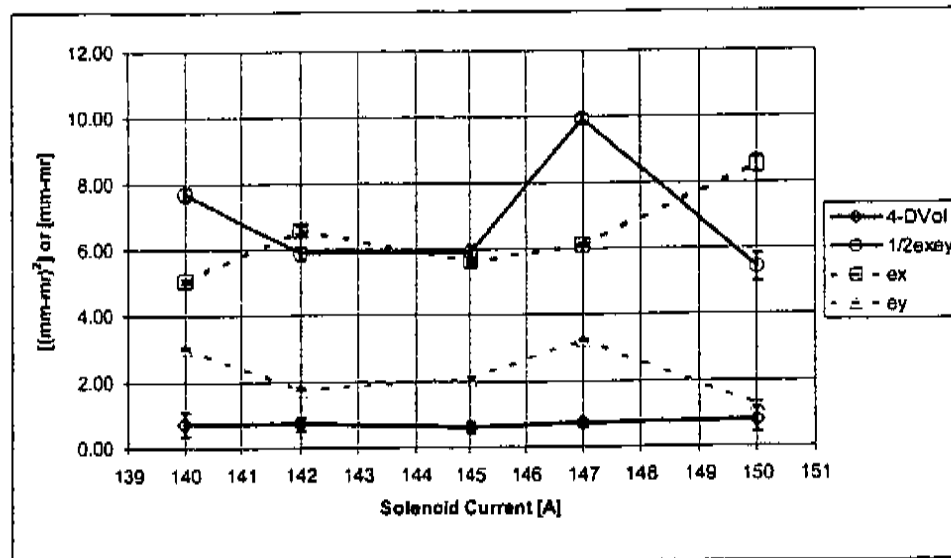


Figure 7.26: Normalized V_{4-D} and projected quantities ϵ_x , ϵ_y and $\frac{1}{2}\epsilon_x\epsilon_y$ vs solenoid strength

In all of the quadrupole scans there is coupling between the transverse coordinates of the beam at the doublet entrance as is indicated by presence of $|r_{13}| > 0$ in all of the quadrupole scans as shown in section 7.4.1. Therefore the projected normalized quantities ϵ_x , ϵ_y and $\frac{1}{2}\epsilon_x\epsilon_y$ are not conserved. From simulations of Chap. 5 a 4 - D symmetric beam subject to a single rotation which is relatively free of error in using projected quantities would have $|r_{13}| \leq 0.01$ for a quadrupole scan. In all of the quadrupole scans presented the transverse couplings are quite strong since the maximum values of $|r_{13}| \geq .6$ in all of the plots. This is reflected in the reduced data, Fig. 7.26, which shows that the projected normalized quantities ϵ_x , ϵ_y and $\frac{1}{2}\epsilon_x\epsilon_y$ are not conserved for the variation of the solenoid strength which changes the transverse coupling in the electron beam. In contrast, in Figs 7.25 and 7.26 the normalized V_{4-D} is constant within the uncertainty of the measurement process for all solenoid settings. The slight variation in the normalized V_{4-D} with solenoid strength may be due to higher order effects, structure in the electron beam distributions, or possible transverse-longitudinal coupling effects. However due to the size of the uncertainty in the measurements of normalized V_{4-D} I do not believe I can assign any significance to the slight variation. The change in the size of the error bars in Figs 7.25 and 7.26 for each data point is mainly due to fluctuations in the laser system. The laser drives the cathode producing the photoelectrons and forms the masterclock of the system. The uncertainty in the measurements is found by combining the fixed resolution of the measurement system and the standard deviation of the data for the images from five shots taken at each quadrupole setting. Recall the uncertainty in the fits for the sigma vector $\vec{\sigma}(0)$ at the quadrupole doublet entrance that is used to determine the V_{4-D} was determined by using Monte Carlo methods that utilized the uncertainty from the individual measurements. Therefore to reduce the error bars and so uncertainty in the measurements of V_{4-D} , the resolution of the imaging system and the laser stability must be improved. A camera and frame grabber with more bits (>8 bits) and a camera with more pixels would increase the resolution of the imaging system. The laser stability could be improved by moving to a diode pumped system instead of the current flash lamp pumped system and investigating cavity stability of both the regen and oscillator. The variation in the value of the normalized V_{4-D} with

solenoid is a much smaller effect than the difference between normalized V_{4-D} and the normalized projected quantity $\frac{1}{2}\epsilon_x\epsilon_y$ as shown in Fig. 7.26. At all of the solenoid settings $V_{4-D} \leq \frac{1}{2}\epsilon_x\epsilon_y$ and the relative difference between the two quantities vary by up to a factor of $\frac{9.94}{.72} = 13.8$ for qs5. Therefore the normalized brightness of the beam is actually an order of magnitude higher if the effects of the transverse coupling in the beam are properly taken into account.

The goal of the GTF was to produce a high brightness electron beam with 1 nC of charge in a temporal duration of 10 ps FWHM and with a normalized projected emittance of 1 mm mrad. With these parameters the beam would have a peak current of:

$$I_{\text{peak}} = \frac{1 \text{ nC}}{10 \text{ ps}} = 100 \text{ A}$$

Assuming no transverse coupling and $\epsilon_x = \epsilon_y = 1$ [mm mrad] the normalized brightness of the beam would be:

$$B_n = \frac{I_{\text{peak}}}{\frac{1}{2}\epsilon_x\epsilon_y} = \frac{100 \text{ A}}{\frac{1}{2}(1 \text{ mm mrad})^2} = 200 \frac{\text{A}}{(\text{mm mrad})^2}$$

For the experimental data presented above the measurement qs2 with $I_{\text{sol}} = 145 \text{ A}$ gave the lowest value for the normalized $V_{4-D} = .61 (\text{mm mrad})^2$. This beam contained .2 nC using a 3 ps FWHM laser pulse on the cathode. I was unable to measure the temporal duration of the electron beam so in order to compare the best measurement with the GTF goal I will use the laser pulse temporal duration as an estimate for the electron beam temporal distribution. Then the estimated peak current of the electron beam will be:

$$I_{\text{peak-est}} = \frac{.2 \text{ nC}}{3 \text{ ps}} = 66.7 \text{ A}$$

And since the measurements of the electron beam contain non-zero r_{13} the V_{4-D} must

be utilized in the normalized brightness relation:

$$B_{n\text{-est}} = \frac{I_{\text{peak-est}}}{V_{4\text{-D}}} = \frac{66.7 \text{ A}}{.61 (1 \text{ mm mrad})^2} = 109 \frac{\text{A}}{(\text{mm mrad})^2}$$

where '-est' indicates an estimated quantity. This estimated normalized brightness is less than a factor of 2 from the GTF goal, $200 \frac{\text{A}}{(\text{mm mrad})^2}$ which is an encouraging result. In comparison the estimated normalized brightness using the non-conserved (since $r_{13} \neq 0$) quantity $\frac{1}{2} \epsilon_x \epsilon_y$ is:

$$\tilde{B}_{n\text{-est}} = \frac{I_{\text{peak-est}}}{\frac{1}{2} \epsilon_x \epsilon_y} = \frac{66.7 \text{ A}}{5.88 (1 \text{ mm mrad})^2} = 11 \frac{\text{A}}{(\text{mm mrad})^2}$$

where the tilde, $\tilde{B}_{n\text{-est}}$, indicates this is a non-conserved quantity. This non-conserved quantity is almost 20 times the goal of the GTF and an order of magnitude smaller than the conserved quantity the normalized $V_{4\text{-D}}$. Clearly if the transverse coupling in the electron beam could be removed the electron beam measured in this thesis would be an excellent starting point for further work.

7.6 Conclusions

In this thesis I have demonstrated the effects of transverse coupling on the emittance measurements of an electron beam which utilizes the quadrupole scan technique. If there is coupling between the transverse dimensions of the beam then the projected quantities such as ϵ_x , ϵ_y and $\frac{1}{2} \epsilon_x \epsilon_y$ are not conserved and the $V_{4\text{-D}}$ of the beam is the conserved quantity. Transverse coupling in the beam can be produced by the rotations present at the entrance and exit of a solenoid magnet or by rotations of beamline elements such as quadrupoles. If there is asymmetry in the electron beam distribution due to the laser or uneven production of electrons from the cathode, or due to higher order modes in the gun or solenoid, this asymmetry combined with rotations produces coupling effects which influence the measured projected values

from the quadrupole scan technique.

The presence of coupling of the transverse dimensions of the beam can be detected by examining the $x - y$ correlation (the σ_{13} beam matrix term) in the beam distributions at the screen location of a quadrupole scan. A non-zero value for σ_{13} is generated only if one or more of the beam matrix elements σ_{13} , σ_{14} , σ_{23} or σ_{24} are non-zero in the initial beam distribution that is being sampled. The beam matrix elements σ_{13} , σ_{14} , σ_{23} and σ_{24} represent coupling between the transverse dimensions of the beam. Further the normalized quantity $-1 \leq r_{13} = \frac{\sigma_{13}}{\sqrt{\sigma_{11}\sigma_{33}}} \leq 1$ found from the beam distributions at the screen location of a quadrupole scan provides a measure of the strength of the coupling of the transverse dimensions of the beam. If $|r_{13}| > 0$ the projected quantities ϵ_x , ϵ_y and $\frac{1}{2}\epsilon_x\epsilon_y$ are not conserved and one must use the V_{4-D} as the conserved quantity. Practically there will always be some amount of r_{13} present in the beam. If $|r_{13}|$ is close to one then the coupling of the transverse dimensions is strong and the projected quantities will definitely not be conserved and if $|r_{13}|$ is close to zero then the projected quantities will be approximately conserved.

I have demonstrated how to calculate the V_{4-D} for beam distributions in simulations and shown that it is immune to the effects of coupling of the transverse dimensions of the beam. This is expected since in the presence of rotations the determinant of the transfer matrices used in beam propagation is equal to one for the four dimensional transforms while the determinant is not equal to one for two dimensional transformations. I have formulated a method to measure the V_{4-D} of an electron beam using information available in the laboratory environment. This method was shown to work for simulated beams and for beams measured in the laboratory if the limited resolution of the measurement technique is taken into account. Applying these concepts to experimental data from the GTF indicated the presence of strong coupling between the transverse dimensions of the beam, since the maximum value of $|r_{13}| \geq .6$ for all quadrupole scans. Therefore the V_{4-D} of the beam must be used in order to obtain a conserved quantity. Utilizing the method of four dimensional trace space measurement I have shown that there is a significant difference between the V_{4-D} and the projected quantity $\frac{1}{2}\epsilon_x\epsilon_y$ for the quadrupole scans. If an estimate of the peak current for the experimental data is used, the brightness of electron beam at the GTF

is within a factor of two from the goal which is an encouraging result.

7.7 Future

Future work would be the extension of the analysis to the full 6 – D volume and the calculation of the additional transverse-longitudinal couplings and correlation coefficients of the beam distribution. I began this work in the PARMELA simulations of Chap. 6. The simulations should be extended to include variation in linac phase and to include bending magnets. This is important since linac phase and bending magnets can be used to manipulate the longitudinal phase space and the coupling of the transverse (bend plane) and longitudinal dimensions of the beam respectively. A full understanding of the beam orientation in six dimensional phase space would be valuable. A new quantity that includes the transverse-longitudinal couplings to replace the normalized brightness must be formulated. While this may seem straightforward there may be complications due to the structure of the distributions in longitudinal phase space. The fields used to accelerate the beam are nonlinear and from PARMELA simulations the longitudinal distributions can be rather complicated. The second moments of the distribution may not be sufficient to fully describe the longitudinal distribution under all conditions. This may either complicate or possibly make the energy normalization of the information more clear. One may consider the normalization of the emittance a bit simplistic since it involves assigning a single number to represent a longitudinal distribution with structure. By utilizing the brightness at least the temporal extent of the distribution is included. The point is that more information about the dimensions and orientation of the distribution in phase space is valuable. And this information may be useful when matching the beam to devices where the beam interacts with other particles or fields.

In the laboratory environment a measurement technique to determine the 6 – D volume and all of the associated couplings and correlation coefficients must be formulated. This may involve utilizing a combination of quadrupole scans, dispersive elements and linac phases. One would check for transverse couplings by sampling r_{13} before a dispersive section to ensure no transverse couplings and thereby reduce

the number of variables that must be solved for. Then by including the transverse-longitudinal coupling terms in the expression for the beam width after a dispersive section one could determine those couplings.

The quantity r_{13} can be used as a measure of success in alignment of beamline elements or the quality of the fields of beamline elements. And r_{13} could be used as a measure of the success in reducing asymmetries in the electron beam distribution. This would be indicated by the minimization of the measured r_{13} in a quadrupole scan measurement after the element or beam source under consideration. For example in the RF photoinjector at the GTF one would remove the solenoid and install a set of quadrupoles to perform a quadrupole scan after the gun. The quadrupole scan would be performed with the quadrupoles aligned with the beamline and then with the quadrupoles rotated by 45° . The first measurement would detect any rotated asymmetry or coupling between the transverse dimensions of the beam and the second measurement would detect any asymmetry between the horizontal and vertical dimensions which would not be detected by the first measurement. Any asymmetry in the distribution would lead to an excitation of the transverse coupling elements by the rotations present in the solenoid when it is in place after the gun. When the beam is determined to have minimal r_{13} correlation after the gun, the solenoid would be replaced and the same quadrupole scan would be performed after the solenoid. This would determine if the solenoid is free from higher order modes such as a quadrupole mode that would lead to an asymmetry in the distribution before the rotation at the solenoid exit. This process would be repeated after the linac and other beamline elements. Finally a series of quadrupoles that could be rotated could be placed before sections of the beamline which require precise beam alignment to remove any residual correlations present in the beam. The orientation of the quadrupoles would be determined by four dimensional trace space analysis of the beam.

Bibliography

- [1] The LCLS Design Study Group, *LCLS Design Study Report*. Technical Report, SLAC-R-521,1998
- [2] J.D. Lawson, *The Physics Of Charged-Particle Beams* 2nd Edition, (Oxford University Press, Oxford 1988) pp158
- [3] C. Lejeune and J. Aubert, in Supplement 13A of *Advances in Electronics and Electron Physics*, (Academic Press, New York, 1983) pp168
- [4] M. Reiser, *Theory And Design Of Charged Particle Beams*, (Wiley-Interscience, New York 1994) pp61
- [5] J.D. Lawson, *The Physics Of Charged-Particle Beams* 2nd Edition, (Oxford University Press, Oxford 1988) pp160
- [6] H. Goldstein, *Classical Mechanics*, (Addison Wesley, Reading, Mass, 1980) pp342
- [7] C. Lejeune and J. Aubert, in Supplement 13A of *Advances in Electronics and Electron Physics*, (Academic Press, New York, 1983) Section A
- [8] D. Carey, *The Optics of Charged Particle Beams*, (Harwood Academic Publishers, 1987) pp35
- [9] C. Lejeune and J. Aubert, in Supplement 13A of *Advances in Electronics and Electron Physics*, (Academic Press, New York, 1983) pp173
- [10] D. Carey, *The Optics of Charged Particle Beams*, (Harwood Academic Publishers, 1987) pp102

- [11] H. Wiedemann, *Particle Accelerator Physics*, Vol I (Springer-Verlag, Berlin, 1993) pp340
- [12] H. Wiedemann, *Particle Accelerator Physics*, Vol I (Springer-Verlag, Berlin, 1993) Sec 12.2
- [13] H. Wiedemann, *Particle Accelerator Physics*, Vol I (Springer-Verlag, Berlin, 1993) Sec 9.2.2
- [14] B.E. Carlsten, "New Photoelectric Injector Design For The Los Alamos National Laboratory XUV FEL," *Nucl. Instrum. Method. Phys. Res.*, A285:313, 1989
- [15] L. Serafini and J.B. Rosenzweig, "Envelope analysis of intense relativistic quasilaminar beams in rf photoinjectors: A theory of emittance compensation," *Phy. Rev. E*, Vol 55 number 6, pp7565-7590, June 1997
- [16] B.E. Carlsten, "Space Charge Induced Emittance Compensation In High-Brightness Photoinjectors," *Particle Accelerators*, Vol 49, pp27-65, 1995
- [17] S. Yencho and D.R. Walz, "A High Resolution Phosphor Screen Beam Profile Monitor," *IEEE Trans.*, 23:2009-2011,1985
- [18] D. Greenwood, *Classical Dynamics*, (Dover, Mineola, New York, 1977) pp168
- [19] M. Spiegel, *Mathematical Handbook of Formulas and Tables*, (Schaum's Outline Series, McGraw-Hill, New York 1968)
- [20] H. Wiedemann, *Particle Accelerator Physics*, Vol I (Springer-Verlag, Berlin, 1993) pp76
- [21] A. Lichtenberg, *Phase Space Dynamics Of Particles*, (John Wiley & Sons, New York, 1969) pp101
- [22] S Friedberg, *Introduction to Linear Algebra with Applications* (Prentice-Hall, Englewoodcliffs , New Jersey, 1986) pp318

- [23] H. Wiedemann, *Particle Accelerator Physics*, Vol I (Springer-Verlag, Berlin, 1993) pp149
- [24] H. Wiedemann, *Particle Accelerator Physics*, Vol II (Springer-Verlag, Berlin, 1993) pp39
- [25] J.D. Lawson, *The Physics Of Charged-Particle Beams* 2nd Edition, (Oxford University Press, Oxford 1988) pp158
- [26] H. Goldstein, *Classical Mechanics*, (Addison Wesley, Reading, Mass, 1980) pp331
- [27] H. Wiedemann, *Particle Accelerator Physics*, Vol I (Springer-Verlag, Berlin, 1993)
- [28] D. Carey, *The Optics of Charged Particle Beams*, (Harwood Academic Publishers, 1987)
- [29] D. Carey, *The Optics of Charged Particle Beams*, (Harwood Academic Publishers, 1987) pp35
- [30] H. Wiedemann, *Particle Accelerator Physics*, Vol I (Springer-Verlag, Berlin, 1993) Sec 5.2
- [31] K. Steffen, *High Energy Beam Optics*, (John Wiley & Sons, New York, 1965)
- [32] K.L. Brown, F. Rothacker, D. Carey, and Ch. Iselin, *TRANSPORT*, SLAC-91, CERN-73, NAL-91, 1977
- [33] D. Carey, *The Optics of Charged Particle Beams*, (Harwood Academic Publishers, 1987) Sec 6.1
- [34] H. Wiedemann, *Particle Accelerator Physics*, Vol I (Springer-Verlag, Berlin, 1993) pp158
- [35] W. Eadie, D. Drijard, F. James, M. Roos, B. Sadoutet, *Statistical Methods In Experimental Physics* (North-Holland Publishing Company, New York 1977) Section 8.4

- [36] W.H. Press, S.A. Teukolsky, W.T. Vetterling, B.P. Flannery, *Numerical Recipes in C* 2nd Edition, (Cambridge University Press, Cambridge 1992) Sec15.4
- [37] MATLAB, version 5.3.0 R11 (The MathWorks Inc 1999)
- [38] R.W. Hockney, J.W. Eastwood, *Computer Simulations Using Particles*, (IOP Publishing LTD, Philadelphia, 1988)
- [39] H. Wiedemann, *Particle Accelerator Physics*, Vol II (Springer-Verlag, Berlin, 1993) pp91
- [40] D. Reis and M. Hernandez, et al, "Transverse emittance measurements from a photocathode RF gun with variable laser pulse length," Nucl. Instrum. Method. Phys. Res., A429:341-346, 1999
- [41] K.L. Brown, F. Rothacker, D. Carey, and Ch. Iselin, *TRANSPORT*, SLAC-91, CERN-73, NAL-91, 1977 pp6
- [42] C. Lejeune and J. Aubert, in Supplement 13A of *Advances in Electronics and Electron Physics*, (Academic Press, New York, 1983) pp176
- [43] D. Carey, *The Optics of Charged Particle Beams*, (Harwood Academic Publishers, 1987) pp205
- [44] H. Anton, *Elementary Linear Algebra* 3rd Edition, (John Wiley & Son, New York 1981) pp162
- [45] C. Lejeune and J. Aubert, in Supplement 13A of *Advances in Electronics and Electron Physics*, (Academic Press, New York, 1983) pp189
- [46] L.M. Young, *PARMELA*, Los Alamos National Laboratory, LA-UR-96-1835
- [47] D. Reis, *Emittance Measurements From A Laser Driven Electron Injector*, Ph.D. thesis (University of Rochester, Rochester, New York 1999)
- [48] Private Communication X.J. Wang Brookhaven National Laboratory

- [49] K. Kim, "RF And Space-Charge Effects In Laser-Driven RF Electron Guns," Nucl. Instrum. Method. Phys. Res., A275:201, 1989
- [50] Private Communication B. Eittlebrick Positive Light Laser Corporation
- [51] E. Part-Enanjer, A. Sjoberg, B. Melin and P. Isaksson, *The Matlab Handbook*, (Addison-Wesley, Reading, Mass 1996) pp124
- [52] W.H. Press, S.A. Teukolsky, W.T. Vetterling, B.P. Flannery, *Numerical Recipes in C* 2nd Edition, (Cambridge University Press, Cambridge 1992) Sec 15.1
- [53] MATLAB, version 5.3.0 R11 (The MathWorks Inc 1999)
- [54] W.H. Press, S.A. Teukolsky, W.T. Vetterling, B.P. Flannery, *Numerical Recipes in C* 2nd Edition, (Cambridge University Press, Cambridge 1992) Sec 15.6
- [55] W. Eadie, D. Drijard, F. James, M. Roos, B. Sadoutet, *Statistical Methods In Experimental Physics* (North-Holland Publishing Company, New York 1977)Section 8.4